micromachines

Special Issue Reprint

Design and Fabrication of Micro/Nano Sensors and Actuators

Edited by
Weidong Wang and Ruiguo Yang

mdpi.com/journal/micromachines

MDPI

Design and Fabrication of Micro/Nano Sensors and Actuators

Design and Fabrication of Micro/Nano Sensors and Actuators

Editors

Weidong Wang
Ruiguo Yang

MDPI

Basel • Beijing • Wuhan • Barcelona • Belgrade • Novi Sad • Cluj • Manchester

Editors

Weidong Wang
School of Mechano-Electronic Engineering
Xidian University
Xi'an
China

Ruiguo Yang
Department of Mechanical and Materials Engineering
University of Nebraska-Lincoln
Lincoln
United States

Editorial Office
MDPI
Grosspeteranlage 5
4052 Basel, Switzerland

This is a reprint of articles from the Special Issue published online in the open access journal *Micromachines* (ISSN 2072-666X) (available at: www.mdpi.com/journal/micromachines/special_issues/Design_Micro_Nano_Sensors_Actuators).

For citation purposes, cite each article independently as indicated on the article page online and as indicated below:

Lastname, A.A.; Lastname, B.B. Article Title. *Journal Name* **Year**, *Volume Number*, Page Range.

ISBN 978-3-7258-1544-9 (Hbk)
ISBN 978-3-7258-1543-2 (PDF)
doi.org/10.3390/books978-3-7258-1543-2

Contents

About the Editors

Weidong Wang

Dr. Weidong Wang received his B.S., M.S., and Ph.D. degrees from Xidian University in 2000, 2003, and 2007, respectively. He is a full-time professor at the School of Mechano-Electronic Engineering, Xidian University. He is also the Director of the Research Center of Micro-Nano Systems and Deputy Director of the CityU-Xidian Joint Lab of Micro/Nano-Manufacturing. Additionally, he holds senior membership positions in other professional societies, including the IEEE (Institute of Electrical and Electronics Engineers), the CSMNT (Chinese Society of Micro-Nano Technology), the CMES (Chinese Mechanical Engineering Society), etc. He mainly engages in research on micro/nano-electromechanical systems (MEMS/NEMS), flexible sensing, and Internet of Things (IoT) technologies.

Ruiguo Yang

Dr. Ruiguo Yang received his Bachelor's degree and Master's degree in Mechanical Engineering from Nanjing University of Aeronautics and Astronautics, Nanjing, China, in 2004 and 2007, respectively, and his Ph.D. degree in Electrical Engineering from Michigan State University in 2014. From 2014 to 2016, he was a postdoctoral fellow at the Department of Mechanical Engineering at Northwestern University. He is an Associate Professor of Biomedical Engineering at the Department of Mechanical and Materials Engineering, University of Nebraska-Lincoln. His current research interests include bioMEMS and mechanobiology.

Preface

With the rapid development of materials science and manufacturing technology, numerous novel MEMS and NEMS devices, such as micro/nano-sensors and micro/nano-actuators, have been developed and applied in various fields. These devices are mostly made of silicon, metals, ceramics, glass, etc., whose mechanical and electrical properties have had a great influence on their working characteristics, including accuracy, sensitivity, and working range. In addition, the design and fabrication method can directly affect the reliability of these MEMS and NEMS devices, especially their lifetime, robustness, and stability under extreme conditions of shock, temperature, humidity, irradiation, chemical exposure, or other challenges. This Special Issue focuses on the structural design and optimization, system modeling and simulation, manufacturing, in situ characterization, and testing technologies of micro/nano-sensors and -actuators, providing research references for the further development and application of MEMS/NEMS devices.

Weidong Wang and Ruiguo Yang
Editors

micromachines

Editorial

Design and Fabrication of Micro/Nano Sensors and Actuators

Weidong Wang [1,*], Ruiguo Yang [2] and Min Liu [1]

[1] School of Mechano-Electronic Engineering, Xidian University, Xi'an 710071, China; mliu_12@stu.xidian.edu.cn
[2] Department of Mechanical and Materials Engineering, University of Nebraska-Lincoln, Lincoln, NE 68588, USA; ryang6@unl.edu
* Correspondence: wangwd@mail.xidian.edu.cn

A micro-electromechanical system (MEMS) is a micro device or system that utilizes large-scale integrated circuit manufacturing technology and microfabrication technology to integrate microsensors, micro-actuators, microstructures, signal processing and control circuits, power supplies, and communication interfaces into one or more chips [1]. There are many types of MEMS devices, mainly including MEMS sensors [2], MEMS converters [3], and MEMS actuators [4]. MEMS sensor components are used to detect various physical properties, such as pressure [5], temperature [6], acceleration [7], and angular velocity [8]. MEMS converters convert electrical signals into mechanical motion or vice versa, including the conversion of sound to electrical signals, and pressure to electrical signals [9]. MEMS actuators, integral to the functionality of MEMS devices, are engineered to facilitate precise mechanical movements at a microscale. They find application in a variety of domains, such as micromotors [10] and micro-valves [11].

MEMS devices are crafted from a variety of materials such as silicon, metal, ceramics, and glass, with the mechanical, electrical, and magnetic properties of these materials significantly influencing the operational performance of MEMS devices [12–15]. The mechanical strength and stiffness of materials determine the reliability and stability of devices [16]. Silicon materials have excellent mechanical and processing properties and are commonly used in the manufacturing of sensors and actuators [17]. Polymer materials or metal films are commonly used for making flexible MEMS devices [18]. The electrical properties of materials determine device attributes such as resistance, capacitance, and inductance, which directly affect its application in circuits [19]. Furthermore, the magnetic properties of materials are essential for specialized MEMS devices such as magnetic sensors and actuators. Tailoring these magnetic properties can significantly boost the sensitivity and stability of sensors, and enhance the precision and response time of actuators [20]. In summary, optimizing the properties of these materials can improve the accuracy, sensitivity, and reliability of MEMS devices, thereby expanding their application scope in various fields.

In addition, process manufacturing is critical to determine the performance and reliability of MEMS devices [21]. The accuracy and stability of process manufacturing directly affect the performance of devices [22]. The accuracy of micro/nano-processing technology determines the exact dimensions and configuration of the device structures, while the process stability of the process ensures the consistency and repeatability of the device. For example, the precise control of process steps such as photolithography, thin film deposition, and ion etching can ensure the accuracy and stability of the device structure, thereby improving the performance and reliability of the device [23,24].

This Special Issue encompasses 11 papers that explore various facets of MEMS/NEMS, including the design and optimization of MEMS devices (Contributions 1–7), micro/nano-materials of MEMS devices (Contributions 8), and micro-manufacturing processes of devices (Contributions 9–11).

In particular, Wei et al. (Contribution 1) designed a high-performance piezoelectric-type MEMS vibration sensor based on $LiNbO_3$ single-crystal cantilever beams. The proposed MEMS vibration sensor has a high output performance, linear dependence, and

check for updates

Citation: Wang, W.; Yang, R.; Liu, M. Design and Fabrication of Micro/Nano Sensors and Actuators. *Micromachines* **2024**, *15*, 674. https://doi.org/10.3390/mi15060674

Received: 13 May 2024
Accepted: 18 May 2024
Published: 22 May 2024

stable sensitivity, and is suitable for broadband high-frequency vibration detection. Zhao et al. (Contribution 2) investigated the effect of the micro-morphology of resistive strain gauges on the gauge factor. The study showed that periodic indentations on the sidewalls of the sensitive grid enhance local strain concentration and weaken strain distribution on the grid body, indicating that a rough microstructure can lead to a decreased strain coefficient, thereby reducing the accuracy and sensitivity of resistive strain gauges. Chen et al. (Contribution 3) proposed a micromechanical transmitter with only one bulk acoustic wave (BAW) magneto-electric (ME) antenna. A single-BAW ME antenna can replace traditional transmitter components and adjust the radiation power of the BAW ME antenna by increasing the input voltage in higher-order resonance modes. Guo et al. (Contribution 4) designed and optimized a MEMS skin friction sensor with a high response frequency and large measurement range. The sensor was statically calibrated using the centrifugal force equivalent method and a single-axis-rotating loading platform. The sensor had good linearity and stability, and high assembly accuracy, which meets the testing requirements of hypersonic wind tunnel experiments. Ren et al. (Contribution 5) proposed a design which improved a bulk acoustic wave magnetic sensor based on magnetoelectric coupling. The material design of inserting an Al_2O_3 thin film layer into an FeGaB and a two-layer piezoelectric magnetic/piezoelectric heterostructure reduced the eddy current loss of the magnetic composite material and elevated the energy conversion efficiency of the sensor. Cai et al. (Contribution 6) presented an improved temperature compensation approach called proportional difference for accelerometers based on differential frequency modulation to cancel out the frequency drift caused by temperature change. A parameter named temperature difference ratio was used to cancel the drift in the frequency of the differential resonators caused by temperature. Liu et al. (Contribution 7) reviewed the research progress of inertial switches. They introduced the design concept of MEMS inertial switches, providing an overview of their performance, including sensitive direction, acceleration threshold, and contact enhancement.

To study MEMS device materials, Tian et al. (Contribution 8) investigated the hydrogen storage performance of γ-graphdiyne-doped Li based on first principles. The results indicated that doping Li atoms could enhance the hydrogen storage property of intrinsic γ-GDY when in large-capacity hydrogen storage. Additionally, vacancy defects can improve hydrogen storage performance, and Li-VGDY possesses better hydrogen storage performance than Li-GDY.

Regarding the manufacturing of MEMS devices, Lou et al. (Contribution 9) reviewed the latest advances in the preparation technologies for micro-metal coils. They discussed the typical structural types of micro-metal coils and applications, summarized the preparation materials and main preparation methods of micro-metal coils, including macroscopic preparation processes (printed circuit board (PCB) process, hand winding method, and wire welding technology), MEMS processing technology, and other manufacturing technologies. Baek et al. (Contribution 10) proposed a manufacturing process of polymeric microneedle sensors for mass production, which can be applied in the electrochemical detection of various biomarkers in interstitial fluid. The proposed manufacturing process effectively produces microneedles with high aspect ratios and different lengths, and can be replicated. Zhong et al. (Contribution 11) proposed a novel method which transfers tactile sensors by using stiction effect temporary handling (SETH). This method simplifies the microelectromechanical system (MEMS)/CMOS integration process, improves the process reliability and electrical performance, and reduces material constriction. Moreover, they introduced the principle of using SETH for CMOS compatible batch transfer tactile sensors and provided the design of temporary adhesive structures to reduce adhesion forces caused by adhesion effects. In addition, Liu et al. (Contribution 7) introduced the manufacturing methods for non-silicon surface microfabrication technology, standard silicon microfabrication technology, and liquid inertial switches.

I would like to take this opportunity to thank all the authors who have submitted their papers to this Special Issue, and all the reviewers for dedicating their time and helping to improve the quality of the submitted papers.

Conflicts of Interest: The authors declare no conflicts of interest.

List of Contributions:

1. Wei, H.; Geng, W.; Bi, K.; Li, T.; Li, X.; Qiao, X.; Shi, Y.; Zhang, H.; Zhao, C.; Xue, G.; et al. High-Performance Piezoelectric-Type MEMS Vibration Sensor Based on $LiNbO_3$ Single-Crystal Cantilever Beams. *Micromachines* **2022**, *13*, 329. https://doi.org/10.3390/mi13020329.
2. Zhao, Y.; Wang, Z.; Tan, S.; Liu, Y.; Chen, S.; Li, Y.; Hao, Q. Dependance of Gauge Factor on Micro-Morphology of Sensitive Grids in Resistive Strain Gauges. *Micromachines* **2022**, *13*, 280. https://doi.org/10.3390/mi13020280.
3. Chen, S.; Li, J.; Gao, Y.; Li, J.; Dong, H.; Gu, Z.; Ren, W.A. Micromechanical Transmitter with Only One BAW Magneto-Electric Antenna. *Micromachines* **2022**, *13*, 272. https://doi.org/10.3390/mi13020272.
4. Guo, H.; Wang, X.; Liu, T.; Guo, Z.; Gao, Y. MEMS Skin Friction Sensor with High Response Frequency and Large Measurement Range. *Micromachines* **2022**, *13*, 234. https://doi.org/10.3390/mi13020234.
5. Ren, W.; Li, J.; Liu, G.; Chen, J.; Chen, S.; Gu, Z.; Li, J.; Li, J.; Gao, Y. Design and Optimization of a BAW Magnetic Sensor Based on Magnetoelectric Coupling. *Micromachines* **2022**, *13*, 206. https://doi.org/10.3390/mi13020206.
6. Cai, P.; Xiong, X.; Wang, K.; Wang, J.; Zou, X. An Improved Difference Temperature Compensation Method for MEMS Resonant Accelerometers. *Micromachines* **2021**, *12*, 1022. https://doi.org/10.3390/mi12091022.
7. Liu, M.; Wu, X.; Niu, Y.; Yang, H.; Zhu, Y.; Wang, W. Research Progress of MEMS Inertial Switches. *Micromachines* **2022**, *13*, 359. https://doi.org/10.3390/mi13030359.
8. Tian, W.; Li, Z.; Cheng, C.; Li, W.; Chen, Z.; Xin, F. Hydrogen Storage Performance of γ-Graphdiyne Doped Li Based on First Principles for Micro/Nano. *Micromachines* **2022**, *13*, 547. https://doi.org/10.3390/mi13040547.
9. Lou, J.; Ren, H.; Chao, X.; Chen, K.; Bai, H.; Wang, Z. Recent Progress in the Preparation Technologies for Micro Metal Coils. *Micromachines* **2022**, *13*, 872. https://doi.org/10.3390/mi13060872.
10. Baek, J.Y.; Kang, K.M.; Kim, H.J.; Kim, J.H.; Lee, J.H.; Shin, G.; Jeon, J.G.; Lee, J.; Han, Y.; So, B.J.; et al. Manufacturing Process of Polymeric Microneedle Sensors for Mass Production. *Micromachines* **2021**, *12*, 1364. https://doi.org/10.3390/mi12111364.
11. Zhong, P.; Sun, K.; Zheng, C.; Yang, H.; Li, X. Transfer of Tactile Sensors Using Stiction Effect Temporary Handling. *Micromachines* **2021**, *12*, 1330. https://doi.org/10.3390/mi12111330.

References

1. Shaeffer, D.K. MEMS inertial sensors: A tutorial overview. *IEEE Commun. Mag.* **2013**, *51*, 100–109. [CrossRef]
2. Algamili, A.S.; Khir, M.H.M.; Dennis, J.O.; Ahmed, A.Y.; Alabsi, S.S.; Ba Hashwan, S.S.; Junaid, M.M. A review of actuation and sensing mechanisms in MEMS-based sensor devices. *Nanoscale Res. Lett.* **2021**, *16*, 16. [CrossRef] [PubMed]
3. Bedair, S.S.; Pulskamp, J.S.; Rudy, R.; Polcawich, R.; Cable, R.; Griffin, L. Boosting MEMS piezoelectric transformer figures of merit via architecture optimization. *IEEE Electron Device Lett.* **2018**, *39*, 428–431. [CrossRef]
4. Ghazali, F.A.M.; Hasan, M.N.; Rehman, T.; Nafea, M.; Ali, M.S.M.; Takahata, K. MEMS actuators for biomedical applications: A review. *J. Micromech. Microeng.* **2020**, *30*, 073001. [CrossRef]
5. Song, P.; Ma, Z.; Ma, J.; Yang, L.; Wei, J.; Zhao, Y.; Wang, X. Recent progress of miniature MEMS pressure sensors. *Micromachines* **2020**, *11*, 56. [CrossRef] [PubMed]
6. Wang, C.; Zhang, Y.; Han, F.; Jiang, Z. Flexible Thermoelectric Type Temperature Sensors Based on Graphene Fibers. *Micromachines* **2023**, *14*, 1853. [CrossRef] [PubMed]
7. Liu, M.; Zhu, Y.; Wang, C.; Chen, Y.; Wu, Y.; Zhang, H.; Wang, W. A novel low-g MEMS bistable inertial switch with self-locking and reverse-unlocking functions. *J. Microelectromech. Syst.* **2020**, *29*, 1493–1503. [CrossRef]
8. Marx, M.; Cuignet, X.; Nessler, S.; De Dorigo, D.; Manoli, Y. An automatic MEMS gyroscope mode matching circuit based on noise observation. *IEEE Trans. Circuits Syst. II Express Briefs* **2019**, *66*, 743–747. [CrossRef]
9. Li, H.; Zhu, K.; Lei, K.; Xu, T.; Wu, H. Integrated MEMS toroidal transformer with Ni-Zn ferrite core for power supply on chip. *IEEE Trans. Power Electron.* **2022**, *37*, 10075–10080. [CrossRef]

10. Ruiz-Díez, V.; Hernando-García, J.; Toledo, J.; Ababneh, A.; Seidel, H.; Sánchez-Rojas, J.L. Piezoelectric MEMS linear motor for nanopositioning applications. *Actuators* **2021**, *10*, 36. [CrossRef]
11. Haefner, S.; Koerbitz, R.; Frank, P.; Elstner, M.; Richter, A. High integration of microfluidic circuits based on hydrogel valves for MEMS control. *Adv. Mater. Technol.* **2018**, *3*, 1700108. [CrossRef]
12. Ma, Z.; Wang, Y.; Shen, Q.; Zhang, H.; Guo, X. Key processes of silicon-on-glass MEMS fabrication technology for gyroscope application. *Sensors* **2018**, *18*, 1240. [CrossRef]
13. Noel, J.G. Review of the properties of gold material for MEMS membrane applications. *IET Circuits Devices Syst.* **2016**, *10*, 156–161. [CrossRef]
14. Dean, R.N.; Surgnier, S.; Pack, J.; Sanders, N.; Reiner, P.; Long, C.W.; Fenner, W.P. Porous ceramic packaging for a MEMS humidity sensor requiring environmental access. *IEEE T Comp. Pack. Man.* **2011**, *1*, 428–435. [CrossRef]
15. Yang, F.; Han, G.; Yang, J.; Zhang, M.; Ning, J.; Yang, F.; Si, C. Research on wafer-level MEMS packaging with through-glass vias. *Micromachines* **2018**, *10*, 15. [CrossRef] [PubMed]
16. Mehmood, Z.; Haneef, I.; Udrea, F. Material selection for micro-electro-mechanical-systems (MEMS) using Ashby's approach. *Mater. Des.* **2018**, *157*, 412–430. [CrossRef]
17. Yang, H.; Liu, M.; Zhu, Y.; Wang, W.; Qin, X.; He, L.; Jiang, K. Characterization of residual stress in SOI wafers by using MEMS cantilever beams. *Micromachines* **2023**, *14*, 1510. [CrossRef] [PubMed]
18. Song, X.; Liu, H.; Fang, Y.; Zhao, C.; Qu, Z.; Wang, Q.; Tu, L.C. An integrated gold-film temperature sensor for in situ temperature measurement of a high-precision MEMS accelerometer. *Sensors* **2020**, *20*, 3652. [CrossRef] [PubMed]
19. Ugale, A.D.; Umarji, G.G.; Jung, S.H.; Deshpande, N.G.; Lee, W.; Cho, H.K.; Yoo, J.B. ZnO decorated flexible and strong graphene fibers for sensing NO2 and H2S at room temperature. *Sens. Actuators B Chem.* **2020**, *308*, 127690. [CrossRef]
20. Perrier, T.; Levy, R.; Bourgeteau-Verlhac, B.; Kayser, P.; Moulin, J.; Paquay, S. Optimization of an MEMS magnetic thin film vibrating magnetometer. *IEEE Trans. Magn.* **2016**, *53*, 1–5. [CrossRef]
21. Qu, H. CMOS MEMS fabrication technologies and devices. *Micromachines* **2016**, *7*, 14. [CrossRef] [PubMed]
22. Liu, M.; Wang, W.; Zhu, Y.; Yuan, Y.; Niu, Y.; Dong, L.; Chen, G. Constrained multiobjective robust optimization of a bistable mechanism for inertial switch. *Sci. China Technol. Sci.* **2023**, *66*, 3186–3196. [CrossRef]
23. Li, Y.; Hong, M. Parallel laser micro/nano-processing for functional device fabrication. *Laser Photonics Rev.* **2020**, *14*, 1900062. [CrossRef]
24. Torunbalci, M.M.; Alper, S.E.; Akin, T. Advanced MEMS process for wafer level hermetic encapsulation of MEMS devices using SOI cap wafers with vertical feedthroughs. *J. Microelectromech. Syst.* **2015**, *24*, 556–564. [CrossRef]

micromachines

MDPI

Article

High-Performance Piezoelectric-Type MEMS Vibration Sensor Based on $LiNbO_3$ Single-Crystal Cantilever Beams

Huifen Wei [1], Wenping Geng [1,*], Kaixi Bi [1], Tao Li [1], Xiangmeng Li [2], Xiaojun Qiao [1], Yikun Shi [3], Huiyi Zhang [1], Caiqin Zhao [1], Gang Xue [1] and Xiujian Chou [1,*]

[1] Science and Technology on Electronic Test and Measurement Laboratory, North University of China, Taiyuan 030051, China; b1806002@st.nuc.edu.cn (H.W.); bikaixi@nuc.edu.cn (K.B.); s2006010@st.nuc.edu.cn (T.L.); xiaojunqiao@nuc.edu.cn (X.Q.); s202106035@stu.nuc.edu.cn (H.Z.); s1906211@st.nuc.edu.cn (C.Z.); s1906061@st.nuc.edu.cn (G.X.)
[2] Shanxi Provincial Key Laboratory of Advanced Manufacturing Technology, North University of China, Taiyuan 030051, China; xmli123@nuc.edu.cn
[3] Beijing Space Trek Technology Co., Ltd., Beijing 100176, China; shiyikun@startrekspace.cn
* Correspondence: wenpinggeng@nuc.edu.cn (W.G.); chouxiujian@nuc.edu.cn (X.C.)

Abstract: It is a great challenge to detect in-situ high-frequency vibration signals for extreme environment applications. A highly sensitive and robust vibration sensor is desired. Among the many piezoelectric materials, single-crystal lithium niobate ($LiNbO_3$) could be a good candidate to meet the demand. In this work, a novel type of micro-electro-mechanical system (MEMS) vibration sensor based on a single crystalline $LiNbO_3$ thin film is demonstrated. Firstly, the four-cantilever-beam MEMS vibration sensor was designed and optimized with the parametric method. The structural dependence on the intrinsic frequency and maximum stress was obtained. Then, the vibration sensor was fabricated using standard MEMS processes. The practical intrinsic frequency of the as-presented vibration sensor was 5.175 kHz, which was close to the calculated and simulated frequency. The dynamic performance of the vibration sensor was tested on a vibration platform after the packaging of the printed circuit board. The effect of acceleration was investigated, and it was observed that the output charge was proportional to the amplitude of the acceleration. As the loading acceleration amplitude is 10 g and the frequency is in the range of 20 to 2400 Hz, the output charge amplitude basically remains stable for the frequency range from 100 Hz to 1400 Hz, but there is a dramatic decrease around 1400 to 2200 Hz, and then it increases significantly. This should be attributed to the significant variation of the damping coefficient near 1800 Hz. Meanwhile, the effect of the temperature on the output was studied. The results show the nearly linear dependence of the output charge on the temperature. The presented MEMS vibration sensors were endowed with a high output performance, linear dependence and stable sensitivity, and could find potential applications for the detection of wide-band high-frequency vibration.

Keywords: MEMS; vibration sensor; four-cantilever beam; single-crystal $LiNbO_3$; output charge sensitivity; temperature dependence

Citation: Wei, H.; Geng, W.; Bi, K.; Li, T.; Li, X.; Qiao, X.; Shi, Y.; Zhang, H.; Zhao, C.; Xue, G.; et al. High-Performance Piezoelectric-Type MEMS Vibration Sensor Based on $LiNbO_3$ Single-Crystal Cantilever Beams. *Micromachines* **2022**, *13*, 329. https://doi.org/10.3390/mi13020329

Academic Editors: Weidong Wang and Ruiguo Yang

Received: 22 January 2022
Accepted: 17 February 2022
Published: 19 February 2022

1. Introduction

Outer-space explorations, equipment health monitoring, the routine maintenance of machinery, and so forth, have an increasing demand for high-performance vibration sensors [1–3]. Compared to piezo-resistive [4] and capacitive [5] transducers, piezoelectric transducers exhibit an expected piezoelectric coupling over wireless passive sensing, a high quality factor, a large linear amplitude range and low power consumption [6,7]. Many studies have focused on piezoelectric vibration devices. Li et al. developed an asymmetric cruciform piezoelectric harvester with PZT-5H under the d_{15} mode [8]. Derakhshani et al. reported clamped–clamped and bi-stable buckled beam vibration energy harvesters with polyvinylidene fluoride (PVDF) [9]. However, piezoelectric vibration devices with large

sizes cannot meet the demand for the miniaturization of sensors with high sensitivity [10]. Particularly, traditional devices have an unstable performance or even fail in extreme environments. Micro-electro-mechanical system (MEMS) piezoelectric vibration devices are considered to be one of the most sensitive among the miniaturized devices, whether measured or in design. Shen et al. reported a micromachined lead zirconate titanate (PZT) cantilever for vibration energy harvesting [11,12]. Jeon developed an interdigitated top electrode to introduce the d_{33} piezoelectric mode [13]. Ren and Zhou et al. proposed a shear mode cantilever using a single-crystal PMN-PT [14,15]. The above analyses based on a coupling bending–torsional model are helpful for the design of piezoelectric sensors. The effects of the material properties and vibration modes on the energy harvesting performance also provide some useful guidelines for the design of piezoelectric sensors.

Lithium niobate ($LiNbO_3$) is a type of lead-free ferroelectric single crystal, and its piezoelectric constant is quite robust and less temperature-dependent. Islam et al. reported the measurement that the piezoelectric coefficient d_{15} of $LiNbO_3$ can decrease only to about 7% even at a rather low temperature, and the coefficient is constant at a temperature below 50 K [16]. Thus, $LiNbO_3$ is a better piezoelectric material candidate for many applications in extreme low-temperature environments. However, thin-film $LiNbO_3$ is a kind of brittle, tough, functional, ceramic material, and it is difficult to etch into a certain shape with a relatively high-aspect-ratio structure. Qu et al. adopted a manner of focused ion beam (FIB) milling to achieve homogeneous and ultra-shallow $LiNbO_3$ structures of several nanometers in thickness [17]. Ying Li et al. used a proton-exchanged wet etching technique to selectively remove a certain area of the $LiNbO_3$ thin film [18]. The abovementioned methods have shown that the etching depth of $LiNbO_3$ is quite shallow, only hundreds of nanometers, while the etching rate is about 10 nm per min. Xiang et al. adopted the technology of proton exchange and ion-beam-enhanced etching to fabricate ridge waveguides with etching depths up to 2.5 μm [19]. The existing difficulties in the patterning of $LiNbO_3$ thin film have hindered the application in MEMS vibration. Therefore, it is desirable to investigate $LiNbO_3$-based MEMS sensors, and to validate their application in a large range of frequencies and temperatures. Fortunately, the commercially available substrate of a thin-film $LiNbO_3$ bonded silicon wafer can reduce the difficulty in fabricating the sensitive structure for the MEMS sensors.

Herein, a novel MEMS vibration sensor based on functional $LiNbO_3$ cantilever beams is proposed. In order to design an applicable vibration sensor, the effect of the geometric dimension on the intrinsic frequency and stress distribution on the cantilever beams was investigated in a numerical simulation. Then, the vibration sensor was fabricated using standard MEMS processes. During the fabrication, $LiNbO_3$ thin-film patterning was achieved using ion-beam etching (IBE) technology. Next, the vibration sensor was packaged on a vibrating test platform in order to investigate the performance of the output charge and sensitivity under input vibration with a large range of acceleration frequencies and amplitudes. Moreover, the effect of the environmental temperature on the performance of the vibration sensor was studied.

2. Methods

2.1. Working Principle

The main function of the proposed MEMS sensor is to sense vibrations with a relatively large range of frequencies in a small amplitude. The piezoelectric $LiNbO_3$ layer plays an important role in response to such mechanical signals dynamically. Figure 1a schematically illustrates the MEMS vibration sensor with a $LiNbO_3$ single-crystalline film bonded on silicon. The four cantilever beams are connected to a central proof mass and a square silicon frame. Meanwhile, the surface electrodes were coated on top of the $LiNbO_3$ layer. With such a structural arrangement and surface electrode distribution, the d_{33} piezoelectric mode could be formed naturally. A good output performance and sensitivity can be obtained using the d_{33} mode owing to its relatively large piezoelectric coefficient [20,21]. As the mechanical vibration is applied to the central proof mass, bending deformation will occur

at the cantilever beams. By this means, the deflection of the cantilever beam will lead to the piezoelectric effect of the $LiNbO_3$ layer, such that the opposite potential will be formed on the surface electrode pairs.

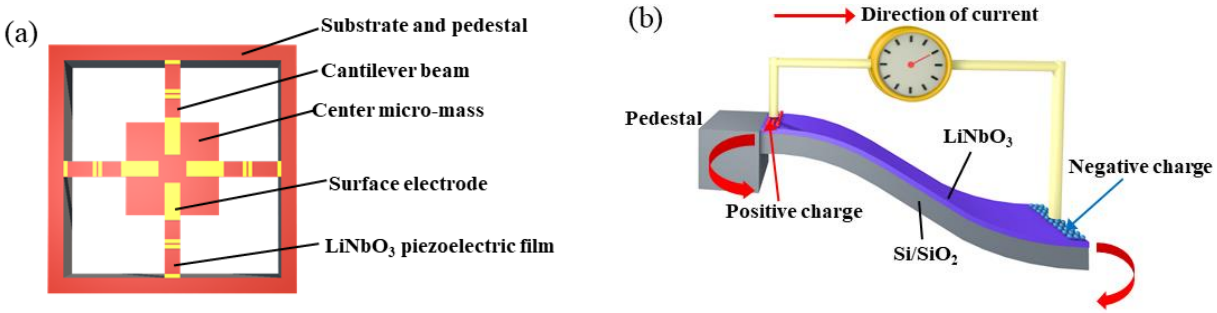

Figure 1. Schematic illustration of (**a**) a structural model of the vibration sensor and (**b**) the opposite electrical charges generated on different regional surfaces on the $LiNbO_3$ films on the cantilever beam.

The electrodes were set on the surface of the $LiNbO_3$ layer regions with tensile stress to generate positive charges and compressive stress to obtain negative charges, as indicated in Figure 1b. By using the d_{33} mode, the positive and negative charges can be extracted from the adjacent interface by a pair of surface electrodes. The design of the electrode distribution can help to collect the generated charges from the piezoelectric layer because it is similar to the interdigital electrode, as shown in reference [20]. Although the d_{33} mode demonstrated here seems different from the classical piezoelectric modes, it is useful for our presented devices, and can obtain a higher performance.

2.2. Design of the Vibration Sensor

The dimensional parameters of the cantilever beam and the center mass have a direct influence on the resonant frequency and maximum stress of the vibration sensor. In order to determine the geometric dimensions of the cantilever beam and the proof mass, parametric analyses should be performed. The reason is that the practical MEMS sensor must work at a range of frequencies far away from the intrinsic frequency. Because the target range of the working frequency in practical applications is about 20 Hz to 2.4 kHz, the intrinsic frequency of the MEMS sensor should be at least 6 kHz. In this work, the $LiNbO_3$ thin films and electrodes are located at the same sides, on the top surface of the cantilever beam. The four-cantilever beam sensor is geometrically symmetric in both the X and Y directions. The thickness of the sputtering-deposited gold electrodes is 200 nm; thus, it can be neglected compared to the total thickness of the cantilever beam. The intrinsic frequency of the cantilever beams was calculated using the following equation [10,11]:

$$f_n = 4 * \frac{v_n^2}{2 * pi} \sqrt{\frac{0.236 * D_p * w_c}{\left(l - \frac{l_m}{2}\right)^3 * (m_e + m)}}, \quad (1)$$

where $D_p = \frac{\left[E_L^2 t_L^4 + E_s^2 t_s^4 + 2E_L E_S t_L t_s \left(2t_L^2 + 2t_s^2 + 3t_L t_s\right)\right]}{12(E_L t_L + E_s t_s)}$, $m_e = 0.236 m' w_c \left(l - \frac{l_m}{2}\right) + m' w_c \frac{l_m}{2}$, $m' = \rho_L t_L + \rho_S t_S$, f_n is the nth mode resonant frequency, v_n is the nth mode eigenvalue (v_1 is 1.875), w_c is the width of the cantilever beam, l is the total length of a single cantilever beam, l_m is the length of the proof mass, m is the mass of the proof mass, D_p is a function of the Young's moduli of the two materials E_L ($LiNbO_3$) and E_S (Si), m_e is the effective mass of the cantilever beam at the center of the proof mass, m' is the mass per unit area of the cantilever beam without the proof mass, ρ_L and ρ_s are the densities of the piezoelectric material $LiNbO_3$ and the supporting layer material Si, and t_L and t_S are the thicknesses of the $LiNbO_3$ layer and Si layers [22,23].

As can be seen in Figure S1, COMSOL Multiphysics software was adopted to investigate the effect of varied geometric dimensions on the resonant frequency and the maximum

stress. The material parameter settings are listed in Table 1. Besides the material settings, a physical setting with a Mutiphysics Interface for piezoelectric devices was used during the design of the four-cantilever beam and mass structures.

Table 1. Physical properties of the two major material settings in the numerical simulation.

Materials	Parameters	Values
Silicon layer	Density (kg/m^3)	2330
	Young's modulus (GPa)	190
$LiNbO_3$ layer	Piezoelectric coefficients ($\times$pC/N)	$d_{15} = 68, d_{33} = 6, d_{22} = 22,\ d_{31} = -1$
	Density (kg/m^3)	4700
	Young's modulus (GPa)	240

Figure 2 shows the resonant frequency and the maximum stress of the vibration sensor subjected to an external force F_z. The force analysis of the cantilever beam is shown in Figure 2a. The resonant frequency and the maximum stress can be changed by varying the geometric dimensions, including the thickness and width of the cantilever beams, and the lengths of both the proof mass and the cantilever beams. In addition, a method of parametric scanning was used to analyze the effect of the structural dimension using Comsol Multiphysics. The parametric setting for the scanning analysis is listed in Table 2. The pedestal was set as a fixed constraint while the other components were set as freely moving parts.

Table 2. Parametric settings for the scanning simulation using Comsol Multiphysics.

Parameters for Scanning	Range of Parameter	Steps
Length of cantilever beams	1860 to 2260 μm	50 μm
Length of proof mass	3000 to 4000 μm	50 μm
Widths of cantilever beam	300 to 600 μm	20 μm
Thicknesses of cantilever beam	30 to 60 μm	5 μm
Thicknesses of proof mass	30 to 60 μm	5 μm

Figure 2b,c shows that the resonant frequency would increase with the increase of the thickness and width of the cantilever beam. On the other hand, the resonant frequency would decrease continuously with the increasing of the lengths of the cantilever beam or the proof mass. Using a parametric scanning simulation with the above geometric parameters, the results can be obtained for the resonant frequency of 6 kHz. Figure 2d,e demonstrates the effect of geometric dimensions on the maximum stresses of the devices under an input acceleration of 20 g at a frequency of 2 kHz. With the increasing of the width and thickness of the cantilever beams, the maximum stress would decrease, while the maximum stress would become larger with a longer proof mass or beam. Despite of the fluctuation of the maximum stress, the total trends of the output changes are consistent within the range of several MPa, which is far below the fatigue strength of the silicon substrate. Based on the calculation of the maximum stress and resonant frequencies, the dimensions of the cantilever beams can be determined, including the length, width and thickness of the beams and proof mass. Once the intrinsic frequency is fixed, a relatively large length of proof mass should be chosen for the sake of fabrication. Meanwhile, the thickness of the proof mass can be same as that of the cantilever beam in order to reduce the difficulty of fabrication.

As soon as we have obtained the geometric dimensions, including the cantilever beam length of 2260 μm, the cantilever beam width of 460 μm, the thickness of 60 μm, the length of a proof mass block with a square length of 3600 μm, the first-ordered to third-ordered modal analyses can be performed. Figure S2 shows resonant frequencies of 6032, 12,608 and 12,682 Hz, for the first-ordered vibration mode to the third-ordered vibration mode, respectively. Among them, a vertical displacement was found for the

first-order resonant mode, whereas there would be torsional displacement in different directions for both the second- and third-order vibration modes. In order to ensure a steady performance, the working frequency of the vibration sensors should be far below the first-order resonant frequency.

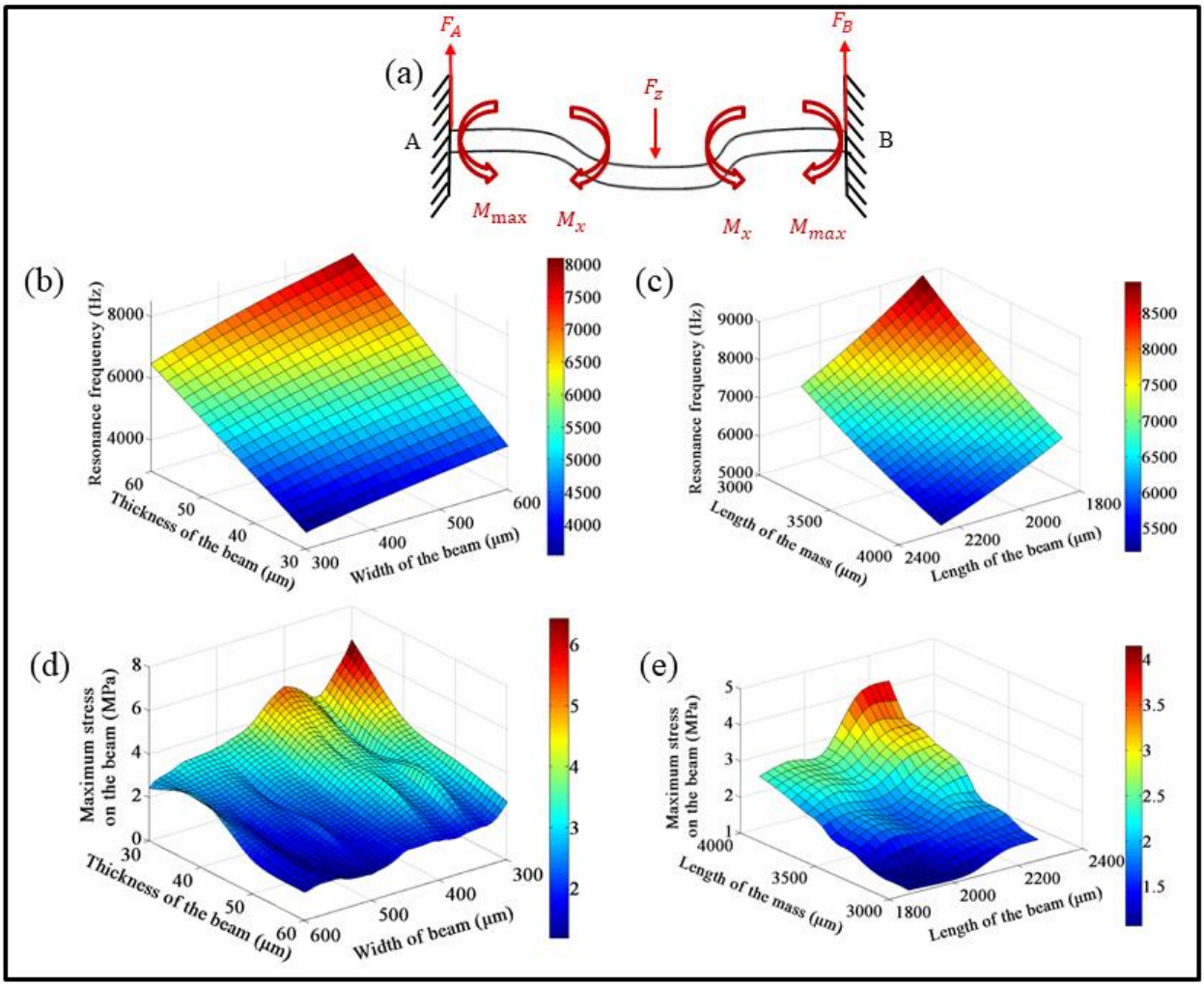

Figure 2. Theoretical calculation and parametric design of the structural dimensions of cantilever beams based on the resonant frequencies and maximum stress. (**a**) Schematic illustration of the force analysis and deflection of the cantilever beam under a vibration shock. (**b**) Dependence of the resonant frequency on the thickness and width of the cantilever beam. (**c**) Dependence of the resonant frequency on the lengths of the proof mass and beams. (**d**) Dependence of the maximum stress on the thickness and width of the cantilever beam. (**e**) Dependence of the maximum stress on the lengths of the proof mass and beams.

2.3. Fabrication of the Vibration Sensor

Based on the results of the above analysis and consideration, the geometric parameters of the MEMS vibration sensors were determined. After this, the vibration sensor was fabricated in the standard clean room. The fabrication process for the MEMS vibration sensor is depicted in Figure 3. Briefly, a set of 5-inch chromium masks were designed and prepared according to the calculation results. Then, a 4-inch silicon wafer bonded with a thin-film single-crystalline $LiNbO_3$ (X-cut, Jinan Jingzheng Electronics Co., Ltd., Jinan, China) was thoroughly cleaned prior to the photolithography and other processes. After the standard photolithography processes, including photoresist spin-coating, pre-baking, ultraviolet exposure, post-baking and development, resistive patterns could be obtained. Then, the surface electrodes could be generated by metal deposition using

magnetic sputtering, as well as the lift-off process. Next, ion-beam etching (ACME POLE, Beijing, China), one of the most difficult steps, was conducted in order to achieve the patterning of the $LiNbO_3$ functional structures. The IBE etching processing includes an ion-beam current of 100 mA, an etching rate of 21 nm/min, and an input of the total etching energy of 500 eV. Then, the RIE etching process was performed to obtain silica patterns. Finally, deep etching was implemented to release the cantilever beams and proof mass by the DRIE process using Omega LPX Dsi equipment (SPTS Technologies Ltd., Newport, UK), both from the front and back sides. The flow rates were 300 sccm: 400 sccm for downward etching with gas plasma of C4F8 and SF6, whereas we used a flow rate of 996 sccm for the sidewall etching with a gas plasma of SF6. The etching cycles could be manipulated to control the etching depth of the silicon precisely. During the fabrication process, common photolithography and etching processes can ensure the precise control of the dimensions of the cantilever beams and central proof mass.

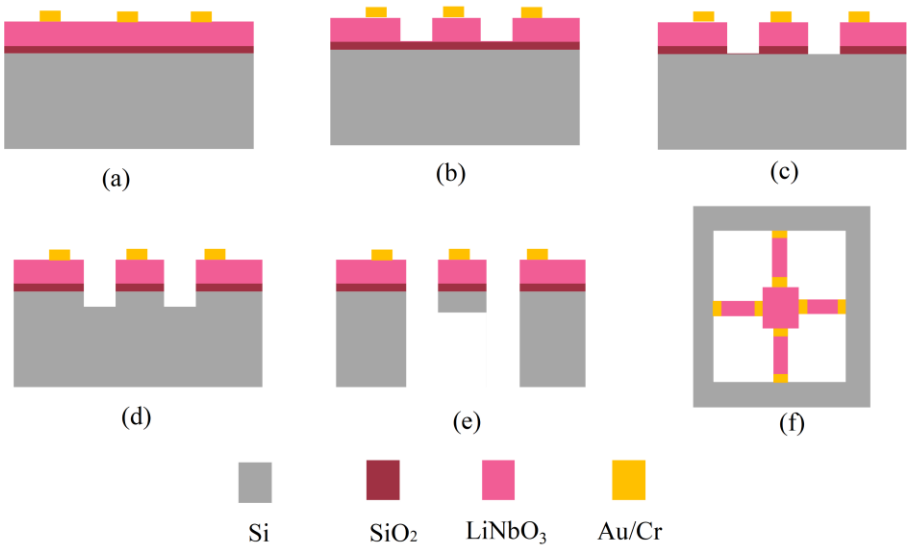

Figure 3. Scheme of the fabrication of the MEMS vibration sensor. (**a**) Photolithography, metal sputtering deposition and lift-off process. (**b**) $LiNbO_3$ pattern produced by photolithography and IBE. (**c**) RIE etching of the SiO_2 layer. (**d**) Cantilever beams and mass fabrication using lithography and etching by the DRIE process. (**e**,**f**) Release of the cantilever beams by the DRIE process.

2.4. Morphology Characterization of the Vibration Sensor

After the fabrication, the appearance of the as-prepared and packaged MEMS vibration sensor was obtained by camera photography. In addition, the detailed morphologies of the sensing parts—including the proof mass, cantilever beams, surface electrodes, and welding points, etc.—were characterized using a scanning electronic microscope (SEM, SUPRA 55, Carl Zeiss, Oberkochen, Germany). In order to investigate the cross-sectional morphology of the cantilever beam more clearly, we deliberately cut out one of the as-prepared sensors after the testing experiment. In particular, the cross-sectional view of the functional structures with $LiNbO_3$ layer patterns bonded onto the silicon wafer was characterized using SEM, and the thicknesses of the three layers were measured.

2.5. Testing of the Performance of the Vibration Sensor

After the fabrication and packaging, a series of tests should be carried out to test the performance of the MEMS vibration sensors. This measurement is mainly composed of two parts: one is the output charge and sensitivity, and the other is the intrinsic frequency of the vibration sensor. The testing platforms can be seen in Figure S3. A MSA-400 Micro System Analyzer (Polytec China Ltd., Beijing, China) was used to test the intrinsic frequency of the vibration sensor (Figure S3a). A driving voltage of 8 V was applied with a sweep frequency

ranging from 30 to 6.3 kHz. The output deflection was observed and recorded during the voltage supply, such that the intrinsic frequency could be obtained.

In order to investigate the performance of the packaged sensors, a vibration testing platform was used for the generation of vibration with frequencies ranging from 20 to 2400 Hz. For the test at room temperature, the testing sample sensor was directly fixed on the metal vibration plate (Figure S3b). The excitation input was generated as a form of sinusoidal wave from a signal generator. Meanwhile, the effect of input acceleration on the vibration sensor was studied by varying the amplitude of the acceleration from 5 to 20 g. A charge amplifier was employed to convert the output charge signal into voltage signals. An oscilloscope was used to display the output signal, and the output data could be downloaded for further analysis.

In order to explore the applicability of the as-fabricated $LiNbO_3$-based MEMS vibration sensor in an extreme environment, another experimental setup was established in an enclosed chamber, where the MEMS sensor was excited with similar vibration signals to those given above, while the testing temperature was tuned from -40 to 70 °C. The experimental set-up for studying the performance of the sensor under a controlled temperature is demonstrated in Figure S4. In order to investigate the characteristics of the vibration sensor with a changing working temperature, the vibration platform should be adaptable. Thus, the sensor was first placed on a wood plate, then a water membrane, followed by a thicker metal vibration plate (Figure S4b). The input of the vibration acceleration with certain frequencies was selected in order to validate the effect of temperature on the MEMS sensor, including frequencies of 20, 50, 100, 500, 1000, 2200 and 2400 Hz.

3. Results and Discussion

3.1. Morphology of the Vibration Sensor

Figure 4 demonstrates the photography and microscopic images of the as-fabricated vibration sensor packaged on the printed circuit board (PCB). The cross-cantilever beams and center mass are clearly shown in a suspended state in the scanning electron microscope (SEM) image (Figure 4a). The metal surface electrode patterns were found intact, and they would ensure the packaging and testing of the sensor. Figure 4b shows that an etching depth of about 5 μm was achieved on the $LiNbO_3$ thin film distributed on the cantilever beams, and that the slope is nearly vertical. Because the $LiNbO_3$ thin film is bonded and adhered to the silicon substrate, the interface of $LiNbO_3$ thin film and the silicon wafer is rather flat and clear. Moreover, the modulus of the cantilever beam is small, and it is helpful for the beam to bend about the external vibration or shock forces, so as to generate an electrical charge on different surfaces. It is the robust mechanical structure that ensures the long-term stable performance of the presented MEMS vibration sensors.

3.2. Performance of the Vibration Sensor

Figure 5a shows the intrinsic frequency of the vibration sensor obtained by testing. A resonant frequency of 5.175 kHz was observed for our presented MEMS vibration sensor. The measurement result agrees well with the theoretical and calculation values. However, there is still some difference between the designed target frequency 6 kHz and that of 5.48 kHz from the finite element analysis based on the Equation (1). The possible reason for the variation should be attributed to the MEMS processing, meaning that the practical geometric dimensions of the cantilever beams and proof mass are somewhat diverse compared to the ideal designed dimension. In any case, the outcome resonant frequency has proven the validation of our design of the vibration sensor.

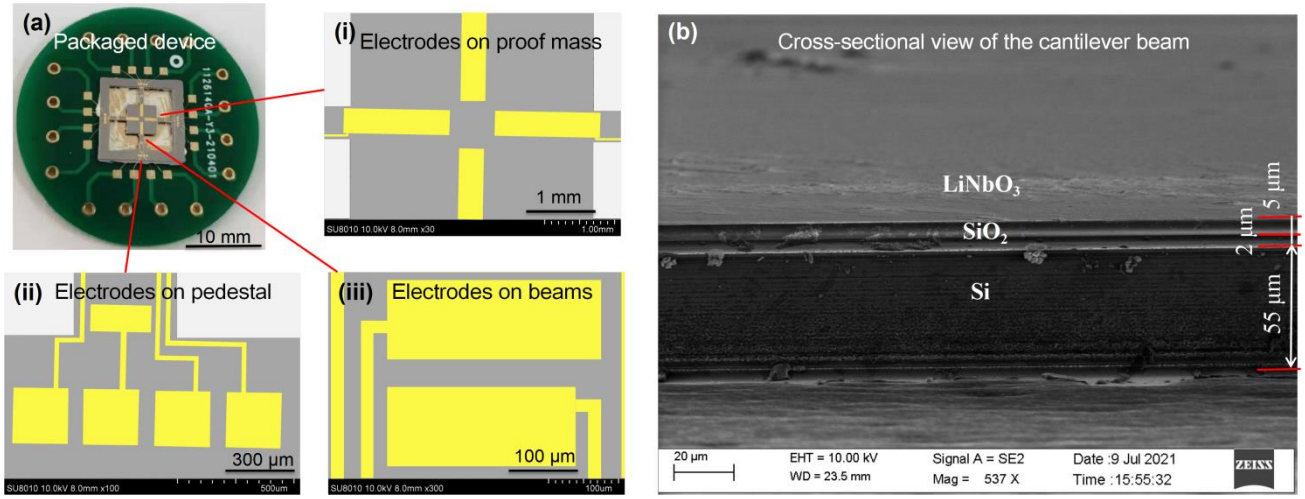

Figure 4. Morphological characterization of the vibration sensor. (**a**) Photograph of the packaged device with an indication of the surface electrodes on the (**i**) proof mass, (**ii**) pedestal, and (**iii**) cantilever beams, respectively. (**b**) SEM image of the cross-sectional view of the cantilever beam, indicating the layers of $LiNbO_3$, SiO_2, and silicon wafer with various thicknesses, respectively.

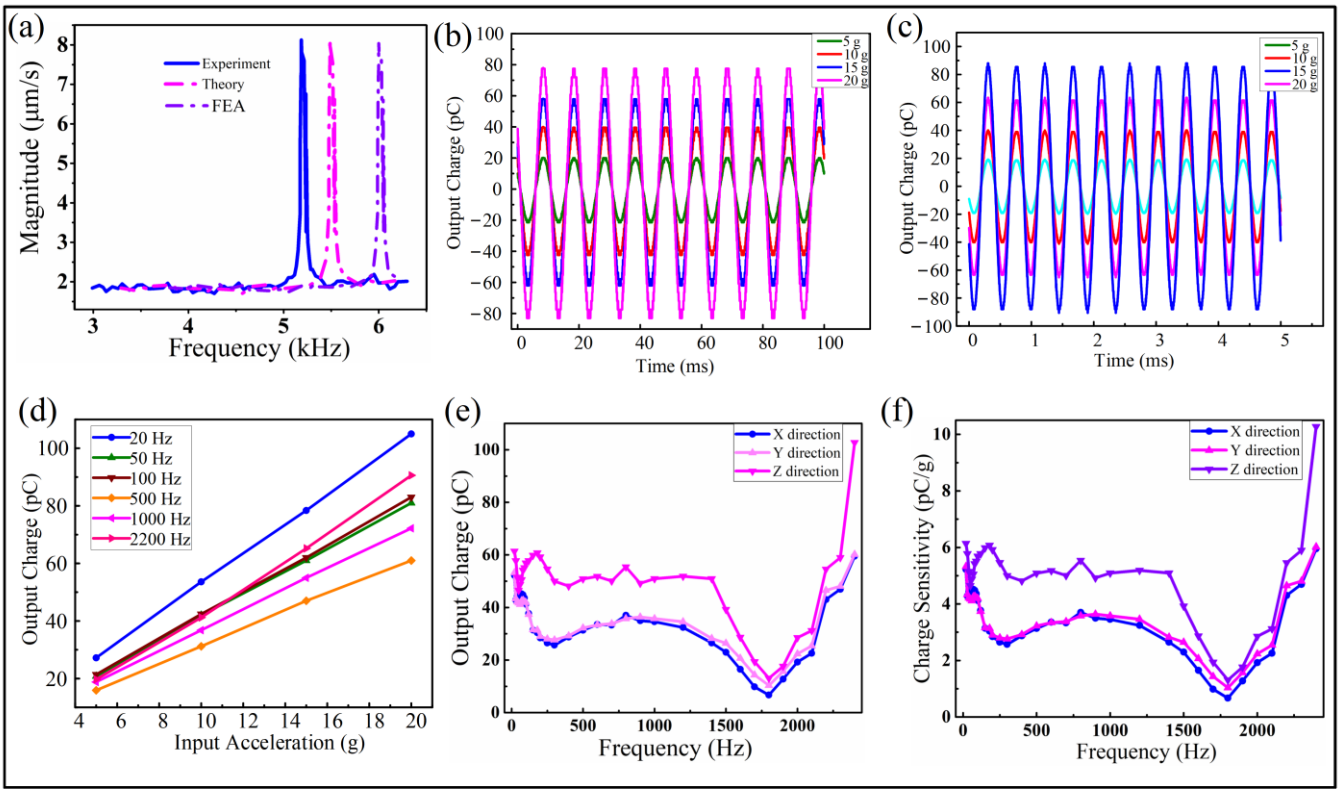

Figure 5. Performance of the vibration sensor. (**a**) Comparison of the intrinsic frequency obtained from the experiment, theory and FEA analysis of the vibration sensor. (**b**,**c**) Output charge performance of the vibration sensor with a sinusoidal wave with vibrations of 100 Hz and 2200 Hz, respectively, for the Z direction. (**d**) Output charge relating to the amplitude of acceleration, ranging from 5 to 20 g for the Z direction input. (**e**) Output charge for the vibration input frequencies ranging from 20 to 2400 Hz, indicating the X, Y, and Z directions. (**f**) Sensitivity of the output charge for the same range of frequencies as (**e**).

Figure 5b,c demonstrate the output signals extracted from the oscilloscope with a perfect sinusoidal wave in testing frequencies of 100 and 2200 Hz, respectively. The results

reveal the perfect response to the input vibration signals, indicating the high-performance sensitivity of the sensor. Meanwhile, by varying the amplitude of the vibration acceleration from 5 to 20 g, the output signal increased proportionally. Figure 5d shows the excellent linearity between the output charge and the input acceleration with amplitude ranging from 5 to 20 g. The slopes of the five representative frequencies are similar, indicating the similar sensitivity of the output charge response to the input acceleration.

In order to investigate the performance of the vibration sensor in a larger range of frequencies, for the potential applications, the output charge was carefully observed and recorded by scanning the input frequency ranging from 20 Hz to 2.4 kHz. Figure 5e shows the amplitude of the output charge at the same acceleration of 10 g along the Z direction, under the condition of frequency scanning. It is clear that the amplitude of the output charge increased from 61.4 to 102.8 pC. Correspondingly, the amplitude of the output charge increased from 52 to 60 pC at the same acceleration of 10 g along the X/Y direction. The output performance of the sensor during the test for 20 Hz, 1 kHz and 2.4 kHz can be also found in Figures S5–S7. For convenience, we simply obtained the sensitivity of the output charge related to the input acceleration amplitude, which was derived from Figure 5e. The results are shown in Figure 5f, indicating the output charge sensitivity increasing from 6.1 to 10.3 pC/g from 20 Hz to 2.4 kHz along the Z direction. Moreover, the output charge sensitivity would increase from 5.2 to 6 pC/g with the corresponding input frequency range along X/Y direction. The output for the Z direction vibration is higher than that of the X and Y directions. Due to the symmetry of the crossing cantilever beam structure, the X and Y directions should have a similar trend. This was verified by the comparable measurement. It was clearly shown that, for the range of frequencies between 200 to 1400 Hz, the sensitivity remained stable. However, there was a drop of output after 1400 Hz, and it reached the bottom around 1800 Hz; then, it went up again dramatically. Unfortunately, the reason for the drop in the frequencies ranging from 1400 to 2200 Hz is unknown. Considering the effect of the systematic dynamics of a mass-spring model of the presented MEMS vibration sensor, it was inferred that the air trapped around the packaged sensor might give an increased damping coefficient at that range of frequencies.

It is noteworthy that the external vibration applied to the MEMS vibration sensor comes with a certain frequency and amplitude along the vertical direction. During the vibration, the cantilever beam is deformed elastically back and forth, and subjected to the dynamic external force F (see Appendix A). For this mode, positive and negative charges will appear on the two electrode surfaces adhering to the $LiNbO_3$ thin films along the X or Y axes, and the charge q can be given by:

$$q = d_{ij} * F = d_{ij} * kx_1 \tag{2}$$

where d_{ij} is the piezoelectric coefficient, k is the effective rigidity coefficient of the vibration model, and x_1 is the actual deflection of the cantilever beam due to the displacement of the proof mass. Finally, according to the analysis in the Supplementary Material, the sensitivity of the output charge of the vibration sensor K_Q can be described as

$$K_Q = \frac{q}{a} = \frac{1}{\omega_0^2} * \frac{d_{33} * k}{\sqrt{(1 - s^2)^2 + (2\xi s)^2}} \tag{3}$$

where m is the proof mass, ξ the effective damping coefficient, $\omega_0^2 = \frac{k}{m} = (2\pi f_n)^2$ is the intrinsic frequency of the acceleration system, and $s = \frac{\omega}{\omega_0}$ depicts the ratio of the input frequency to the intrinsic frequency. On basis of a theoretical analysis for the silicon cantilever beam and piezoelectric effect, the output charge and the sensitivity of the sensor can be obtained according to the piezoelectric modes.

3.3. Effect of the Temperature on the Performance the Vibration Sensor

In order to investigate the effect of the temperature on the performance of the sensor, a further experiment was performed at a relatively large range of temperatures. Upon reaching a stable temperature in the testing platform, a similar vibration signal was applied to the packaged sensor along different orientations of X/Y/Z, with an acceleration amplitude of 10 g. Figure 6 shows the testing results for the temperature ranging from −40 to 70 °C. Figures S5 and 6d show the photo and flow chart illustrating the test platform with the control of the testing temperatures. By comparison, we emphasized the performance of the vibration sensors under the temperature conditions of −40, −10, 20, 50 and 70 °C, respectively. Figure 6a,b show the output charge performance from the application of vibrations from X direction and Z direction, respectively. It is clearly seen that the performance is quite stable for a wide-band input in the frequencies ranging from 20 to 2400 Hz.

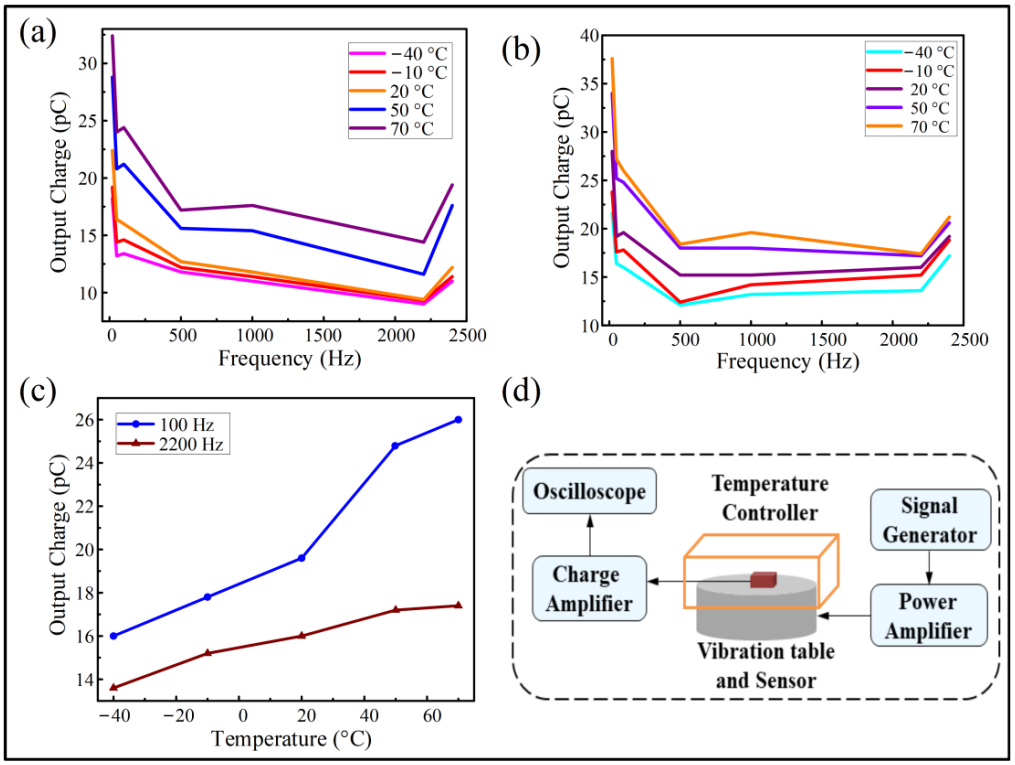

Figure 6. Temperature performance of the vibration sensor from −40 °C to 70 °C. Relationship of the output performance of the vibration sensor corresponding to the vibration input with frequencies from 20 to 2400 Hz, at an acceleration amplitude of 10 g, by applying vibration from the directions of the (**a**) X and (**b**) Z axes, respectively. (**c**) Curve indicating the variation of the output charge with the temperature (Z direction). (**d**) Flow chart illustrating the experimental setup for the temperature test.

Figure 6c indicates the variation of the output charge with the temperature from below freezing point to above the ambient temperature conditions. As shown in Figure 6c, the trend is nearly upwardly linear. It is noteworthy that the output charge slope for 100 Hz is larger than that of 2200 Hz from 20 °C to 70 °C, while they are almost the same below 20 °C (for vibration input in the Z direction). Nevertheless, for most frequencies, the variation of the output performance related to the large temperature ranging from −40 °C to 70 °C is about 5 to 7 pC for both input in X-direction and Z-direction. From the above-mentioned results, it is implied that the slight variations of the piezoelectric coefficients should be considered for the $LiNbO_3$-based sensor when the temperature is changed. According

to the reference [24], the piezoelectric coefficients may have an increasing trend within a certain range of temperatures. The variation can be explained with the following equation:

$$(T) = d_{T_{ref}} * \left[1 + k_d * \left(T - T_{ref}\right)\right], \quad (4)$$

where $d(T)$ is the piezoelectric coefficient, k_d is the changing rate with the temperature, T_{ref} is the reference temperature (20 °C for this work), and T is the environment temperature.

Due to the differences in the platform settings, the actual input acceleration acting on the sensor should be less than that under ambient conditions, with the output charge shown in Figure 6 being only about half of that in Figure 5 for the same temperature. Nevertheless, we can obtain a similar trend of variation at a certain range of frequencies. In addition, the data acquired is comparable for the same test platform in the temperature controller.

4. Conclusions

In summary, in order to investigate their applicability in extreme environments, a novel-type piezoelectric MEMS vibration sensor-based $LiNbO_3$ single crystal was designed to determine the geometric structural dimensions, fabricated using standard process, and tested on a vibration platform under ambient and temperature-controllable conditions. The effect of the input vibration with varying frequencies and acceleration amplitudes on the output charge was investigated. As a result, an intrinsic frequency of 5.175 kHz was observed with the presented MEMS vibration sensor, which is close to the design. During the fabrication of the vibration sensor, the patterned structure of the 5-μm-thick $LiNbO_3$ layer was achieved using an ion beam etching process. The morphological characterization indicated the intact pattern and structure of the $LiNbO_3$-bonded-silicon cantilever beams and the surface electrodes. The vibration sensor was tested on a standard testing platform under a vibration input with accelerations ranging from 5 g to 20 g and frequencies ranging from 20 Hz to 2.4 kHz. The results demonstrated an excellent linear trend between the output charge and the acceleration for a large range of frequencies. In the range of 1400 to 1800 Hz, the local decrease of the output charge performance might be due to the air-damping effect, with an unknown relationship. In any case, a good output charge was obtained for the wide-band vibration input, with the output charge ranging from 61.4 to 102.8 pC for the Z-direction input, and 52 to 60 pC, respectively, for the X- and Y-direction vibration inputs. In addition, the corresponding sensitivity of the output voltage increased from 6.1 to 10.2 pC/g and from 5.2 to 6 pC/g for the Z direction and X/Y directions, respectively. Moreover, the results of a wide range of temperature tests showed that there was a variation of performance. With increasing temperatures, the performance of the vibration sensor will be enhanced proportionally, indicating a change of piezoelectric coefficients with the $LiNbO_3$ functional layer. Moreover, the variation of the temperature is regular and controllable. Future work will be focused on the damping effect on the performance of the vibration sensor, and for higher frequencies and lower temperatures, for practical applications in extreme environments. The presented piezoelectric-type MEMS vibration sensors—endowed with excellent linear outputs, high sensitivity to a wide-band vibration environment, and good temperature dependence—can find a potential application in extreme environment exploration.

Supplementary Materials: The following supporting information can be downloaded at: https://www.mdpi.com/article/10.3390/mi13020329/s1, Figure S1: Comsol Multiphysics model indicating the substrate and pedestal, proof mass, and cantilever beams; Figure S2: Modal analysis using Comsol Multiphysics, indicating (a) the first-ordered resonance, (b) second-ordered resonance, and (c) third-ordered resonance, respectively; Figure S3: Photograph of (a) the test system and (b) the vibration platform of the MEMS vibration sensor in ambient conditions; Figure S4: Photographs of the appearance of (a) the outside and (b) the inside of the vibration platform for the testing sensor with a temperature controller; Figure S5: Signal of the output voltage at 20 Hz; Figure S6: Signal of the output voltage at 1 kHz; Figure S7: Signal of the output voltage at 2.4 kHz; Video S1: Movie displaying the output signal of the sinusoidal wave at 2.4 kHz in response to the input vibration.

Author Contributions: Conceptualization, H.W. and W.G.; data curation, T.L. and X.Q.; formal analysis, H.W., Y.S. and G.X.; funding acquisition, X.C.; investigation, X.Q., H.Z. and C.Z.; methodology, H.W.; resources, K.B.; software, K.B. and Y.S.; supervision, X.C.; validation, T.L. and X.L.; writing—original draft, H.W. and W.G.; writing—review and editing, W.G., X.L. and X.C. All authors have read and agreed to the published version of the manuscript.

Funding: This research was supported by the National Natural Science Foundation of China (Grant No. 62171415), the Shanxi Scholarship Council of China (Grant No. 2021-112), the Fundamental Research Program of Shanxi Province (Grant No. 20210302123013), and STIP (Grant No. 2020L0286).

Conflicts of Interest: The authors declare no conflict of interest.

Appendix A

The output performance for the MEMS vibration sensor was tested on the vibration testing platform. Thus, the actual output of the sensor itself should be subjected to the whole vibration platform. The testing system can be seen as a single-freedom two-level damping vibration model, mainly including the vibration platform, the central proof mass, the crossing cantilever beams as the elastic component, and the interior damping due to the air resistance (Figure A1). The practical displacement of the vibration platform x_f can be expressed as

$$x_f t = De^{i\omega t} \tag{A1}$$

where D is the amplitude of the platform and ω is the frequency of the vibration.

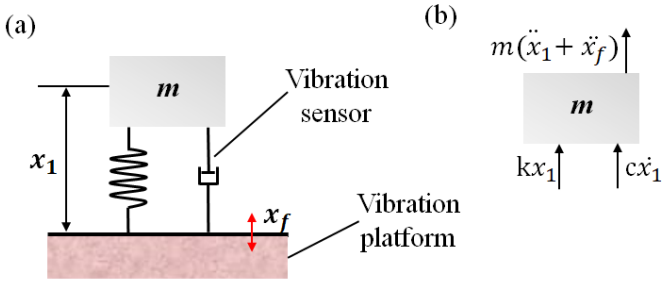

Figure A1. Model of the vibration system. Diagram illustration of (**a**) the vibration system model and (**b**) forces acting on the mass, according to the d Alembert principle.

According to the d Alembert principle, the vibration system dynamic equation for the above model can be described as:

$$m\left(\ddot{x_1}(t) + \ddot{x}_f(t)\right) + c\dot{x_1}(t) + kx_1(t) = 0 \tag{A2}$$

where x_1 is the displacement of the proof mass related to the vibration platform, m is the proof mass, c is the effective damping coefficient, and k is the effective rigidity coefficient.

Substituting the second derivative of x_f, we obtain the governing equation:

$$m\ddot{x_1}(t) + c\dot{x_1}(t) + kx_1(t) = mD\omega^2 e^{i\omega t} \tag{A3}$$

Solving this governing equation, we obtain the analytic solution of $x_1(t)$, which is written as:

$$x_1(t) = \beta B e^{i(\omega t-\theta)} \tag{A4}$$

where $mD\omega^2 = F_0$, $B = \frac{F_0}{k}$ is the static displacement, $\omega_0^2 = \frac{k}{m} = (2\pi f_n)^2$ is the intrinsic frequency of the acceleration system, and $s = \frac{\omega}{\omega_0}$ is the ratio of the excitation frequency to the intrinsic frequency.

By substituting the above factors, the analytic solution of $x_1(t)$ can be expressed as

$$x_1(t) = \frac{s^2}{\sqrt{(1-s^2)^2 + (2\xi s)^2}} De^{i(\omega t-\theta)} \tag{A5}$$

where ξ is the relative damping coefficient. Thus, according to the amplitude and phase frequency distinction curves of the second-order system of a single degree of freedom, the displacement subjected to the acceleration is described as

$$\left|\frac{x_1(t)}{a}\right| = \frac{1}{\omega_0^2} * \frac{1}{\sqrt{(1-s^2)^2 + (2\xi s)^2}} \tag{A6}$$

where the lagging phase angle θ of the response displacement of the central proof mass related to the excitation displacement is given by

$$\theta = \tan^{-1}\frac{2\xi s}{1-s^2} \tag{A7}$$

Working in the range of elastic displacement, the deformation of the cantilever beams of the vibration sensor equals the relative deflection x_1. For the inertia force F acting on the sensor, we obtain the expression $F = kx_1$. Thus, the output charge generated from the piezoelectric layer can be described as:

$$q = d_{ij} * F = d_{ij} * kx_1 \tag{A8}$$

Therefore, we obtain the relationship of the deflection of the cantilever beam and the acceleration, expressed as

$$\frac{x_1}{a} = \frac{q}{a} * \frac{1}{d_{ij} * k} \tag{A9}$$

Finally, the sensitivity of the output charge of the vibration sensor can be described as

$$K_Q = \frac{q}{a} = \frac{1}{\omega_0^2} * \frac{d_{ij} * k}{\sqrt{(1-s^2)^2 + (2\xi s)^2}} \tag{A10}$$

References

1. Campeiro, L.; Silveira, R.; Baptista, F.G. Impedance-based damage detection under noise and vibration effects. *Struct. Health Monit.* **2017**, *17*, 654–667. [CrossRef]
2. Fatima, S.; Guduri, B.; Mohanty, A.; Naikan, V. Transducer invariant multi-class fault classification in a rotor-bearing system using support vector machines. *Measurement* **2014**, *58*, 363–374. [CrossRef]
3. Wang, F.; Song, G. Bolt early looseness monitoring using modified vibro-acoustic modulation by time-reversal. *Mech. Syst. Signal Process.* **2019**, *130*, 349–360. [CrossRef]
4. Zarnik, M.S.; Novak, F. Effect of condensing environments on characteristics of piezoresistive ceramic pressure sensors. *Sens. Actuators A Phys.* **2017**, *267*, 385–392. [CrossRef]
5. Lian, Y.-S.; Sun, J.-Y.; Ge, X.-M.; Yang, Z.-X.; He, X.-T.; Zheng, Z.-L. A theoretical study of an improved capacitive pressure sensor: Closed-form solution of uniformly loaded annular membranes. *Measurement* **2017**, *111*, 84–92. [CrossRef]
6. Kuo, C.-L.; Lin, S.-C.; Wu, W.-J. Fabrication and performance evaluation of a metal-based bimorph piezoelectric MEMS generator for vibration energy harvesting. *Smart Mater. Struct.* **2016**, *25*, 105016. [CrossRef]
7. Grall, S.; Dufour, I.; Aubry, V.; Debéda, H. Fabrication and characterisation of piezoelectric screen-printed in plane resonant microcantilevers used as gravimetric sensors. *Smart Mater. Struct.* **2019**, *28*, 105055. [CrossRef]
8. Li, M.; Gao, R.; Liu, S.; Tong, L. Modeling, analysis and validation of a novel asymmetric cruciform harvester with d 15 mode. *Smart Mater. Struct.* **2019**, *29*, 025014. [CrossRef]
9. Derakhshani, M.; Momenzadeh, N.; Berfield, T.A. Analytical and experimental study of a clamped-clamped, bistable buckled beam low-frequency PVDF vibration energy harvester. *J. Sound Vib.* **2021**, *497*, 115937. [CrossRef]
10. Zhang, C.; Jiang, W.; Ghosh, A.; Wang, G.; Wu, F.; Zhang, H. Miniaturized langasite MEMS micro-cantilever beam structured resonator for high temperature gas sensing. *Smart Mater. Struct.* **2020**, *29*, 055002. [CrossRef]
11. Shen, D.; Park, J.-H.; Ajitsaria, J.; Choe, S.-Y.; Wikle, H.; Kim, D.-J. The design, fabrication and evaluation of a MEMS PZT cantilever with an integrated Si proof mass for vibration energy harvesting. *J. Micromechan. Microeng.* **2008**, *18*, 055017. [CrossRef]
12. Shen, D.; Park, J.-H.; Noh, J.H.; Choe, S.-Y.; Kim, S.-H.; Wikle, H.; Kim, D.-J. Micromachined PZT cantilever based on SOI structure for low frequency vibration energy harvesting. *Sens. Actuators A Phys.* **2009**, *154*, 103–108. [CrossRef]
13. Jeon, Y.; Sood, R.; Jeong, J.-H.; Kim, S.-G. MEMS power generator with transverse mode thin film PZT. *Sens. Actuators A Phys.* **2005**, *122*, 16–22. [CrossRef]

14. Ren, B.; Or, S.W.; Zhang, Y.; Zhang, Q.; Li, X.; Jiao, J.; Wang, W.; Liu, D.; Zhao, X.; Luo, H. Piezoelectric energy harvesting using shear mode $0.71Pb(Mg_{1/3}Nb_{2/3})O_3 \mp 0.29PbTiO_3$ single crystal cantilever. *Appl. Phys. Lett.* **2010**, *96*, 083502. [CrossRef]
15. Zhou, L.; Sun, J.; Zheng, X.; Deng, S.; Zhao, J.; Peng, S.; Zhang, Y.; Wang, X.; Cheng, H. A model for the energy harvesting performance of shear mode piezoelectric cantilever. *Sens. Actuators A Phys.* **2012**, *179*, 185–192. [CrossRef]
16. Islam, M.S.; Beamish, J. Shear Piezoelectric and Dielectric Properties of LN, PMN-PT and PZT-5A at Low Temperatures. *J. Low Temp. Phys.* **2018**, *194*, 285–301. [CrossRef]
17. Qu, M.; Shen, Y.; Wu, L.; Fu, X.; Cheng, X.; Wang, Y. Homogenous and ultra-shallow lithium niobate etching by focused ion beam. *Precis. Eng.* **2020**, *62*, 10–15. [CrossRef]
18. Li, Y.; Lan, T.; Yang, D.; Xiang, M.; Dai, J.; Li, C.; Wang, Z. Research of selective etching in $LiNbO_3$ using proton-exchanged wet etching technique. *Mater. Res. Express* **2020**, *7*, 056202. [CrossRef]
19. Xiang, B.-X.; Wang, L.; Ma, Y.-J.; Yu, L.; Han, H.-P.; Ruan, S.-C. Supercontinuum Generation in Lithium Niobate Ridge Waveguides Fabricated by Proton Exchange and Ion Beam Enhanced Etching. *Chin. Phys. Lett.* **2017**, *34*, 24203. [CrossRef]
20. Kim, S.-B.; Park, H.; Kim, S.-H.; Wikle, H.; Park, J.-H.; Kim, D.-J. Comparison of MEMS PZT Cantilevers Based on d_{31} and d_{33} Modes for Vibration Energy Harvesting. *J. Microelectromechan. Syst.* **2012**, *22*, 26–33. [CrossRef]
21. Shivashankar, P.; Gopalakrishnan, S. Design, modeling and testing of d_{33}-mode surface-bondable multilayer piezoelectric actuator. *Smart Mater. Struct.* **2019**, *29*, 045016. [CrossRef]
22. Payam, A.F.; Trewby, W.; Voïtchovsky, K. Simultaneous viscosity and density measurement of small volumes of liquids using a vibrating microcantilever. *Analyst* **2017**, *142*, 1492–1498. [CrossRef] [PubMed]
23. Sun, Z.; Liu, J.; Yu, C.; Zheng, Y. A Small Range Six-Axis Accelerometer Designed with High Sensitivity DCB Elastic Element. *Sensors* **2016**, *16*, 1552. [CrossRef] [PubMed]
24. Altieri, L.; Tonoli, A. Piezoelectric Injectors for Automotive Applications: Modeling and Experimental Validation of Hysteretic Behavior and Temperature Effects. *J. Dyn. Syst. Meas. Control* **2012**, *135*, 011005. [CrossRef]

micromachines

Article

Dependance of Gauge Factor on Micro-Morphology of Sensitive Grids in Resistive Strain Gauges

Yinming Zhao [1,2], Zhigang Wang [3], Siyang Tan [3], Yang Liu [3], Si Chen [2], Yongqian Li [3,*] and Qun Hao [1]

[1] School of Optics and Photonics, Beijing Institute of Technology, No.5 South Zhongguancun Street, Haidian District, Beijing 100081, China; zhaoyinming@cimm.com.cn (Y.Z.); qhao@bit.edu.cn (Q.H.)
[2] Beijing Changcheng Institute of Metrology & Measurement, Beijing 100095, China; chensi@cimm.com.cn
[3] Key Laboratory of Micro/Nano Systems for Aerospace of Ministry of Education, Northwestern Polytechnical University, Xi'an 710072, China; zgwang@mail.nwpu.edu.cn (Z.W.); sytan@mail.nwpu.edu.cn (S.T.); ly201169@mail.nwpu.edu.cn (Y.L.)
* Correspondence: liyq@nwpu.edu.cn; Tel.: +86-29-8846-0353 (ext. 610)

Abstract: The effect of micro-morphology of resistive strain gauges on gauge factor was investigated numerically and experimentally. Based on the observed dimensional parameters of various commercial resistive strain gauges, a modeling method had been proposed to reconstruct the rough sidewall on the sensitive grids. Both the amplitude and period of sidewall profiles are normalized by the sensitive grid width. The relative resistance change of the strain gauge model with varying sidewall profiles was calculated. The results indicate that the micro-morphology on the sidewall profile led to the deviation of the relative resistance change and the decrease in gauge factor. To verify these conclusions, two groups of the strain gauge samples with different qualities of sidewall profiles have been manufactured, and both their relative resistance changes and gauge factors were measured by a testing apparatus for strain gauge parameters. It turned out that the experimental results are also consistent with the simulations. Under the loading strain within 1000 μm/m, the average gauge factors of these two groups of samples are 2.126 and 2.106, respectively, the samples with rougher profiles have lower values in gauge factors. The reduction in the gauge factor decreases the sensitivity by 2.0%. Our work shows that the sidewall micro-morphology on sensitive grids plays a role in the change of the gauge factor. The observed phenomena help derive correction methods for strain gauge measurements and predict the measurement errors coming from the local and global reinforcement effects.

Keywords: resistive strain gauge; gauge factor; sensitive grids; micro-morphology; force sensor

Citation: Zhao, Y.; Wang, Z.; Tan, S.; Liu, Y.; Chen, S.; Li, Y.; Hao, Q. Dependance of Gauge Factor on Micro-Morphology of Sensitive Grids in Resistive Strain Gauges. *Micromachines* **2022**, *13*, 280. https://doi.org/10.3390/mi13020280

Academic Editor: Weidong Wang

Received: 31 December 2021
Accepted: 3 February 2022
Published: 10 February 2022

1. Introduction

Strain gauges are commonly used in aerospace, transportation, automotive industry, civil engineering, and even in the medical field. Based on a combination of elastic elements and strain gauges, the physical quantities acting on structures, such as strain, displacement, bending, torque, and acceleration, can be measured directly or indirectly [1–3].

The strain gauge incorporates the resistance change linearly with deformation in its sensitive grids [1]. During the measurement process, strain gauges sense the elastomeric strain and translate it into a change of resistance value. The term to describe the correlation between these two variables is called gauge factor (GF), which is defined as the ratio of the relative resistance change (RRC) to the strain [4]:

$$GF = \frac{\Delta R/R}{\varepsilon} \quad (1)$$

where the $\Delta R/R$ is RRC in strain gauges, and ε is the corresponding strain.

When strain is transmitted from the elastic element to the strain gauge, the strain reduction is caused by a mismatch in stiffness between the sensitive grid and the tested

sample [3], and so do strain distortions on the edges [5,6]. Compared with strains experimented by elastic elements in the absence of strain gauges, those measured with strain gauges have lower values. This strain reduction and redistribution in resistive strain gauges contribute to the known reinforcement effect [7,8] which can lead to significant errors in determining the GF.

The structure configuration of the resistive strain gauge has a profound effect on electrical conductivity, which results in a varying GF of the strain gauge. The surface topographies from three typical metallic materials have been quantitatively characterized and analyzed to investigate the effect of micro-stress concentrations within the sensitive grids [7]. The integrated influences of characteristic surface parameters on micro-stress behavior have been considered to estimate the impact of surface conditions on the performance of GFs. The geometrical dimensional sizes of the strain gauge determine the GF and the measurement uncertainties due to strain disorder distributions [9,10]. It has been confirmed that the thinner film has a higher value of GF [11], and that the increased island sizes of sensitive grids decrease the GF [12,13]. The optimized end structures and corner arcs of susceptible grids reduce the transverse effect and improve their GFs [14].

In fact, strain gauges deflected from the perfect cross-section and the ideal sidewall profile of sensitive grids have defects in creep-lag effect, long-term stability and temperature self-compensation [15]. However, the sensitive grid patterns are usually fabricated by the processes of lithography and wet etching, whose poor selectivity of the damp etching results in irregular sidewall micro-morphology on sensitive grids [6]. These defects induce the electrical conductivity deviation of resistive strain gauges. By now, few works of literature focus on correlations between the property of the GF and the micro-morphology on the sidewall profiles. In order to calibrate the GF obtained by strain gauges during measurements and improve the long-term stability of resistive strain sensors, we observed the micro-morphology on various commercial strain gauges and calculated the geometrical parameters of the sidewall profiles. The finite element and experiment method had been used to investigate the GF determined by strain transfer characteristics of the strain gauges. Thereby, the focus has been laid on the sidewall micro-morphology of the sensitive grids, which would change the stress–strain characteristics of resistive strain gauges.

2. Geometrical Model and Simulations

For specific manufacturing equipment and processes, the micro-morphology on sensitive grids of strain gauges obtained by wet etching is controllable within a certain tolerance. However, it is this varying degree of tolerance that can result in strain gauges of very different qualities from one manufacturer to another. In detail, this difference mainly lies in the roughness of the sidewall profile on sensitive grids. To have a visual and analytical understanding, the sidewall micro-morphology of a typical strain gauge have been observed by confocal microscopy (KH-7700 by HIROX company in Shanghai, China). Additionally, the geometric characteristics of the sensitive grids were obtained through a scanning electron microscopy (SEM). As shown in Figure 1a, the shallow gray area in the SEM image refers to sensitive grids, while the dark gray is the blank gap between them. With image processing methods, Figure 1b,c show the sidewall profile of a sensitive grid from the viewpoint of a binary image.

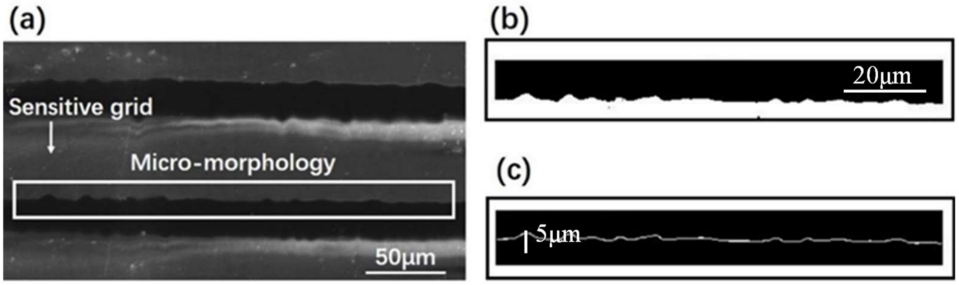

Figure 1. The microscopy image and the obtained sidewall micro-morphology of a typical strain gauge. (**a**) Scanning electron microscope image, (**b**) Binary image, and (**c**) Sidewall profile of a single sensitive grid.

In this study, geometrical parameters of the sidewall profile on sensitive grids include average profile unit width R_a, average profile unit length R_{sm}, the maximum width R_{ai} and maximum length R_{smi} of each unit. For a certain sidewall profile line, the R_a is defined by:

$$R_a = \frac{1}{m}\sum_{i=1}^{m}|R_{ai}|, \tag{2}$$

where m is the total number of discrete points. Similarly, the R_{sm} is written as:

$$R_{sm} = \frac{1}{n}\sum_{i=1}^{n} R_{smi}, \tag{3}$$

where n is the total number of the profile units. These definitions describe the amplitude and frequency of rough sidewall profiles.

By random observation and measurement, we obtained the above geometrical parameters of the sidewall profiles from four kinds of commercial resistive strain gauges, and the number of which were dozens of. Here we need to add that, after further research [16], we have demonstrated that textures left on the upper surfaces of sensitive grids due to resistance trimming also affect the performance of strain gauges, and in this study, in order to control the study variables, we chose commercial strain gauges without significant upper surface textures. Based on the data obtained, we classified these strain gauges according to their sidewall qualities and grouped them into a total of four categories. Additionally, we selected the most representative binarized image from each of these four categories and obtained the geometrical parameters for each group by averaging, as shown in Table 1, their geometrical parameters vary. From the horizontal view of Table 1, R_a, R_{ai} and R_{sm} increase sequentially. Moreover, the R_a, as the arithmetic mean of R_{ai}, is the smallest among the three. From the longitudinal view, the first image shows a smooth sidewall and smaller geometrical parameters, whereas Sample 4 takes on a rough and worse condition of sensitive grids. All three sets of values gradually increase as the sidewall profile becomes progressively rougher from the first to the fourth image. When the sidewalls are rough to a certain degree, R_{ai} and R_{sm} can even reach the order of tens of microns.

Table 1. Typical sidewall profile parameters of sensitive grids (Units: μm).

Serial Number	Binarized Image	R_a	R_{ai}	R_{sm}
1		0.4	2.2	2.7
2		1.2	6.7	45.4
3		2.3	14.1	38.1
4		6.0	26.0	36.5

Among the above four kinds of resistive strain gauges, the basic dimensional sizes corresponding to the type HBM1-DY13-3/350 were selected to build the simulation model, in which the grid width is 50 μm and the thickness is 5 μm [17]. Following the parameters in Table 1, a geometrical model of the sidewall profile was constructed to study the GF. As

shown in Figure 2, the complex waveforms or zigzag sidewalls demonstrated in Table 1 are simplified to be a standard cosine curve, where the amplitude (A) and period (T) describe the cosine type profile. In real work situations, the strain in elastic elements produced by an applied tension force is passively transferred to the sensitive grids through the substrate and adhesive layer [14], to apply a uniform shear force into the sensitive grid and reduce the reinforcement effect, the sizes of both substrate and adhesive layer are set to be larger than that of the sensitive grid.

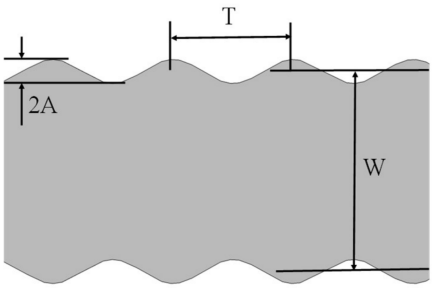

Figure 2. The geometry model for a segment of a sensitive grid in a strain gauge. The parameters of amplitude (A) and period (T) describe the cosine-curve profile. The width (W) of the sensitive grid is located between two dashed lines estimated by the least square methods.

In addition, the Poisson's ratio of each elastic modulus and material's layer plays a role in GF; however, since we chose fixed materials, only the sidewall defects were mainly investigated here.

The piezo-resistance property of metal materials is defined as the bulk resistivity change due to applied stress or strain. The resistivity change induced by stress in cubic symmetry materials is expressed as below general form [18]:

$$\begin{bmatrix} \Delta\rho_1/\rho_0 \\ \Delta\rho_2/\rho_0 \\ \Delta\rho_3/\rho_0 \\ \Delta\rho_4/\rho_0 \\ \Delta\rho_5/\rho_0 \\ \Delta\rho_6/\rho_0 \end{bmatrix} = \begin{bmatrix} \pi_{11} & \pi_{12} & \pi_{12} & 0 & 0 & 0 \\ \pi_{12} & \pi_{11} & \pi_{12} & 0 & 0 & 0 \\ \pi_{12} & \pi_{12} & \pi_{11} & 0 & 0 & 0 \\ 0 & 0 & 0 & \pi_{44} & 0 & 0 \\ 0 & 0 & 0 & 0 & \pi_{44} & 0 \\ 0 & 0 & 0 & 0 & 0 & \pi_{44} \end{bmatrix} \begin{bmatrix} \sigma_1 \\ \sigma_2 \\ \sigma_3 \\ \sigma_4 \\ \sigma_5 \\ \sigma_6 \end{bmatrix} \quad (4)$$

where ρ_0 is the initial resistivity, $\Delta\rho_i/\rho_0$ is the resistivity change, σ_i is the stress, and π_{ij} is the piezo-resistance coefficient. The properties of the constantan material used for the strain gauge in our calculations are summarized in Table 2, which are consistent with the data in [18,19].

Table 2. Material properties of constantan.

Density (kg/cm^3)	Young's Modulus (GPa)	Poisson's Ratio	Resistivity ($\Omega\cdot\mu m$)	π_{ij} ($\times 10^{-12}$ Pa^{-1})
8.88	160	0.329	0.48	π_{11}= 2.3, π_{12}= 2.3, π_{44} = 0

The parameters of both amplitude (A) and period (T) in the cosine profile model (Figure 2) are normalized by the widths of the sensitive grids (W). Numerically, they are expressed as A/W (relative amplitude, RA) and T/W (relative period, RP), respectively. On this basis, RRC and GF were calculated in varying sidewall profiles and external stress conditions. In Figure 3a, RRC related with RA and RP were presented. In the interested strain range of 0 to 2000 μm/m, RRCs are almost linearly proportional to the applied strain. For a certain strain (1000 μm/m), the growing tendency of RRC resulting from the increase of RA and RP can be easily told in the partial enlarged view (Figure 3a). This phenomenon is well confirmed by the calculation results in Figure 3b. Particularly, it is worth noting that

the scale of the abscissa interval in Figure 3b is much larger than the 0.06×10^{-4} variation range of the ordinate; therefore, the actual curves are very close to horizontal straight lines, which means GFs approximately maintain constant. As for the small-scale increase in GFs caused by RA and RP, we can understand it as: the stress redistribution affected by the sidewall profile will aggravate the creep effect of the material [16], which eventually affect GF. From above, the varying sidewall micro-morphology of sensitive grids leads to changes in both RRC and GF. Consequently, the deviations between the rough sidewall profile and perfectly smooth one should be taken into account so as to improve the measurement accuracy of the sensitive grids [7,20].

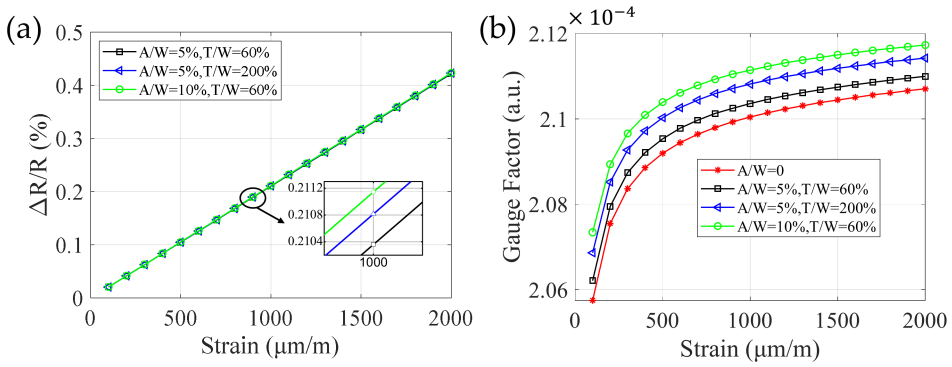

Figure 3. The dependence of RRC and GF on RA and RP in sensitive grids. (**a**) Three susceptible grids with different RA and RP are calculated and increasing RRCs were led by both. (**b**)The calculated GFs increase with the strain load in varying RA and RP conditions. Here, an ideal profile with A/W = 0 is used to be the reference for a clear demonstration in (**b**).

As shown in Figure 4, increasing RA (A/W) or RP (T/W) results in growing RRC. In the case of a constant RP, Figure 4a shows a sharp rising of RRC over the increasing RA, and this variation in RRC is nonlinear over a tenth of the sensitive gate width, meaning that the amplitudes of sidewall profiles gradually amplify the deviation of relative resistance change in the strain gauge under a constant load. However, as shown in Figure 4b, the results are much different. For a given RA, the RRCs fluctuate in a small range around a certain value. Take A/W = 4% for example, the waveform length would almost not lead to relative resistance change, and this is in line with the theory [21]. Still, the volatility of the RRC at the beginning step of the curve is more pronounced, while it flattens out more in the rest section. It is not difficult to understand, with a fixed RA, an increasing RP represents a smoother sidewall profile of the sensitive grid that possess a steady RRC.

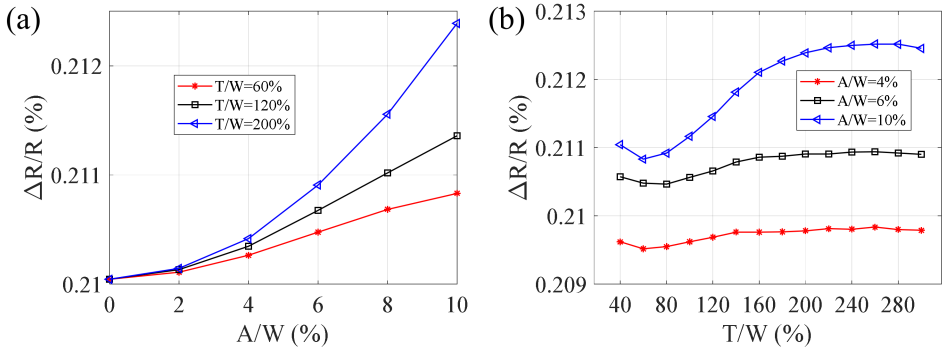

Figure 4. RRC and GF are affected by the geometrical parameters of (**a**) RP and (**b**) RA in the cosine profile. The loaded strain is 500 μm/m.

These phenomena seem reasonable when considering the correlation between sidewall roughness and stress deformations. As stated above, when RP becomes long enough, the sidewall profile equally becomes smooth. The smooth profile would reduce the local

strain concentration until a homogeneous strain distribution forms. Under this condition, the deformation in resistive strain gauges would represent the strain in elastic elements to the greatest extent, and the measured GF is a standard one. Yet, there is no way to produce strain gauges with absolutely smooth sidewalls on sensitive grids. As the non-ideal sensitive grid is subjected to external stress, the deformation of each aera is uneven and the concave parts produce local stress concentrations. As shown in Figure 5, when RAs are the same in Figure 5a,b, the longer RP (Figure 5b) reduces the maximum local strain concentration within the sharp dimensional area, which results in a relatively even strain distribution within the sensitive body. Further, the even distribution induces a much larger change of relative resistance, or a more accurate sensitivity. In Figure 5a, a sharper shape on the sidewall profile produces a worse local strain concentration than that in Figure 5b, and the lower strain distribution over the grid body decreases the resistance change and leads to measurement deviation. For the same reason, for an RA that is less than 4% of the grid width (Figure 4b), the RRC becomes a basically unchanged number even the RP range from 40% to 80% in our simulations, meaning that as long as the sidewall is relatively smooth, the RRC basically maintains at the standard constant no matter how high or low RA/RP is.

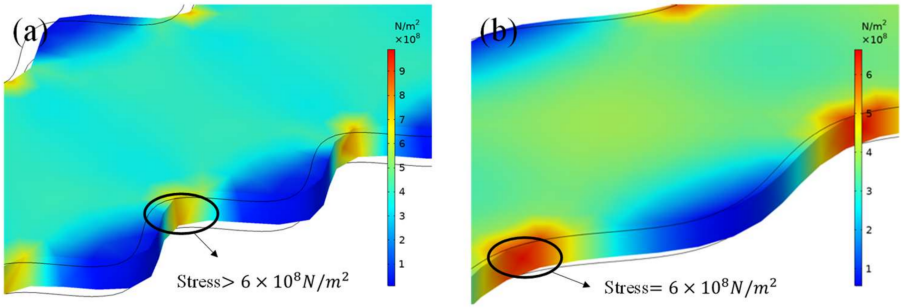

Figure 5. The strain distributions due to the sidewall profile roughness of the sensitive grids under the same load. The sidewall profile is assumed to be (**a**) T/W = 60% and (**b**) T/W = 120%.

3. Experimental Results and Discussion

The micro-morphology of sensitive grids depends on the fabrication processes. Especially, during lithography, both mask and photoresist determine the quantity of fabricated pattern and the sidewall profile of sensitive grids. Figure 6 shows two process flows fabricating strain gauges, in which the discrepant sidewall profiles can be obtained. A Cr-mask and positive photoresist are used in the craft I, and a film mask and negative photoresist are adopted in the craft II. The former produces a smoother profile with finer resolution while the later brings out a rough one with micro-bulges on [22,23].

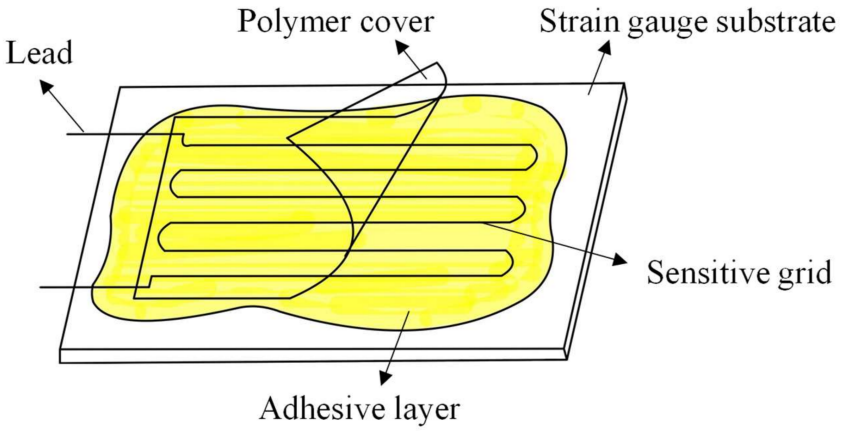

Figure 6. Structural diagram of the strain gauges used in the experimental test [6].

To have clear demonstration and contrast in the following experiment, two groups of strain gauges we used were manufactured by the above two processes, respectively, and there were dozens of samples per group. The structures of all these samples are the same (Figure 6) [6], and the materials of the main layers of the structure are shown in Table 3. Based on the principle of random measurement, it turned out that the quality of the sidewalls of the samples within the group were all about the same, while there were large differences between the two groups. The sidewall of the most representative sample in each group is shown in Figure 7b,c. Estimated with Equations (2) and (3), their geometrical parameters are listed in Table 4. In addition, we selected two more strain gauges with almost the same qualities of sidewall profiles from each group, that is, based on the three strain gauges in each group, we obtained their stress response and GF by the experiment.

Table 3. Materials of the main layers of strain gauges used in the experimental test.

Strain Gauge Substrate	Adhesive Layer	Sensitive Grids
Polyimide	Epoxy resin	Constantan alloy

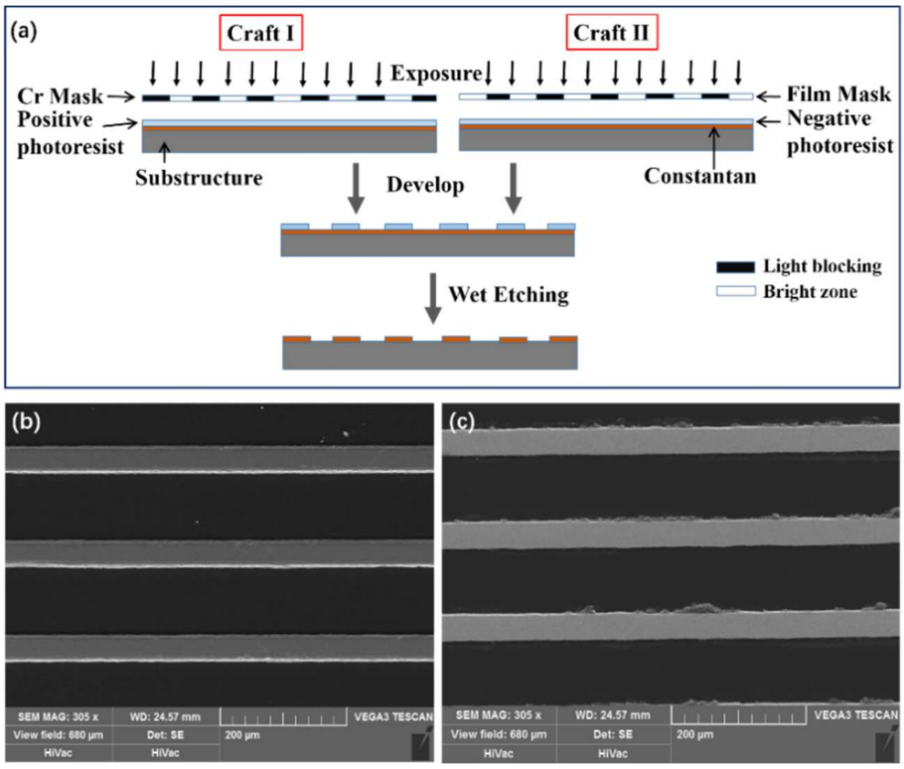

Figure 7. Fabrication processes for obtaining strain gauges and the resulting sidewall quantity. (**a**) Two fabrication processes. The SEM images of micro-morphology produced by (**b**) the Cr-mask and positive photoresist and (**c**) film mask and negative photoresist.

Table 4. The sidewall surface in two groups of fabricated strain gauge samples.

Sample	Craft	SEM Images	R_a	R_{ai}	R_{sm}
Group I	Craft I		0.48	2.79	4.00
Group II	Craft II		1.37	9.90	29.40

All the six samples were measured in a testing apparatus for strain gauge parameters [17,24]. As shown in Figure 8c,d, in order to be identical to actual use, the strain gauges were glued to the surface of the rigid standard elastic beam and then solidified by

thermal curing process. A standard applied force produces a uniform strain in the middle of the standard flexible beam. As shown in Figure 8a,b, the pressure on the power arms bends the elastic beam delivering both negative and positive strain to the standard elastic beam. There are equal strain zones in the center area of the standard elastic beam. The strain values are calculated by the deflection theory, in which the deflection displacement of f+ and f− are measured by a standard flexometer. In addition, a Wheatstone bridge for converting the strain into an electrical signal was connected to a data acquisition amplifier (HBM QuantumX MX1615B) [17].

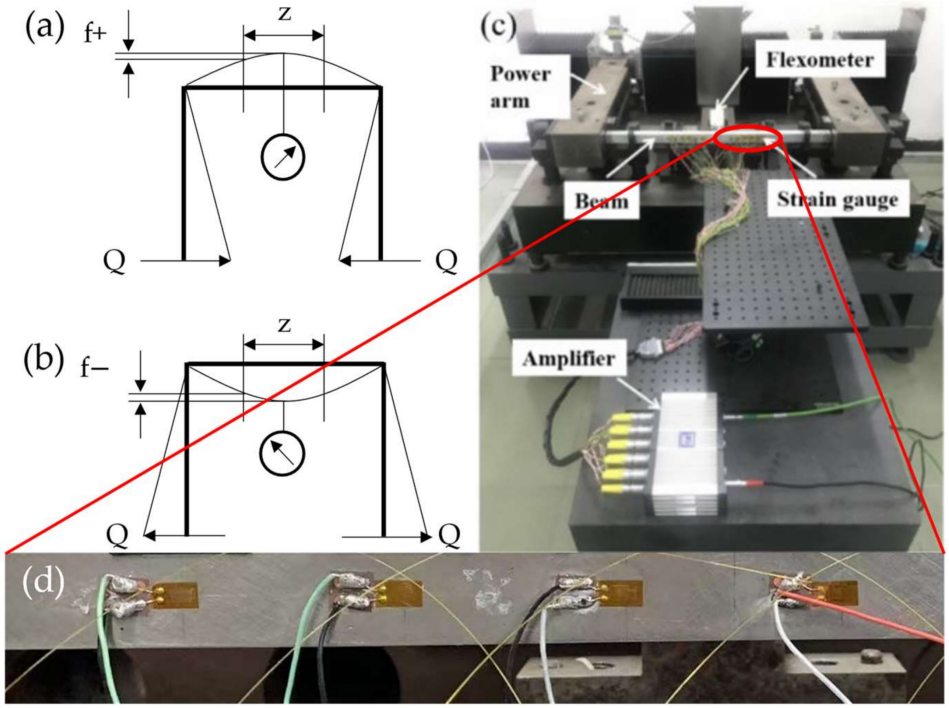

Figure 8. Testing apparatus for strain gauge parameters. A schematic diagram of the negative (**a**) and positive (**b**) strain produced in a standard elastic beam by a linear loading Q applied on the power arms. (**c**) The picture of the testing apparatus for strain gauge parameters. (**d**) Photo of a standard elastic beam with strain gauges glued.

The linear loading force Q provides an elastic beam strain ranging from 0 to 1000 μm/m. Two groups of strain gauge samples were measured and the strain responses are presented in Figure 9. In the initial region of small strain values, the measured values from two groups are almost indistinguishable. However, with the strain increasing up to 500 μm/m~1000 μm/m, the strain deviation in Group II increases in a small range compared to the Group I. Considering that commercial strain gauges are inherently high-precision components, this small difference in the measurement due to microscopic sidewall profiles still makes sense. Numerically speaking, using the data in Figure 9, the linearities of the two groups can be obtained using the least squares method and they are 1.005 (Group I) and 1.023 (Group II), respectively. The deviations of the linearities from standard value 1 are 0.5% and 2.3%, which results from the sidewall profile difference between the two groups of fabricated samples.

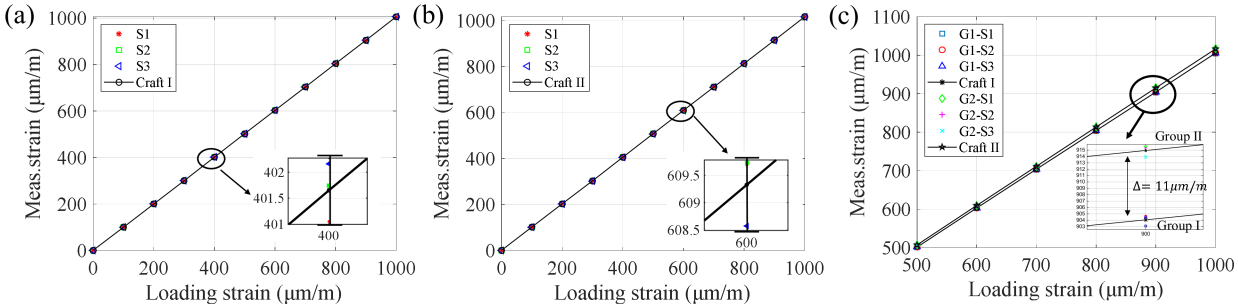

Figure 9. The strain response from two groups of samples to the standard strains. The geometrical parameters of (**a**) Group I and (**b**) Group II are listed in Table 3. (**c**) The parts of (**a**,**b**) in the range 500–1000 μm/m are plotted onto the same graph. The strain in the ordinate was measured by the samples, while the strain in the abscissa was calculated by the loading force and the displacements coming from the flexometer.

Moreover, within 1000 μm/m of the loading strain, we measured the GFs from the two groups of samples. In Figure 10, The results indicate that the strain gauges in Group I, which have smaller roughness of sidewall profiles, have larger GFs than those in Group II. Although the measurements were approximately linearly correlated between the measured strain gauges and the standard test apparatus, the data in Figure 10a,b show that the GF values for Group I are definitely greater than those for Group II, in other words, the strain gauge with a smooth sidewall profile have a better sensitivity. Among the measured data in Figure 10, the average GFs in two groups are 2.126 and 2.106, respectively, and the difference between these two values is 0.02. The reduction of the GF decreases the sensitivity by 2.0%. Furthermore, we have shown that the roughness of the textured surface on sensitive grids also shortens the fatigue lifetime and enhances the creep effect of strain gauges [23]. The deterioration of the GF leads to a great amount of measurement uncertainty against the long-term reproducibility in metrology force sensors. The experiment's conclusion agrees well with the obtained simulation results shown in Figures 3 and 4.

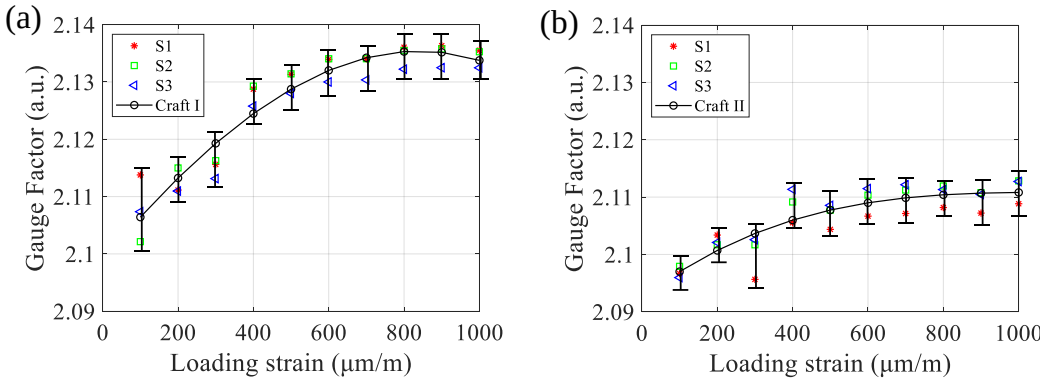

Figure 10. The GF was measured from two groups of fabricated strain gauges. Three samples with smoother sidewall profiles manufactured by Craft I (**a**), while the other three fabricated by Craft II have rougher sidewall profiles (**b**). The loading strain increases from 100 to 1000 μm/m.

4. Conclusions

The dependence of the micro-morphology on resistance changes and gauge factors in resistive strain gauges were investigated numerically and experimentally. The dimensional sizes and their geometrical parameters of the sidewall profiles on sensitive grids are obtained utilizing scanning electron microscopic and the image processing techniques. Based on these data, a model of the sensitive grid with variable cosine profiles had been built and used in simulations, where cosine curves are approximately equivalent to the actual complex waveforms or zigzag sidewall profiles. Subsequently, the relative resistance

changes and gauge factors under different amplitudes and periods of the cosine model have been analyzed by simulations. Additionally, using testing apparatus for strain gauge parameters, we tested two groups of strain gauges which were manufactured by two fabrication processes and have sensitive grids with different sidewall qualities. The results in both the simulation and experiments show that the periodic depression on the sidewall enhances the local strain concentration and weakens the strain distribution over the grid body, indicating that the rough micro-morphology leads to the decrease in gauge factors and results in the relative reduction of accuracy and sensitivity of strain gauges. These results make it clear that the rough sidewall profiles exacerbate to the measurement uncertainty. For ultra-high-precision sensors, such deviations are not allowed; therefore, the disadvantages caused by the micro-morphology of strain gauges must be taken into consideration, and the measurement must be calibrated in the best possible way.

Author Contributions: Conceptualization, Y.Z. and Z.W.; methodology, Y.L. (Yongqian Li), Y.Z. and Z.W.; software, Z.W. and Y.L. (Yang Liu); validation, Y.L. (Yongqian Li); formal analysis, Y.L. (Yang Liu); investigation, S.T. and S.C.; resources, Y.Z. and Y.L. (Yongqian Li); data curation, Y.L. (Yang Liu); writing—original draft preparation, Y.Z. and Y.L. (Yongqian Li).; writing—review and editing, S.T.; visualization, Y.L. (Yang Liu) and S.T.; supervision, Q.H.; project administration, Y.Z. and Y.L. (Yongqian Li); funding acquisition, Y.Z. and Y.L. (Yongqian Li). All authors have read and agreed to the published version of the manuscript.

Funding: The work was supported by the National Key R&D Program of China (2017YFF0105500), and partly by the National Natural Science Foundation of China (NSFC-No. 51575455).

Conflicts of Interest: The authors declare no conflict of interest.

References

1. Kervran, Y.; De Sagazan, O.; Crand, S.; Coulon, N.; Mohammed-Brahim, T.; Brel, O. Microcrystalline silicon: Strain gauge and sensor arrays on flexible substrate for the measurement of high deformations. *Sens. Acttors A Phys.* **2015**, *236*, 273–280. [CrossRef]
2. Shakeel, M.; Khan, W.A.; Rahman, K. Fabrication of cost effective and high sensitivity resistive strain gauge using DIW technique. *Sens. Actuators A Phys.* **2017**, *258*, 123–130. [CrossRef]
3. Xia, Q.; Liu, H. Multi-axis dynamic displacement measurement based on a strain shunt structure. *Sens. Actuators A Phys.* **2018**, *272*, 62–74. [CrossRef]
4. Barlian, A.A.; Park, W.T.; Mallon, J.R., Jr.; Rastegar, A.J.; Pruitt, B.L. Review: Semiconductor Piezoresistance for Microsystems. *Proc. IEEE Inst. Electr. Electron. Eng.* **2009**, *97*, 513–552. [CrossRef] [PubMed]
5. Stehlin, P. Strain distribution in and around strain gauges. *J. Strain Anal.* **1972**, *7*, 228–235. [CrossRef]
6. Li, Y.; Wang, Z.; Xiao, C.; Zhao, Y.; Zhu, Y.; Zhou, Z. Strain transfer characteristics of resistance strain-type transducer using elastic-mechanical shear lag theory. *Sensors* **2018**, *18*, 2420. [CrossRef]
7. Parker, R.L.; Krinsky, A. Electrical Resistance-Strain Characteristics of Thin Evaporated Metal Films. *J. Appl. Phys.* **1963**, *34*, 2700–2708. [CrossRef]
8. Ajovalasit, A.; Fragapane, S.; Zuccarello, B. The Reinforcement Effect of Strain Gauges Embedded in Low Modulus Materials. *Strain* **2013**, *49*, 366–376. [CrossRef]
9. D'Andrea, L.A.; Masson, R.W. Strain Sensor. U.S. Patent US5347871A, 20 September 1994.
10. Ajovalasit, A.; Zuccarello, B. Local Reinforcement Effect of a Strain Gauge Installation on Low Modulus Materials. *J. Strain Anal. Eng. Des.* **2006**, *40*, 643–653. [CrossRef]
11. Meiksin, Z.H.; Hudzinski, R.A. A Theoretical Study of the Effect of Elastic Strain on the Electrical Resistance of Thin Metal Films. *J. Appl. Phys.* **1967**, *38*, 4490–4494. [CrossRef]
12. Neuman, M.R.; Sutton, W.G. Structural Dependence of Strain Gauge Effect and Surface Resistivity for Thin Gold Films. *J. Vac. Sci. Technol.* **1969**, *6*, 710–713. [CrossRef]
13. Hrovat, M.; Belavic, D.; Samardzija, Z.; Holc, J. A characterisation of thick film resistors for strain gauge applications. *J. Mater. Sci.* **2001**, *36*, 2679–2689. [CrossRef]
14. Hilbig, D.; Hannemann, B. Rapid prototyping of silicon microstructures by means of a new masking process and crystal orientation dependent etching. *Sens. Actuators A Phys.* **2010**, *163*, 388–392. [CrossRef]
15. Yadollahi, A.; Mahtabi, M.; Khalili, A. Fatigue Life Prediction of Additively Manufactured Material: Effects of Surface roughness, Defect size, and Shape. *Fatigue Fract. Eng. Mater. Struct.* **2018**, *41*, 1602–1614. [CrossRef]
16. Zhao, Y.; Tan, S.; Zhang, C.; Liu, Y.; Li, Y.; Hao, Q. Dependence of Creep Strain and Fatigue Behavior on Surface Characteristics of Resistive Strain Gauges. (To Be Submitted). Available online: https://www.mdpi.com/journal/micromachines (accessed on 22 January 2022).

17. HBM Strain Gauges. Available online: https://www.hbm.com/cn/3053/quantumx-mx1615b-bridge-amplifier-for-strain-gauges (accessed on 11 July 2020).
18. Hu, C.Y.; Gao, Y.Q.; Sheng, Z.Y. The piezoresistance coefficients of copper and copper-nickel alloys. *J. Mater. Sci.* **2000**, *35*, 381–386. [CrossRef]
19. Moradi, M.; Sivoththaman, S. Strain Transfer Analysis of Surface-Bonded MEMS Strain Sensors. *IEEE Sens. J.* **2013**, *13*, 637–643. [CrossRef]
20. Liu, Z.; Qi, D.; Guo, P.; Liu, Y.; Zhu, B.; Yang, H.; Liu, Y.; Li, B.; Zhang, C.; Yu, J.; et al. Thickness-Gradient Films for High Gauge Factor Stretchable Strain Sensors. *Adv. Mater* **2015**, *27*, 6230–6237. [CrossRef] [PubMed]
21. Wang, Z. *Finite Element/Smooth Contour Method for Flow and Heat Transfer Problems with Complex Boundary Conditions*; Graduate School of Chinese Academy of Sciences, Institute of Engineering Thermophysics: Beijing, China, 2013. (In Chinese)
22. Nie, L.; Shi, T.; Liao, G.; Zhong, F. Application of Cr Mask in wet etching of silicon. *Semicond. Technol.* **2005**, *26–28*, 34. (In Chinese)
23. Oleshkevich, A.N.; Lapchuk, N.M.; Odzhaev, V.B.; Karpovich, I.A.; Prosolovich, V.S.; Brinkevich, D.I.; Brinkevich, S.D. Electronic Conductivity in a P^+-Ion Implanted Positive Photoresist. *Springer Nat. J.* **2020**, *49*, 55–61.
24. Zubin, D. A Highly Accurate Strain Gauge Parameters Testing Apparatus Based-on Rigid-Framed Beam. *J. Instrum. Tech. Sens.* **1997**, *6*, 16–19 + 26. (In Chinese)

micromachines

Article

A Micromechanical Transmitter with Only One BAW Magneto-Electric Antenna

Si Chen [1,†], Junru Li [2,*,†], Yang Gao [1,3], Jianbo Li [1], Hongmei Dong [1], Zhijun Gu [1] and Wanchun Ren [1]

[1] School of Information Engineering, Southwest University of Science and Technology, Mianyang 621010, China; chensi@mails.swust.edu.cn (S.C.); gaoy@swust.edu.cn (Y.G.); lijb@mails.swust.edu.cn (J.L.); donghongmei@mails.swust.edu.cn (H.D.); guzj@mails.swust.edu.cn (Z.G.); rwch_qw@163.com (W.R.)
[2] College of Optoelectronic Engineering, Chongqing University, Chongqing 400044, China
[3] Robot Technology Used for Special Environment Key Laboratory of Sichuan Province, Mianyang 621010, China
* Correspondence: li_junru@foxmail.com
† Si Chen and Junru Li are co-first authors of this article.

Abstract: Implantable medical devices have been facing the severe challenge of wireless communication for a long time. Acoustically actuated magnetoelectric (ME) transducer antennas have attracted lots of attention due to their miniaturization, high radiation efficiency and easy integration. Here, we fully demonstrate the possibility of using only one bulk acoustic wave (BAW) actuated ME transducer antenna (BAW ME antenna) for communication by describing the correspondence between the BAW ME antenna and components of the traditional transmitter in detail. Specifically, we first demonstrate that the signal could be modulated by applying a direct current (DC) magnetic bias and exciting different resonance modes of the BAW ME antenna with frequencies ranging from medium frequency (MF) (1.5 MHz) to medium frequency (UHF) (2 GHz). Then, two methods of adjusting the radiation power of the BAW ME antenna are proposed to realize signal amplification, including increasing the input voltage and using higher order resonance. Finally, a method based on electromagnetic (EM) perturbation is presented to simulate the transmission process of the BAW ME antenna via the finite element analysis (FEA) model. The simulation results match the radiation pattern of magnetic dipoles perfectly, which verifies both the model and our purpose.

Keywords: bulk acoustic wave (BAW); magnetoelectric transducer; antenna; transmitter; implantable medical devices (IMDs); resonance modes; frequency modulation; radiation power; FEA

Citation: Chen, S.; Li, J.; Gao, Y.; Li, J.; Dong, H.; Gu, Z.; Ren, W. A Micromechanical Transmitter with Only One BAW Magneto-Electric Antenna. *Micromachines* **2022**, *13*, 272. https://doi.org/10.3390/mi13020272

Academic Editors: Weidong Wang, Ruiguo Yang and Mark L. Adams

Received: 26 December 2021
Accepted: 7 February 2022
Published: 8 February 2022

1. Introduction

Wireless implantable medical devices (IMDs) have sparked a new wave of research on biomedical technology [1–3]. However, the problem of wireless communication has, for a long time, been an arduous challenge in the development of IMDs [4–6]. One of the main reasons is that the sizes of the antennas used for signal transmission are too large to be integrated in IMDs [7–9]. In addition, the existing IMDs require an additional power source, which could further increase the size of the entire IMDs [10–12]. A number of transducers used to provide power sources in IMDs have successfully reduced the size to the scale of the diameter of a piece of human hair [13–16]. However, the transducing efficiency of the current prototypes is too low to apply. Therefore, new antenna technologies need to be developed to solve the problem of wireless communication of IMDs in the Industrial, Scientific and Medical (ISM) band. A novel bulk acoustic wave (BAW) actuated magnetoelectric (ME) antenna was proposed theoretically in 2015, the efficiency bandwidth product of which was close to Chu's limit [17]. In 2017, Northeastern University successfully prepared this antenna and found that it can work comfortably in the ISM band [18]. The size of the antenna can be greatly reduced because the electromagnetic (EM) resonance of

the traditional antenna is replaced by the acoustic resonance of the BAW ME antenna. In addition, the BAW ME antenna is also an EM energy harvester from the view of receiving signals [19]. The magnetostrictive layer in the BAW ME antenna is used for sensing magnetic signals, and the piezoelectric layer is used for generating charges. This means that no additional power source is required to provide the energy supply of IMDs, which further reduces the size of the IMDs.

In fact, Jensen et al. successfully used a carbon nanotube antenna to play music back in 2007, which gives us a great inspiration [20]. The BAW ME antenna may have a more profound meaning, that is, using a single BAW ME antenna can also achieve wireless communication. If this view can be confirmed, it will have important implications for the definition of potential application scenarios of the BAW ME antenna. To complete the verification, we considered a solution using finite element analysis (FEA) simulation under the existing conditions, since Xu et al. recently constructed an EM radiation model of ME composites using FEA software [21]. However, the existing commercial FEA software hardly involves magnetization dynamics and magnetic spin simulations, so it is difficult to build a radiation model of the BAW ME antenna to verify its signal transmission behavior.

In this article, we explain and demonstrate how to achieve the wireless transmission of signals using only one BAW ME antenna. We first review the basic components and working principles of the traditional transmitter. For the benchmarking modulator, three kinds of modes of vibration are used to realize frequency modulation. Regarding the benchmarking power amplifier, the influence of the input voltage and higher order resonant frequency on the radiated power is demonstrated, which enables the signal to be amplified. Based on EM perturbations and multiphysics coupling, we used FEA simulation to analyze the whole operating process for the BAW ME transmitter. The focus of this simulation was to evaluate the near-field radiation of the BAW ME antenna by using the amplitude and distribution of the EM field with regular variation in the EM environment. We also compared the simulated data with the near-field pattern of an ideal magnetic dipole to verify the simulation scheme based on EM perturbation.

2. BAW ME Transmitter

2.1. Fundamentals of Radio Transmitters

A transmitter is an electrical system that can transmit a signal according to a certain frequency. A typical transmitter includes four essential components: an oscillator, a modulator, an amplifier and an antenna, as shown in Figure 1. The modulated signal is amplified by a power amplifier and radiated through the antenna into free space.

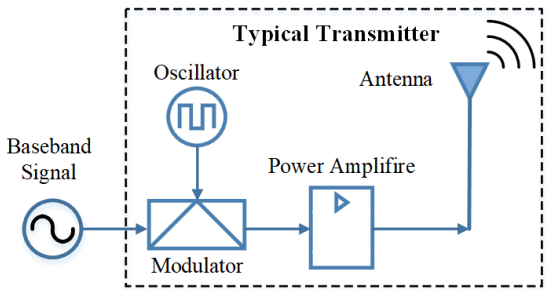

Figure 1. Block diagram for a typical transmitter. The four essential components can be replaced by a BAW ME antenna.

The four essential components of a transmitter can be replaced by just one BAW ME antenna, as shown in Figure 2. The piezoelectric layer and electrodes form a BAW resonator to power the antenna. The magnetostrictive layer, the radiation source of the antenna, is coupled with the piezoelectric layer through stress/strain. From the perspective of the operating principle, the actuating source of the antenna is the BAW resonator, and the radiation source is magnetostrictive film integrated on the resonator. When the alternating voltage that is consistent with the resonant frequency is applied to the top and bottom

electrodes of the BAW resonator, the BAW resonator generates acoustic resonance to induce magnetization oscillation of the magnetostrictive film [22]. Finally, dynamic flux forms and an EM wave transmits.

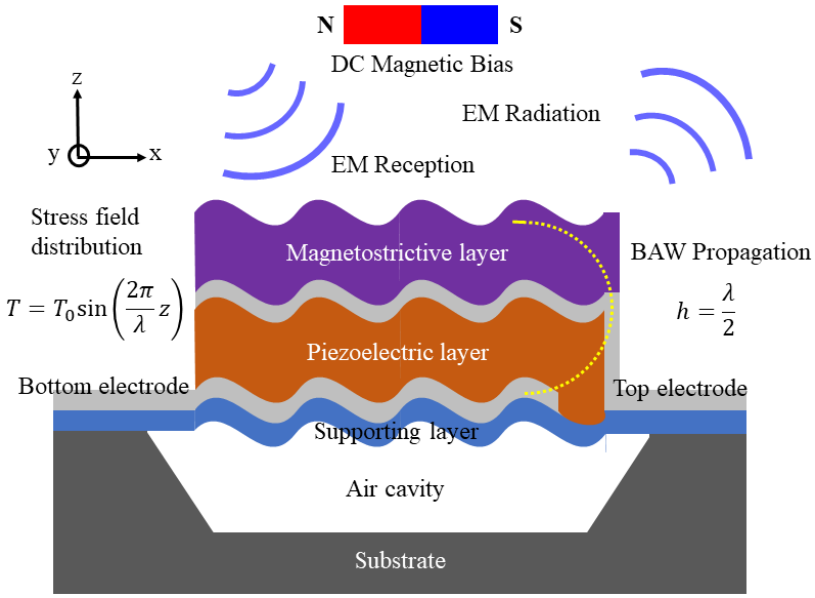

Figure 2. Schematic of the BAW ME antenna in resonance. The direct current (DC) magnetic bias is used to apply prestress, which can be achieved using a DC wire.

2.2. Oscillator and Modulator

The BAW ME antenna is essentially a mechanical oscillator (also known as an acoustic resonator); this state is achieved by alternating the voltages applied to both sides of the piezoelectric layer.

The BAW resonator can be designed to operate in different vibration modes, including longitudinal, contour and thickness resonance mode. According to Equation (1), the frequency calculation for the shear and longitudinal wave, different resonant modes correspond to different resonant frequencies f.

$$f = \begin{cases} \frac{1}{2L}\sqrt{\frac{Y}{\rho}} \\ \frac{1}{2h}\sqrt{\left(c_{33} + \frac{d_{33}}{e_{33}}\right)/\rho} \end{cases}, \quad (1)$$

where L is the length or width of the materials, h is the thickness of the materials, Y is the Young's modulus of the materials, ρ is the mass density of the materials, and c_{33}, d_{33} and e_{33} are the elastic, piezoelectric and dielectric coefficients of the materials, respectively. Therefore, frequency tunableness in the BAW ME antenna could be accomplished by exciting different resonance modes of the BAW resonator. Its operating frequency ranges from medium frequency (MF) to ultra-high frequency (UHF), entirely depending on its size. As shown in Figure 3, the three vibration modes of the BAW resonator can be identified according to the admittance characteristics of the FEA simulation at different frequencies. It can be seen that the BAW resonator frequency spans a wide range including about 1.5 MHz, 7.8 MHz and 2 GHz, which is conducive to the frequency selection of the BAW antenna at large scales. In order to achieve frequency modulation, a DC magnetic bias is applied to change the tension of the active region. The signal can be applied to this bias to modulate the resonant frequency. The film is prestressed, and the resonant frequency (also known as the carrier) changes with the information signal.

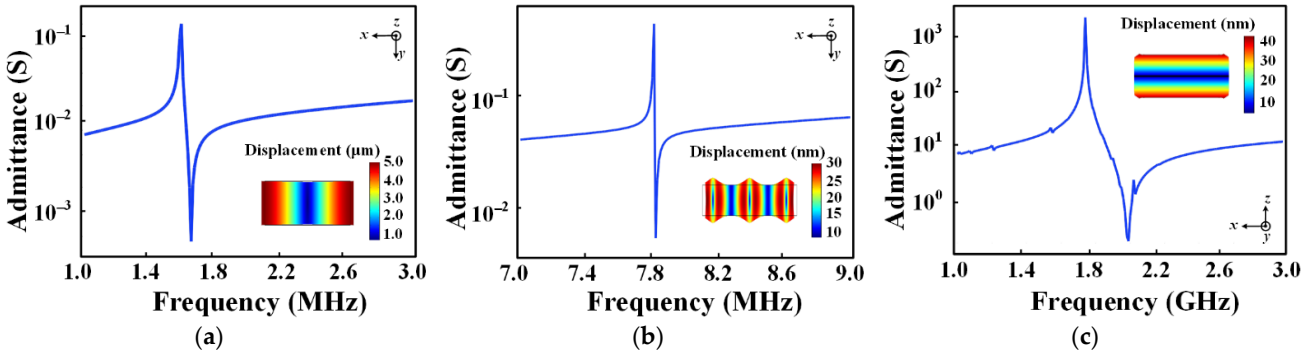

Figure 3. Admittance characteristic curve of the BAW resonator corresponding to the three resonant modes. The inset is the displacement field distribution at different resonance modes: (**a**) longitudinal resonance mode; (**b**) contour resonance mode; (**c**) thickness resonance mode.

2.3. Power Amplifier (PA)

The function of the PA is to enhance the antenna radiation power by enhancing the signal amplitude. For the BAW ME antenna, there are two ways to control the radiated power effectively. Taking the BAW ME antenna working in thickness resonance mode as an example, our team [23] proposed a method for calculating the average radiated power of the BAW ME antenna considering the eddy current loss, which describes the relationship between the average radiated power and the design parameters, as shown in (2). According to this relation, schemes can be made to improve the average radiated power.

$$P_{rad} = \frac{\omega^2 h^2 d_{33}^2}{2\eta} \iint_s |\boldsymbol{T}|^2 ds \approx \frac{\omega^2 h^2 d_{33}^2 |\boldsymbol{T}|^2 A}{2\eta}, \tag{2}$$

where η is the wave impedance of the free space, d_{33} is the piezomagnetic coefficient of the magnetostrictive layer in the z-direction, ω is the angular frequency, which represents the resonant frequency of the device, h is the thickness of the magnetostrictive layer, A is the area of the active region, and $\boldsymbol{T}$ is the longitudinal stress tensor. After designing and fabricating the BAW ME antenna, the structure and material parameters in Equation (2) are fixed and cannot be changed. Only the two parameters of stress $\boldsymbol{T}$ and frequency ω can be used to control the average radiated power. Next, we will demonstrate two ways to increase the internal stress and operating frequency of the device to achieve power amplification without additional PA.

The first method we propose is to increase the stress by increasing the excitation voltage. We demonstrate this process by FEA simulation, as shown in Figure 4. The result shows that the internal stress of the BAW ME antenna increases linearly with the amplitude of the input voltage, which means that increasing the excitation voltage within the power handing of the BAW resonator can easily achieve the purpose of increasing the radiated power.

The second method we propose is to increase the stress by using the higher order resonance characteristics of the BAW resonator, which is a solution that raises both the stress and the frequency. However, it is worth noting that the effect of ferromagnetic resonance (FMR) on the performance of the antenna should be considered [24], which means that the resonance frequency should be controlled below the FMR frequency. In order to investigate whether the higher order resonant frequency would have an effect on the stress, we used FEA simulation to analyze the harmonic response of the antenna and plotted the stress field distribution at the resonant frequency. As shown in Figure 5, the average stress of the antenna at the first-order resonant frequency is about 70 MPa, while that at the second-order resonant frequency is about 200 MPa. The results confirm that the radiation power of the antenna can be improved by using higher order resonance frequencies. In addition, it was previously reported that by keeping the FMR frequency of

the magnetostrictive layer consistent with the resonance frequency of the BAW ME antenna, the radiation power of the device can be further improved [25].

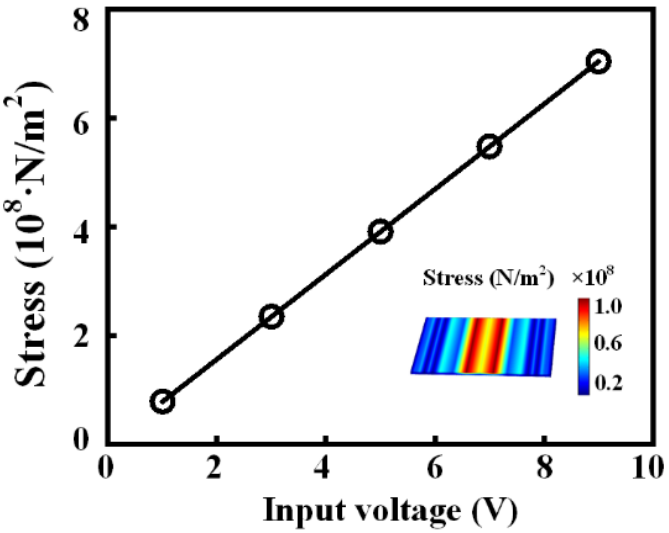

Figure 4. Relationship between stress and input voltage at resonance. The inset shows the stress field distribution of the magnetostrictive layer at particular input voltages. The size of the antenna is 100 × 50 × 1 μm^3, and the resonant frequency is about 2.6 GHz.

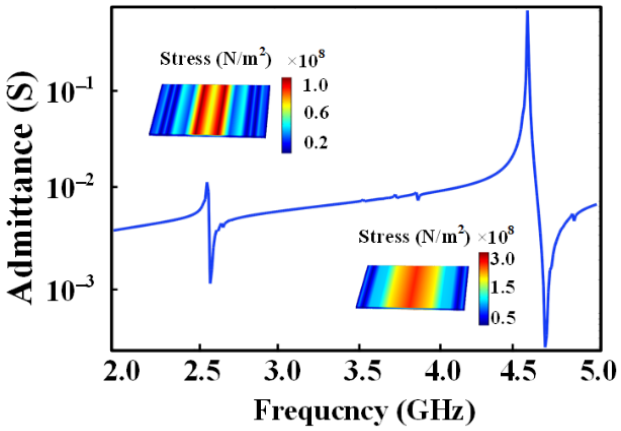

Figure 5. Admittance characteristic curve of the BAW ME antenna. An excitation voltage of 1 V is applied to obtain the admittance curve in the first-order and second-order resonant frequency. The inset is the stress field distribution of the antenna at different resonant frequencies.

In short, all the four essential components of a typical transmitter can be compactly and efficiently replaced by the BAW ME antenna to realize wireless communication.

3. Simulation of Transmission Process

This section focuses on the simulation of the transmitting process of the BAW ME antenna, which is not a small challenge, since the transmitting process of the BAW ME antenna involves magnetic spin. However, most existing commercial modeling software applications are limited to simulating simple magnetic behaviors such as magnetostriction. The response to magnetic spin that is usually achieved by magnetization dynamics is not available in FEA software. Therefore, there is no reference report on modeling the transmitting process of the BAW antenna using FEA. However, it is well known that the

aperture EM field of the material's surface is easy to obtain via FEA simulation based on the constitutive relation of ME material as shown in (3).

$$\begin{bmatrix} \boldsymbol{S} \\ \boldsymbol{E},\boldsymbol{H} \end{bmatrix} = \begin{bmatrix} s_{D,B} & \frac{d_{E,H}}{\varepsilon,\mu} \\ \frac{d_{E,H}}{\varepsilon,\mu} & \frac{1}{\varepsilon,\mu} \end{bmatrix} \begin{bmatrix} \boldsymbol{T} \\ \boldsymbol{D},\boldsymbol{B} \end{bmatrix}, \tag{3}$$

where $\boldsymbol{S}$ and $\boldsymbol{T}$ are the stress and strain tensors satisfying the boundary conditions, respectively, $\boldsymbol{E}$ and $\boldsymbol{H}$ are the vectors of the electric and magnetic field intensity, respectively, $\boldsymbol{D}$ and $\boldsymbol{B}$ are the vectors of the electric and magnetic flux density, respectively, ε and μ are the dielectric constant and permeability of the film, respectively, under a no-stress condition, $s_{D,B}$ are the compliance constants of the piezoelectric and magnetostrictive layers, respectively, and $d_{E,H}$ are the strain constants of the piezoelectric and magnetostrictive layers, respectively. This aperture EM field will inevitably act as a perturbation source to break the uniform and balanced EM environment around it. If the amplitude and distribution of EM field change regularly in this EM environment, this variation is used to evaluate the near-field radiation of the BAW antenna.

Therefore, a simulation scheme of near field EM perturbations is proposed, which also solves the problem of huge physical scale differences between models and reality. The size of the BAW ME antenna is on the micron scale and the far field distance ($r >> \lambda$, λ is the EM wavelength) is over 0.1 m even at the resonant frequency of gigahertz. Therefore, extrapolating the far-field solution from the near-field distribution derived from EM perturbations is the only feasible FEA simulation method.

Specifically, the whole FEA model of the BAW ME antenna, including the magnetostrictive layer, piezoelectric layer, and air domain, is constructed to simulate the acoustic resonance, inverse ME effect and EM perturbations. The BAW ME antenna of $100 \times 50 \times 1$ μm^3 in size is located in the central point of the air domain, whose first-order resonance frequency is about 2.6 GHz. The radius of the air domain is set to 1000 μm. Then, the 3D model is solved in the frequency domain by coupling the electrostatic, solid mechanical and magnetic fields, as shown in (4)–(6), respectively.

$$\text{Electrostatic field}: \begin{cases} \nabla \cdot \boldsymbol{D} = \rho_V \\ \boldsymbol{E} = -\nabla \boldsymbol{V} \\ \boldsymbol{D} = \varepsilon \boldsymbol{E} + \boldsymbol{P} \end{cases}, \tag{4}$$

$$\text{Solid mechanical field}: \begin{cases} \nabla \cdot \boldsymbol{T} = \rho \frac{\partial^2 \boldsymbol{u}}{\partial t^2} \\ \boldsymbol{S} = \frac{1}{2}\left(\nabla \boldsymbol{u} + \nabla \boldsymbol{u}^T\right) \end{cases}, \tag{5}$$

$$\text{Magnetic field}: \begin{cases} \nabla \times \boldsymbol{H} = \boldsymbol{J} \\ \boldsymbol{B} = \nabla \times \boldsymbol{A} \\ \boldsymbol{E} = -j\omega \boldsymbol{A} \end{cases}, \tag{6}$$

where ∇ is the Laplace operator, ρ_V is the charge density, ε is the permittivity, $\boldsymbol{P}$ is the polarization vector, $\boldsymbol{u}$ is the displacement vector, $\boldsymbol{J}$ is the ampere density vector, and $\boldsymbol{A}$ is the magnetic vector potential. The air domain is used for simulating the near-field of the antenna and analyzing the magnetic flux density of different positions near the antenna. Under the action of EM perturbations, the change rule of the flux density near the antenna can be detected. Of course, this is not used to simulate the EM radiation of the antenna by FEA, but to replace the radiation with EM perturbation at different positions, which means that the simulated EM field represents the near-field of the BAW ME antenna that does not propagate.

When the BAW ME antenna operates at the first-order resonant frequency, the amplitudes and distributions of magnetic flux density $\boldsymbol{B}$ in the range of 0~900 μm from the antenna along the z-direction are obtained. As shown in Figure 6, the magnetic flux density distributions along the red dotted line tracking on the horizontal plane in the insets at distances of 50 μm, 200 μm and 500 μm away from the antenna are enumerated, respectively.

It can be found that the amplitude of $\boldsymbol{B}$ is larger at a relatively close distance of 50 µm away from the antenna, and the distribution is concentrated directly above the center of antenna. The amplitude of $\boldsymbol{B}$ decays exponentially with distance, while the distribution of $\boldsymbol{B}$ diffuses outwards gradually with distance. In order to ensure that the change of magnetic flux density in the air domain can be used to characterize the near-field radiation of the BAW ME antenna, the near-field pattern of an ideal magnetic dipole, as shown in Equation (7), is used for comparison.

$$\begin{cases} H_r = \frac{m_0}{2\pi r} j\omega\varepsilon \left[\frac{1}{jkr} + \frac{1}{(jkr)^2}\right] e^{-jkr}\cos\theta \\ H_\theta = \frac{m_0}{4\pi r} j\omega\varepsilon (1 + \frac{1}{jkr} + \frac{1}{(jkr)^2}) e^{-jkr}\sin\theta \\ E_\varphi = \frac{m_0}{4\pi r} jk(1 + \frac{1}{jkr}) e^{-jkr}\sin\theta \end{cases}, \tag{7}$$

where k is the free-wave wavenumber, H_r and H_θ are the magnetic field vectors in the r and θ directions, respectively, E_φ represents the electric field vectors in the φ direction, ε is the permittivity of the vacuum, r is the propagation distance, and m_0 is the equivalent magnetic dipole moment, which is the volume integral of magnetization in the magnetostrictive layer. It is worth noting that, based on the pointing vector, H_r is a non-radiative standing wave, which indicates the storage and mutual conversion of EM energy. Therefore, the attenuation of H_r with distance and its radiation pattern can be compared with the simulation value to verify the FEA model.

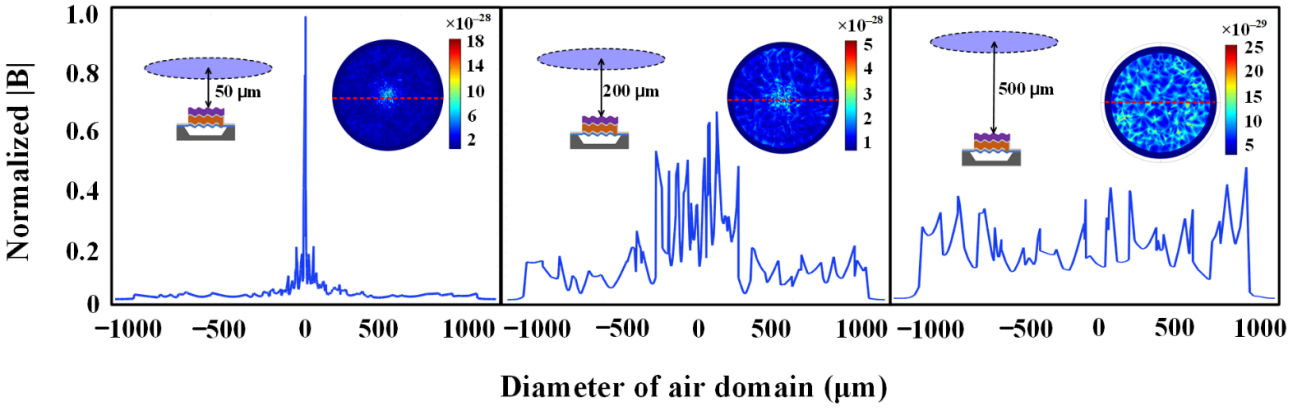

Figure 6. Simulation of near field normalized flux density. The insets show the distribution of the magnetic flux density on the horizontal plane 50 µm, 200 µm and 500 µm away from the antenna.

Since the magnetic field data changes dramatically in the near-field region, in order to allow accurate comparison with the simulated data, the decibel (dB) values are used to represent the attenuation of the magnetic flux density. As shown in Figure 7a, the $|\boldsymbol{B}|$ decays exponentially with distance and by 45 dB over a distance of 900 µm, which is highly consistent with the calculated results of the ideal dipole. Furthermore, as shown in Figure 7b, by extracting simulation values at different θ and comparing them with the near field of the ideal dipole, it can be found that the magnetic flux density distribution of these discrete positions is equivalent to the radiation pattern of an ideal magnetic dipole. Therefore, this consistency not only proves the feasibility of simulating the near-field radiation of the BAW antenna based on EM perturbations, but also indirectly illustrates that the BAW antenna can be used as a transmitter.

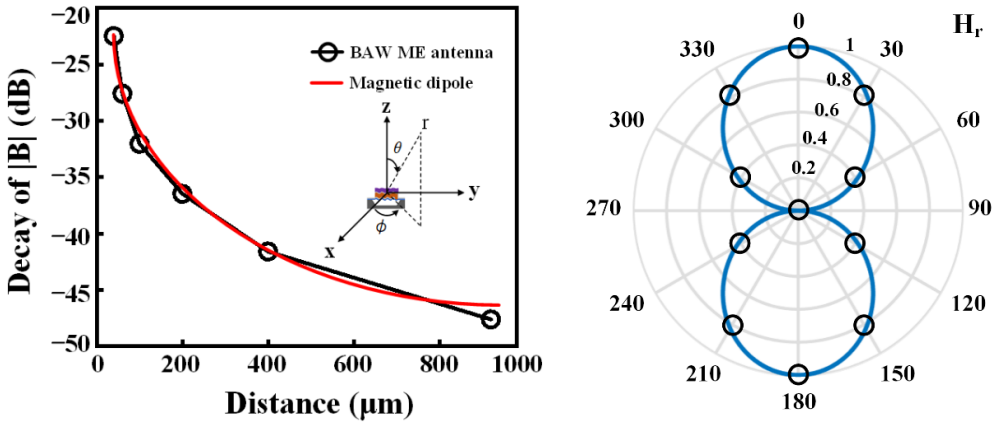

(**a**) (**b**)

Figure 7. Comparison of near field radiation characteristics between the BAW antenna and the magnetic dipole. (**a**) The magnetic flux density $|\boldsymbol{B}|$ decays with distance. The inset shows the BAW ME antenna placed in a spherical coordinate system. (**b**) $\boldsymbol{H_r}$ pattern of the magnetic dipole (blue line) and BAW ME antenna (small circle). Each small circle represents the normalized value of simulation $|\boldsymbol{H_r}|$ of different θ at the first-order resonant frequency of 2.6 GHz.

4. Conclusions

We demonstrate in principle how to replace the traditional transmitter with one BAW ME antenna to realize the functions of four components. Specifically, a DC magnetic bias and three different modes of a BAW resonator can be excited to use frequency modulation from MF to UHF. Taking the thickness resonant mode as an example, two methods of power amplification are presented, including the increasing of the input voltage and the use of a higher order resonant mode. In particular, a method based on EM perturbation is proposed to evaluate the near-field radiation of the BAW ME antenna, which completely solves the problem that there is no magnetization dynamics model in FEA software. The main characteristic of this simulation is that the variation of magnetic flux density near the antenna is used to replace EM radiation. The simulation results are in good agreement with the radiation theory of magnetic dipole, which not only verifies the model, but also provides a new simulation solution to evaluate the near field distribution of the BAW ME antenna. However, the EM perturbation is different from the EM radiation, so the simulation method in this work cannot be used for modeling the far-field of radiation. The authors are working on the radiation far-field modeling and device preparation of the BAW ME antenna to complete the communication experiment in further work. This work can also provide a simulation idea for the design and analysis of magnetoelectric antennas or transducers.

Author Contributions: Conceptualization, J.L. (Junru Li); methodology, J.L. (Junru Li) and S.C.; software, S.C. and J.L. (Jianbo Li); validation, W.R.; resources, Y.G.; writing—original draft preparation, S.C.; writing—review and editing, J.L. (Junru Li), H.D. and Z.G.; supervision, J.L. (Junru Li) and Y.G. All authors have read and agreed to the published version of the manuscript.

Funding: This research was funded in part by the Science and Technology on Electronic Information Control Laboratory under Grant 6142105200203 and 61428060303, in part by the Fund of Robot Technology of the Special Environment Key Laboratory of Sichuan Province under Grant 20kfkt02, and in part by the Science and Technology Foundation of Southwest University of Science and Technology under Grant 20zx7114, in part by the Sichuan Science and Technology Program under Grant 2021YJ0105, in part by the Key laboratory of Aerodynamic Noise Control under Grant 2001ANCL20200307.

Conflicts of Interest: The authors declare no conflict of interest. The funders had no role in the design of the study; in the collection, analyses, or interpretation of data; in the writing of the manuscript, or in the decision to publish the results.

References

1. Liu, C.; Zhang, Y.; Liu, X. Circularly polarized implantable antenna for 915 MHz ISM-Band far-field wireless power transmission. *IEEE Antennas Wirel. Propag. Lett.* **2018**, *17*, 373–376. [CrossRef]
2. Singer, A.; Dutta, S.; Lewis, E.; Chen, Z.; Chen, J.C.; Verma, N.; Avants, B.; Feldman, A.K.; O'Malley, J.; Beierlein, M.; et al. Magnetoelectric materials for miniature, wireless neural stimulation at therapeutic frequencies. *Neuron* **2018**, *107*, 631–643.e5. [CrossRef]
3. He, W.; Yang, A. A shear-mode piezoelectric heterostructure for electric current sensing in electric power grids. *Micromachines* **2019**, *10*, 421. [CrossRef] [PubMed]
4. Kim, J.; Rahmat-Samii, Y. Implanted antennas inside a human body: Simulations, designs, and characterizations. *IEEE Trans. Microw. Theory Tech.* **2004**, *52*, 1934–1943. [CrossRef]
5. Kiourti, A.; Psathas, K.A.; Nikita, K.S. Implantable and ingestible medical devices with wireless telemetry functionalities: A review of current status and challenges. *Bioelectromagnetics* **2014**, *35*, 1–15. [CrossRef]
6. Stoecklin, S.; Yousaf, A.; Volk, T.; Reindl, L. Efficient wireless powering of biomedical sensor systems for multichannel brain implants. *IEEE Trans. Instrum. Meas.* **2016**, *65*, 754–764. [CrossRef]
7. Faisal, F.; Yoo, H. A miniaturized novel-shape dual-band antenna for implantable applications. *IEEE Trans. Antennas Propag.* **2019**, *67*, 774–783. [CrossRef]
8. Zhang, H.; Li, L.; Liu, C.; Guo, Y.X.; Wu, S. Miniaturized implantable antenna integrated with split resonate rings for wireless power transfer and data telemetry. *Microw. Opt. Technol. Lett.* **2017**, *59*, 710–714. [CrossRef]
9. Xu, L.J.; Guo, Y.X.; Wu, W. Miniaturized dual-band antenna for implantable wireless communications. *IEEE Antennas Wirel. Propag. Lett.* **2014**, *13*, 1160–1163.
10. Johansson, A.J. Wireless Communication with Medical Implants: Antennas and Propagation. Ph.D. Thesis, Lund University, Scania, Sweden, 2004.
11. Sauer, C.; Stanacevic, M.; Cauwenberghs, G.; Thakor, N. Power harvesting and telemetry in CMOS for implanted devices. *IEEE Trans. Circuits Syst.* **2005**, *52*, 2605–2613. [CrossRef]
12. Moradian, S.; Akhkandi, P.; Huang, J.; Gong, X.; Abdolvand, R. A battery-less wireless respiratory sensor using micro-machined thin-film piezoelectric resonators. *Micromachines* **2021**, *12*, 363. [CrossRef] [PubMed]
13. Khalifa, A.; Liu, Y.; Karimi, Y.; Wang, Q.; Eisape, A.; Stanacevic, M.; Thakor, N.; Bao, Z.; Etienne-Cummings, R. The microbead: A 0.009 mm^3 implantable wireless neural stimulator. *IEEE Trans. Biomed. Circuits Syst.* **2019**, *13*, 971–985. [CrossRef] [PubMed]
14. Biederman, W.; Yeager, D.J.; Narevsky, N.; Koralek, A.C.; Carmena, J.M.; Alon, E.; Rabaey, J.M. A fully-integrated, miniaturized (0.125 mm^2) 10.5 μW wireless neural sensor. *IEEE J. Solid-State Circuits* **2013**, *48*, 960–970. [CrossRef]
15. Lee, S.; Cortese, A.J.; Gandhi, A.; Agger, E.R.; McEuen, P.L.; Molnar, A.C. A 250 μm × 57 μm microscale opto-electronically transduced electrodes (MOTEs) for neural recording. *IEEE Trans. Biomed. Circuits Syst.* **2019**, *12*, 1255–1256.
16. Leung, V.W.; Lee, J.; Li, S.; Yu, S.; Kilfovle, C.; Larson, L.; Nurmikko, A.; Laiwalla, F. A CMOS distributed sensor system for high-density wireless neural implants for brain-machine interfaces. In Proceedings of the ESSCIRC 2018-IEEE 44th European Solid State Circuits Conference (ESSCIRC), Dresden, Germany, 3–6 September 2018; pp. 230–233.
17. Yao, Z.; Wang, Y.E.; Keller, S.; Carman, G.P. Bulk Acoustic Wave-Mediated Multiferroic Antennas: Architecture and Performance Bound. *IEEE Trans. Antennas Propag.* **2015**, *63*, 3335–3344. [CrossRef]
18. Nan, T.; Lin, H.; Gao, Y.; Matyushov, A.; Yu, G.; Chen, H.; Sun, N.; Wei, S.; Wang, Z.; Li, M.; et al. Acoustically actuated ultra-compact NEMS magnetoelectric antennas. *Nat. Commun.* **2017**, *8*, 296. [CrossRef]
19. Zaeimbashi, M.; Nasrollahpour, M.; Khalifa, A.; Romano, A.; Liang, X.; Chen, H.; Sun, N.; Matyushov, A.; Lin, H.; Dong, C.; et al. Ultra-compact dual-band smart NEMS magnetoelectric antennas for simultaneous wireless energy harvesting and magnetic field sensing. *Nat. Commun.* **2021**, *12*, 3141. [CrossRef]
20. Jensen, K.; Weldon, J.; Garcia, H.; Zettl, A. Nanotube Radio. *Nano Lett.* **2007**, *7*, 3508–3511. [CrossRef]
21. Xu, G.; Xiao, S.; Li, Y.; Wang, B.Z. Modeling of electromagnetic radiation-induced from a magnetostrictive/piezoelectric laminated composite. *Phys. Lett. A* **2021**, *385*, 126959. [CrossRef]
22. Yao, Z.; Tok, R.U.; Itoh, T.; Wang, Y.E. A Multiscale Unconditionally Stable Time-Domain (MUST) Solver Unifying Electrodynamics and Micromagnetics. *IEEE Trans. Microw. Tech.* **2018**, *66*, 2683–2696. [CrossRef]
23. Li, J.; Peng, C.; Chen, S.; Gao, Y.; Ren, W.; He, X. Modeling and suppression of eddy current loss for BAW magnetoelectric devices. *IEEE Trans. Magn.* **2021**, *57*, 1–6. [CrossRef]
24. Chavez, A.C.; Schneider, J.D.; Barra, A.; Tiwari, S.; Candler, R.N.; Carman, G.P. Voltage-controlled ferromagnetic resonance of dipole-coupled $Co_{40}Fe_{40}B_{20}$ nanoellipses. *Phys. Rev. Appl.* **2019**, *12*, 044071. [CrossRef]
25. Yao, Z.; Tiwari, S.; Lu, T.; Rivera, J.; Luong, K.Q.T.; Candler, R.N.; Carman, G.P.; Wang, Y.E. Modeling of Multiple Dynamics in the Radiation of Bulk Acoustic Wave Antennas. *IEEE J. Multiscale Multiphys. Comput. Tech.* **2020**, *5*, 5–18. [CrossRef]

micromachines

Article

MEMS Skin Friction Sensor with High Response Frequency and Large Measurement Range

Huihui Guo [1,2], Xiong Wang [3,*], Tingting Liu [1,*], Zhijiang Guo [1] and Yang Gao [1]

[1] School of Information Engineering, Southwest University of Science and Technology, Mianyang 621010, China; easonguo@swust.edu.cn (H.G.); guozhijiang@swust.edu.cn (Z.G.); gaoy@swust.edu.cn (Y.G.)
[2] Robot Technology Used for Special Environment Key Laboratory of Sichuan Province, Mianyang 621010, China
[3] Hypervelocity Aerodynamics Institute, China Aerodynamics Research and Development Center, Mianyang 621010, China
* Correspondence: wangx81@cardc.cn (X.W.); liutingting@swust.edu.cn (T.L.); Tel.: +86-816-2465206 (X.W.); +86-816-6089322 (T.L.)

Abstract: Micro-electromechanical system (MEMS) skin friction sensors are considered to be promising sensors in hypersonic wind tunnel experiments owing to their miniature size, high sensitivity, and stability. Aiming at the problem of short test duration (a few milliseconds) and heavy load in a shock wind tunnel, the fast readout circuit and the sensor head structures of a MEMS skin friction sensor are presented and optimized in this work. The sensor was fabricated using various micro-mechanical processes and micro-assembly technology based on visual alignment. Meanwhile, the sensor head structure was integrated with the fast readout circuit and tested by using a centrifugal force equivalent method. The calibration results show that this sensor provides good linearity, sensitivity, and stability. The measurement ranges are 0–2000 Pa with good performance. The resolution is better than 10 Pa at 3000 Hz detection frequency of the readout circuit for the sensor in ranges from 0 to 1000 Pa. In addition, the repeatability and linearity of static calibration for sensors are better than 1%.

Keywords: skin friction sensors; shock tunnel experiment; MEMS; fast readout circuit

Citation: Guo, H.; Wang, X.; Liu, T.; Guo, Z.; Gao, Y. MEMS Skin Friction Sensor with High Response Frequency and Large Measurement Range. *Micromachines* **2022**, *13*, 234. https://doi.org/10.3390/mi13020234

Academic Editors: Weidong Wang and Ruiguo Yang

Received: 29 December 2021
Accepted: 26 January 2022
Published: 30 January 2022

1. Introduction

The skin friction resistance of an aircraft surface is an important part of its total resistance, which greatly limits the performance of hypersonic vehicles. Therefore, the skin friction measurement of an aircraft model is an important basic item in aerodynamic research. MEMS skin friction sensors are considered promising sensors in hypersonic wind tunnel experiments owing to their miniature size, high sensitivity, and stability. In recent years, several researchers have developed MEMS sensors to measure skin friction, including the capacitance-type and comb differential capacitance-type [1–5], piezoresistive-type [6–8], and piezoelectric-type [9]. For example, Mills et al. [5] reported a fully differential capacitive wall shear stress sensor for low-speed wind tunnels with the high sensitivity of 196 mV/Pa and a minimum detection limit of 12 mPa at 1000 Hz in a range from 0–10 Pa; Von, P. et al. [8] reported a wall shear stress sensor using four piezoresistors in the cantilever, and the resolution was 0.01 Pa in the range of 2 Pa; Kim, T. et al. [9] reported a piezoelectric floating element shear stress sensor for the wind tunnel flow measurement with the high sensitivity of 56.5 pc/Pa and with the frequency range of the sensor up to 800 Hz. The common characteristics of those sensors are their usually high sensitivity, high resolution (10^{-2} Pa), and small measurement range (several Pa). Therefore, these sensors are mainly used in low wind tunnels to measure skin friction because their sensing elements, such as the comb capacitance, were exposed in the flow field. To adapt to the harsh measurement environments and large normal loads in hypersonic fields, a novel MEMS skin sensor was developed in our previous work [10,11]. The sensor adopts the floating element so that

it is even with the measured wall, and the signal output micro-structure is isolated from the hypersonic field, which was fabricated using various micro-mechanical processes and micro-assembly technology. Experimental results show that this sensor has some good characteristics, such as good linearity, small size, high sensitivity, and repeatability of static calibration. Furthermore, the measurement ranges were 0–100 Pa, and the minimum detectable skin friction was 0.1 Pa. However, the natural frequency of the sensor was 410 Hz, and the detection frequency of a weak capacitance readout circuit for a skin friction sensor is only 10 Hz.

According to the hypersonic flow field characteristics of high temperature, high total pressure, and short test time in the shock wind tunnel, the test ambient temperature is usually increased to hundreds of degrees centigrade, and the measurement ranges increase to hundreds, or even thousands, of Pa. Meanwhile, the sampling frequency of the readout circuit for the sensor also increases to thousands of Hz with higher loads, and only several milliseconds in duration of the working time. Therefore, greater measurement ranges and higher response frequencies of sensors for skin friction in shock wind tunnels need to be developed.

In this work, the static force analysis and modal analysis of the sensor head structure were carried out by finite element analysis (FEA) to optimize the head structure of the MEMS skin friction sensor with a high response frequency and large measurement ranges. In addition, to improve the detection frequency of the weak capacitance of the sensor, the fast readout circuit with 3000 Hz detection frequency was designed and integrated with the sensor head structure.

2. Structural Simulation and Optimization of the Sensor Head Structure

The structure of the MEMS skin friction sensor is shown in Figure 1. The sensor was composed of a silicon differential capacitor embedded with a floating element, a signal readout circuit, and a metal shell package. The working principle of this sensor is explained as the skin friction caused the torsional deflection of clamped-clamped elastic beams by the floating element, and the torsional deflection was transferred into a capacitance variation by one pair of differential capacitors.

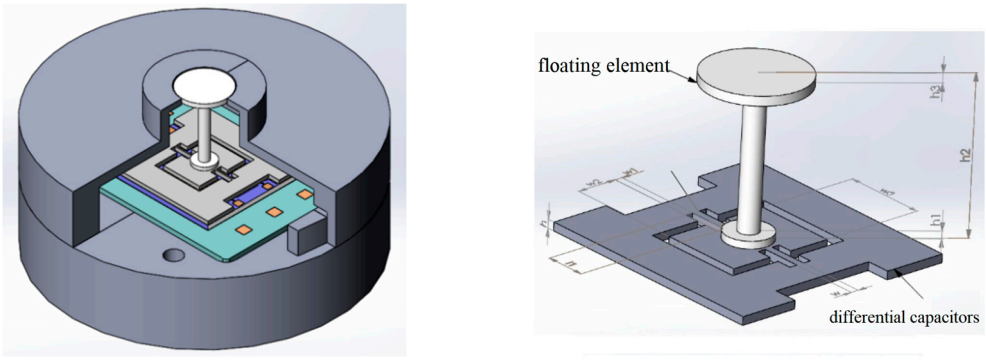

(**a**) (**b**)

Figure 1. (**a**) Schematic of the sensor; (**b**) the sensing structure parameters of the sensor head.

For a typical shock tunnel with a short test time (a few milliseconds), the lowest frequency to obtain high measurement accuracy within the effective test time is 1000 Hz. Because the mechanical vibration of the measurement system is excited and cannot be attenuated rapidly enough by damping characteristics during the short test time, to obtain higher measurement accuracy, the natural frequency of the MEMS skin friction sensor should, therefore, be raised to 3000 Hz.

For an undamped single freedom system, the natural frequency calculation formula is defined as shown in the following equation:

$$f_n = \frac{1}{2\pi}\sqrt{\frac{k}{m}} \tag{1}$$

where f_n is the natural frequency, and k and m are the stiffness and mass of the structure, respectively. From Equation (1), it can be seen that increasing the stiffness of the beam and reducing the mass of the floating element was an effective way to improve the natural frequency of a MEMS skin friction sensor. Then, the sensitivity of the sensor deteriorated rapidly because the torsional deflection of the elastic beams decreased with an increase in the stiffness (with increasing w and h) under the same loads. The sensitivity of the sensor can be defined according to conformal transformation theory [11]:

$$S \approx \frac{\tau_w A}{\Delta C} = \frac{h_0^2}{\varepsilon_0(2w_1 + w_2)w_2 w_3} \times \frac{\beta}{1+\nu} \times \frac{Ew^3 h}{l_1 h_2} \tag{2}$$

where τ_w is the measured skin friction, ΔC is the variation of differential capacitance, A is the area of the floating element, β, ν, ε_0 and E are the elastic deformation parameters of the torsion beam, respectively, w, l_1 and h are the length width and thickness of the silicon beam, and h_0 and h_2 are the gaps of the capacitor and the height of the floating element as a force arm. To fabricate the high-performance skin friction sensor for a shock wind tunnel experiment, the sensitivity and the natural frequency were considered together.

To obtain the main structural parameters of the silicon beam and the floating element, three-dimensional FEA models of the sensor head structures were built with the help of FEA software, using our previous parameters. The optimized three-dimensional FEA model of the sensor head structure is shown in Figure 2a.

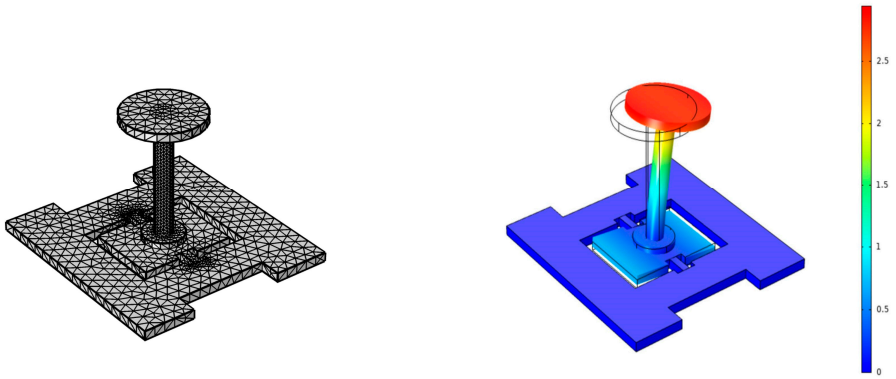

(**a**) (**b**)

Figure 2. (**a**) Three-dimensional FEA model of the sensor head structure; (**b**) the normal deformation of the vibrating plate under 2000 Pa equivalent loads.

Combining the designed indexes and our previous research results, we determined that increasing the width of the silicon beam was key to improving the stiffness of the sensor head structure. To ensure the working state of the torsion beam, the width was not allowed to exceed its thickness (the thickness of the wafer was about 500 μm). The natural frequency of the sensor head with different widths of the silicon beam is shown in Figure 3a. It can be seen that the natural frequency of the sensor head was from 410 Hz to 1000 Hz as the width of the silicon beam was increased from 180 μm to 420 μm. However, the natural frequency increase tended to slow down when the width of the silicon beam was increased to 420 μm. Meanwhile, the sensitivity of the sensor was down 90 percent by Equation (2). The maximum width of the beam can be determined as 420 μm without considering the sensitivity of the sensor in this work.

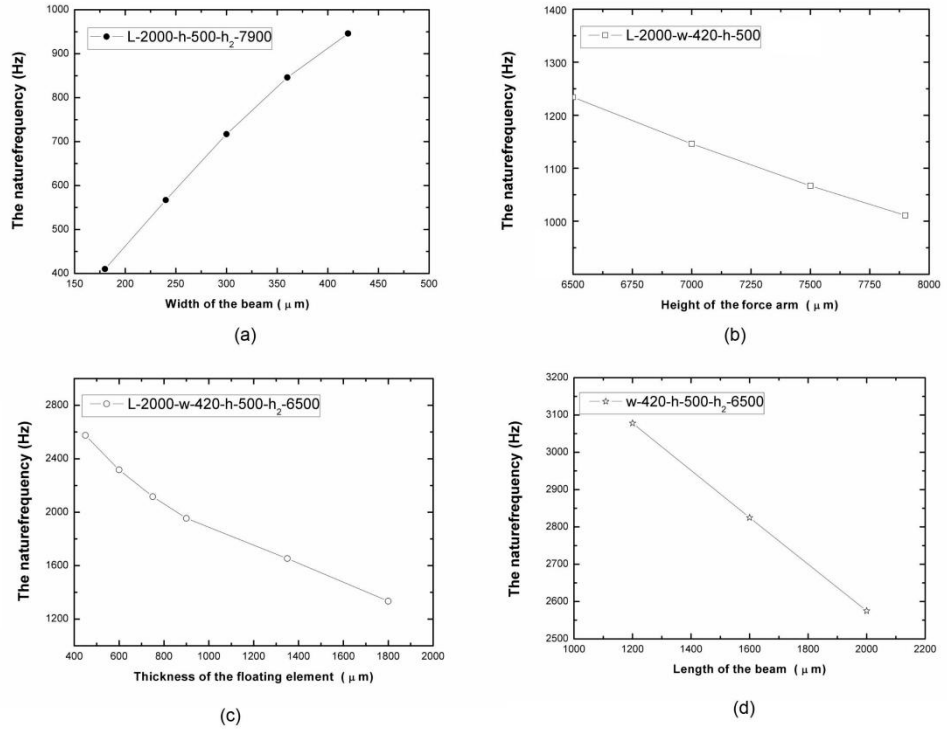

Figure 3. The variation of the natural frequency with different structure parameters of the sensor head: (**a**) the width changes of the silicon beam; (**b**) the height changes of the force arm; (**c**) the thickness changes of the floating element; (**d**) the length changes to the silicon beams.

To further enhance the natural frequency, the height of the floating element as a force arm and the mass of the floating element were reduced. The frequency increased from 1000 Hz to 1250 Hz as the height of the force arm was decreased from 7900 μm to 6500 μm, as shown in Figure 3b. It can also be seen that reducing the force arm had little effect on improving the natural frequency of the sensor head. The reason is that the reduction of the length of the floating element has little effect on the overall quality of m.

Therefore, reducing the thickness of the floating element can quickly reduce its overall mass to improve the natural frequency of the sensor, as shown in Figure 3c. However, the rapid reduction of the overall mass led to the rapid reduction of the equivalent torque and the sensitivity. Combining the influence rule of the skin friction measurements model [12,13] and the precision machining process, the thickness parameters of the floating element were determined as 450 μm in this work.

The influence of the length of the beam on the natural frequency of the sensor was also simulated, as shown in Figure 3d. The simulation results show that the natural frequency of the sensor head increased linearly with the decreasing length of the beam.

Finally, to increase the natural frequency of the sensor to over 3000 Hz, the main structure parameters were achieved, as shown in Table 1.

Table 1. The main structural parameters of the sensor.

Width of Silicon Beam (μm)	Length of Silicon Beam (μm)	The Thickness of the Silicon Beam (μm)	Diameter of the Floating Element (μm)	Thickness of Floating Element (μm)	Height of Floating Element (μm)	Gap of Capacitor (μm)
400	1200	500	5000	450	7000	10

Meanwhile, the skin friction τ_w was equivalent to the shear stress load on the surface of the floating element in the finite element simulation. The displacement of the differential capacitor plate under 2000 Pa loads is shown in Figure 2b. It can be seen that the maximum normal deformation of the edge of the vibrating plate away from the torsion beam was

+1.06 μm and −1.05 μm, respectively. To ensure the good linearity of the sensor in the total measurement range, the gap of the differential capacitor was larger than 6 μm. In this work, the gap of the differential capacitor was designed as 10 μm, and the initial capacitance was about 9 pF by calculation. At the same time, the design sensitivity was about 2.5 Pa/fF in the range of 0–2000 Pa by Equation (2).

3. The Fast Readout Circuit Design

Considering the previous simulation and calculation results, the variation of the capacitance under the skin friction load was very small, within 0.01~1.00 pF. Thus, the circuit needs not only high measurement precision but also a high detection frequency for a shock tunnel with the short time of a few milliseconds. To improve the measurement precision, the signal wire between the sensor head and readout circuit were as short as possible, thus, the readout circuit was integrated with the MEMS chip, as shown in Figure 4a. The relationship between the detection frequency and the measurement accuracy of the sensor was contradictory. It was key to select a weak capacitance detection chip with a high detection frequency and measurement accuracy. The readout circuit included weak capacitance testing, and the processing circuit part and the software real-time display part were designed in this work. A Pcap01 chip is an application-specific integrated circuit for a MEMS capacitance sensor with a low-power capacitance-to-digital converter with a wide input range (fF to nF) and versatile configuration options, and it can be configured for the highest sampling rates of up to 500 kHz, the lowest current consumption of down to 2 uA, or the lowest noise of 15 aF (RMS). In this work, the capacitance signal testing and processing circuit were mainly composed of a Pcap01 chip and single chip (STM32F411CEU6) due to the limitation of the volume, as shown in Figure 4b, which was fabricated by a precision ceramic micro-strip circuit process. The real-time detection and display functional interfaces of the MEMS skin friction sensor were designed using LabVIEW software, as shown in Figure 4c.

Although the measurement accuracy deteriorated with the increase in sampling frequency, the readout circuit for the MEMS skin sensor still had sufficiently high detection accuracy at 3000 Hz to meet the testing requirements in a shock wind tunnel. The resolution was about 10 Pa by static calibration test using a centrifugal force equivalent method.

The components of the MEMS skin friction sensors, including the MEMS chip, floating element, signal readout circuit, and package shell, were fabricated using MEMS and precision machining process technology. MEMS chips were fabricated using the MEMS process, which consists of a silicon structure and glass electrode substrate. The photo of a single chip is shown in Figure 5a. The signal readout circuit was fabricated by precise microstrip circuit technology to ensure the precision of the components and processing. The photo of the ceramic circuit board is shown in Figure 5b. The material of the floating elements and package shells was aluminum alloy to be consistent with the test model material. The precision turning and milling technologies with 10 μm geometrical precision were used to fabricate the floating element and package shells. A photo of the separate components is shown in Figure 5c.

The accuracy of the skin friction measurements is very closely related to the assembly error of the sensor and the flow characteristics of the measured wall [11]. To reduce assembly error, a micro-assembly method for MEMS skin friction sensor assembly based on visual alignment was developed in our previous work [10]. The key parts mainly included the floating element and MEMS chip assembly, the MEMS chip and readout circuit assembly, and the sensor head and package assembly, which are shown in Figure 5d.

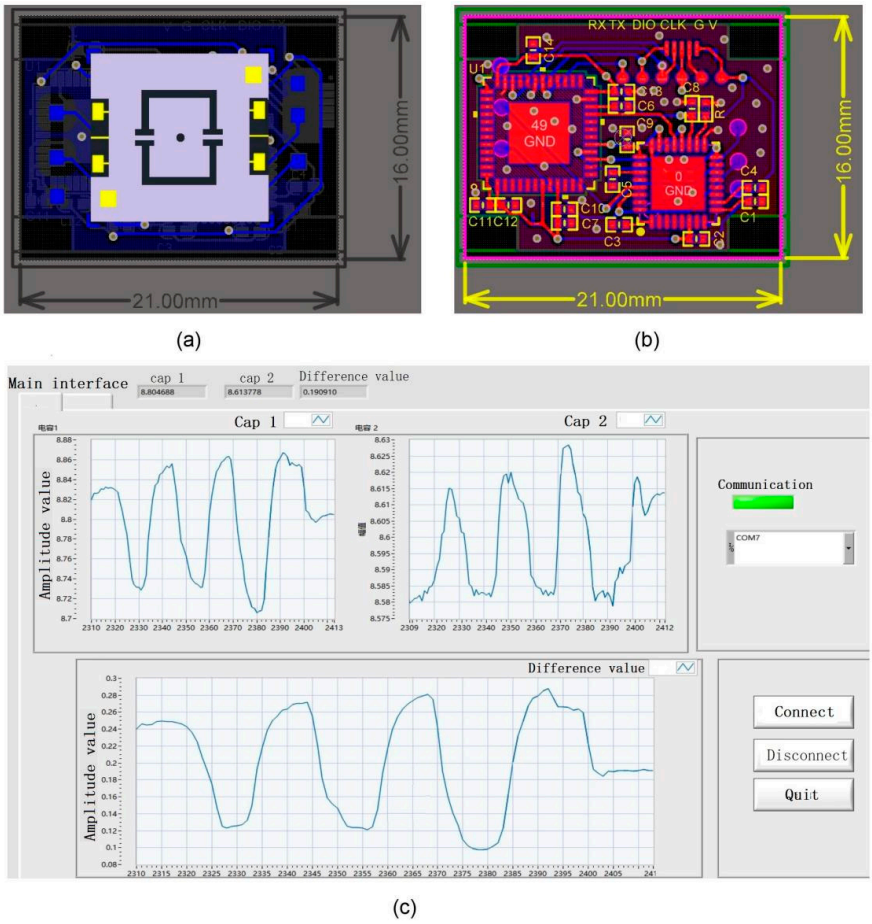

Figure 4. (**a**) Schematic of the readout circuit integrated with MEMS chip; (**b**) the PCB of the circuit; (**c**) the display functional interfaces for the MEMS skin friction sensor.

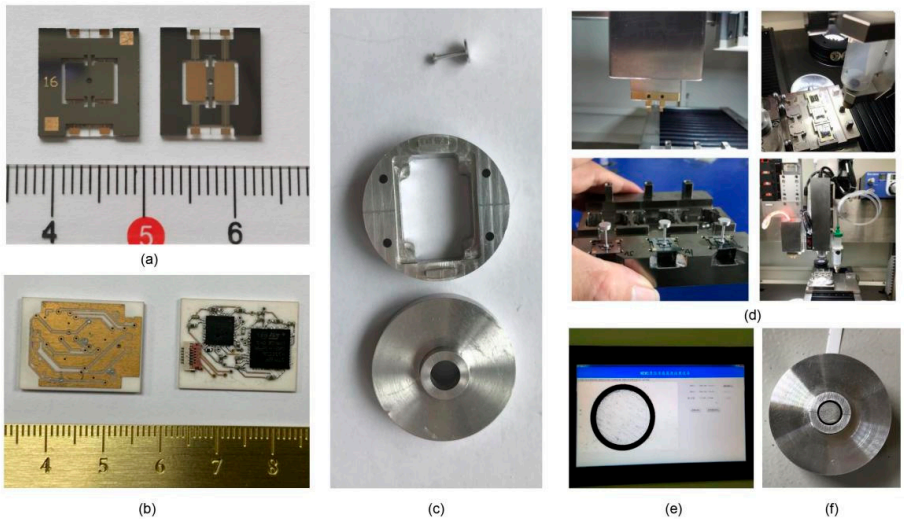

Figure 5. The photos of the separate components for MEMS sensor (**a**–**c**); (**d**) the micro-assembly processes for MEMS sensor; (**e**) the coaxiality measurement for sensor; (**f**) the photo of the assembled sensor.

The assembly results show that the assembly error can be well controlled by using visual alignment and a micro-operating assembly system. The coaxiality of the MEMS skin friction sensor was very good, and the error was only 2 μm by calculating pixels, as shown

in Figure 5e. A photo of the sensor with good electrical characteristics and small assembly error is shown in Figure 5f.

4. Static Calibration of the Sensor

The performances of the MEMS skin friction sensor were determined after assembly. With an experiment of static loading force, the static performance parameters of the sensor were obtained. Due to the small skin friction and volume of the MEMS sensor, the centrifugal force equivalent method and a single-spindle rotary loading platform were adopted to statically calibrate the sensor [11]. The static calibration system for the sensor is shown in Figure 6.

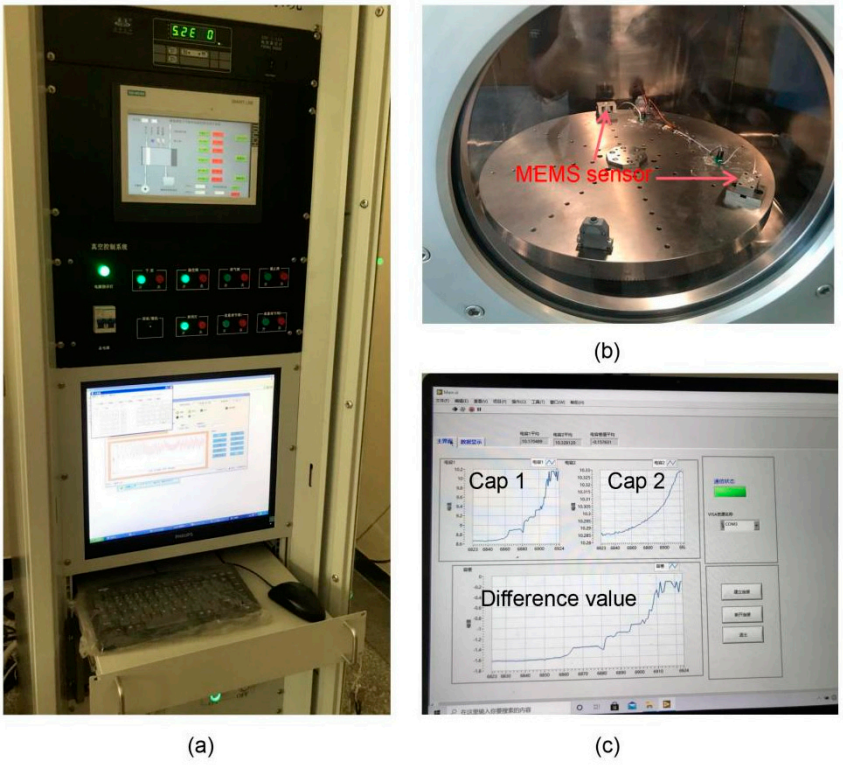

Figure 6. (**a**) Control system of the loading platform; (**b**) rotary loading platform in vacuum environment; (**c**) signal real-time detection, storage, and display window of the MEMS skin friction sensor.

The MEMS sensors were fixed onto a turntable in a vacuum environment, as shown in Figure 6b. The skin friction sensed by the floating element was in some cases equivalent to the rotating speed of the turntable when the structure parameters of the sensor were determined. Then, the relationship between the equivalent friction and capacitance were obtained. The variation of capacitance under the equivalent friction loads was displayed and stored in real time, as shown in Figure 6c.

The maximum equivalent load was set to 1000 Pa, which was limited by the rotating speed of the turntable. The output response of the MEMS skin friction sensor under different equivalent loads is shown in Figure 7. The detection limit of the sensors was determined by the head structure of the sensor and the noise of the readout circuit. The inset shows the responses of the sensor under small equivalent loads. It can be seen that the response curve displays a clear stepwise increase when the load was increased from 0 to 10 Pa. The resolution of the sensor was better than 10 Pa at the same time.

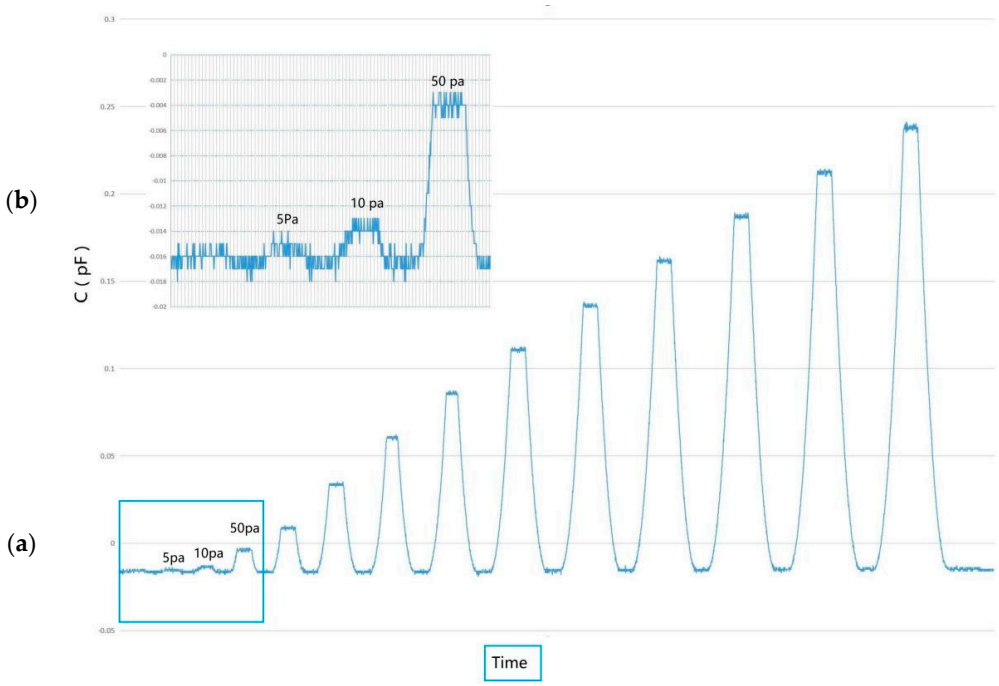

Figure 7. (**a**) The output response of the MEMS skin friction sensor under different equivalent loads; (**b**) the output response of the sensor under small loads.

To obtain the repeatability characteristics of the sensor, seven groups of response values under the same loading conditions were collected and stored at one time. To obtain the response curve of the sensor under different loads, the response values were averaged during a steady load. The repeatability curve of sensor #1 under different loads is shown in Figure 8a. It can be seen that the sensor has good linearity and stability. The linearity and repeatability are both better than 1% in the range from 0 to 1000 Pa, the sensitivity is about 3.8 Pa/fF, and the detection limit is about 10 Pa. In addition, the inset of Figure 8a shows the responses of the sensor in a range up to 100 Pa.

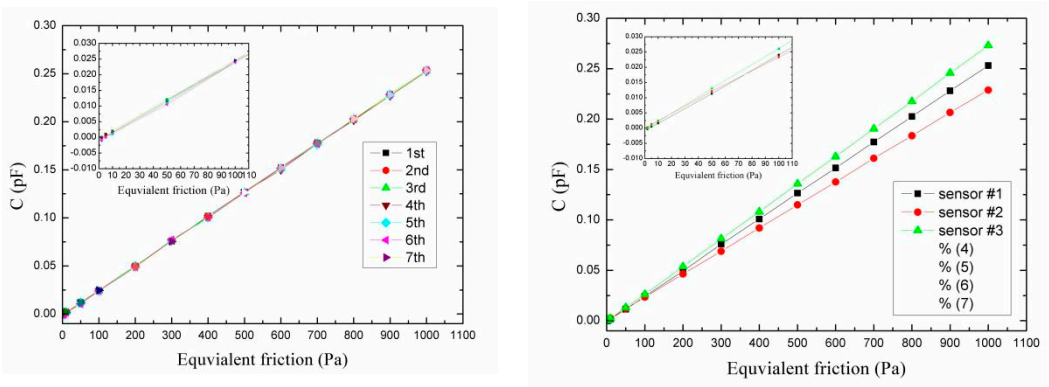

(**a**) (**b**)

Figure 8. (**a**) The repeatability curves of sensor #1; (**b**) the response curves of three sensors under different loads.

Although all components of the sensors were manufactured in the same batch, the machining errors and assembly errors still affected the consistency of the sensors. The response characteristics of the three sensors are shown in Figure 8b. Those sensors also had good linearity and stability in the range of 0 to 1000 Pa. The sensitivities were 3.8 Pa/fF, 4.3 Pa/fF, and 3.6 Pa/fF, respectively, and the resolution was better than 10 Pa, which met the needs of the shock wind tunnel experiment.

5. Conclusions

This paper developed a MEMS skin friction sensor with high detection frequency and a large measurement range in a shock wind tunnel experiment. With the help of finite element analysis software, the sensor head structure of an MEMS sensor was optimized to enhance the natural frequency to 3000 Hz. A key factor was to quickly increase the natural frequency of the sensor head with coarse-tuning by increasing the width of the beam and reducing the mass of the floating element. Then, the length of the torsional beam and the floating element as the force arm was used to achieve fine-tuning. However, the sensitivity deteriorated rapidly with the increasing natural frequency. In addition, to meet the testing requirement in the shock wind tunnel with a short test duration (a few milliseconds), it was key to design a weak capacitance detection circuit with high detection frequency and measurement accuracy. The readout circuit of the sensor was designed and integrated with the sensor head. The components of the sensor, including the MEMS chip, floating element, signal readout circuit, and package shell, were fabricated by using various micro-mechanical processes.

The sensors were assembled using micro-assembly technology based on visual alignment with small assembly errors. The coaxiality of the MEMS skin friction sensor was very good, and the error was only 2 μm. This is the main reason for the good manufacturing consistency of the sensor.

Then, the static performance parameters of the sensor were obtained using the centrifugal force equivalent method and the single-spindle rotary loading platform. The calibration results show that the sensors have good linearity and stability in a range from 0 to 1000 Pa. The repeatability and linearity of static calibration for sensors are better than 1%, and the resolution is better than 10 Pa at the 3000 Hz detection frequency of the sensor. Due to the maximum deformation values of the vibrating plate under 2000 Pa being only 10 percent of the differential capacitor gap, the sensor will have good linearity in a large range (greater than 2000 Pa). Moreover, the gap of the differential capacitor is also one of the important parameters affecting the sensitivity of the sensor. The reduction of the capacitance gap is a key factor to quickly enhance the sensitivity of the sensor. For example, the sensitivity will double with the decrease of the gap of the capacitor from 10 μm to 7 μm in future work.

Author Contributions: Conceptualization, X.W. and H.G.; methodology, T.L.; Validation, H.G. and Y.G., data curation, Z.G.; writing—original draft preparation, H.G.; writing—review and editing, X.W.; visualization, Z.G.; project administration, H.G.; funding acquisition, H.G. All authors have read and agreed to the published version of the manuscript.

Funding: This research received no external funding.

Institutional Review Board Statement: Not applicable.

Informed Consent Statement: Not applicable.

Data Availability Statement: Data are contained within the article.

Conflicts of Interest: The authors declare no conflict of interest.

References

1. Jiang, Z.; Farmer, K.R.; Vijay, M. A MEMS device for measurement of skin friction with capacitive sensing. In Proceedings of the Microelectromechanical Systems Conference, Interlaken, Switzerland, 21–25 January 2001; Volume 8, pp. 4–7.
2. Zhao, Z.; Gallman, J.; White, R. A MEMS floating element with bump shear stress sensor array on a chip. In Proceedings of the 51st AIAA Aerospace Sciences Meeting Including the New Horizons Forum and Aerospace Exposition, Grapevine, TX, USA, 7–10 January 2013; p. 626.
3. Meloy, J.; Griffin, J.; Sells, J.; Cattafesta, L.; Sheplak, M.; Chandrasekharan, V. Experimental verification of a MEMS-based skin friction sensor for quantitative wall shear stress measurement. In Proceedings of the 41st AIAA Fluid Dynamics Conference and Exhibit, Honolulu, HI, USA, 27–30 June 2011; Volume 6, pp. 1–18.
4. Freitas, B.; Mills, D.A.; Keane, C.; Kelley, L.S.; Sheplak, M. Development of a two-dimensional wall shear stress sensor for wind tunnel applications. In Proceedings of the AIAA SciTech, San Diego, CA, USA, 5–9 January 2019; p. 2045.

5. Mills, D.A.; Patterson, W.C.; Keane, C.; Sheplak, M. Characterization of a fully-differential capacitive wall shear stress sensor for low-speed wind tunnels. In Proceedings of the 2018 AIAA Aerospace Sciences Meeting, Kissimmee, FL, USA, 8–12 January 2018; p. 301.
6. Brian, A.A.; Park, S.J.; Mukundan, V.; Pruitt, B.L. Design and characterization of microfabricated piezoresistive floating element-based shear stress sensors. *Sens. Actuators A Phys.* **2007**, *134*, 77–87.
7. Weiss, J.; Jondeau, E.; Giani, A.; Charlot, B.; Combette, P. Static and dynamic calibration of a MEMS calorimetric shear-stress sensor. *Sens. Actuators A Phys.* **2017**, *265*, 211–216. [CrossRef]
8. Von Papen, T.; Buder, U.; Ngo, H.D.; Obermeier, E. A second generation MEMS surface fence sensor for high-resolution wall shear stress measurement. *Sens. Actuators A Phys.* **2004**, *113*, 151–155. [CrossRef]
9. Kim, T.; Saini, A.; Kim, J.; Gopalarathnam, A.; Zhu, Y.; Palmieri, F.L.; Jiang, X. Piezoelectric floating element shear stress sensor for the wind tunnel flow measurement. *IEEE Trans. Ind. Electron.* **2016**, *64*, 7304–7312. [CrossRef] [PubMed]
10. Wang, X.; Zhu, T.; Xu, X.; Shi, Y. Fabrication, calibration and proof experiments in the hypersonic wind tunnel for a novel MEMS skin friction sensor. *Microsyst. Technol.* **2017**, *23*, 3601–3611. [CrossRef]
11. Xiong, W.; Nantian, W.; Xiaobin, X.; Tao, Z. Fabrication and Hypersonic Wind Tunnel Validation of a MEMS Skin Friction Sensor Based on Visual Alignment Technology. *Sensors* **2019**, *19*, 3803. [CrossRef] [PubMed]
12. Meritt, R.J.; Dunbar, M.J.; Molinaro, J.N.; Schetz, J.A. Error source studies of direct measurement skin friction sensors. In Proceedings of the 53rd AIAA Aerospace Sciences Meeting, Kissimmee, FL, USA, 5–9 January 2015; p. 1916.
13. Tian, Y.; Han, Y.; Yang, S.; Zhong, F.; Le, J. Investigation of fluctuating characteristics of wall shear stress in supersonic flow. *Phys. Fluids* **2019**, *31*, 125110.

micromachines

Article

Design and Optimization of a BAW Magnetic Sensor Based on Magnetoelectric Coupling

Wanchun Ren [1,2,*], Jintong Li [1], Guo Liu [3], Jiarong Chen [1], Si Chen [1], Zhijun Gu [1], Jianbo Li [1], Junru Li [4] and Yang Gao [1,*]

[1] School of Information Engineering, Southwest University of Science and Technology, Mianyang 621010, China; lijt@mails.swust.edu.cn (J.L.); chenjr@mails.swust.edu.cn (J.C.); chensi@mails.swust.edu.cn (S.C.); guzj@mails.swust.edu.cn (Z.G.); lijb@mails.swust.edu.cn (J.L.)
[2] Robot Technology Used for Special Environment Key Laboratory of Sichuan Province, Mianyang 621010, China
[3] Science and Technology on Electronic Information Control Laboratory, Southwest China Research Institute of Electronic Equipment, Chengdu 610036, China; liuguosgg@hotmail.com
[4] College of Optoelectronic Engineering, Chongqing University, Chongqing 400044, China; li_junru@foxmail.com
* Correspondence: wanchun_ren@swust.edu.cn (W.R.); gaoy@swust.edu.cn (Y.G.)

Abstract: Magnetic sensors actuated by bulk acoustic wave (BAW) have attracted extensive attention due to the fact of their high sensitivity, GHz-level high frequency, and small size. Different from previous studies, suppression of energy loss and improvement in energy conversion efficiency of the BAW magnetoelectric (ME) sensor were systematically considered during the device design in this work. Finite element analysis models of material (magnetic composite), structure (ME heterostructure), and device (BAW ME magnetic sensor) were established and analyzed in COMSOL software. Additionally, the magnetic composite was prepared by radio frequency magnetron sputtering, and its soft magnetism was characterized by magnetic hysteresis loop and surface roughness. The research results demonstrate that after inserting four layers of 5 nm Al_2O_3 films, a performance of 86.7% eddy current loss suppression rate, a less than 1.1% magnetostriction degradation rate, and better soft magnetism were achieved in 600 nm FeGaB. Furthermore, compared with other structures, the two-layer piezomagnetic/piezoelectric heterostructure had a better ME coupling performance. Eventually, the design of the BAW ME magnetic sensor was optimized by the resonance-enhanced ME coupling to match the resonance frequency between the magnetic composite and the BAW resonator. When a 54,500 A/m direct current bias magnetic field was applied, the sensor worked at the first-order resonance frequency and showed good performance. Its linearity was better than 1.30%, the sensitivity was as high as 2.33 μmV/A, and the measurement range covered 0–5000 A/m.

Keywords: magnetic sensor; bulk acoustic wave; magnetic composite; ME heterostructure; resonance enhanced; magnetoelectric coupling

Citation: Ren, W.; Li, J.; Liu, G.; Chen, J.; Chen, S.; Gu, Z.; Li, J.; Li, J.; Gao, Y. Design and Optimization of a BAW Magnetic Sensor Based on Magnetoelectric Coupling. *Micromachines* **2022**, *13*, 206. https://doi.org/10.3390/mi13020206

Academic Editors: Weidong Wang and Ruiguo Yang

Received: 30 December 2021
Accepted: 25 January 2022
Published: 28 January 2022

1. Introduction

Strong strain-mediated magnetoelectric (ME) coupling in magnetic/electric heterostructures have demonstrated good energy conversion between magnetic and electric fields. It shows great potential for practical devices such as sensors and tunable radio-frequency (RF)/microwave devices. The ME coupling effect is derived from the piezoelectric effect of the piezoelectric phase and the magnetostrictive effect of the piezomagnetic phase [1,2]. Generally, there are two types of ME heterostructures: bulk ME composites and thin-film ME heterostructures. Over the last two decades, many magnetic sensors with bulk ME composites have been reported; however, the device size was at the cm level or larger and difficult to reduce in size [3–5]. Compared to the bulk composites, micro-magnetic

sensors based on thin-film ME heterostructures driven by acoustic waves have become a hot topic for their advantages of miniaturization, excellent elastic interactions, low cost, and the potential capability to integrate with conventional complementary metal oxide semiconductor (CMOS) technology [6–9]. Two types of magnetic sensors actuated by acoustic waves have been demonstrated: surface acoustic waves (SAWs) and bulk acoustic waves (BAWs). The sensor based on the SAW type is limited to working in the low- and medium-frequency band of kHz or measuring static/quasi-static magnetic field signals, although its static sensitivity is pretty high [10–15]. Whereas the sensor based on BAW excitation has attracted tremendous attention in recent years because of its high-frequency characteristics, high power capacity, and high energy conversion efficiency. The mechanism of the BAW ME magnetic sensor is shown in Figure 1; when the external RF magnetic field acts on the magnetostrictive material, strain occurs due to the magnetostrictive effect. Furthermore, because of the ME coupling between the piezomagnetic and piezoelectric phase, the strain transmitted to the piezoelectric material induces the longitudinal piezoelectric effect, resulting in positive and negative opposite charges on the opposite surface of the piezoelectric material, which are output by the electrode as a voltage. Especially, the ME coupling between the two types of films via elastic interaction becomes maximum at the mechanical resonant frequency of the heterostructures. Such resonance enhanced ME coupling greatly benefits the performance of the BAW ME magnetic sensor.

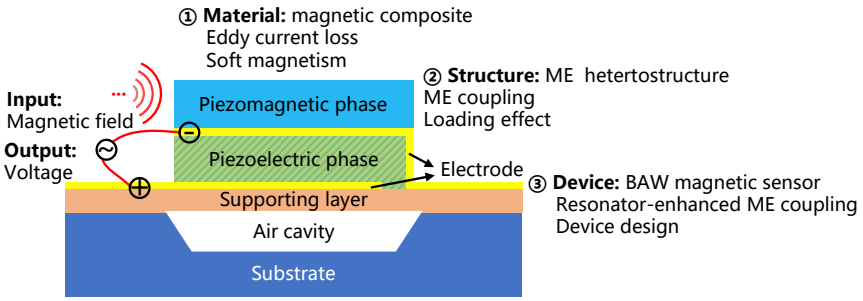

Figure 1. Mechanism of the BAW ME magnetic sensor and the optimizing method of the sensor's performance by fine-tuning the design of the material, structure, and device to improve the energy coupling efficiency and decrease the energy loss.

Much effort has been focused on the experimental and theoretical investigations of the BAW ME magnetic sensors. Hui et al. reported a MEMS resonant magnetic field sensor based on an AlN/FeGaB bilayer nano-plate resonator [16], ME coupling by depositing a composite ME heterostructure of a monolayer AlN/10 layers FeGaB/Al_2O_3 on an AlN CMR, and a ME structure based on nano-plate resonators was reported by Nan et al., which had good magnetic resolution [17,18]. Simultaneously, some works through modeling and simulation methods are also demonstrated. Wu et al. reported a flexible magnetic sensor based on a BAW resonator, the equivalent Mason model of the sensor circuit was established, and its sensitivity was improved by selecting the electrode of giant magnetostrictive material with a large frequency offset [19]. Martos et al. proposed a circuit simulation model of a novel miniaturized magnetoelectric antenna which is applied in low-power sensing [20]. However, there is little systematic research on the material, structure, and device simulation and performance optimization of the micro-magnetic sensor based on BAW actuation yet [21–23].

In order to design and optimize the BAW ME magnetic sensor, as shown in Figure 1, this paper proposes a method to decrease the eddy current loss of the magnetic composite and improve the energy coupling of different layers in the device by finite element analysis (FEA) simulation and experiments. Additionally, models of material (magnetic composite), structure (ME heterostructure), and device (BAW ME magnetic sensor) were established and analyzed. Meanwhile, the magnetic composite was prepared by the RF magnetron

sputtering method and characterized to optimize its soft magnetism. Eventually, the design of a BAW ME magnetic sensor with higher sensitivity and better linearity can be achieved.

2. Materials and Methods

As shown in Figure 2a, a 3D simulation model of the magnetostrictive layer (FeGaB) was built in COMSOL Multiphysics software, and parameters of the films were referenced from data from Northeastern University. A magnetic field, *Hy*, and an electric field, *Ex*, were applied to the magnetostrictive layer in an air-filled cavity to generate high-frequency dynamic magnetic flux, which induced eddy current loops and magnetostriction in Figure 2a(i). The alumina films with different thickness (0~100 nm) and layers (0~10 pieces) were uniformly inserted into the magnetostrictive layer to form a magnetic composite in Figure 2a(ii), which induced a dramatic decrease in the eddy current density and somehow degradation of the magnetostriction in Figure 2a(iii) [24,25]. Furthermore, the thickness of the composite film was optimized in the range of 0~3000 nm. In order to characterize the soft magnetism of the magnetic composite, FeGaB (600 nm) and (FeGaB (120 nm)/Al_2O_3 (5 nm))$_4$/FeGaB (120 nm) were layer by layer deposited on the SiO_2 substrates with 100 Oe bias field by an RF magnetron sputtering tool at the frequency of 13.56 MHz, there was no vacuum broken between the FeGaB and Al_2O_3 deposition. The sputtering power was RF 80 W for FeGaB and RF 90 W for Al_2O_3, while the sputtering pressure and base pressure were 0.7 and 4×10^{-4} Pa, respectively. The cross-section and diffraction pattern were characterized by TEM (transmission electron microscope) and EDX (energy-dispersive X-ray spectroscopy). Magnetic hysteresis loops and surface roughness were tested by VSM (vibrating sample magnetometer) and AFM (atomic force microscope), respectively. Furthermore, the permeability of the magnetic composite was measured by ESR (electron spin resonance).

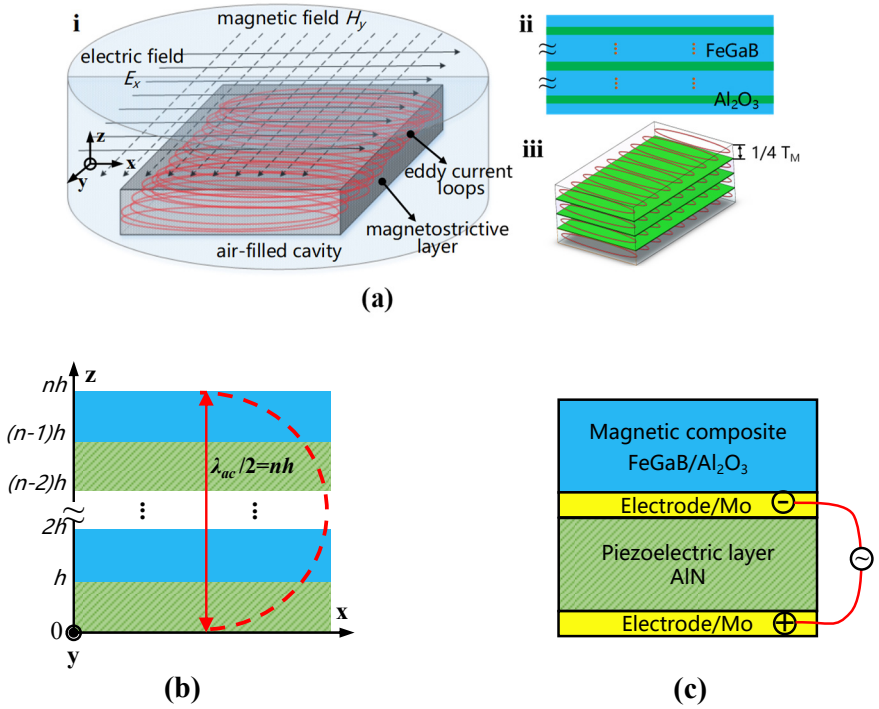

Figure 2. FEA models in COMSOL software. (**a**) Material: the magnetic composite, (**i**) a 3D model in an air-filled cavity for eddy current and magnetostriction simulation; (**ii**) magnetic composite—FeGaB inserted by alumina layers; (**iii**) suppression of eddy current loss—eddy current loops isolated by uniformly laminated alumina in FeGaB. (**b**) Structure: ME coupling effect of the piezomagnetic/piezoelectric heterostructure. (**c**) Device: resonance frequency matching between the FMR of the magnetic composite and the resonance frequency of the BAW resonator.

As shown in Figure 2b, the structure based on the 2–5 layer ME heterostructure was simulated in the COMSOL Multiphysics software [6]. The FEA models of the ME heterostructure, including the piezomagnetic phase, piezoelectric phase, and air domain, were constructed by coupling the magnetic field, solid mechanics module, and electrostatic module in the 3D geometric model. The strain, ME coefficient, and voltage were simulated and compared under the conditions of DC bias to optimize the structure of the ME heterostructure.

As shown in Figure 2c, based on the optimization result of the material and structure, an FEA model of the magnetic sensor was constructed to analyze resonance enhanced ME coupling between ferromagnetic resonance (FMR) of the magnetic composite and resonance frequency of the resonator by fine-tuning the device size. Eventually, the design of the BAW ME magnetic sensor was finalized, and the sensitivity, linearity, and full scope of the sensor were optimized.

3. Results and Discussion

3.1. Material Design: Magnetic Composite

3.1.1. Eddy Current Loss

As shown in Figure 3a, the suppression rate of the ECL increased sharply with the increase in Al_2O_3 thickness; then, it reached its saturation value at a thickness of 10 nm. In particular, at a thickness of 5 nm, the suppression rate reached 98.5% of the saturation value, but its overall suppression value was not higher than 66.8%. Therefore, the effective ECL suppression could not be achieved yet just by increasing the thickness of the Al_2O_3 film. At the same time, the degradation rate of the strain tensor kept increasing almost linearly with the increase in the thickness of the Al_2O_3 film. After inserting a single 5 nm Al_2O_3 film, the degradation rate of strain tensor could be controlled within 1.6% and obtained a 66.8% saturated suppression rate of ECL.

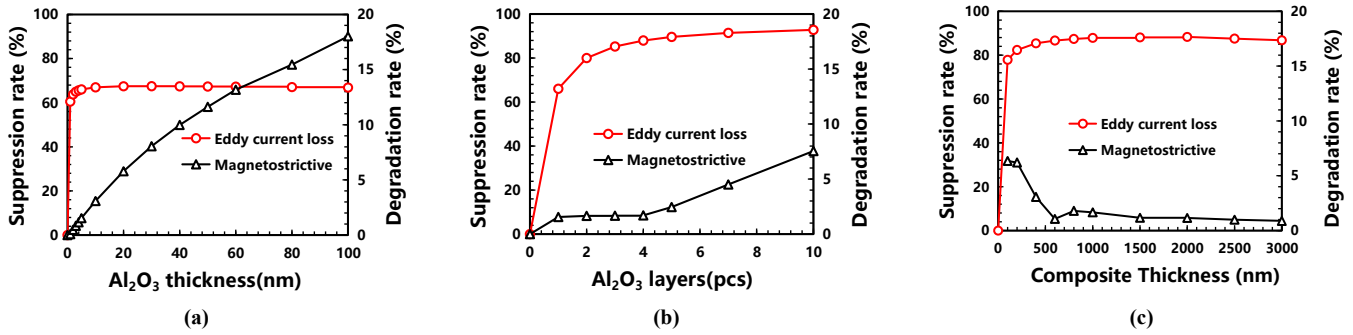

Figure 3. Suppression of the eddy current loss and degradation of magnetostriction by inserting an alumina insulation layer into the FeGaB: (**a**) the thickness effect of the single-layer alumina; (**b**) the layer number effect of the inserted 5 nm alumina; (**c**) the thickness effect of the magnetic composite.

Multi-layer Al_2O_3 films were inserted into the magnetic material, and a significant improvement in the suppression rate can be observed in Figure 3b. The increasing rate of ECL suppression gradually slowed down and then reached the maximum of 95.6%. To insert multi-layer Al_2O_3 with a thickness of 5 nm, a higher suppression rate of over 90% can be achieved, because the inserted insulation film can separate the eddy current loop into several weaker ones by limiting the eddy current within a narrower space. Simultaneously, the magnetostriction degradation rate of the magnetic film increased slowly with the increase in the number of layers. It was less than 1.8% with 1~4 layers of inserted Al_2O_3 film; then, it increased near-linearly beyond four layers, reaching 7.8% for 10 layers. Therefore, with a trade-off between magnetostriction and ECL suppression, inserting four layers of 5 nm Al_2O_3 films into 1000 nm FeGaB film, the degradation rate of the magnetostriction was less than 1.8%, and the ECL suppression reached more than 85.1%.

As shown in Figure 3c, with the increase in composite thickness, the suppression rate changed into the shape of a "rainbow", which is supposed to be caused by the interaction of the isolation effect and size effect. These two effects alternately dominate before and after the thickness of 800 nm, respectively. Moreover, less degradation of magnetostriction for thicker magnetic composites, especially at an ultralow 1.1% magnetostriction degradation and 86.7% ECL suppression of the composites, was found at a thickness of 600 nm, which may be enhanced by well magnetic coupling between two laminated magnetostrictive layers after introducing a certain number of interfaces.

3.1.2. Soft Magnetism

As depicted in Figure 4a, the magnetic composite showed an amorphous state by the cross-section and diffraction pattern, which can effectively suppress the crystallization and grain growth of the film. Therefore, the soft magnetism of the composite can be enhanced by decreasing the magnetocrystalline anisotropy and raising the inter-grain exchanging coupling [25]. In Figure 4b,c, the magnetic hysteresis loops and surface roughness were measured to compare the soft magnetism between the FeGaB film and the composite, and a 98.9% and 35.2% decrease in the coercivity and surface roughness, respectively, were achieved after inserting the four-layer alumina into the FeGaB film. Magnetostatic interaction and surface roughness were also considered to play positive roles in improving soft magnetic properties.

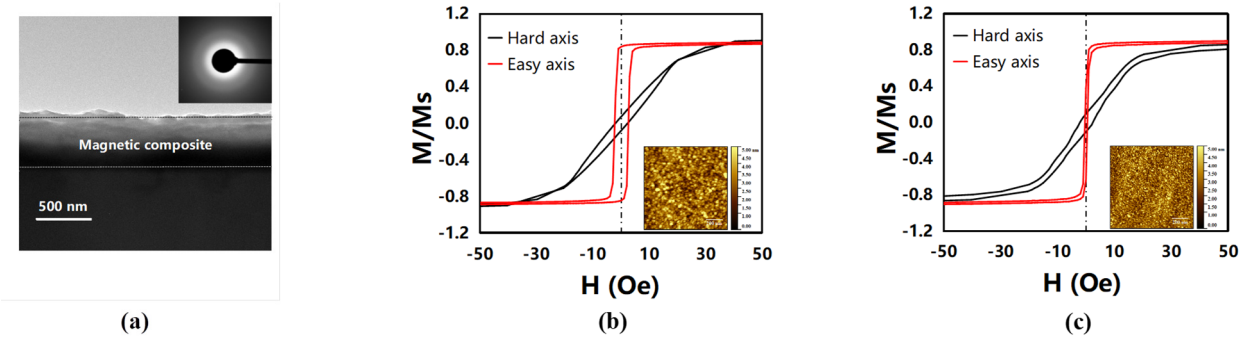

(a) (b) (c)

Figure 4. Soft magnetism of the magnetic composite: (**a**) the cross-section and diffraction pattern of (FeGaB (120 nm)/Al_2O_3 (5 nm))$_4$/FeGaB (120 nm) by TEM and a comparison of the soft magnetism between (**b**) FeGaB and (**c**) (FeGaB (120 nm)/Al_2O_3 (5 nm))$_4$/FeGaB (120 nm) through a magnetic hysteresis loop by VSM and surface roughness by AFM.

3.2. Structure Design: ME Heterostructure

Under different bias magnetic fields, the energy coupling of the ME heterostructure was analyzed through the energy conversion of the magneto–electro–mechanical. Its coupling generated an induced charge on the surface of the piezoelectric layer, resulting in an induced voltage. Therefore, the structure of the sensor can be optimized by comparing the strain, ME coefficient, and the output voltage of the ME heterostructures in different layers. The strain and ME coefficient, α_{ME}, are the most important parameters to evaluate the coupling performance of the ME heterostructure. Their calculation formulas are as following equations [26]:

$$S_H = \frac{1}{2}[(\nabla \mathbf{u})^T + \nabla \mathbf{u}] \quad (1)$$

$$\alpha_{ME} = \frac{\partial E_z}{\partial H_{bias}} = \frac{\partial E_z}{\partial H_y} \quad (2)$$

As shown in Equation (1), S_H, T, and **u** are the strain tensor, stress tensor, and displacement of the magnetostrictive layer, respectively. The strain of the magnetostrictive layer varies with its displacement gradient. Therefore, the ME coupling effect of the piezomagnetic/piezoelectric heterostructure is mediated by strain or mechanical energy. As shown

in Equation (2), E_z is the electric field added along the z-direction, and the DC bias, H_{bias}, is the magnetic field added along the y-direction, H_y. The ME coefficient can be used to characterize the ME coupling efficiency of heterostructures.

As shown in Figure 5a, the strain in the two-layer structure was the largest. This is because the strain of the magnetostrictive layer was affected by the displacement gradient (Equation (1)), and its strain change law was consistent with that of the displacement gradient. Furthermore, the variation law of the ME coefficient was analyzed under the bias magnetic field (0~500 Oe) (Equation (2)). The ME coefficient firstly increased and then decreased with the addition of the bias magnetic field. The two-layer ME heterostructure with the highest ME coefficient had the highest sensitivity, which also means the best magnetoelectric conversion efficiency and the largest output voltage. As shown in Figure 5c, the output voltage value of the two-layer structure was the largest one, too. Therefore, the structure based on the two-layer ME heterostructure can achieve the best energy coupling.

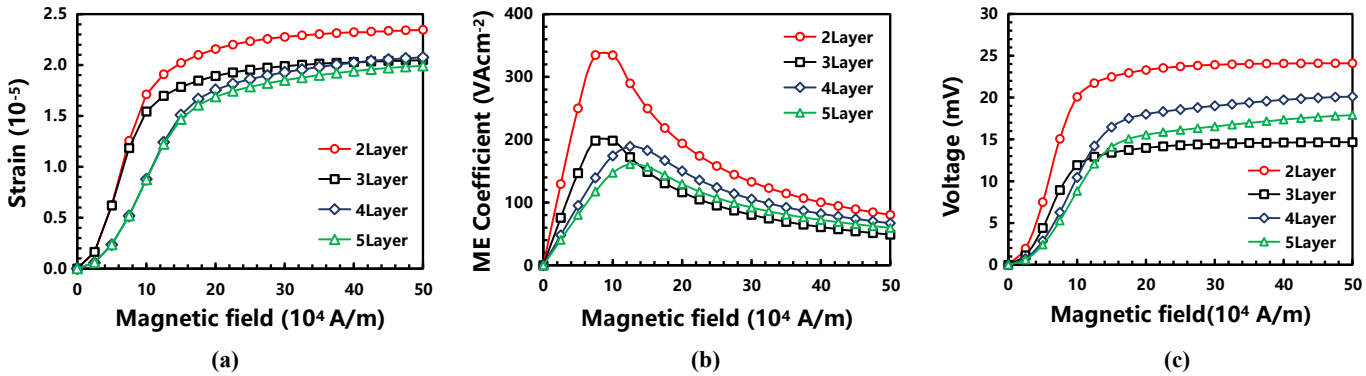

Figure 5. With the increase in the bias DC magnetic field: (**a**) the variation curve of the strain, (**b**) the variation curve of the ME coefficient, and (**c**) the output voltage of the ME heterostructures in different layers.

In summary, the result demonstrates a two-layer structure for improving the sensitivity of the magnetic sensor by optimizing its strain, ME coefficient, and the output voltage of the ME heterostructure layers.

3.3. Device Design: BAW Magnetic Sensor

The permeability of the magnetic composite is shown in Figure 6a, and its resonance frequency was 1.51 GHz. In order to obtain the highest output voltage by resonance enhanced ME coupling, the BAW ME magnetic sensor should work at the same resonance frequency [27]. Therefore, the device size, including the thickness of the piezoelectric/magnetic layer and the electrode, needs to be optimized to match the FMR of the magnetic composite and the resonance frequency of the BAW resonator. Figure 6b,c show that the resonance frequency of the sensor can be fine-tuned by adjusting the thickness of the ME heterostructure and the electrode. As shown in Figure 6d, the resonance frequency matched well between the BAW resonator (2.65 GHz) and films (piezoelectric 600 nm/magnetic 600 nm; Mo electrode 200 nm) by considering the mass load effect. The first-order and second-order resonance frequencies of the sensor were 1.51 and 3.60 GHz, respectively.

3.4. Performance Analysis

As shown in Figure 7a, the design of the BAW ME magnetic sensor was optimized, including the magnetic composite (FeGaB with a four-layer alumina uniformly inserted; T_A was 5 nm), the structure (two-layer piezomagnetic/piezoelectric heterostructure; h was 600 nm), and the electrode (δ was 200 nm). In order to evaluate the performances of the magnetic sensor, different DC biases magnetic fields (20,000–80,000 A/m) were applied to characterize the output voltage and ME coefficients (Figure 7b). The output voltage at the resonance frequency was significantly higher than that of others; additionally, the

maximum output voltage at the first-order resonance frequency was larger than that of the second-order one.

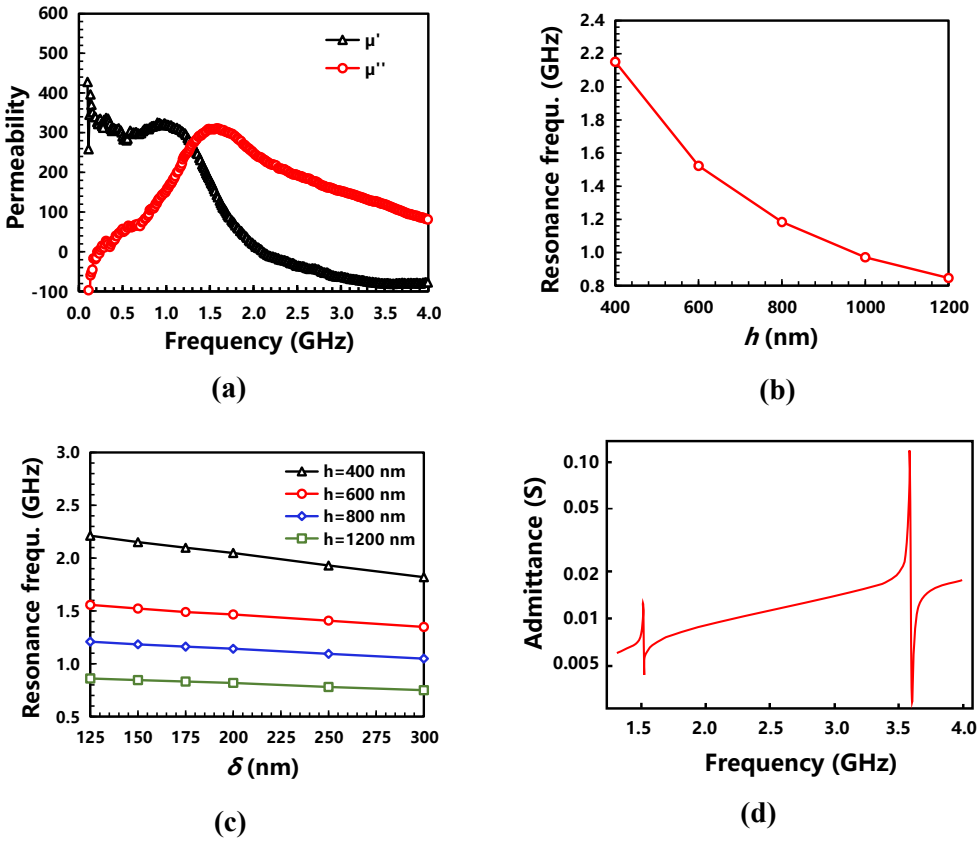

Figure 6. Design of the magnetic sensor by resonance enhanced ME coupling: (**a**) permeability of the FeGaB/Al_2O_3 composite by ESR and the FMR matching by changing the thickness of (**b**) the piezomagnetic/piezoelectric heterostructure and (**c**) the electrode; (**d**) after matching the frequency, the admittance curve of the two-layer device was obtained by applying an AC voltage to the piezoelectric layer of the ME heterostructure without a bias magnetic field.

The sensitivity and linearity were the most important parameters to evaluate the BAW ME magnetic sensor. Their calculation formulas are shown in the following equations:

$$S = \frac{\partial V}{\partial H_y} = \frac{\partial E_z}{\partial H_y} h \tag{3}$$

$$\alpha_L = \frac{\Delta Y_{max}}{Y_{FS}} \times 100\% \tag{4}$$

As shown in Equation (3), S, V, and h are the sensitivity, output voltage, and thickness of the piezoelectric phase, respectively. It was found that the sensitivity of the sensor was dependent on the ME coupling of piezomagnetic/piezoelectric heterostructure, α_{ME}, and thickness of piezoelectric phase, h. In order to obtain good ME coupling, it can thus be seen that it is extremely necessary to improve energy conversion efficiency and suppress eddy current loss in the design of the BAW ME magnetic sensor. In Equation (4), a_L, ΔY_{max}, and Y_{FS} are the linearity, the maximum deviation between the calibration curve and the fitting line, and the output voltage difference over the full-scale range. Therefore, the linearity of the sensor was directly related to a selection of the fitting line and a full-scale range. In this work, the fitting line was obtained by the least squares method. In Figure 7c, it can be found that the output voltage at the first-order resonance frequency increased to be the highest and then decreased at the bias magnetic field of 60,000 A/m; meanwhile, the

sensitivity at the DC bias magnetic field of 54,500 A/m was found to be the highest by the differential analysis method of the *V–H* curve. As shown in Figure 7d, a high sensitivity of 2.33 μmV/A, a good linearity better than 1.30%, and a wide measurement range of 0–5000 A/m could be achieved while the DC bias magnetic field applied on the sensor was kept at 54,500 A/m.

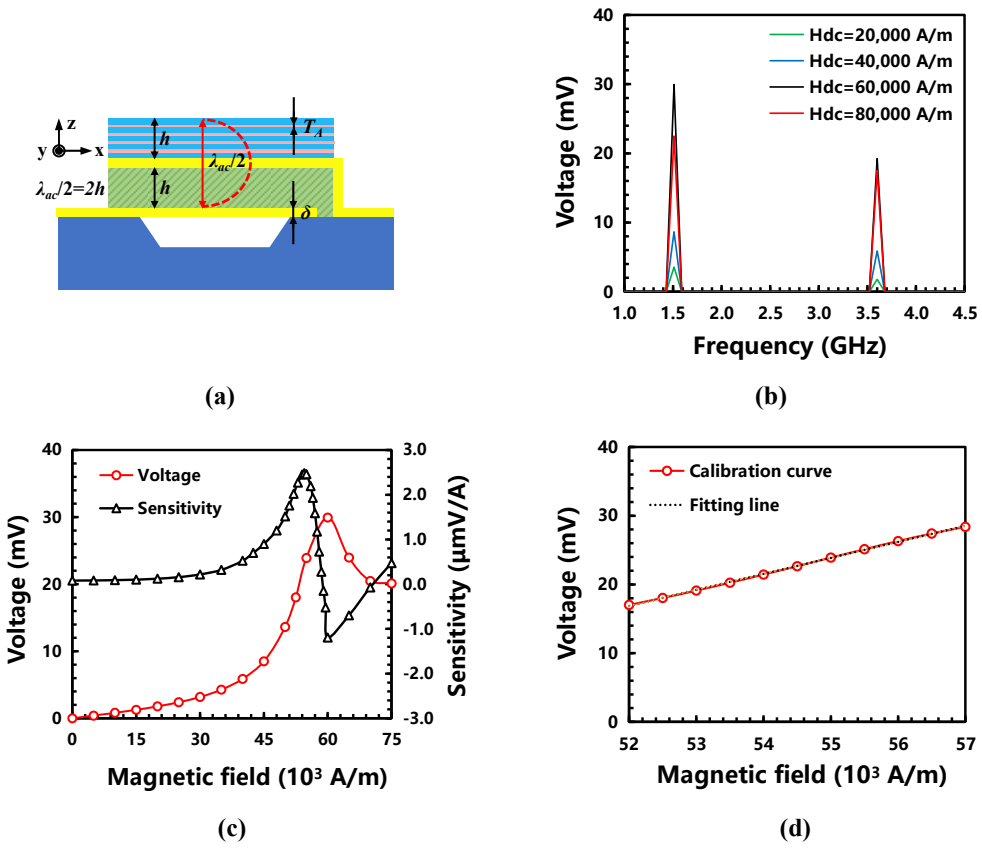

Figure 7. The performance of the BAW ME magnetic sensor: (**a**) the finalized design of the BAW ME magnetic sensor; (**b**) the output voltage variation at the first-order and the second-order resonance frequencies; (**c**) the output voltage and sensitivity at the first-order resonance frequency under different DC bias magnetic fields; (**d**) the linearity and the measurement range with a DC bias of 54,500 A/m.

4. Conclusions

In this work, a method was proposed to design and optimize the BAW ME magnetic sensor; especially, the energy loss suppression and the energy conversion efficiency improvement were systematically considered. FEA models of material (magnetic composite), structure (ME heterostructure), and device (BAW ME magnetic sensor) were established and analyzed in COMSOL software. Additionally, the magnetic composite was prepared by RF magnetron sputtering, and its soft magnetism was characterized by magnetic hysteresis loop and surface roughness.

After inserting four-layers of 5 nm Al_2O_3 films, the performance of an 86.7% eddy current loss suppression rate, less 1.1% magnetostriction degradation rate, and smaller coercivity and roughness were achieved for (FeGaB (120 nm)/Al_2O_3 (5 nm))$_4$/FeGaB (120 nm). Furthermore, the strain, ME coefficient, and output voltage of the heterostructure were simulated and analyzed. Compared with other structures, the two-layer piezomagnetic/piezoelectric heterostructure had a better ME coupling performance. Eventually, the design of the BAW ME magnetic sensor was optimized by matching the resonance frequency between the magnetic composite and the BAW resonator as the first-order of 1.51 GHz. When a 54,500 A/m DC bias magnetic field was applied, the sensor worked at

the first-order resonance frequency and showed good performance. The linearity was better than 1.30%, the sensitivity was as high as 2.33 μmV/A, and the measurement range could cover 0–5000 A/m. With the advantages of the highest energy conversion efficiency based on resonance enhanced ME coupling and the lowest eddy current loss and the integrated capability with CMOS technology, the BAW ME magnetic sensor has a bright future for compact receiving antennas, biomedical application, and the Internet of Things (IoT) due to the fact of its unique and particular properties. Furthermore, this achievement will further guide the structural design and performance optimization of other ME coupling devices.

Author Contributions: Conceptualization, W.R. and G.L.; methodology, S.C.; software, J.C. and S.C.; validation, J.L. (Jintong Li), G.L. and J.L. (Junru Li); formal analysis, J.L. (Jianbo Li); investigation, J.L. (Jintong Li); resources, W.R. and Y.G.; data curation, W.R., J.C., J.L. (Jianbo Li) and J.L. (Jintong Li); writing—original draft preparation, W.R. and Z.G.; writing—review and editing, Y.G.; visualization, J.L. (Junru Li); supervision, Y.G.; project administration, W.R.; funding acquisition, G.L. All authors have read and agreed to the published version of the manuscript.

Funding: This research was funded by the Science and Technology on Electronic Information Control Laboratory (grant number: 6142105200203), the Foundation of Southwest University of Science and Technology (grant number: 20ZX7114), the Sichuan Science and Technology Program (grant number: 2021YJ0105), and the Key Laboratory of Aerodynamic Noise Control (grant number: 2001ANCL20200307).

Acknowledgments: We are grateful to Xiling Li for soft magnetism testing of the magnetic composite, Tao Wei and Bo Liu for sample preparation of the magnetic composite.

Conflicts of Interest: The authors declare no conflict of interest.

References

1. Jin, J.; Lu, S.-G.; Chanthad, C.; Zhang, Q.; Haque, M.A.; Wang, Q. Multiferroic polymer composites with greatly enhanced magnetoelectric effect under a low magnetic bias. *Adv. Mater.* **2011**, *23*, 3853–3858. [CrossRef] [PubMed]
2. Zhuang, X.; Saez, S.; Sing, M.L.C.; Cordier, C.; Dolabdjian, C.; Li, J.; Viehland, D.; Mandal, S.K.; Sreenivasulu, G.; Srinivasan, G. Investigation on the Magnetic Noise of Stacked Magnetostricitive-Piezoelectric Laminated Composites. *Sens. Lett.* **2012**, *10*, 961–965. [CrossRef]
3. Dong, S.; Zhai, J.; Li, J.; Viehland, D. Small dc magnetic field response of magnetoelectric laminate composites. *Appl. Phys. Lett.* **2006**, *88*, 82907. [CrossRef]
4. Das, J.; Gao, J.; Xing, Z.; Li, J.F.; Viehland, D. Enhancement in the field sensitivity of magnetoelectric laminate heterostructures. *Appl. Phys. Lett.* **2009**, *95*, 92501. [CrossRef]
5. Gao, J.; Shen, L.; Wang, Y.; Gray, D.; Li, J.; Viehland, D. Enhanced sensitivity to direct current magnetic field changes in Metglas/Pb$(Mg_{1/3}Nb_{2/3})O_3$-$PbTiO_3$ laminates. *J. Appl. Phys.* **2011**, *109*, 074507. [CrossRef]
6. Chen, S.; Ren, W.-C.; Li, J.; Peng, C.-R.; Gao, Y. Modeling of magnetic sensor based on BAW magnetoelectric coupling microheterostructure. In Proceedings of the 2021 IEEE 16th International Conference on Nano/Micro Engineered and Molecular Systems (NEMS), Xiamen, China, 25–29 April 2021; pp. 1259–1263.
7. Hayes, P.; Salzer, S.; Reermann, J.; Yarar, E.; Röbisch, V.; Piorra, A.; Meyners, D.; Höft, M.; Knöchel, R.; Schmidt, G.; et al. Electrically modulated magnetoelectric sensors. *Appl. Phys. Lett.* **2016**, *108*, 182902. [CrossRef]
8. Hayes, P.; Schell, V.; Salzer, S.; Burdin, D.; Yarar, E.; Piorra, A.; Knöchel, R.; Fetisov, Y.K.; Quandt, E.; Knoechel, R.H. Electrically modulated magnetoelectric AlN/FeCoSiB film composites for DC magnetic field sensing. *J. Phys. D Appl. Phys.* **2018**, *51*, 354002. [CrossRef]
9. Liang, X.; Dong, C.; Chen, H.; Wang, J.; Wei, Y.; Zaeimbashi, M.; He, Y.; Matyushov, A.; Sun, C.; Sun, N. A Review of Thin-Film Magnetoelastic Materials for Magnetoelectric Applications. *Sensors* **2020**, *20*, 1532. [CrossRef]
10. Ge, F.; Zhao, L.Y.; Zhang, Y. Design and Optimization of a Novel SAW Gyroscope Structure Based on Amplitude Modulation with 1-D Phononic Crystals. *Micromachines* **2021**, *12*, 1485. [CrossRef]
11. Zhou, H.; Talbi, A.; Tiercelin, N.; Matar, O.B. Multilayer magnetostrictive structure based surface acoustic wave devices. *Appl. Phys. Lett.* **2014**, *104*, 114101. [CrossRef]
12. Huang, L.; Lyu, Q.; Wen, D.; Zhong, Z.; Zhang, H.; Bai, F. Theoretical investigation of magnetoelectric surface acoustic wave characteristics of ZnO/Metglas layered composite. *AIP Adv.* **2016**, *6*, 015103. [CrossRef]
13. Polewczyk, V.; Dumesnil, K.; Lacour, D.; Moutaouekkil, M.; Mjahed, H.; Tiercelin, N.; Watelot, S.P.; Mishra, H.; Dusch, Y.; Hage-Ali, S.; et al. Unipolar and Bipolar High-Magnetic-Field Sensors Based on Surface Acoustic Wave Resonators. *Phys. Rev. Appl.* **2017**, *8*, 024001. [CrossRef]
14. Kittmann, A.; Durdaut, P.; Zabel, S.; Reermann, J.; Schmalz, J.; Spetzler, B.; Meyners, D.; Sun, N.X.; McCord, J.; Gerken, M.; et al. Wide Band Low Noise Love Wave Magnetic Field Sensor System. *Sci. Rep.* **2018**, *8*, 278. [CrossRef] [PubMed]

15. Liu, X.; Ou-Yang, J.; Tong, B.; Chen, S.; Zhang, Y.; Zhu, B.; Yang, X. Influence of the delta-E effect on a surface acoustic wave resonator. *Appl. Phys. Lett.* **2019**, *114*, 062903. [CrossRef]
16. Hui, Y.; Nan, T.; Sun, N.X.; Rinaldi, M. MEMS resonant magnetic field sensor based on an AlN/FeGaB bilayer nano-plate resonator. In Proceedings of the 2013 IEEE 26th International Conference on Micro Electro Mechanical Systems (MEMS), Taipei, Taiwan, 20–24 January 2013; pp. 721–724.
17. Nan, T.; Hui, Y.; Rinaldi, M.; Sun, N.X. Self-Biased 215MHz Magnetoelectric NEMS Resonator for Ultra-Sensitive DC Magnetic Field Detection. *Sci. Rep.* **2013**, *3*, srep01985. [CrossRef]
18. Nan, T.; Lin, H.; Gao, Y.; Matyushov, A.; Yu, G.; Chen, H.; Sun, N.; Wei, S.; Wang, Z.; Li, M.; et al. Acoustically actuated ultra-compact NEMS magnetoelectric antennas. *Nat. Commun.* **2017**, *8*, 296. [CrossRef]
19. Wu, Y.; Dong, S.; Jin, H.; Wang, X.; Chen, G. Flexible magnetic sensor based on FBAR. In Proceedings of the 2016 IEEE International Nanoelectronics Conference (INEC), Chengdu, China, 9–11 May 2016; pp. 1–2.
20. Martos-Repath, I.; Mittal, A.; Zaeimbashi, M.; Das, D.; Sun, N.X.; Shrivastava, A.; Onabajo, M. Modeling of Magnetoelectric Antennas for Circuit Simulations in Magnetic Sensing Applications. In Proceedings of the 2020 IEEE 63rd International Midwest Symposium on Circuits and Systems (MWSCAS), Springfield, MA, USA, 9–12 August 2020; pp. 49–52.
21. Wang, Y.; Xiao, N.; Xiao, R.; Wen, Y.; Li, P.; Chen, L.; Ji, X.; Han, T. Enhanced dc Magnetic Field Sensitivity for Coupled ac Magnetic Field and Stress Driven Soft Magnetic Laminate Heterostructure. *IEEE Sens. J.* **2020**, *20*, 14756–14763. [CrossRef]
22. Rasly, M.; Nakatani, T.; Li, J.; Sepehri-Amin, H.; Sukegawa, H.; Sakuraba, Y. Magnetic, magnetoresistive and low-frequency noise properties of tunnel magnetoresistance sensor devices with amorphous CoFeBTa soft magnetic layers. *J. Phys. D Appl. Phys.* **2021**, *54*, 095002. [CrossRef]
23. Pan, L.; Pan, M.; Hu, J.; Hu, Y.; Che, Y.; Yu, Y.; Wang, N.; Qiu, W.; Li, P.; Peng, J.; et al. Novel Magnetic Field Modulation Concept Using Multiferroic Heterostructure for Magnetoresistive Sensors. *Sensors* **2020**, *20*, 1440. [CrossRef]
24. Shahid, I.; Yin, G.; Yuan, J.; Ma, Y.G.; He, S.L. FeGaB(25 nm)/Al_2O_3/FeGaB(25 nm) Multilayer Structures: Effects of Variation of Al_2O_3Thickness on Static and Dynamic Magnetic Properties. *Rare Met. Mater. Eng.* **2018**, *47*, 1951–1957.
25. Wang, X.; Gao, Y.; Chen, H.; Chen, Y.; Liang, X.; Lin, W.; Sun, N.X. Size-dependent magnetic properties of FeGaB/Al_2O_3 multilayer micro-islands. *Phys. Lett. A* **2018**, *382*, 1505–1508. [CrossRef]
26. Reis, S.; Silva, M.P.; Castro, N.; Correia, V.; Martins, P.; Lasheras, A.; Gutierrez, J.; Barandiarán, J.M.; Rocha, J.G.; Lanceros-Mendez, S. Characterization of Metglas/poly (vinylidene fluoride)/Metglas magnetoelectric laminates for AC/DC magnetic sensor applications. *Mater. Des.* **2016**, *92*, 906–910. [CrossRef]
27. Tu, C.; Chu, Z.-Q.; Spetzler, B.; Hayes, P.; Dong, C.-Z.; Liang, X.-F.; Chen, H.-H.; He, Y.-F.; Wei, Y.-Y.; Lisenkov, I.; et al. Mechanical-Resonance-Enhanced Thin-Film Magnetoelectric Heterostructures for Magnetometers, Mechanical Antennas, Tunable RF Inductors, and Filters. *Materials* **2019**, *12*, 2259. [CrossRef] [PubMed]

micromachines

MDPI

Article

An Improved Difference Temperature Compensation Method for MEMS Resonant Accelerometers

Pengcheng Cai [1,2], Xingyin Xiong [1], Kunfeng Wang [1,2], Jiawei Wang [1,2] and Xudong Zou [1,2,*]

[1] The State Key Laboratory of Transducer Technology, Aerospace Information Research Institute, Chinese Academy of Sciences, Beijing 100190, China; caipengcheng16@mails.ucas.ac.cn (P.C.); xyxiong@mail.ie.ac.cn (X.X.); wangkunfeng17@mails.ucas.ac.cn (K.W.); jiaweiw0901@foxmail.com (J.W.)

[2] School of Electronic, Electrical and Communication Engineering, University of Chinese Academy of Sciences, Beijing 100049, China

* Correspondence: zouxd@aircas.ac.cn; Tel.: +86-10-58887528

Abstract: Resonant accelerometers are promising because of their wide dynamic range and long-term stability. With quasi-digital frequency output, the outputs of resonant accelerometers are less vulnerable to the noise from circuits and ambience. Differential structure is usually adopted in a resonant accelerometer to achieve higher sensitivity to acceleration and to reduce common noise at the same time. Ideally, a resonant accelerometer is only sensitive to external acceleration. However, temperature has a great impact on resonant accelerometers, causing unexcepted frequency drift. In order to cancel out the frequency drift caused by temperature change, an improved temperature compensation method for differential vibrating accelerometers without additional temperature sensors is presented in this paper. Experiment results demonstrate that the temperature sensitivity of the prototype sensor is reduced from 43.16 ppm/°C to 0.83 ppm/°C within the temperature range of −10 °C to 70 °C using the proposed method.

Keywords: resonant accelerometer; temperature compensation; difference

Citation: Cai, P.; Xiong, X.; Wang, K.; Wang, J.; Zou, X. An Improved Difference Temperature Compensation Method for MEMS Resonant Accelerometers. *Micromachines* **2021**, *12*, 1022. https://doi.org/10.3390/mi12091022

Academic Editor: Weidong Wang

Received: 29 July 2021
Accepted: 22 August 2021
Published: 27 August 2021

1. Introduction

Microelectromechanical systems (MEMS) accelerometers have been widely used in many applications, such as mobile devices, gaming, automobile and healthcare [1,2] for its advantages of small volume, light weight, low power consumption and low cost [3]. However, MEMS accelerometers still need further development for high precision applications, such as inertial navigation, tilt measurement and geophysical measurements [4–9]. Among various kinds of MEMS accelerometers, silicon resonant accelerometers are promising for high sensitivity, large linear range, low bias instability and so on [10–13]. A silicon resonant accelerometer converts external acceleration input into modulated frequency output as the acceleration will change the stiffness of resonator. With frequency modulation output, the signal is easy to measure and not vulnerable to the circuit noise [14,15].

To reduce common noise and improve the sensitivity to external acceleration, differential structure is often adopted. Ideally, the frequency of the resonator is only sensitive to the external acceleration. However, the material of differential vibrating accelerometers, normally single crystalline silicon, is temperature dependent, causing the device to be sensitive to temperature as well [16,17]. Moreover, the temperature sensitivity of the two resonators in an accelerometer may be different due to process and fabrication tolerances. To improve the performance against temperature, two typical approaches are explored. One way is to keep the temperature in the accelerometer stable with an inner oven [18–21]. Salvia presented a real time temperature compensation for MEMS oscillators using an integrated oven, achieving a frequency stability of ±1 ppm from −20 °C to +80 °C. Yang adopted a micro oven-control system to keep temperature in inertial sensors, providing the temperature-induced root of sum of squares bias error 1.920 mg from −40 °C

to 85 °C for three-axis accelerometers in their Invensense MPU-6050. Another way is to remove the side effects caused by temperature change with thermal compensation [22–24]. In [22], an integrated temperature sensor is set to sense the temperature and the compensation algorithm is implemented in FPGA. The zero bias is reduced from 345 mg to 1.9 mg over the temperature range from −10 °C to 80 °C. The work presented in [23] uses an additional resonator to sense the temperature and the result is used to make temperature compensation. Temperature is captured and a temperature compensation algorithm is implemented to make electrostatic stiffness control to cancel out the side effects caused by temperature change in [24], achieving about 100 times the improvement compared to without compensation. In the first way, an oven is needed additionally, and a heating controller as well. The heating controller and the oven form a closed loop for temperature, where the heating controller can sense the temperature and control the oven power, making the temperature a constant, thus removing the side effects caused by temperature change. An inner oven means not only a more complex system, but also higher power consumption. The second way is a usual alternative method to cancel the thermal affection. Aiming to compensate the impact of temperature fluctuation, a thermometer used to make a real-time measurement of temperature and a compensation algorithm used to cancel the side effect of temperature are required in the second method. The main drawback of using a temperature sensor is that temperature measurement error and thermal lags are inevitable. Besides the two typical methods mentioned above, there are some other novel approaches proposed to improve performance. Behbahani et al. proposed a wafer-level technique that can tune the frequency of axisymmetric resonators precisely and reduce the frequency mismatches of a subset of the wafer's resonators greatly [25]. An in situ bias drift compensation by using multiple rate measurements derived from a single resonator has been proved to be effective for reducing bias drifts caused by temperature in work [26]. These novel approaches are either in need of additional process steps or difficult to be applied on MEMS resonant accelerometers.

To overcome the drawbacks mentioned above, we proposed an improved approach called proportional difference to accomplish the thermal compensation in a differential vibrating accelerometer with recognition of approximate linear drift in frequency caused by temperature change.

2. Architecture and Temperature Sensitivity Analysis of the Sensor

The schematic of the accelerometer is shown in Figure 1. Two double-ended tune fork resonators are connected to the proof mass through a pair of micro-lever force amplifiers on each side. The two resonators are driven and sensed by parallel-plate capacitor at two sides of the resonators. External acceleration will generate a force through the proof mass. This force is applied on and amplified by the micro-lever, and then acts on the resonator of each side, causing stiffness change of resonators and making their resonant frequency change with the external acceleration. As the force direction is opposite for the two resonators, a differential effect is achieved.

The device is fabricated using silicon-on-insulator (SOI) foundry process and vacuum packaged by wafer-level package. Some parameters of the accelerometer are summarized in the Table 1.

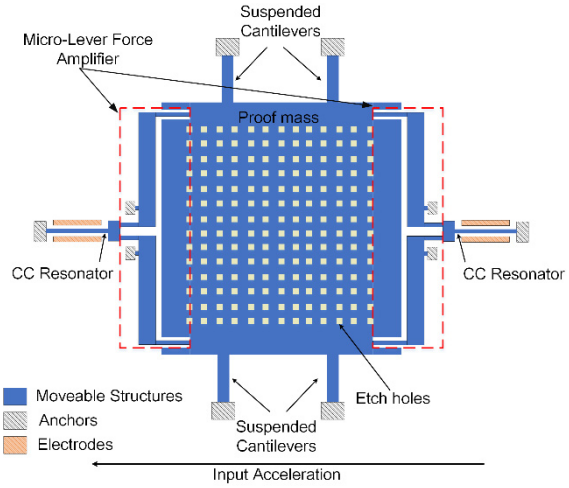

Figure 1. Schematic of the accelerometer.

Table 1. Parameters of the accelerometer.

Parameter	Value
Device thickness	40 μm
Length of CC resonant beam	400 μm
Width of CC resonant beam	6 μm
Gap of resonant beam	2 μm
Quality of proof mass	1.50 mg
Quality factor	15,600
Resonant frequency 1 (at 30 °C)	197.2495 kHz
Resonant frequency 2 (at 30 °C)	195.6092 kHz
Scale factor of resonator 1	512 Hz/g
Scale factor of resonator 2	508 Hz/g

The resonant frequency of the resonator is affected by temperature for many factors, where the temperature sensitivity of elasticity is considered mainly responsible for temperature drift in frequency in our accelerometer. In general, the elasticity of a material is represented by the Young's modulus (E). The change in Young's modulus with temperature is designated as temperature coefficient of elasticity (TCE) and the expression of the temperature-dependent Young's modulus can be given by:

$$E = E(298.15K)\left(1 - 6.382 \times 10^{-5}\Delta T - 5.199 \times 10^{-9}\Delta T^2\right) \quad (1)$$

The change of temperature will also lead to thermal expansion of the silicon, which can be expressed by thermal expansion coefficient (TEC).

$$TEC(T) = -4 \times 10^{-12}T^2 + 8 \times 10^{-9}T + 4.7 \times 10^{-7} \quad (2)$$

The size of the resonant beam will change with temperature, which can be calculated by:

$$L(T) = L_0 + L_0(T - T_0)\bullet TEC(T) \quad (3)$$

$$w(T) = w_0 + w_0(T - T_0)\bullet TEC(T) \quad (4)$$

$$h(T) = h_0 + h_0(T - T_0)\bullet TEC(T) \quad (5)$$

where L is the length of the beam, w is the width of the beam and h is the height or thickness of the beam. Then, the resonant frequency can be estimated as following with considering of the effect caused by temperature.

$$\begin{aligned} f &= \frac{\beta^2}{2\pi L^2}\sqrt{\frac{EI}{\rho A}} \\ &= f(T_0) + \frac{\beta^2}{2\pi L^2}\sqrt{\frac{E(T_0)I}{\rho A}}\frac{1}{2E(T_0)}\frac{\partial E}{\partial T}\Delta T + \frac{\beta^2}{2\pi L^2}\sqrt{\frac{E(T_0)I}{\rho A}}\left(-\frac{5}{2}\frac{1}{L}\frac{\partial L(T)}{\partial T} + \frac{1}{h}\frac{\partial h(T)}{\partial T} + \frac{1}{2}\frac{\partial w(T)}{T}\right)\Delta T \\ &\approx f(T_0) + \frac{\beta^2}{2\pi L^2}\sqrt{\frac{E(T_0)I}{\rho A}}\frac{1}{2E(T_0)}\frac{\partial E}{\partial T}\Delta T = f(T_0) + k_E(T_0)\Delta T \end{aligned} \tag{6}$$

where E is Young's modulus of the material, I. is moment of inertia, A is the cross-sectional area of the beam, ρ is the material density. Both change in Young's modulus and in geometry with temperature can cause drift in resonant frequency. The sensitivity to temperature is nearly -8 Hz/°C due to the change of Young's modulus with temperature and -0.1 Hz/°C for thermal expansion in geometry size. The temperature sensitivity caused by change of Young's modulus k_E is also relative to the geometry as:

$$k_E = k_E(L_0, w_0, h_0) + \frac{\beta^2}{2\pi L_0^2}\sqrt{\frac{E(T_0)I_0}{\rho A_0}}\frac{1}{2E(T_0)}\frac{\partial E}{\partial T}\left(-\frac{5}{2}\frac{\Delta L}{L_0} + \frac{1}{2}\frac{\Delta w}{w_0} + \frac{\Delta h}{h_0}\right) \tag{7}$$

According to Equation (7), the relative change in length of the resonator would make the most change to temperature sensitivity, and the relative change in thickness would make the least.

To get the characteristic of resonant frequency drift caused by temperature variations, a finite element multiphysics (FEM) simulation was taken with COMSOL (COMSOL Lnc., Stockholm, Sweden). Figure 2 shows the result of the simulation. Over the temperature from -40 °C to 80 °C, a linear approximation is fairly good over the range with a residual norm no more than 0.44841 Hz, corresponding to 0.018 ppm/°C, which is quite small.

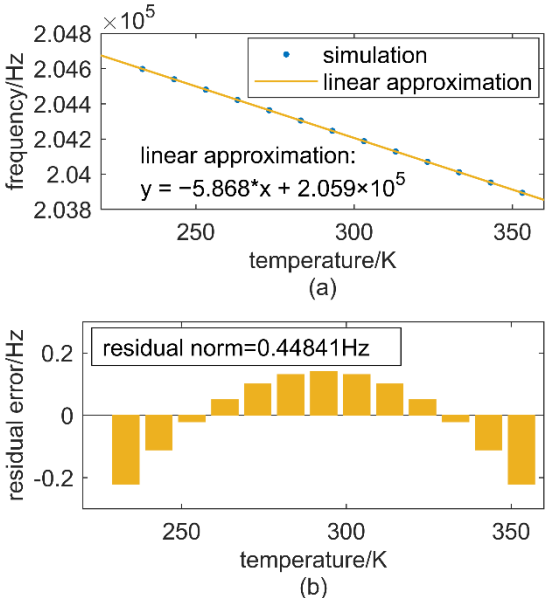

Figure 2. (**a**) frequency drift caused by Young's modulus and thermal expansion with temperature and linear approximation, (**b**) residual error between simulation and linear approximation.

3. Temperature Compensation

3.1. Temperature Model of Sensor and Method for Temperature Compensation

To improve the sensitivity to external acceleration of a MEMS resonant accelerometer, differential frequency output is often adopted, which has the opposite sensitivity to external acceleration, but the same direction sensitivity to temperature. The dependency of frequency on temperature has an approximately linear relationship for single crystalline

silicon in a large range as discussed before. So, the output frequency of the two differential outputs may be expressed as follows with considering of the impact of temperature in frequency drift of a MEMS resonant accelerometer based on differential output.

$$\begin{cases} f_1 = f_{10} + S_{F1}a + k_1 T \\ f_2 = f_{20} + S_{F2}a + k_2 T \end{cases} \tag{8}$$

$$S_{F1} > 0, S_{F2} < 0; k_1 < 0, k_2 < 0 \tag{9}$$

where f_1 and f_2 are the resonant frequency of the resonators respectively, S_{F1}, S_{F2} are the scale factors for the resonators to the external acceleration and k_1, k_2 are the temperature factors. The absolute value of scale factor S_{F1} and S_{F2} or temperature factor k_1 and k_2 are ideally equal to each other, but there may be some difference due to process deviation and other reasons. To implement temperature compensation, this work proposed a self-temperature compensation method called proportional difference without additional temperature sensor. The main idea of the promoted approach can be formulated as

$$df = f_1 - \alpha f_2 = f_b + (S_{F1} - \alpha S_{F2})a + (k_1 - \alpha k_2)T \tag{10}$$

$$\alpha = \frac{k_1}{k_2} \tag{11}$$

$$f_b = f_{10} - \alpha f_{20} \tag{12}$$

The impact on frequency drift caused by temperature can be cancelled by the proportional difference of the two resonators within an accelerometer. α is called as temperature difference-ratio in this paper, and it is always a positive value as k_1, k_2 have the same sign in an accelerometer, ensuring $S_{F1} - \alpha S_{F2}$ be nonzero for the fact that S_{F1} and S_{F2} have opposite signs to each other because of the opposite sensitivity to the external acceleration. Without considering temperature compensation, the two resonant frequencies are made different directly to achieve external acceleration. This conventional method is called direct difference in this paper in contrast with the proposed approach.

3.2. Calibration of Temperature Difference Ratio

With the linear model, a self-calibration of temperature difference-ratio is proposed. In a typical way, a set of output frequencies from both resonators at N different temperature are recorded and linear fittings between frequencies and temperature are made to get the parameter k_1, k_2 of the temperature model. In this process, a temperature chamber which can keep and monitor the temperature precisely as expected is necessary. Manual operation is required in most steps for the duration. This work proposed a simpler approach by calculating the temperature difference ratio directly using the least squares method instead of computing temperature factors of both resonators. For the zero-bias of the proposed approach of thermal compensation:

$$f_1(T)|_{a=0} = \alpha f_2(T)|_{a=0} + f_b \tag{13}$$

Because both α and f_b are independent of the value of temperature, a group of frequencies from the two resonators in different temperatures would be sufficient, which means much more convenience and simplicity in operation.

$$\begin{pmatrix} f_2(T_1)|_{a=0} & 1 \\ f_2(T_2)|_{a=0} & 1 \\ \vdots & \vdots \\ f_2(T_n)|_{a=0} & 1 \end{pmatrix} \times \begin{pmatrix} \alpha \\ f_b \end{pmatrix} = \begin{pmatrix} f_1(T_1)|_{a=0} \\ f_1(T_2)|_{a=0} \\ \vdots \\ f_1(T_n)|_{a=0} \end{pmatrix} \tag{14}$$

then

$$\begin{pmatrix} \alpha \\ f_b \end{pmatrix} = (A^T A)^{-1} A^T B \tag{15}$$

where

$$A = \begin{pmatrix} f_2(T_1)|_{a=0} & 1 \\ f_2(T_2)|_{a=0} & 1 \\ \vdots & \vdots \\ f_2(T_n)|_{a=0} & 1 \end{pmatrix}, B = \begin{pmatrix} f_1(T_1)|_{a=0} \\ f_1(T_2)|_{a=0} \\ \vdots \\ f_1(T_n)|_{a=0} \end{pmatrix} \quad (16)$$

With the proposed calibration method, equipment which can change temperature meets the need. No additional temperature sensor is required to measure the temperature, which means no error caused by temperature measurement error and thermal lags. In this paper, a procedure of recording frequencies from the two channels during a process of cooling down while keeping the external acceleration as zero is implemented to calculate α and f_b. Using the proposed approach, the process can be simplified as Figure 3b shows, where little manual operation is needed.

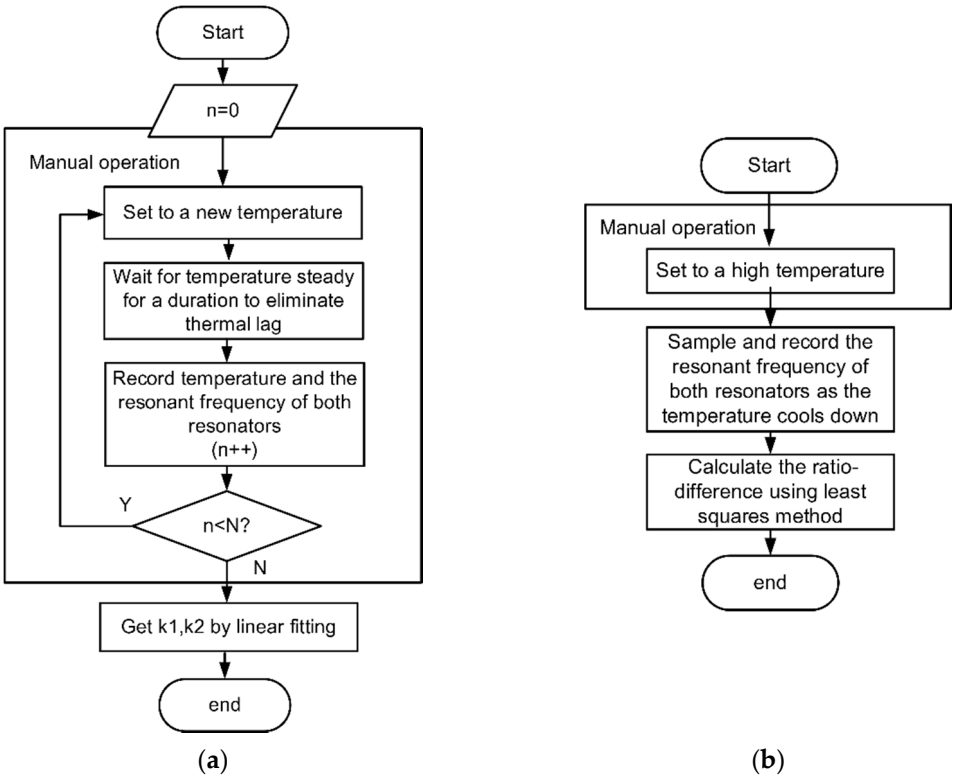

Figure 3. (**a**) Calibration of temperature factor. (**b**) Calibration of temperature difference ratio.

4. Experiments and Results

4.1. Experimental Setup

Each resonator is capacitively excited by an oscillator circuit. The photograph of driving circuit and accelerometer is shown in Figure 4a and the schematic of the circuit is shown in Figure 4b. A 10 V DC voltage is applied to provide bias, with a 5 mV AC voltage applied across the electrodes of the parallel-plate capacitor to generate actuating force, driving the resonator. TIA (Trans-Impedance Amplifier) converts the movement current to voltage as the input of the oscillation loop. An AGC is used in every oscillation loop to provide a stable amplitude of oscillation, aiming to reduce the phase noise and limit the loop gain [27].

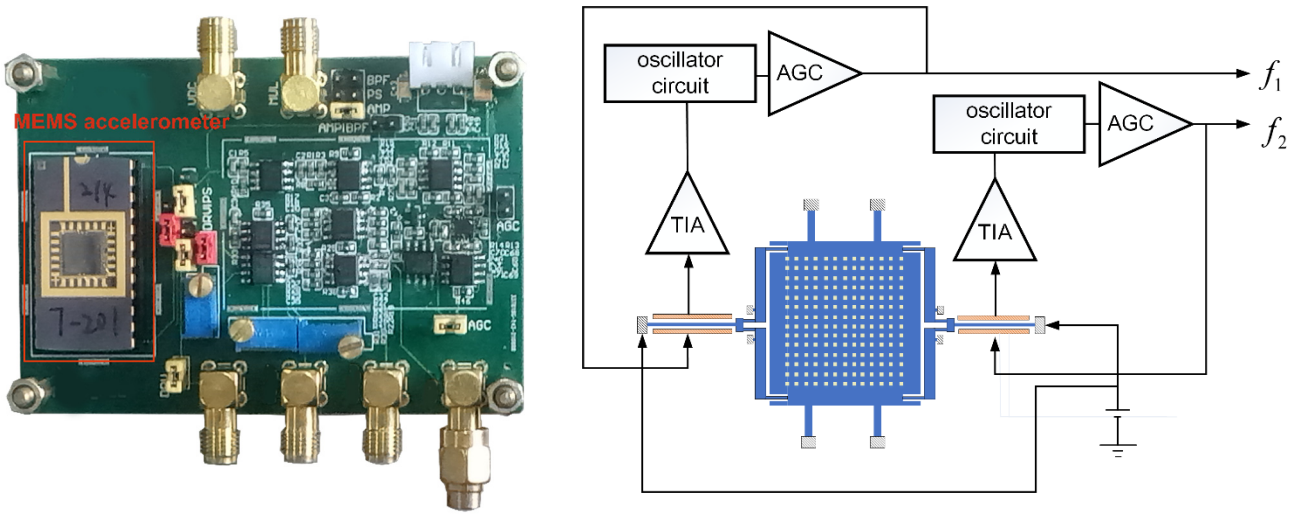

(**a**) (**b**)

Figure 4. (**a**) Photograph of driving circuit PCB (Printed Circuit Board) and packaged accelerometer. (**b**) Schematic of driving circuit.

The device consisting of accelerometer and driving circuit was placed in the temperature chamber with a thermometer monitoring the temperature. A DC (Direct Current) power source was used to supply power for the device and two frequency counters (Keysight 53230A, Keysight Technologies, Santa Rosa, CA, USA) were used to measure the oscillating frequencies from the two differential resonators. The test platform and temperature chamber are shown in Figure 5a,b, respectively.

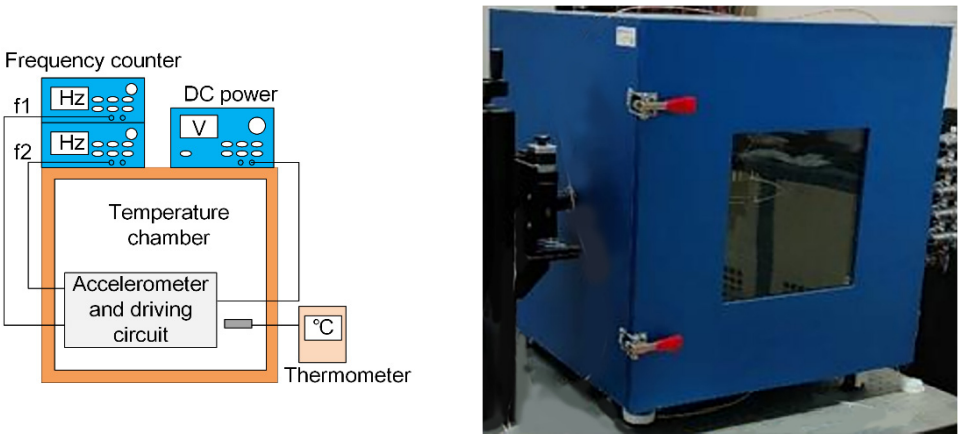

(**a**) (**b**)

Figure 5. (**a**) The platform for temperature test. (**b**) Temperature chamber.

4.2. Results and Discussion

To prove the proposed approach of calibration, an experiment of getting temperature factor k_1, k_2 and calculating temperature difference ratio by k_1/k_2 was performed as well. The accelerometer was put in the temperature chamber, −10 °C to 70 °C with a 10 °C step is set, and the frequency of the two resonators is recorded after two hours, when the temperature becomes steady, to eliminate the thermal lag.

Then a linear fitting between frequency with temperature is made for each resonator, as shown in Figure 6a,b. Results show that f_1 has a sensitivity of −8.777 Hz/K and f_2 is −7.615 Hz/K.

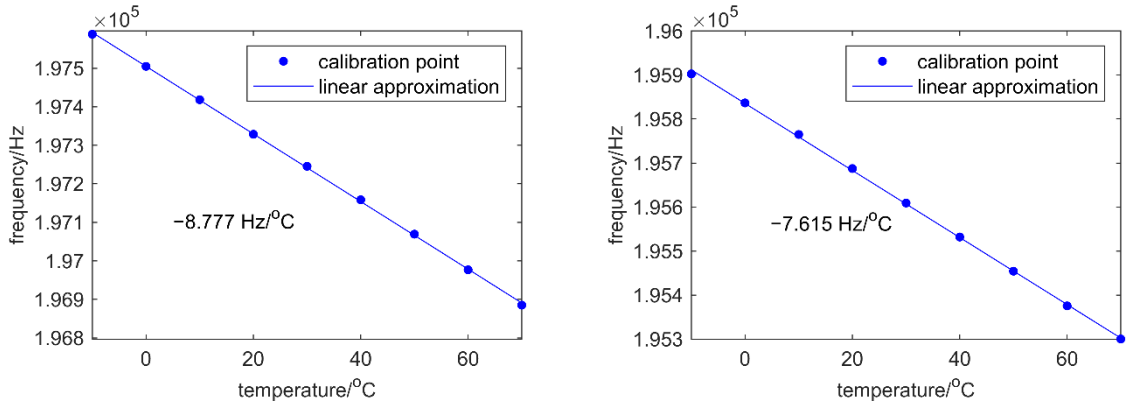

Figure 6. (**a**) Calibration of temperature factor for resonator 1. (**b**) Calibration of temperature factor for resonator 2.

Then, an experiment of dynamic temperature ramp down has been performed and the temperature difference ratio is calculated by proposed approach of calibration. After the temperature reached to 70 °C, the target temperature was set to −10 °C. The output frequency of both resonators was sampled at an interval of 50 ms and recorded as the temperature dropped down. The temperature difference ratio was calculated using the recorded frequencies from both resonators. The results of temperature difference ratio calculated by the two methods are summarized in Table 2. The proposed approach is proved to be effective according to the result by calculating with k_1/k_2.

Table 2. Calculated temperature difference ratio through the two method.

	Temperature Factor 1	**Temperature Factor 2**	**Temperature Difference Ratio**
k_1/k_2	−8.777	−7.615	0.867
proposed	~	~	0.878

To verify the approach of temperature compensation, another temperature ramp down experiment was taken. In the experiment, the temperature difference-ratio calculated by the proposed approach was used for compensation. The temperature is set to 70 °C for a duration of 2 h. Then target temperature of the chamber was set as −10 °C, making temperature cool down to −10 °C in about 6 h. The frequencies, measured by Keysight 53230A, of the two output signals were recorded at a time interval of 50 ms for the duration, and the proportional difference proposed and direct difference were implemented with the output frequencies, respectively. In Figure 6, resonator 1 and resonator 2 showed 43.16 ppm/°C and 38.48 ppm/°C drift without any temperature compensation, respectively. A comparison between direct difference and proportional difference proposed is also shown in Figure 7. The direct difference can reduce the drift to 5.26 ppm/°C as it can offset a part of side effects in frequency drift caused by temperature change, while the proposed proportional difference can cancel out the impact of temperature the most and reduce the drift to 0.83 ppm/°C. Proportional difference performs much better than direct difference because proportional difference copes with the differential outputs while considering the effect of temperature and the fact that there may be differences of sensitivity to temperature between the two resonators.

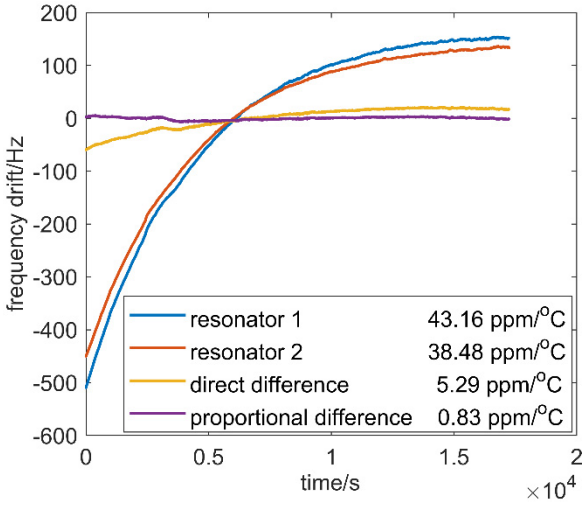

Figure 7. Frequency drift in different cases.

Allan deviation anaysis is shown in Figure 8. with proportional difference implemented. The long-term noise, which is mainly caused by the change of temperature, is reduced the most. Compared with the frequency of a single resonator without any temperature compensation, the two kinds of differential methods perform evidently better at the start of about 10 s. The differential ouputs reduce the frequency drift caused by temperature changes. Within time more than 100 s, the proportional difference evidently reduces the noise in contrast to direct difference as proportional difference can cancel out frequency drift to the greatest extent. As temperature changes over a large range for a long time, the proportional difference performed the best by achieving the least drift.

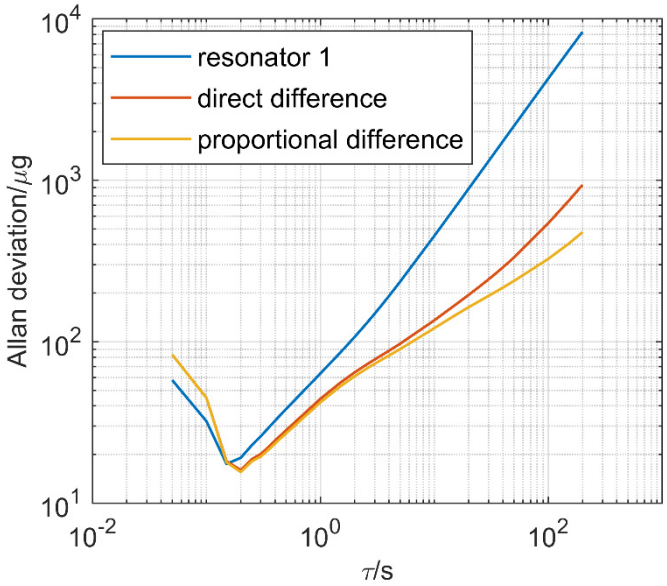

Figure 8. Measured Allan deviation during the temperature ramp down.

5. Conclusions and Future Work

This article proposed an improved temperature compensation approach called proportional difference for accelerometers based on differential frequency modulation. A parameter named temperature difference ratio is used to cancelled the drift in the frequency of the differential resonators caused by temperature. A method using the least squares method is promoted to calculate the temperature difference ratio instead of measuring the temperature factor of each resonator, which is simpler and is proved to be effective. The approach of temperature compensation called proportional difference performs better than direct difference, which is usually used in accelerometers based on differential frequency

modulation without considering the thermal impact, especially if there is a large difference in sensitivity to temperature of both resonators. The nonlinearity between temperature and bias drift over a large temperature range limits the performance of our approach. This may be improved in future work by making an optimization design on MEMS accelerometer and adding an oven controller which can tune the temperature in a small range.

Author Contributions: Conceptualization, X.Z.; data curation, P.C.; formal analysis, K.W.; investigation, J.W.; methodology, P.C.; resources, X.Z.; supervision, X.Z.; validation, P.C.; writing—original draft, P.C.; writing—review and editing, X.X. All authors have read and agreed to the published version of the manuscript.

Funding: This research was funded by the National Key Research and Development Program of China, grant No. 2018YFB2002300.

Acknowledgments: The authors would like to thank Zheng Wang for his efforts with the sensors and Yunfei Liu for his assistance with the mathematical analysis. Thanks to everyone who helped us in our work.

Conflicts of Interest: The authors declare no conflict of interest.

References

1. Judy, M.W. Evolution of Integrated Inertial Mems Technology. In Proceedings of the 2004 Solid-State, Actuators, and Microsystems Workshop, Hilton Head Island, SC, USA, 6–10 June 2004.
2. Marek, J. MEMS for automotive and consumer electronics. In Proceedings of the 2010 IEEE International Solid-State Circuits Conference—(ISSCC), Bucharest, Romania, 16–20 September 2010.
3. Weinberg, M.S.; Bernstein, J.; Borenstein, J.T.; Campbell, J.; Sohn, J.B. Micromachining inertial instruments. In Proceedings of the SPIE—The International Society for Optical Engineering, Austin, TX, USA, 23 September 1996.
4. Hopkins, R.; Miola, J.; Setterlund, R. The silicon oscillating accelerometer: A high-performance MEMS accelerometer for precision navigation and strategic guidance applications. In Proceedings of the 2005 National Technical Meeting of The Institute of Navigation, San Diego, CA, USA, 24–26 January 2006.
5. Zou, X.; Thiruvenkatanathan, P.; Seshia, A.A. Micro-electro-mechanical resonant tilt sensor. In Proceedings of the IEEE International Frequency Control Symposium, Baltimore, MD, USA, 21–24 May 2012.
6. Zwahlen, P.; Nguyen, A.M.; Dong, Y.; Rudolf, F.; Schmid, H. Navigation grade MEMS accelerometer. In Proceedings of the IEEE International Conference on Micro Electro Mechanical Systems, Hong Kong, China, 24–28 January 2010.
7. Shan, X.; Zou, T.; Forbes, J.R.; Angeles, J. Design Specifications for Biaxial Navigation-Grade MEMS Accelerometers. In Proceedings of the ASME International Mechanical Engineering Congress and Exposition, Montreal, QC, Canada, 14–20 November 2014.
8. Zhao, C.; Pandit, M.; Sobreviela, G.; Steinmann, P.; Mustafazade, A.; Zou, X.; Seshia, A. JMEMS Letters A Resonant MEMS Accelerometer With 56ng Bias Stability and 98ng/Hz1/2 Noise Floor. *J. Microelectromech. Syst.* **2019**, *28*, 324–326. [CrossRef]
9. Rao, K.; Liu, H.; Wei, X.; Wu, W.; Tu, L.C. A High-resolution Area-change-based Capacitive MEMS Accelerometer for Tilt Sensing. In Proceedings of the 2020 IEEE International Symposium on Inertial Sensors and Systems (INERTIAL), Hiroshima, Japan, 23–26 March 2020.
10. Comi, C.; Corigliano, A.; Langfelder, G.; Longoni, A.; Tocchio, A.; Simoni, B. A Resonant Microaccelerometer With High Sensitivity Operating in an Oscillating Circuit. *J. Microelectromech. Syst.* **2010**, *19*, 1140–1152. [CrossRef]
11. Seshia, A.A.; Palaniapan, M.; Roessig, T.A.; Howe, R.T.; Montague, S. A vacuum packaged surface micromachined resonant accelerometer. *J. Microelectromech. Syst.* **2003**, *11*, 784–793. [CrossRef]
12. Omura, Y.; Nonomura, Y.; Tabata, O. New resonant accelerometer based on rigidity change. In Proceedings of the International Conference on Solid State Sensors & Actuators, Chicago, IL, USA, 19 June 1999.
13. Seo, Y.H.; Cho, Y.-H. Design, fabrication, static test and uncertainty analysis of a resonant microaccelerometer. *Sens. Mater.* **2002**, *14*, 91–108.
14. Wang, Y.; Zhang, J.; Yao, Z.; Lin, C.; Tong, Z.; Su, Y.; Zhao, J. A MEMS Resonant Accelerometer With High Performance of Temperature Based on Electrostatic Spring Softening and Continuous Ring-Down Technique. *IEEE Sens. J.* **2018**, *18*, 7023–7031. [CrossRef]
15. Meldrum, M.A. Application of vibrating beam technology to digital acceleration measurement. *Sens. Actuators A Phys.* **1990**, *21*, 377–380. [CrossRef]
16. Liu, G.J.; Jiang, T.; Jiang, Q.K.; Wang, A.L. Characterization of a MEMS Accelerometer Considering Environmental Temperature Fluctuations. *Mater. Sci. Forum* **2011**, *697–698*, 801–804. [CrossRef]
17. Watanabe, H.; Yamada, N.; Okaji, M. Linear Thermal Expansion Coefficient of Silicon from 293 to 1000 K. *Int. J. Thermophys.* **2004**, *25*, 221–236. [CrossRef]
18. Yang, D.; Woo, J.K.; Lee, S.; Mitchell, J.; Challoner, A.D.; Najafi, K. A Micro Oven-Control System for Inertial Sensors. *J. Microelectromech. Syst.* **2017**, *26*, 507–518. [CrossRef]

19. Kwon, H.K.; Ortiz, L.C.; Vukasin, G.D.; Chen, Y.; Kenny, T.W. An Oven-Controlled MEMS Oscillator (OCMO) With Sub 10mw, ± 1.5 PPB Stability Over Temperature. In Proceedings of the 2019 20th International Conference on Solid-State Sensors, Actuators and Microsystems & Eurosensors XXXIII (TRANSDUCERS & EUROSENSORS XXXIII), Berlin, Germany, 23–27 June 2019.
20. Xu, C.; Segovia-Fernandez, J.; Kim, H.J.; Piazza, G. Temperature-Stable Piezoelectric MEMS Resonators Using Integrated Ovens and Simple Resistive Feedback Circuits. *J. Microelectromech. Syst.* **2017**, *26*, 187–195. [CrossRef]
21. Salvia, J.C.; Melamud, R.; Chandorkar, S.A.; Lord, S.F.; Kenny, T.W. Real-Time Temperature Compensation of MEMS Oscillators Using an Integrated Micro-Oven and a Phase-Locked Loop. *J. Microelectromech. Syst.* **2010**, *19*, 192–201. [CrossRef]
22. Li, B.; Li, C.; Zhao, Y.; Han, C.; Zhang, Q. An integrated packaged resonant accelerometer with temperature compensation. *Rev. Sci. Instrum.* **2020**, *91*, 105004. [CrossRef] [PubMed]
23. Chiang, C.; Graham, A.B.; Lee, B.J.; Ahn, C.H.; Kenny, T.W. Resonant pressure sensor with on-chip temperature and strain sensors for error correction. In Proceedings of the 2013 IEEE 26th International Conference on Micro Electro Mechanical Systems (MEMS), Taipei, Taiwan, 20–24 January 2013.
24. Lee, J.; Rhim, J. Temperature compensation method for the resonant frequency of a differential vibrating accelerometer using electrostatic stiffness control. *J. Micromech. Microeng.* **2012**, *22*, 95016–95026+95011. [CrossRef]
25. Behbahani, A.H.; Kim, D.; Stupar, P.; Denatale, J.; M'Closkey, R.T. Tailored Etch Profiles for Wafer-Level Frequency Tuning of Axisymmetric Resonators. *J. Microelectromech. Syst.* **2017**, *26*, 333–343. [CrossRef]
26. Ge, H.H.; Behbahani, A.H.; Closkey, R.T.M. MEMS gyro drift compensation using multiple rate measurements derived from a single resonator. In Proceedings of the 2018 IEEE/ION Position, Location and Navigation Symposium (PLANS), Monterey, CA, USA, 23–26 April 2018; pp. 288–293.
27. Lee, S.; Nguyen, T.C. Influence of automatic level control on micromechanical resonator oscillator phase noise. In *Frequency Control Symposium and PDA Exhibition Jointly with the 17th European Frequency and Time Forum, 2003, Proceedings of the 2003 IEEE International, Tampa, FL, USA, 4–8 May 2003*; IEEE: Tampa, FL, USA, 2003.

micromachines

Review

Research Progress of MEMS Inertial Switches

Min Liu †, Xinyang Wu †, Yanxu Niu, Haotian Yang, Yingmin Zhu and Weidong Wang *

School of Mechano-Electronic Engineering, Xidian University, Xi'an 710071, China; mliu_12@stu.xidian.edu.cn (M.L.); wuxinyang_1999@163.com (X.W.); nikx_1999@163.com (Y.N.); 17040210008@stu.xidian.edu.cn (H.Y.); ymzhu@xidian.edu.cn (Y.Z.)

* Correspondence: wangwd@mail.xidian.edu.cn

† These authors contributed equally to this work.

Abstract: As a typical type of MEMS acceleration sensor, the inertial switch can alter its on-off state while the environmental accelerations satisfy threshold value. An exhaustive summary of the design concept, performance aspects, and fabrication methods of the micro electromechanical system (MEMS) inertial switch is provided. Different MEMS inertial switch studies were reviewed that emphasized acceleration directional and threshold sensitivity, contact characteristics, and their superiorities and disadvantages. Furthermore, the specific fabrication methods offer an applicability reference for the preparation process for the designed inertial switch, including non-silicon surface micromachining technology, standard silicon micromachining technology, and the special fabrication method for the liquid inertial switch. At the end, the main conclusions of the current challenges and prospects about MEMS inertial switches are drawn to assist with the development of research in the field of future engineering applications.

Keywords: MEMS; inertial switch; threshold acceleration; sensitive direction; contact effect; fabrication

Citation: Liu, M.; Wu, X.; Niu, Y.; Yang, H.; Zhu, Y.; Wang, W. Research Progress of MEMS Inertial Switches. *Micromachines* **2022**, *13*, 359. https://doi.org/10.3390/mi13030359

Academic Editor: Eui-Hyeok Yang

Received: 30 December 2021
Accepted: 19 February 2022
Published: 24 February 2022

1. Introduction

Inertial switches are more and more widely used in automotive electronics, inertial navigation, and weapon equipment products [1–6]. They can be nested in wearable systems, transport devices for monitoring health, maintenance needs, and transportation of special goods [2,7–9]. As the rapid expansion of the Internet of Things (IoT) [10] and the requirements of the application environment increase, the research interest in MEMS inertial switches is growing [9,11,12]. Compared to piezoelectric microswitches, electrostatic microswitches, and accelerometers, inertial MEMS switches have some distinctive characteristics, such as less power consumption, a simple structure, and an interface circuit, which can maintain strong durability in environments with inconvenient power supply. However, accelerometers always consume a certain amount of power even without an external excitation [13–15]. The main disadvantages of electrostatic and piezoelectric microswitches are their high drive voltage and low reliability [16–18]. An inertial MEMS switch combines sensing and actuation. When sufficient acceleration is sensed, the movable electrode contacts the fixed electrode and the external circuit is triggered [19]. This kind of switch with only acceleration excitation is also superior to electrostatic and piezoelectric accelerometers because they avoid electromagnetic interference in applications [3].

Based on the state of the inertial switch "on" after the acceleration excitation is removed, inertial microswitches have been classified into two categories: the intermittent switch and the persistent switch. The intermittent switch refers to the switch resuming the initial disconnected condition after the acceleration dissipates, and the persistent switch means that the switch performs a keep-closed function after the acceleration is evacuated. The most obvious feature of the intermittent switch is that the switch does not have self-blocking capability. Intermittent inertial switches work on the principle that

the movable electrode (mainly a suspended mass) comes into contact with a fixed electrode when the acceleration reaches its threshold. The model of a spring–mass system is shown in Figure 1 [1,11,20]. Here, the intermittent inertial switches are mainly classified and discussed by means of the different properties containing the following three groups: directional switches, various acceleration threshold switches, and contact enhanced switches. For the persistent inertial switch, the realization of the locking function is carried out by various structures, so the classification is mainly dependent on the feature structures. These switches are embodied in three aspects, including latching switches [8,21,22], bistable switches [23–26], and microfluidic switches [27–31]. Persistent switches have an excellent contact effect due to special structural features or external auxiliary units.

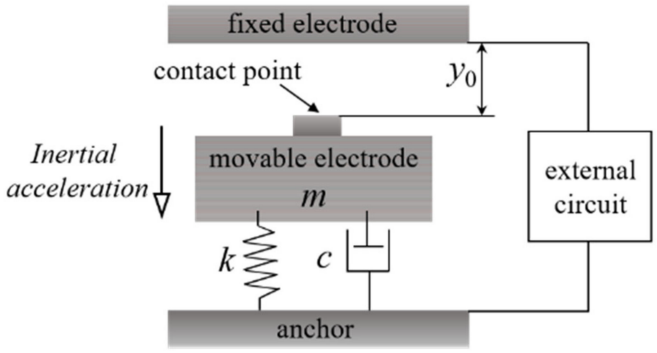

Figure 1. Schematic diagram of the spring (k)–mass (movable electrode m)-damping (c) system model of a uniaxial inertial switch. y_0 means the initial distance between the movable electrode and the fixed electrode.

2. Intermittent Inertial Switches

2.1. Sensitive Direction

Axial sensitivity has always been an important research topic for MEMS inertial devices. In the actual working environment, the inertial switch is inevitably impacted in different directions. For the inertial switch, it is important to prevent spurious triggering from shocking interference in non-sensitive directions. Therefore, reducing the disturbances and improving the sensitivity of the working axis of the device have attracted the attention of many researchers. MEMS inertial switch studies with different direction sensitivity are summarized in the following sections.

2.1.1. Uniaxial Inertial Switches

A uniaxial sensitivity inertia switch has only one sensing direction. The main structure of a uniaxial inertial switch is a well-known spring–mass damper system. Consider the vibration model of a traditional single-degree-of-freedom switch system (Figure 1) under acceleration (a) excitation. The dynamic equilibrium model of the MEMS inertial switch can be described with Equation (1).

$$m\ddot{y} + c\dot{y} + ky = ma \tag{1}$$

where m, y, c, and k represent the weight and the displacement of the proof mass, the squeeze film damping coefficient, and the stiffness of the spring beam, respectively.

When the inertial switch senses an acceleration (i.e., equal to or at more than the threshold level) in the sensitive direction, the movable electrode overcomes the damping force and moves along the sensitive direction. When the movement displacement is greater than the initial gap y_0, the movable electrode contacts the fixed electrode and the inertial switch is turned on. When the acceleration signal is removed, the movable electrode is pulled back under the action of elastic force, which finally returns to its initial position.

At present, a variety of single-axis inertial switches have been reported. For a uniaxial sensitive inertial switch, it is necessary to increase the structural stiffness in the insensitive

directions, as then the device is less susceptible to disturbance from off-axis or rotational accelerations. In order to obtain a lower off-axis sensitivity inertial switch, the key method is designing a symmetrical structure for the proof mass, or using the constrained structure to limit the off-axis movement of the action unit.

Yang et al. [32] designed a vertically driven MEMS inertial switch. The switch consisted of the proof mass as the movable electrode and two compliant bridge beams as the fixed electrode. The proof mass was suspended by two conjoined serpentine springs. However, the first two frequencies of this kind of device by modal analysis are discussed in the subsequent study [33]. It was seen that the first and the second frequencies were very close, which indicates that the cross-coupling effect of the microswitch was very obvious. They improved the previous design of the fixed electrode in order to prolong the contact time of the switch. A new bridge-type fixed electrode was applied, but this design limited where the suspension springs of the mass could be placed, resulting in the suspension springs only being arranged on both sides of the head and tail of the mass. This design of the fixed electrode made the switch affect the off-axis accelerations easily. Therefore, they redesigned the switch, designed the device structure as a centrally symmetric structure, and changed the fixed electrode from two bridge beams to a cross beam to reduce off-axis sensitivity [34], as well as improve the fixed electrode overload capability. The ratio of the second-order and first-order frequencies of the simulation increased from 1.04 to 5.21, indicating that the off-axis sensitivity of the redesigned device was largely reduced. The threshold acceleration of the redesigned MEMS inertial switch was 70 g and the tested turn-on response time was 30 μs.

Wang et al. [7] designed a novel horizontally driven inertia microswitch with an elastic cantilever as the fixed electrode. By minimizing the clearance, the reverse-resist block worked well to reduced rebound force and enhance the contact time to 230 μs. The unique design of the sensitive mass improved the overall stability and reliability of the switch. Zhang et al. [35] proposed a laterally-driven MEMS inertial switch. The multi-directional tightly constrained structural design effectively reduced off-axis sensitivity and improved impact resistance. The constrainting plate with holes above the sensitive mass limited the radom motion of the proof mass and reduced the off-axis sensitivity of the inertial microswitch. In order to avoid rotation, in the new design of the inertia switch a symmetrically distributed double-layer serpentine spring beam was introduced [36]. When the inertial switch was impacted in the sensitive direction, there was no collision between the sensitive mass and the constraining structure, which improved the uniaxial sensitivity.

As mentioned above, many uniaxial inertial switches are constructed from a proof mass suspended by springs. Some schematic illustrations of these are displayed in Figure 2. Their vibration models are described in Equation (1). When these systems act as shock switches, according to the S.R.S., for the pulse time of acceleration, reliability is a serious problem. These traditional single-mass inertial switches may misoperate at shock levels less than the threshold, resulting in reduced switch reliability. Fathalilou et al. [37] proposed a dual-mass MEMS shock switch. An auxiliary mass spring was attached to the main mechanism of the switch, and the safety performance of the sensor under shocks below the threshold was improved by adjusting the auxiliary system. In addition, Ren et al. [38] proposed a self-powered MEMS inertial switch for a potential wake-up application without additional power consumption. When the switching device sensed a small vibration acceleration, the suspended mass vibrated continuously at the equilibrium position. During the movement of the movable mass, the capacitance of the parallel plates also changed, causing induced charge transfer. At this time, the alternating current of the device was converted into direct current, which could be stored in an energy storage device using a self-charging unit. Once an exceeding threshold acceleration was sensed, the movable electrode contacts the fixed electrode and carried out the circuit conduction. Then the charges stored in the energy storage device were released. When this device was impacted by an acceleration of 40 g, it generated a pulse signal.

Switches used in extreme acceleration environments (such as ballistic rockets) need to withstand accelerations of up to 100,000 g and operate with high fidelity at a low impact of 100 to 10,000 g. Raghunathan et al. [39] presented a novel MEMS low-g switch with serpentine flexures based on single-crystal silicon, which could withstand high load shocks 200 times the trigger load. The switch was capable of responding at low acceleration (60–131 g) and withstanding a high-g impact shock acceleration load of 24,000 g.

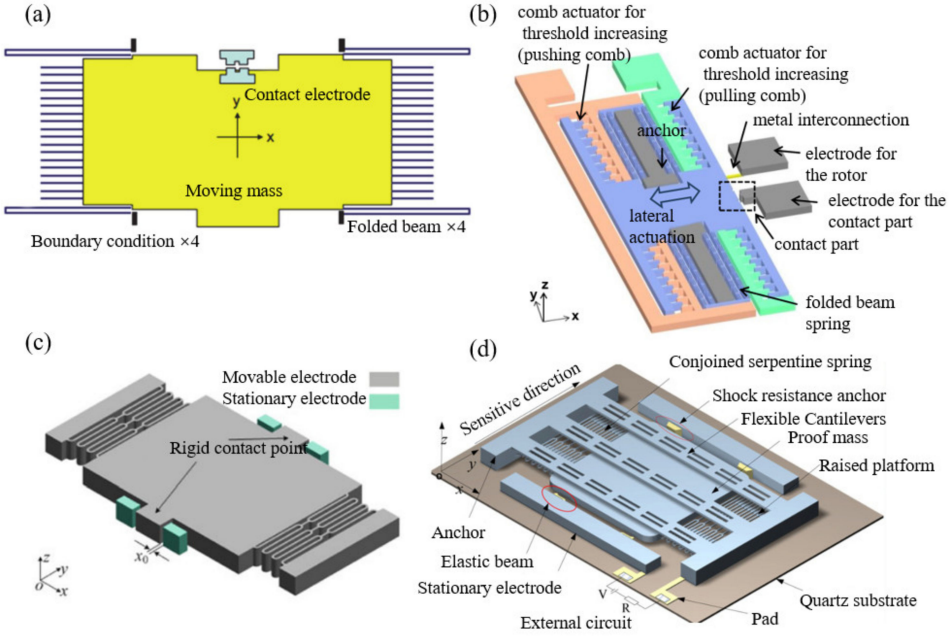

Figure 2. Some uniaxial inertial switches: (**a**) [40], (**b**) [12], (**c**) [41], (**d**) [42].

2.1.2. Biaxial Inertial Switches

An inertial switch with biaxial sensitivity means that it can operate in two axes. There are two main methods to achieve biaxial directional sensitivity for the switch. One of the ways is to assemble two single-axial switches into one chip, and the new switch can realize biaxial sensitivity in a plane [43]. Although the direct assembly of single-axis switches improves the directional sensitivity, it also has some problems and defects, including assembly errors [44], excessive bulk [45], packaging difficulty [46], and high manufacturing costs [45]. Another method is to utilize multiple springs to support the mass, and the fixed electrode is placed around the mass in multiple directions to achieve biaxial sensitivity. That layout allows a more uniform distribution of the stiffness of the mass–spring system in all directions. Greywall et al. [47] claimed patents for two biaxial inertial switch designs. Both designs had a circular proof mass suspended by springs, but varied in the fact that the fixed electrodes were outer and inner. Lin et al. [48] presented another design of a two-axis low-g acceleration threshold switch. The switch utilized buffer springs connected to the proof mass and contacted the fixed electrode, which would reduce the bounce of the switch when the shock exceeded the acceleration threshold, thereby prolonging the contact time of the switch, as illustrated in Figure 3. Niyazi et al. [49] designed a novel bidirectional multi-threshold mems inertia switch capable of acceleration-based actuation of separate circuits. The design implemented a spring-suspended mass with fixed electrodes positioned in the sensitive direction, consuming no power in the stationary state. The acceleration thresholds were 69 g and 121 g. Xu et al. [50] fabricated a dual-axis MEMS shock sensor that could be triggered in each direction in a single plane. The device consisted of a movable electrode, which was a proof mass suspended by four serpentine springs, and three cantilever beams forming the first, second, and third stationary electrodes. The switch could sense an acceleration range of 800–2600 g.

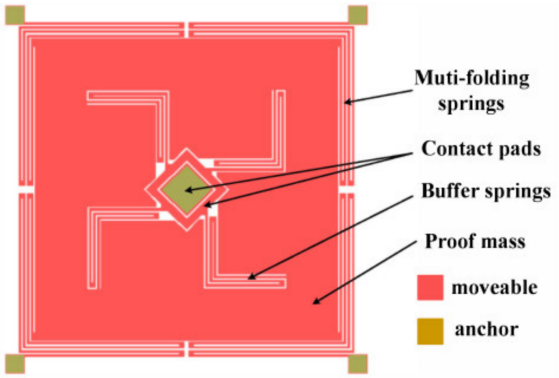

Figure 3. Schematic of the two-axis low-g inertial switch.

2.1.3. Triaxial Inertial Switches

A triaxial inertial switch can sense an acceleration signal in the x, y, and z axes, which usually includes the proof mass and three pairs of fixed electrodes in the orthogonal sensitive directions. Chen et al. [2] introduced an all-metal contact-enhanced triaxial inertial microswitch with low axial disturbance, which consisted of a proof mass as the movable electrode, and the fixed electrode of the switch in the horizontal and vertical directions composed of two L-shaped flexible cantilever beams and a multi-hole crossbeam. The acceleration threshold in the horizontal direction was 255 g and the contact time was 60 μs, whereas in the vertical direction, the threshold acceleration was 75 g with a contact time of 80 μs. Currano et al. [51] designed a triaxial MEMS inertial switch using a single mass–spring assembly. The device consisted of an annular mass and a centrally clamped suspension composed of four spiral springs. The spiral spring was used to realize compliance in all directions. The switch had an acceleration threshold range between 50 g and 250 g.

2.1.4. Multidirectional/Omnidirectional Inertial Switches

Omni-directional switches can sense a shock signal in all the radial directions of a hemisphere. For the actual engineering environment, the acceleration excitation may come from any direction. If a single-axis or dual-axis switch is simply combined to monitor multi-directional acceleration, it is easy to cause installation errors and centroid deviations, affecting the reliability of test results. Besides, the fabrication cost of the switch increases. Therefore, it is of great practical significance to develop triaxial or omnidirectional inertia switches. Such switches have been widely applied in the field of military weapons. Inertia switches are often used in automotive airbags and vibration monitoring fields.

Xi et al. [19] presented a novel MEMS omnidirectional inertial switch consisting of a proof mass and an axial and four radial flexible electrodes to form a dual mass–spring system. The switch had omnidirectional sensitivities in a half sphere. The switch could sense an acceleration range from 380 g to 500 g. Liu et al. [52] presented a MEMS-based low-g inertial switch that consisted of an annular proof mass suspended by a helix spring. The helix spring could sense a weak signal. The acceleration threshold was 20 g. Yang et al. [53] designed a multidirectional-sensitive inertial microswitch with an electrophoretic flexible composite fixed electrode to enhance the contact effect. The contact time of the switch was prolonged because the new vertical composite fixed electrode was capable of reducing the stiffness, and the threshold was around 70 g, which was uniform in different sensitive directions. The fully axisymmetric serpentine spring was used to support the sensitive mass to sense any radial acceleration in the *xoy* plane. The T-shaped cantilever with a maple leaf shape on the top was used as a vertical fixed electrode, which could monitor the acceleration of the *z*-axis. Du et al. [54] studied a low-g omnidirectional microswitch via non-silicon surface micromachining technology, and the distribution of the threshold acceleration was uniform. The device consisted of combination of an annular-shaped

proof mass and supporting Archimedes spiral springs as the moving electrode and static electrode located in the center of the ring. The structural sketch of the proposed inertial switch is shown in Figure 4. The threshold acceleration of the switch dropped to 38 g. Moreover, they improved the design, redesigning the structure of the central springs [55]. The switch adopted an S-type flexible connection that could reduce the stiffness of the electrode to extend the contact time of the switch. The dynamic threshold of the switch was 7.9 g to 11.3 g, and the response time in each direction was less than 2 ms. Chen et al. [56] designed an omnidirectional inertial switch with a rectangular spring. The omnidirectional switching system's stability was reinforced, due to the design of rectangular springs. The threshold acceleration of the designed inertial switch was about 58 g in the x direction and 37 g in the z direction, and the contact time was about 18 µs. A summary of some examples of typical sensitive direction inertial switch performance is shown in Table 1.

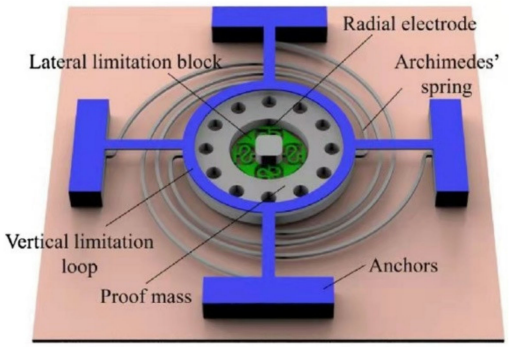

Figure 4. Structural sketch of the omnidirectional inertial switch.

Table 1. A summary of some examples of typical sensitive direction inertial switch performance.

Sensitive Direction	References	Material	Acceleration Threshold	Contact Time	Special Design and Function	Application
Uniaxial	Wang et al. [5]	Ni	180 g	1050 µs	Compliant cantilever fixed electrode to contact enhancement	—
	Wang et al. [7]	Ni	38 g	230 µs	Elastic fixed electrode	Safety airbags
	Kim et al. [12]	Si	2.0–17.25 g	—	—	Environments and applications require accurate threshold
	Yang et al. [32]	Ni	100 g	12 µs	Bridge-type elastic beams to enhance contact time	—
	Cai et al. [34]	Ni	70 g	30 µs	Stationary electrode changed from two bridge-type beams to one cross beam to reduce the off-axis sensitivity.	—
	Zhang et al. [35]	Ni	165 g	35 µs	Double-stair shape cantilever beam	Internet of Things (IoT) system to remote detection of vibration shock
	Yang et al. [36]	Ni	272 g	20 µs	Double-layer suspended springs for improving single-axis sensitivity	IoT system

Table 1. *Cont.*

Sensitive Direction	References	Material	Acceleration Threshold	Contact Time	Special Design and Function	Application
	Fathalilou et al. [37]	—	154 g	—	A dual-mass switch with auxiliary mass spring	Automobile, medicine, and aerospace
	Ren et al. [38]	Ni	40 g	80 μs	Self-powered	Vibration energy harvester (VEH) and potential wake-up application
	Raghunathan et al. [39]	SOI	60–131 g	—	Surviving acceleration loads 200 times greater than its designed trigger load	Ballistic rockets
	Chen et al. [42]	Ni	297 g	80 μs	Compliant cantilever beam	Automotive safety crash airbags
Biaxial	Lin et al. [48]	Si	60 g	—	Buffering springs to extend the contact time	—
	Niyazi et al. [49]	Si	69 g and 121 g	—	Separate digital outputs for each threshold	Active suspension systems
	Xu et al. [50]	Si	800–2600 g	—	High-resolution digital quantitative acceleration measurements	IoT system
Triaxial	Chen et al. [2]	Ni	255–260 g (+x and +y axis) ~75 g (+z axis)	~60 μs (+x and +y axis) ~80 μs (+z axis)	Flexible fixed electrode can prolong the contact time and eliminate the rebound	IoT system
	Currano et al. [51]	Si	50–250 g	255 μs	Compliance in all axes identical	Early warning for traumatic brain injury (TBI)
Omnidirectional	Xi et al [19]	Ni	450 g	60 μs	A dual mass–spring system	—
	Liu et al. [52]	Si	20 g	—	The response time of 0.46 ms is short enough	—
	Du et al. [54]	Ni	35–40 g	~100 μs	Electrode with a spherical contact surface	Automotive airbags
	Du et al. [55]	Ni	7.9–11.3 g	>300 μs (XOY plane) >230 μs (axial)	Method of "thickness compensation" to control threshold accuracy	Wearable systems and airbags
	Chen et al. [56]	Ni	58 g x direction 37 g z direction	18 μs	Rectangular spring to reinforce switching system's stability	Transport of special goods and drop detection
Multidirectional	Yang et al. [53]	Ni	70 g	110 μs	Polymer–metal composite fixed electrode	—

2.2. Threshold Acceleration

2.2.1. Low-g Threshold Inertial Switches

MEMS inertial switches sensing a low-g threshold acceleration can find representative application in ISDs (ignition safety devices), consumer electronics, and automotive and aerospace domains.

Chen et al. [57] designed a nickel low-g MEMS inertial switch with horizontal sensitivity, as shown in Figure 5a. The forward novel L-shaped elastic cantilever beams were used as the fixed electrode. The threshold acceleration was about 18 g, with the contact time of the switch around 216 µs. However, switches made of metal are not suitable for missile equipment with operating temperatures between −51 °C and 75 °C. Deformation due to thermal expansion of the metal would significantly change the acceleration threshold. When the inertia switch is used in the aerospace field, mainly in the climb and descent stages of an airplane, the requirement of the acceleration threshold is less than 30 g. Xiong et al. [58] designed a silicon-based low-g MEMS inertial switch with an acceleration threshold of 7.4 g, as shown in Figure 5b. The structure of the device was mainly composed of a large-volume mass block and a low-stiffness coil spring. Rectangular springs were designed in a spiral shape with a thin thickness in order to reduce the stiffness of the switch and facilitate flexible movement of the mass under applied load. Moreover, to further decrease the threshold, they redesigned the structure of the spring–mass system [59], as shown in Figure 5c. By reducing the spring thickness and increasing the spring length, the design obtained lower stiffness and the threshold value was 5 g. Furthermore, they introduced the conceptual design of a new MEMS inertial microswitch, which adopted the method of direct contact sensing to eliminate the bouncing effect when the electrodes were in contact. The measured threshold was approximately 11.8 g [60]. Field et al. [61] studied a low-g switch with a threshold value of 25 g. The fabrication was based on a silicon-on-insulator (SOI) wafer, and the sensing direction was along the thickness of the wafer. Hwang et al. [62] designed a low-g MEMS acceleration switch with a threshold acceleration of 6.61 g. The structural material was single-crystal silicon, the structure was stress-free, and the stability was good at high temperature. However, common SOI wafers have an unexpected disadvantage in that the balance of structure is hard to maintain, mainly due to over-etching by poor etching verticality, which causes quality deviation, shifts in the center of mass and the contact area becoming smaller, and the mass tilting or rotating when it moves along the shock direction, potentially leading to contact uncertainties. One solution is to adopt a double-buried layer SOI wafer to replace the original common SOI wafer. Massad et al. [63] designed a low-g inertial switch made of silicon, whose plate was suspended by four folded beams that acted as springs. The electrodes closed when an acceleration from 6 g to 10 g was applied.

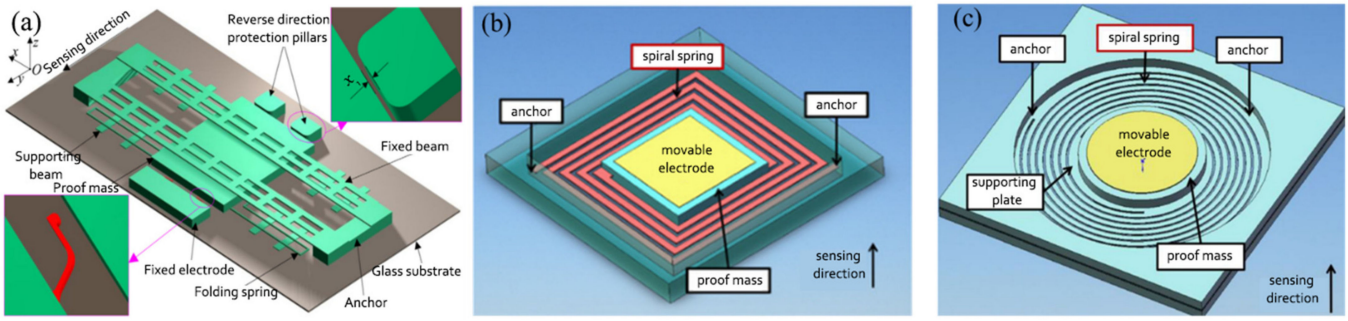

Figure 5. Schematic diagrams of three low-g inertial switches. (**a**) The nickel low-g MEMS inertial switch [57]. (**b**) The silicon-based low-g MEMS inertial switch [58]. (**c**) The lower stiffness of the redesigned inertial switch [59].

2.2.2. High-g Threshold Inertial Switches

In recent years, owing to the intelligent requirements of weapon systems, MEMS technology has also been closely integrated with advanced weapon systems. In smart

ammunition fuse applications, the survivability of MEMS inertial switches under high mechanical loads is a key to measure the performance of switch devices. More miniaturization, strong anti-interference ability, high sensitivity and reliability of high-g MEMS inertial switches have been studied to better adapt to the development trend of military weapons.

Nie et al. [64] presented a MEMS high-g electronic inertial switch for medium- and large-caliber projectile fuses. This switch mainly consisted of four parts: a zigzag groove in the center of the sensitive mass, a latch, an electrical connection structure, and a movement-limiting mechanism, as shown in Figure 6. The zigzag groove had a damping effect on the mass movement, which had the function of sensitively distinguishing the fuse launch acceleration and accidental fall shock. The switch could withstand accelerations of 3000 g. A method for identifying the acceleration load of the zigzag groove of the mass block was established, which was of great significance for the parameter optimization of the switch structure under different accelerations. Singh et al. [65] designed a passive high-g inertial switch for critical applications without electricity. The switch consisted of a serpentine spring–mass system, the dimensions of which were optimized for the natural frequency [66], and the switch was closed at 3500 g acceleration. Xu et al. [67] presented an inertial microswitch with synchronously following flexible electrodes, and its spring-shaped structure was used not only to prolong the contact duration but also to reduce shock bounce. The switch achieved a contact time of 350 us at 500 g acceleration. Xi et al. [68] proposed a high-g inertial switch consisting of five individual electrical switches and a sensitive mass–spring system. This switch could detect not only the acceleration threshold, but also the direction of acceleration in three-dimensional space. The contact time of the switch was 119 μs when the acceleration shock was 1200 g.

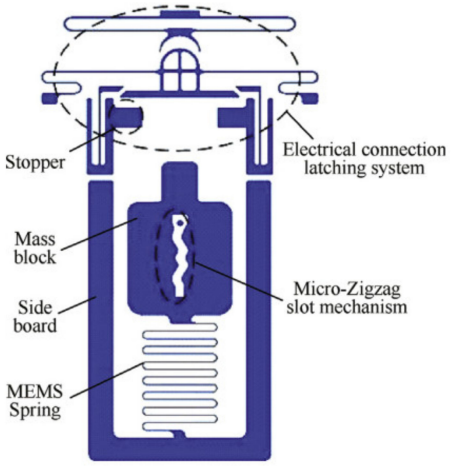

Figure 6. Schematic diagrams of the MEMS inertial high-g switch.

2.2.3. Threshold-Tuning Inertial Switches

If the threshold acceleration of the inertia switch is adjustable, its application can be extended to a wider range of environments. Kim et al. [12] designed a bidirectional adjustable acceleration switch that could simultaneously increase and decrease the threshold acceleration in the same mechanism. In their previous paper [69], they proposed a tunable acceleration switch, but the switch design could not decrease the threshold acceleration and the tunability was limited. It could be used in secure/armed position switching and mechanical locking adjustable switches for military applications. Threshold acceleration could be increased or decreased by electrostatic forces created by the electrical potential between the contact portion and the comb structure. The threshold acceleration without tuning voltage was 10.25 g, and then it was tuned to 2.0 g and 17.25 g by applying 30 V to the push and pull combs, respectively. Subsequently, a fully digital MEMS accelerometer was implemented using the concept of a MEMS accelerometer switch [70]. The accelerometer consisted of a proof mass and a number of parallel plate electrostatic actuators that could be

turned on and off in a sequential manner by a digital controller (as shown in Figure 7). By changing the bias voltage and working voltage of the electrode, the full-scale acceleration and acceleration range of the most significant bit and least significant bit could be set to any value, thereby adjusting the acceleration range of the device. This design realized the adjustment of threshold acceleration between 0 and ~1 g. Ma et al. [71] presented an inertial switch with adjustable acceleration thresholds based on a MEMS digital-to-analog converter (M-DAC). The selected adjustable plates were pushed by diverse PDMS caps to produce a specific displacement of the sensitive mass, thus realizing the adjustment of the acceleration threshold. By using different upper PDMS caps, the acceleration thresholds changed between 40 g and 75 g. Abbasalipour et al. [72] expanded on the original design of the fully digital MEMS accelerometer and designed a micromechanical accelerometer with 8-bit digital control. The tuning force of each electrode group was three times that of the adjacent electrode group. The full-scale acceleration of the tested 8-bit prototype was 2.7 g. Table 2 shows a summary of some examples of typical threshold acceleration inertial switch performance.

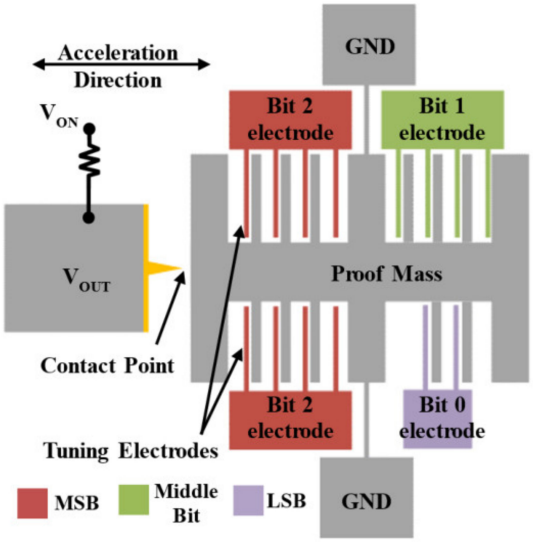

Figure 7. Simplified schematic view of a 3-bit digitally operated MEMS switch.

Table 2. A summary of some examples of typical threshold acceleration inertial switch performance.

Threshold Acceleration	References	Material	Acceleration Threshold	Special Design and Function	Application
Low-g	Chen et al. [57]	Ni	18 g	L-shaped elastic cantilever beam fixed electrode	Health monitoring and special industrial transportation
	Xiong et al. [58]	Double buried SOI	7.4 g	Low-stiffness spiral spring	Linear acceleration sensing
	Zhang et al. [59]	Double buried SOI	5 g	Circular spiral springs	—
	Hwang et al. [62]	Si	6.61 g	Displacement-restricting structures for all directions to prevent breakage of the spring	Military applications
	Massad et al. [63]	Gold	6–10 g	Four folded beams as springs	RF MEMS

Table 2. *Cont.*

Threshold Acceleration	References	Material	Acceleration Threshold	Special Design and Function	Application
High-g	Nie et al. [64]	Ni	3000 g	Zigzag groove to distinguish the fuse launch acceleration and the accidental fall shock	Medium- and large-caliber projectile fuses
	Singh et al. [65]	SOI	3500 g	Independent angled latching mechanism	Critical applications without electricity
	Xu et al. [67]	Ni	500 g	Synchronous follow-up compliant electrodes for extending the contact	—
	Xi et al. [68]	Ni	1200 g	Detecting the acceleration threshold and direction	Directional warheads impacting targets at high speed
Threshold tuning	Kim et al. [12,69]	Si and glass	2–17.25 g	Comb drive actuators to tune the acceleration threshold	Secure/armed position convertibility for military applications
	Kumar et al. [70]	Si	0~1 g	Bias voltage and working voltage are used to adjust acceleration	Integrated systems
	Ma et al. [71]	Si	40–75 g	MEMS digital-to-analog converter (M-DAC) to adjust acceleration thresholds	Crash recorders and arming and firing systems

2.3. Contact-Enhanced Inertial Switches

Solid–solid rigid contact can easily cause contact bounce, making it unsuitable for small signal switches. It also causes arcing and welding of the contacts, resulting in contact surface damage and material transfer. This contact degradation restricts the reliability and longevity of these devices. Avoiding solid-to-solid mechanical contact means there are no issues associated with contact bounce or contact degradation, thus extending the life of the switch.

Contact time is a critical property for an intermittent inertial switch in some application environments because the longer contact time, the less difficult the signal processing is. A short contact time requires an external circuit with higher signal identification performance [3]. Insufficient contact between two electrodes is usually caused by a rigid contact process, resulting in a strong rebound of the movable electrode after touching the fixed electrode (usually a rigid substrate for conventional inertial switches). These switches have extremely short contact times (less than 10 μs), which is difficult for the external circuit to recognize [1]. Furthermore, contact bounce can damage the interface between the two motors due to mechanical hammering and arcing, subsequently affecting the durability of the system, which may result in permanent adhesion between the two electrodes [73]. In recent years, in order to eliminate the bounce phenomenon and enhance the contact effect of the intermittent switches, considerable efforts have been put into inertial microswitches. The methods mainly include some special structures and flexible materials.

2.3.1. Special Structures to Extend Contact Time

Cai et al. [1] developed a new double mass–spring system that is completely different from the traditional system design. In addition to the proof mass–spring system, instead of being rigidly fixed to the proof mass, the contact point was suspended in the middle of the proof mass by an inner spring. The experiment results demonstrate that the threshold

acceleration of the MEMS inertial switch was about 175 g and the contact time of the contact point was 56 μs. The steady turn-on time of more than 50 μs was much longer than the 12 μs in the research [74]. The switch was driven vertically and the elastic beam above the proof mass block could be used as a fixed switch electrode. However, there were two switch-on signals under an acceleration of 200 g acceleration, which would lead to secondary closure of the switch and have a bad effect on the reliability of the switch. Wang et al. [5] proposed a new type of L-shaped flexible cantilever fixed electrode, and long contact was possible in a transverse MEMS inertial switch. The sensitive mass was suspended by two pairs of conjoined serpentine springs as the motion electrode and the fixed electrodes were suspended from the blocks. The flexible cantilever electrode could realize a flexible deformation to enhance contact time and avoid the rebound phenomenon of the MEMS inertial switch. The contact time was extended to 1050 μs, which was much longer than the time without cantilever buffer effect of 5 μs. Moreover, according to the characteristics of the cantilever arm, its special elastic deformation could be designed to realize the control method of switch contact time. With the increasing acceleration, the contact time also decreased until it tended to a stable value. At the same time, based on the same inertial switch structure, Chen et al. [3] analyzed the influence of the applied acceleration loads on contact time. Combining the tested results, it was concluded that as the pulse width of the applied shock load increased, so did the contact time. Yang et al. [32] investigated an inertial microswitch with bridge-type elastic fixed electrodes for prolonged contact. Specifically, they designed two parallel perforated elastic beams as fixed electrodes. The microswitch was equipped with a relatively good contact effect, but the switch could be triggered with an effective contact of only 12 μs when 100 g acceleration was applied. By adding a group of cantilever beams on the mass block as the buffer between the electrodes [73], the contact time could be prolonged and the phenomenon of jumping contact could be avoided. Another advantage of this is that the contact time of the microswitch could be extended to 240 μs. It was more than 15 times that of a microswitch without cantilever beam. Table 3 shows a comparison of contact times for simulated and experimental tests of three kinds of inertial switches. In addition, Yang et al. [33] also discussed three other devices with different structures (types II, III, and IV), as shown in Figure 8. Types II and III used a cross-beam stationary electrode to realize a long contact time with deformation. The contact times for the two switches (types II and III) utilizing beam deformation were 20 μs and 30 μs, respectively. However, due to the limitation of deformation, the contact effect of the switch was not effectively improved. Therefore, type IV adopted a double spring–mass system, which greatly improved the contact effect. The experimental results show that the contact time was about 55 μs, which greatly enhanced contact performance. Xu et al. [6] introduced a laterally actuated inertial switch. As a moving electrode, the sensitive mass was connected to two L-shaped elastic cantilever beams. The switch had an inductive acceleration threshold of 288 g with a contact time of 150 μs.

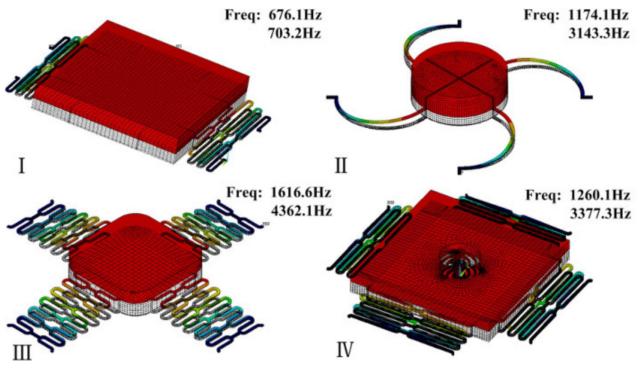

Figure 8. Modal analysis of various microswitches and their first two frequencies. Type I adopted a vertically driven structure with low off-axis sensitivity. Type II and III used a fixed contact point on the proof mass. Type IV realized a longer duration contact with a movable contact point.

Table 3. Comparison of the contact time of inertial microswitches from different designs.

Inertial Microswitches of Different Designs	Simulated Contact Time (μs)	Measured Contact Time (μs)	Sketch of the Microswitches Movable Electrode Fixed Electrode
Conventional microswitch	~1	–	
Microswitch with a bridge-type compliant fixed electrode	~5(t_1), ~10(Δt), ~2(t_2) skip contact	~13(t_1), ~60 (Δt), ~8(t_2) skip contact	
Improved microswitch with cantilevers	~160 no skip contact	~240 no skip contact	

2.3.2. Materials and Assistive Force to Extend Contact Time

Unlike the inertial switches described above with specific structures to increase contact time, some studies have proposed the use of special materials or external assistive forces to improve contact characteristics. Lee et al. [75] proposed a new inertial microswitch. Its contact mode was carbon nanotubes (CNTs) in contact with carbon nanotubes. Due to the high mechanical flexibility and elasticity of CNT material itself, it was prone to elastic deformation when used as contact pad material [76], so the contact time was prolonged. At present, the contact time of the existing traditional switch is only 7.5 μs, but with this inertial micro switch, the contact time could be extended to 114 μs. The results show that the new inertial microswitch proposed by Lee et al. could significantly prolong the contact time. Yang et al. [77] developed an inertial microswitch with polymer metal composite as a fixed electrode. It not only had the characteristics of multidirectional features and high sensitivity, but also prolonged the contact time of the switch and improved the stability and reliability of the inertial microswitch. The contact time was improved to 110 μs, which was longer than that one without polymer (~65 μs). In addition, an inertial microswitch with a flexible carbon nanotube/copper (CNT/Cu) composite array layer between movable and fixed electrodes was designed in [78]. The interaction between carbon nanotubes, i.e., adhesion, was one of the main reasons for the extension of contact time. Li et al. [79] designed a MEMS inertial switch to prolong the contact time through electrostatic assistance and multi-step pull action. Through the test, the contact time was about 540 μs and showed no bounce. Table 4 shows a summary of some examples of typical contact-enhanced inertial switch performance.

Table 4. A summary of some examples of typical contact-enhanced inertial switch performance.

Methods of Contact Enhancement		References	Material	Acceleration Threshold	Contact Time	Application
Special structure	Double mass–spring system	Cai et al. [1]	Ni	145 g	>50 μs	Automotive airbag system
	L-shaped flexible cantilever fixed electrode	Wang et al. [5]	Ni	180 g	1050 μs	Circuit analyzing in many applications
	L-shaped compliant cantilever beam	Chen et al. [3]	Ni	259 g	75 μs	Small-scale or longlifetime systems
	Bridge-type elastic fixed electrodes	Yang et al. [32]	Ni	100 g	12 μs	Accessories and automobile applications

Table 4. *Cont.*

Methods of Contact Enhancement		References	Material	Acceleration Threshold	Contact Time	Application
	Cantilever beams on the mass block as the buffer	Yang et al. [73]	Ni	55 g	240 μs	—
	Two L-shaped elastic cantilever beam electrodes	Xu et al. [6]	Ni	288 g	150 μs	Small-scale or long-lifetime systems with limited supply power
Materials	Carbon nanotubes (CNTs)	Lee et al. [75]	SOI	—	108 μs	Airbag restraint systems and geriatric healthcare systems
	Polymer metal composite	Yang et al. [77]	Ni	70 g	110 μs	Detecting multidirectional vibration shocks
	Carbon nanotubes/copper(CNTs/Cu)	Wang et al. [78]	Ni	80 g	112 μs	—
Electrostatic force assistance		Li et al. [79]	Ni	22 g	540 μs	Hard conditions or remote monitoring

3. Persistent Inertial Switches

Compared to an intermittent inertial switch without a self-locking function, a persistent inertial switch can achieve a stable contact property with a mechanical lock and a bistable structure. Furthermore, a fluidic MEMS inertial switch can also accomplish a locking function when flowing liquid (as a movable electrode) contacts the metal fixed electrode.

3.1. Latching Switches

When the acceleration increases to the threshold of the inertia switch, the mass will move and pass through the hook. When the acceleration is slowly reduced to 0, the latching mechanism prevents the proof mass from returning to the initial state. Then the switch stays in an "on" state. Lee et al. [80] introduced a hooked latch to an electrode for the contact part, which improved the reliability of the contact. The power consumption directly affected the practicability and reliability of the sensor system. An analog front-end is required to detect and interpret the output in the present commercial application of accelerometers. It leads the power consumption to be in the range of hundreds of μW to a few mW. Reddy et al. [81] developed a MEMS passive impact sensor that could be applied to multiple thresholds and had a good latch device. It could measure an impact in the range of 20–250 g at a threshold 10 times higher than itself. Ramanathan et al. [82] designed a new MEMS inertial switch design framework. The mass block was mainly supported by a group of four folded beams and it could design the accelerometer according to the parameters input by people. It was verified that the optimal threshold acceleration of the framework was about 60 g. Guo et al. [22] presented a latching switch with an easy-latching/difficult-releasing (ELDR) latching mechanism and cylindrical contacts. The ELDR locking mechanism could reliably lock the switch. The measured latching shock was over 4600 g and the response time was less than 0.2 ms. Currano et al. [83] discussed a MEMS inertial switch that was used to monitor the shock event over a specified threshold level with a latching mechanism. However, introducing a latch structure led a recovery issue, which is not beneficial to early testing and unlocking. Therefore, Zhang et al. [84] designed a novel heterogeneous integrated inertial microswitch with an adjustable acceleration threshold that could get the switch to keep a stable "on" state due to the pull-in phenomenon of a predefined bias voltage. Besides, the switch was easily unlocked by removing the bias voltage.

3.2. Bistable Inertial Switches

Additionally, the concept of a bistable mechanism has been brought to micro-inertial switches [85,86], which utilizes a bistable post-buckling structure to achieve a similar latching function. Taking advantage of the ability of the bistable mechanism to maintain two bistable positions without consuming power, the bistable structure has great superiority in designing an inertial switch with a self-locking function. Sandia National Laboratories presented a fully compliant bistable microswitch with a tapered beam in [87] and a three-segment bistable inertial switch [23] consisting of a large mass suspended on the four bistable beams, which could achieve the on-off function of a high g-value acceleration. Bistable microstructures as nonlinear elastic spring elements to precisely define two static stable states have been involved [25]. However, bistable structures have not been used to decrease the contact resistance. To reduce the contact resistance, a novel magnetic actuated bistable acceleration switch was proposed in [26], which included an asymmetric bistable mechanism with a parallel beam and three magnets arranged three-dimensionally. Zhao et al. [88] presented a wireless inertial microswitch incorporating a bistable flexible mechanism. When the bistable structure underwent buckling deformation under an excitation of external acceleration, the proof mass at the contact position could be stabilized. Liu et al. [89] studied a novel low-g MEMS bistable inertial switch with dual self-locking functions under an 8 g acceleration and reverse unlocking under a 105 g acceleration threshold, which was expected to carry out the reuse of the switch. The schematic of the designed bistable inertial switch is shown in Figure 9. This switch used a fully mechanical structure to greatly improve the anti-electromagnetic interference ability.

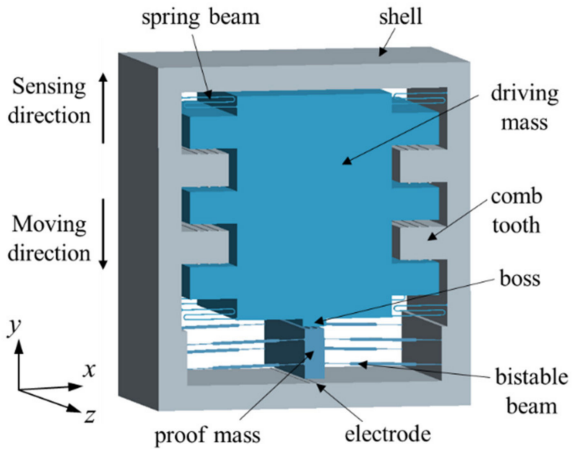

Figure 9. Schematic and structural parameters of the designed MEMS bistable inertial switch.

3.3. Liquid Inertial Switches

Unlike the conventional solid-to-solid-type micro inertial switch, a liquid inertial switch realizes contact through liquid–solid mode so as to improve its stability. The liquid–solid contact-based liquid switch mechanism can avoid problems such as signal bounce and contact wear during switch movement. Moreover, a liquid–metal (LM) microswitch [90] has been used in safety and arming (S&A) applications for time-delay fuses.

Yoo et al. [91] designed an inertial switch with a liquid–metal contact method, which greatly improved the stability of the switch contact. Kuo et al. [28] designed a passive inertial switch and integrated an *L*-*C* resonator to realize wireless signal transmission. The working fluid was water. In another design [92] introducing multiwall carbon nanotube (MWCNT)-hydrogel composite material, they proposed a liquid-type inertial switch integrated with a passive inductor/capacitor (*L*-*C*) resonator. This switch could achieve various threshold levels of acceleration by various channel configurations. Huang et al. [27] designed a microfluidic time-delay switch. The device consisted of glycerol (as the working fluid), a microcapillary valve (as the time-delay mechanism), and sensing electrodes. The

schematics are shown in Figure 10. By changing the geometric design of the microfluidic system (such as channels and valves), the delay time of the microfluidic switch could be easily adjusted. The experimental test showed that the delay time range of the switch was 4.1 to 10.9 s.

Nie et al. [29] developed an innovative microfluidic inertial switch structure. It had the characteristics of accurate delay response. The results showed that the actual delay time was 114.1 ms under an inertia load of 75 g. Most studies used mercury as a conductive metal liquid, but it is toxic. Gallium indium (EGaIn) was used as the conductive element of the mobile electrode, which had the obvious advantages of non-toxicity, low viscosity, and high conductivity. Shen et al. [30] designed a self-recovery inertial switch, and its working liquid was a gallium-indium (EGaIn) metal droplet. The switch employed a U-type microchannel in order to reduce air resistance in the microchannel. There were sensing electrodes in the rectangular microchannel. After the acceleration signal disappeared, the droplet returned to the reservoir. This demonstrated the automatic-recovery characteristic of the switch. Liu et al. [93] used Galinstan and designed a microfluidic inertial switch. The test results showed that the response time was 0.66 ms and the contact time was 0.88 ms under a 51.2 g acceleration threshold. Liu et al. [31,94,95] conducted further research on the LM switch. An increase in the contact angle would increase the viscous force of the droplet on the capillary valve, thereby prolonging the response time. Furthermore, the switch structure introduced a two-stage microvalve, which facilitated adjustment of the threshold by changing the mercury volume. Huh et al. [96] designed a dual-axis accelerometer based on a liquid–metal droplet. The movement of droplet was leaded by the induced inertial force. Then they proposed an opposite design [97], which was to etch the cone-shaped guiding channel on the upper cover. The droplet was located in the channel. The switch could sense the acceleration signal in the range of 0–1 g, with high resolution and long service life.

The droplet used in the switch was selected according to its density, toxicity, melting point, and other characteristics. The following Table 5 lists the characteristics of several commonly used droplets in microfluidic switches. However, because liquid metals are volatile, the sealing problem of the switch requires special attention. Fluid is greatly affected by temperature, and cannot be kept constant at different temperatures. Therefore, the applications of fluid switches are seriously limited. A summary of some examples of typical persistent inertial switch performance is shown in Table 6.

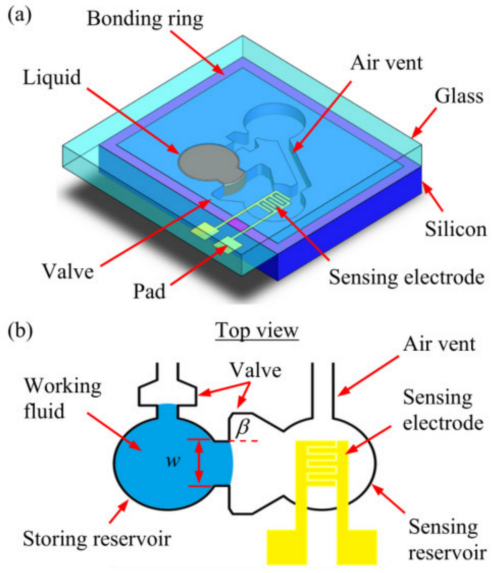

Figure 10. Schematics of the proposed microfluidic system design: (**a**) the S-A device and (**b**) top view of the device.

Table 5. Characteristics of some droplets in microfluidic switches.

Working Droplet	Density (g/cm^3)	Melting Point (°C)	Toxicity	Surface Tension (mN/m)	Others Characteristic
Water	1.0	0	Non-toxic	73	–
Mercury	5.43	−38.83	Toxic	485.5	Opaque High reliability
Glycerol	1.26	−17.8	Non-toxic	63.4	High dielectric constant
gallium-indium (EGaIn)	6.25	15.7	Non-toxic	445	Low viscosity High conductivity
Galinstan [98]	6.44	−19	Non-toxic	534.6	Low vapor pressure Easy to oxidize

Table 6. A summary of some examples of typical persistent inertial switch performance.

Type	References	Material	Acceleration Threshold	Performance	Application
Latching switches	Lee et al. [80]	Si and glass	43.7 g	Mechanical hooked latch	Airbags, parachutes, and military devices
	Reddy et al. [81]	SOI	20–250 g	Robust latching mechanism with mass-spring assembly	Long-term remote monitoring applications
	Ramanathan et al. [82]	SOI	60 g	Semi-circular latch key	Projectiles or the separation of rocket stages
	Guo et al. [22]	Si and glass	4600 g	Easy-latching/difficult-releasing (ELDR) latching mechanism	—
	Zhang et al. [84]	Si and Ni	57 g	Stable "on" state due to a predefined bias voltage	Monitoring the transportation of special goods
Bistable inertial switches	Zhao et al. [88]	Ni	32.38 g	V-shaped slender bistable beams	Remote detection of threshold acceleration and corresponding response time
	Liu et al. [89]	SOI	8 g (self-locking) 105 g (self-locking)	Three-segment fully compliant bistable beams	Military applications
Liquid inertial switches	Yoo et al. [91]	Si and glass	—	Liquid–metal (LM) droplet combined with selective surface modification inside the channel	—
	Kuo et al. [92]	Si, glass, and PDMS	∼60 g	Multiwall carbon nanotube (MWCNT)–hydrogel composite integrated with an inductor/capacitor (L–C) resonator	Sensing acceleration inducing by impact
	Nie et al. [29]	Si (EGaIn)	75.1 g, 46.6 g, 36.5 g	Precise time-delay response characteristic	Fuze safety and arming systems
	Liu et al. [93]	Glass and PDMS	51.2 g	Automatic-recovery inertial switch and Galinstan marbles	—

4. Typical Fabrication Methods

The design and fabrication method can directly affect the reliability of MEMS inertial switches, especially the lifetime, robustness, and stability under extreme conditions of shock temperature, humidity, chemical exposure, or other challenges. Depending on the design and materials of the inertial switch, fabrication methods can be divided into three categories: (1) standard silicon micromachining technology, (2) non-silicon surface micromachining technology, and (3) the special fabrication method for liquid inertial switches.

4.1. Standard Silicon Micromachining Technology

Standard silicon micromachining is mainly manifested as a combination of bonding and deep eclipsing technologies to pursue large mass, stress reduction, and three-dimensional processing. Direct silicon bonding is completed by heating to promote the polymerization of hydrogen bonds to generate SiO_2, so the surface treatment of the silicon wafer before bonding is key to making the surface of the silicon wafer absorb more OH^-. Besides, gold–gold thermocompression bonding has been used in the preparation of bistable inertial switches to obtain a mass block of large thickness [89].

The main process of the standard silicon micromachine is sketched as follows and illustrated in Figure 11.

(1) SOI wafer preparation: A BOE rinse is performed to remove the native oxide layer on the SOI wafer.
(2) Thermal oxidation: An SiO_2 layer is grown and patterned, which serves as the etching mask layer for deep reactive ion etching (DRIE).
(3) Oxidation pattern: A thin layer of Al_2O_3 is deposited on the SOI device layer via atomic layer deposition. Then the Al_2O_3 film is patterned as a hard mask for a silicon etch.
(4) Device layer etching: The inertial switch silicon skeleton is then formed in the SOI device layer via silicon dry etching.
(5) Backside lithography: Backside etching is carried out, followed by long DRIE technology, to remove the handle layer underneath the device and avoid any potential stiction issues for the large proof mass. Other Bosch technology is acceptable to ensure the verticality of the etching.
(6) Moveable electrode: The moveable electrode (Ti/Pt/Au) is deposited on the back side.
(7) Back side of the proof mass: Another DRIE process is applied to reveal the back side of the proof mass.
(8) Microswitch release: The MEMS switch is finally released after removing the excessive SiO_2 layer in the BHF solution.

4.2. Non-Silicon Surface Micromachining Technology

Non-silicon surface micromachining technology on a different substrate such as silicon, metal, and glass, etc., mainly includes sputtering, electroforming, and sacrificial layer technologies. Some typical new inertial microswitches, including vertical [1] and lateral actuation [3], uniaxial [35], multiaxial [4], and omnidirectional sensitive [19] and flexible electrodes using CNT/Cu composites to enhance contact [78], are fabricated by this technology.

The following is a summary of the surface micromachining process of a MEMS inertial switch combined with the preparation of a uniform omnidirectional sensitivity inertial switch. The main procedure is sketched in Figure 12 and described as follows:

(1) Preprocessing of the substrate: The roughness of the substrate surface is reduced via polishing techniques and by cleaning.
(2) Photoresist lithography: A spin-coating photoresist on the substrate and photolithography are carried out. Table 7 shows some common photoresists, including their performance and coating thickness. Mostly, negative photoresist (SU-8) and positive photoresist [6] are used for the mold and sacrificial layers, respectively.

(3) Micro electroforming: As the structure material, electroplated metal nickel (Ni) has good mechanical properties and can effectively solve the problem of switch breakage under a high acceleration impact. Volume error can be reduced by controlling the plating time.
(4) Seed layer: Sputtered Cr/Cu on the substrate is used as a seed layer for device electroplating.
(5) Multilayer repetition of micro electroforming: Multilayer plating technology can overcome etching difficulties of a high slim ratio of inertial switches.
(6) Microswitch release: The photoresist and seed layer are removed, and then the inertial microswitch can be obtained. Usually, acetone or boiled inorganic are used to remove negative photoresist SU-8 and an ammonia/peroxide solution is used to remove the seed layer.
(7) Rinsing and drying the device: The released microswitch is rinsed with isopropyl alcohol or deionized water, and then dried to avoid stiction.

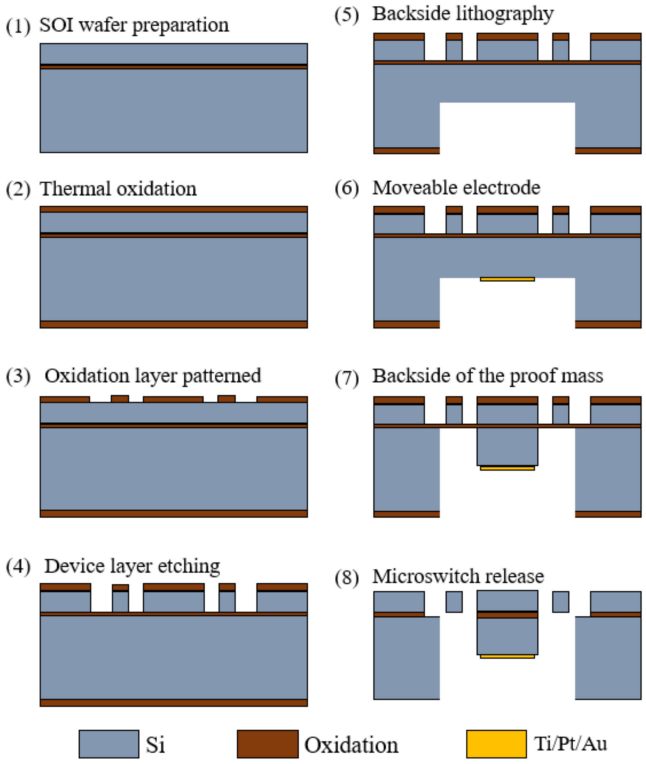

Figure 11. Schematic view showing the fabrication process of a standard silicon micromachine.

4.3. Special Fabrication Method for Liquid Inertial Switches

For liquid inertial microswitches, the key difficulty in the fabrication process is the problem of the tightness of the liquid electrode (movable electrode). Micro-channels are formed on a silicon substrate by microfabrication technology, and the covered glass substrate is convenient for observing the movement of droplets. The specific fabrication process is illustrated in Figure 13 and expressed as follows.

Microchannels with different cross-sections can be etched by micromachining processes. The silicon wafer is etched by DRIE technology, and the bonding between the silicon wafer and the glass cover is realized by anodic bonding.

(1) Silicon substrate photolithography: The microchannel is SOI material, with a photoresist masking pattern for ICP etching microchannels on the SOI material.
(2) Silicon substrate ICP etching: The microchannel is etched by ICP technique, and then the photoresist is removed.

(3) First metal electrode layer: The photolithography, sputtering, and lift-off techniques are applied on the glass substrate. The first metal electrode layer is achieved on the glass.
(4) Second metal layer: The same technology as above is used to achieve the second metal layer on the glass substrate.
(5) Glass cover plate laser drilling: To achieve the adjustment of the volume of the flowing droplets, the adjustment holes and channels are laser etched.
(6) Anode bonding and dicing: After wafer-level packaging, chips are obtained through precise dicing technology.

Table 7. The performance and coating thickness of common photoresists.

Type	Name	Performance	Coating Thickness
Positive	AZ P4620	Ultra-thick film, high-contrast, and high-speed positive-tone standard photoresist for semiconductor and/or GMR head manufacturing processes.	10–15 μm
	AZ 50XT	Stable, excellent coating characteristics and sidewall profiles for developing plating and wafer-bumping applications.	40–80 μm
	AZ 9260	Small absorption coefficient and a typical photoresist for thick resist etching processes.	6.2–15 μm
Negative	SU-8 series	High aspect ratio imaging, improved adhesion, reduced coating stress, vertical sidewalls, and faster drying for increased throughput.	0.5–300 μm
Variable	AZ 5214E	Wide viscosity variation suitable for high resolution process (lift-off process) and available for positive/negative patterning.	0.5–6 μm

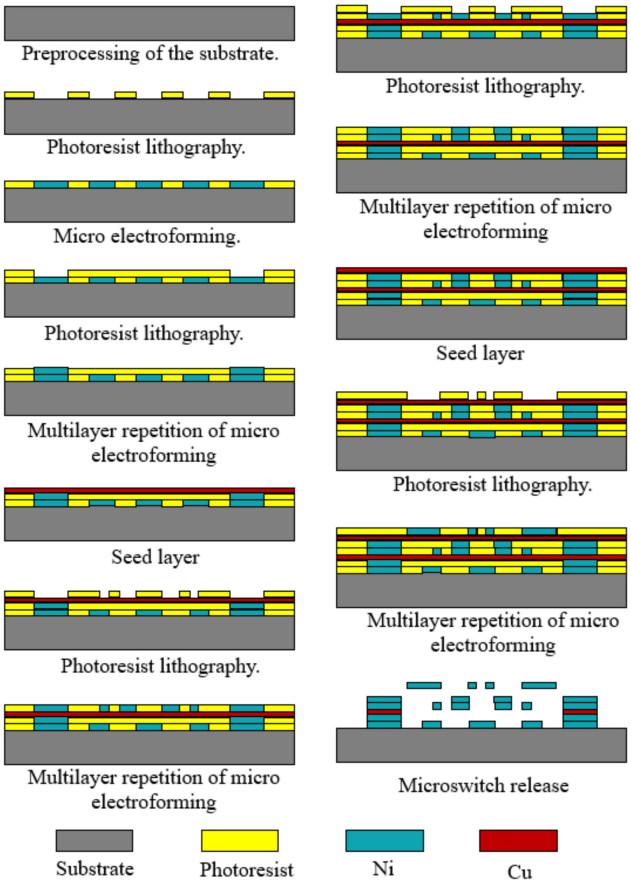

Figure 12. Sketch of the main fabrication process of surface micromachining.

After completing the structural preparation of the fluid switch, the droplets are injected into the adjustment hole and the channel is adjusted to make the droplet enter the initial position. Although gold has good conductivity, its application is limited due to its high solubility with mercury. Therefore, chromium (Cr) can be chosen as the electrode material due to its proper electrical conductivity and low solubility with mercury. In addition, the preparation process of an alternative fluid inertial switch including a package shell is given, as shown in Figure 14 [27]. The detailed process is as follows, which mainly consists of three parts, including a glass wafer, silicon wafer, and package.

(a) Glass wafer

(1) Adhesive layer and electrodes: A chrome film as an adhesion layer and a gold film as a sensing electrode are evaporated and patterned on a glass substrate by lift-off technology.

(2) Parylene film: Parylene thin films are deposited by chemical vapor deposition (CVD) and patterning by oxygen plasma. In the subsequent silicon-to-glass bonding process, the parylene film serves as a hydrophobic surface and bonding interface.

(b) Silicon wafer

(3) Thermal oxidation: Silicon dioxide is processed by thermal growth and then patterned on a silicon wafer.

(4) Microchannel and fluidic components: The DRIE process is used to prepare structures required for microfluidic work, such as capillary valves, reservoirs, and vents.

(5) Parylene film: Parylene film plays a role in surface modification and bonded adhesion layers, which is deposited by the CVD process.

(c) Packaging

(6) The Si substrate is filled with fluid and then sealed to glass by bonding technology.

(7) The liquid inertial switch device is created after dicing the Si substrate and electrical routing.

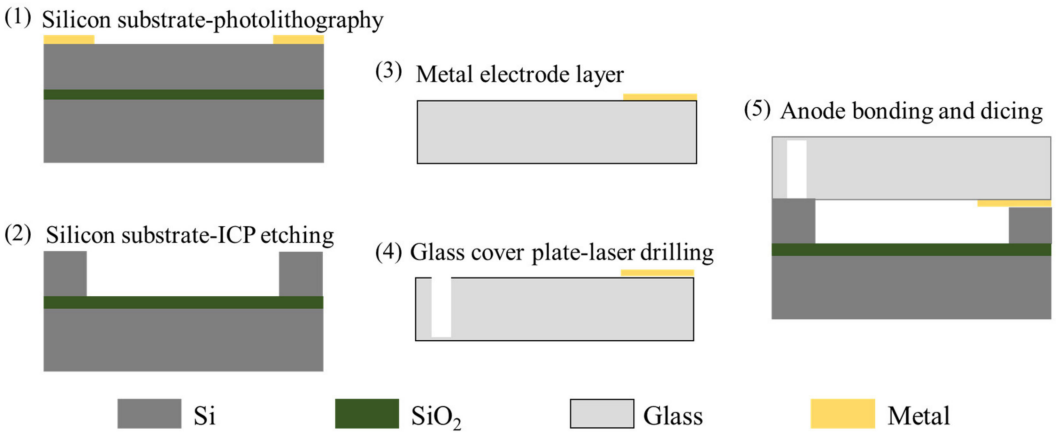

Figure 13. The special fabrication method for a liquid inertial switch.

MEMS manufacturing process technology is the basis for supporting the development of mechanically robust, high-performance inertial switch designs. It is combined with the hermetic silicon process, which is the key to realizing a truly reliable long-life MEMS switch. An airtight protective casing is formed around the MEMS inertial switch device. Regardless of the external packaging technology used, this airtight enclosure can improve the environmental robustness and service life of the inertial switch.

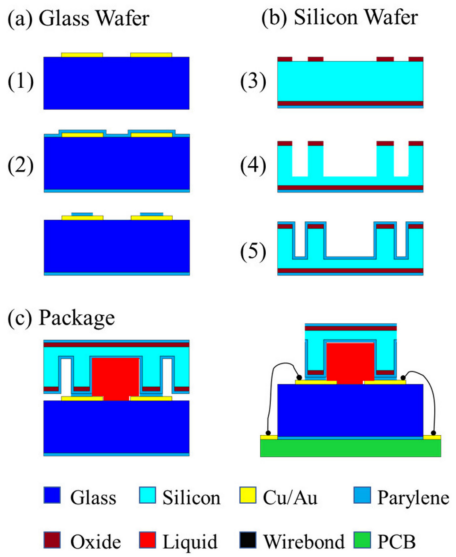

Figure 14. Manufacturing and packaging process for a fluid switch.

5. Challenges and Prospects

In engineering practice, it is always difficult to break through bottlenecks such as inertial switch manufacturability, threshold repeatability, and threshold inconsistency. Both the bottlenecks and the opportunities for MEMS inertial switches are in progress. In order to successfully commercialize MEMS inertial switches, there are some challenges that remain and prospective trends that are worthy of attention.

(1) Persistent switches can achieve stable closure. However, they are not suitable for an engineering environment wherein repeated application is required. In addition, in early experimental tests, its one-time use feature will cause a great waste of devices, so it is necessary to study the self-unlocking method for this type of switch.

(2) DRIE and Bosch technology are able to achieve large mass preparation, and multi-layer electroforming technology makes complicated inertial switches possible with multiple direction and threshold sensitivities. However, the inherent fabrication errors and the residual stress lead to low threshold accuracy. Thence, the method of error compensation can significantly improve the threshold accuracy and sensitivity.

(3) Mature SOI technology can effectively guarantee the fabrication accuracy of the inertial switch. However, the packaging process of the inertial switch in the later stage affects the final size and application of the switch. Usually, the package shell of the inertial switch needs to have high sealing and pressure resistance to ensure air film damping, and the packaged chip is also easier to install and transport. However, most of the current switch research is limited to experimental test packaging, which is far from the packaging requirements of the actual application environment. Therefore, it is of great significance to select appropriate materials and packaging processes to bring the switch from research and development to practical applications.

(4) The surface micromachining process is compatible with the integrated circuit production process, and the integration is high. Furthermore, integrating and applying the inertial switches with integrated circuits for systematic integration is a significant trend as well.

Author Contributions: M.L., Project administration, Writing—review and editing; X.W., Resources; Y.N., Data curation; H.Y., Supervision; Y.Z., Formal analysis; W.W., Project administration. All authors have read and agreed to the published version of the manuscript.

Funding: This work is supported by the National Natural Science Foundation of China (No. 42004157), and the Key Research and Development Program of Shaanxi (Program No. 2021GY-277).

Conflicts of Interest: The authors declare no conflict of interest.

References

1. Cai, H.; Ding, G.; Yang, Z.; Su, Z.; Zhou, J.; Wang, H. Design, simulation and fabrication of a novel contact-enhanced MEMS inertial switch with a movable contact point. *J. Micromech. Microeng.* **2008**, *18*, 115033. [CrossRef]
2. Chen, W.; Wang, Y.; Ding, G.; Wang, H.; Zhao, X.; Yang, Z. Simulation, fabrication and characterization of an all-metal contact-enhanced triaxial inertial microswitch with low axial disturbance. *Sens. Actuators A Phys.* **2014**, *220*, 194–203. [CrossRef]
3. Chen, W.; Yang, Z.; Wang, Y.; Ding, G.; Wang, H.; Zhao, X. Influence of applied acceleration loads on contact time and threshold in an inertial microswitch with flexible contact-enhanced structure. *Sens. Actuators A Phys.* **2014**, *216*, 7–18. [CrossRef]
4. Currano, L.J.; Becker, C.R.; Lunking, D.; Smith, G.L.; Isaacson, B.; Thomas, L. Triaxial inertial switch with multiple thresholds and resistive ladder readout. *Sens. Actuators A Phys.* **2013**, *195*, 191–197. [CrossRef]
5. Wang, Y.; Chen, W.; Yang, Z.; Ding, G.; Wang, H.; Zhao, X. An inertial micro-switch with compliant cantilever fixed electrode for prolonging contact time. In Proceedings of the 2013 IEEE 26th International Conference on Micro Electro Mechanical Systems (MEMS), Taipei, Taiwan, 20–24 January 2013; pp. 600–603.
6. Xu, Q.; Yang, Z.; Fu, B.; Li, J.; Wu, H.; Zhang, Q.; Sun, Y.; Ding, G.; Zhao, X. A surface-micromachining-based inertial micro-switch with compliant cantilever beam as movable electrode for enduring high shock and prolonging contact time. *Appl. Surf. Sci.* **2016**, *387*, 569–580. [CrossRef]
7. Wang, Y.; Feng, Q.; Wang, Y.; Chen, W.; Wang, Z.; Ding, G.; Zhao, X. The design, simulation and fabrication of a novel horizontal sensitive inertial micro-switch with lowgvalue based on MEMS micromachining technology. *J. Micromech. Microeng.* **2013**, *23*, 105013. [CrossRef]
8. Whitley, M.R.; Kranz, M.; Kesmodel, R.; Burgett, S.J. Latching shock sensors for health monitoring and quality control. In *MEMS/MOEMS Components and Their Applications II*; International Society for Optics and Photonics: San Jose, CA, USA, 2005; pp. 185–194.
9. Ongkodjojo, A.; Tay, F.E.H. Optimized design of a micromachined G-switch based on contactless configuration for health care applications. *J. Phys. Conf. Ser.* **2006**, *34*, 1044–1052. [CrossRef]
10. Xu, Q.; Yang, Z.; Sun, Y.; Lai, L.; Jin, Z.; Ding, G.; Zhao, X.; Yao, J.; Wang, J. Shock-Resistibility of MEMS-Based Inertial Microswitch under Reverse Directional Ultra-High g Acceleration for IoT Applications. *Sci. Rep.* **2017**, *7*, 45512. [CrossRef]
11. Gerson, Y.; Schreiber, D.; Grau, H.; Krylov, S. Meso scale MEMS inertial switch fabricated using an electroplated metal-on-insulator process. *J. Micromech. Microeng.* **2014**, *24*, 025008. [CrossRef]
12. Kim, H.; Jang, Y.H.; Kim, Y.K.; Kim, J.M. MEMS acceleration switch with bi-directionally tunable threshold. *Sens. Actuators A Phys.* **2014**, *208*, 120–129. [CrossRef]
13. Campanella, H.; Plaza, J.A.; Montserrat, J.; Uranga, A.; Esteve, J. High-frequency sensor technologies for inertial force detection based on thin-film bulk acoustic wave resonators (FBAR). *Microelectron. Eng.* **2009**, *86*, 1254–1257. [CrossRef]
14. Riaz, K.; Iqbal, A.; Mian, M.U.; Bazaz, S.A. Active gap reduction in comb drive of three axes capacitive micro accelerometer for enhancing sense capacitance and sensitivity. *Microsyst. Technol.* **2014**, *21*, 1301–1312. [CrossRef]
15. Wung, T.S.; Ning, Y.T.; Chang, K.H.; Tang, S.; Tsai, Y.X. Vertical-plate-type microaccelerometer with high linearity and low cross-axis sensitivity. *Sens. Actuators A Phys.* **2015**, *222*, 284–292. [CrossRef]
16. Raeisifard, H.; Bahrami, M.N.; Yousefi-Koma, A. Mechanical characterization and nonlinear analysis of a piezoelectric laminated micro-switch under electrostatic actuation. *Proc. Inst. Mech. Eng. Part L J. Mater. Des. Appl.* **2013**, *229*, 299–308. [CrossRef]
17. Bahrami, M.N.; Yousefi-Koma, A.; Raeisifard, H. Modeling and nonlinear analysis of a micro-switch under electrostatic and piezoelectric excitations with curvature and piezoelectric nonlinearities. *J. Mech. Sci. Technol.* **2014**, *28*, 263–272. [CrossRef]
18. Raeisifard, H.; Nikkhah Bahrami, M.; Yousefi-Koma, A.; Raeisi Fard, H. Static characterization and pull-in voltage of a micro-switch under both electrostatic and piezoelectric excitations. *Eur. J. Mech.-A/Solids* **2014**, *44*, 116–124. [CrossRef]
19. Zhanwen, X.; Ping, Z.; Weirong, N.; Liqun, D.; Yun, C. A novel MEMS omnidirectional inertial switch with flexible electrodes. *Sens. Actuators A Phys.* **2014**, *212*, 93–101. [CrossRef]
20. Jia, M.; Li, X.; Song, Z.; Bao, M.; Wang, Y.; Yang, H. Micro-cantilever shocking-acceleration switches with threshold adjusting and 'on'-state latching functions. *J. Micromech. Microeng.* **2007**, *17*, 567–575. [CrossRef]
21. Guo, Z.Y.; Yang, Z.C.; Lin, L.T.; Zhao, Q.C.; Ding, H.T.; Liu, X.S.; Chi, X.Z.; Cui, J.; Yan, G.Z. A Latching acceleration switch with multi-contacts independent to the proof-mass. In Proceedings of the 2009 IEEE 22nd International Conference on Micro Electro Mechanical Systems, Sorrento, Italy, 25–29 January 2009; pp. 813–816.
22. Guo, Z.Y.; Zhao, Q.C.; Lin, L.T.; Ding, H.T.; Liu, X.S.; Cui, J.; Yang, Z.C.; Xie, H.; Yan, G.Z. An acceleration switch with a robust latching mechanism and cylindrical contacts. *J. Micromech. Microeng.* **2010**, *20*, 055006. [CrossRef]
23. Brake, M.R.; Baker, M.S.; Moore, N.W.; Crowson, D.A.; Mitchell, J.A.; Houston, J.E. Modeling and Measurement of a Bistable Beam in a Microelectromechanical System. *J. Microelectromech. Syst.* **2010**, *19*, 1503–1514. [CrossRef]
24. Frangi, A.; De Masi, B.; Confalonieri, F.; Zerbini, S. Threshold Shock Sensor Based on a Bistable Mechanism: Design, Modeling, and Measurements. *J. Microelectromech. Syst.* **2015**, *24*, 2019–2026. [CrossRef]
25. Tsay, J.; Su, L.Q.; Sung, C.K. Design of a linear micro-feeding system featuring bistable mechanisms. *J. Micromech. Microeng.* **2005**, *15*, 63–70. [CrossRef]

26. Zhao, J.; Yang, Y.; Wang, H.; Jia, J. A Novel Magnetic Actuated Bistable Acceleration Switch with Low Contact Resistance. *IEEE Sens. J.* **2010**, *10*, 869–876. [CrossRef]
27. Huang, Y.C.; Sung, W.L.; Lai, W.C.; Liu, C.Y.; Fang, W. Design and implementation of time-delay switch triggered by inertia load. In Proceedings of the 2013 IEEE 26th International Conference on Micro Electro Mechanical Systems (MEMS), Taipei, Taiwan, 20–24 January 2013; pp. 729–732.
28. Kuo, J.C.; Yang, Y.J. A passive hydrogel-based inertial switch integrated with micromachined LC resonator. In Proceedings of the 2012 IEEE 25th International Conference on Micro Electro Mechanical Systems (MEMS), Paris, France, 29 January–2 February 2012; pp. 515–518.
29. Nie, W.; Liu, G.; Zhang, R. Microfluidic inertial switch with delay response characteristics. *J. Phys. Conf. Ser.* **2020**, *1507*, 102001. [CrossRef]
30. Shen, T.; Zhang, D.; Huang, L.; Wang, J. An automatic-recovery inertial switch based on a gallium-indium metal droplet. *J. Micromech. Microeng.* **2016**, *26*, 115016. [CrossRef]
31. Liu, T.; Su, W.; Yang, T.; Xu, Y. Vibration interference analysis and verification of micro-fluidic inertial switch. *AIP Adv.* **2014**, *4*, 031313.
32. Yang, Z.; Ding, G.; Cai, H.; Zhao, X. A MEMS Inertia Switch with Bridge-Type Elastic Fixed Electrode for Long Duration Contact. *IEEE Trans. Electron Devices* **2008**, *55*, 2492–2497. [CrossRef]
33. Yang, Z.; Ding, G.; Cai, H.; Wang, H.; Chen, W.; Zhao, X. Development of a shock acceleration microswitch with enhanced-contact and low off-axis sensitivity. In Proceedings of the TRANSDUCERS 2009–2009 International Solid-State Sensors, Actuators and Microsystems Conference, Denver, CO, USA, 21–25 June 2009; pp. 1940–1943.
34. Cai, H.; Yang, Z.; Ding, G.; Wang, H. Development of a Novel MEMS Inertial Switch with a Compliant Stationary Electrode. *IEEE Sens. J.* **2009**, *9*, 801–808. [CrossRef]
35. Zhang, Q.; Yang, Z.; Xu, Q.; Wang, Y.; Ding, G.; Zhao, X. Design and fabrication of a laterally-driven inertial micro-switch with multi-directional constraint structures for lowering off-axis sensitivity. *J. Micromech. Microeng.* **2016**, *26*, 055008. [CrossRef]
36. Yang, Z.; Shi, J.; Yao, J.; Zhang, X.; Ding, G.; Zhao, X. A Laterally Driven MEMS Inertial Switch with Double-Layer Suspended Springs for Improving Single-Axis Sensitivity. *IEEE Trans. Compon. Packag. Manuf. Technol.* **2018**, *8*, 1845–1854. [CrossRef]
37. Fathalilou, M.; Soltani, K.; Rezazadeh, G.; Cigeroglu, E. Enhancement of the reliability of MEMS shock sensors by adopting a dual-mass model. *Measurement* **2020**, *153*, 107428. [CrossRef]
38. Ren, C.; Wang, K.; Zhang, P.; Li, Y.; Zhao, Z.; Shi, X.; Zhang, H.; Tao, K.; Yang, Z. A Self-Powered MEMS Inertial Switch for Potential Zero Power-Consumption Wake-Up Application. *J. Microelectromech. Syst.* **2021**, *30*, 550–559. [CrossRef]
39. Raghunathan, N.; Tsutsui, W.; Chen, W.; Peroulis, D. A single crystal silicon low-g switch tolerant to impact accelerations up to 24,000 g. In Proceedings of the 2015 Transducers—2015 18th International Conference on Solid-State Sensors, Actuators and Microsystems (TRANSDUCERS), Anchorage, AK, USA, 21–25 June 2015; pp. 1144–1147.
40. Kansal, P.; Kasturi, P.; Kim, N.H.; Jang, S.G. Sensitivity-Based Reliability Analysis of MEMS Acceleration Switch. *Mod. Appl. Sci.* **2017**, *11*, 123–136. [CrossRef]
41. Yang, Z.; Cai, H.; Ding, G.; Wang, H.; Zhao, X. Dynamic simulation of a contact-enhanced MEMS inertial switch in Simulink®. *Microsyst. Technol.* **2011**, *17*, 1329–1342. [CrossRef]
42. Chen, W.; Wang, Y.; Wang, Y.; Zhu, B.; Ding, G.; Wang, H.; Zhao, X.; Yang, Z. A laterally-driven micromachined inertial switch with a compliant cantilever beam as the stationary electrode for prolonging contact time. *J. Micromech. Microeng.* **2014**, *24*, 065020. [CrossRef]
43. Jean, D.; Smith, G.; Kunstmann, J. MEMS Multi-Directional Shock Sensor with Multiple Masses. U.S. Patent 7194889, 27 March 2007.
44. Rödjegård, H.; Andersson, G.I.; Rusu, C.; Löfgren, M.; Billger, D. Capacitive slanted-beam three-axis accelerometer: I. Modelling and design. *J. Micromech. Microeng.* **2005**, *15*, 1989–1996. [CrossRef]
45. Wang, X.H.; Chen, Z.H.; Xiao, D.B.; Wu, X.Z. Design and Analysis of a Monolithic 3-Axis Micro-Accelerometer. *Key Eng. Mater.* **2012**, *503*, 122–127. [CrossRef]
46. Bütefisch, S.; Schoft, A.; Büttgenbach, S. Three-Axes Monolithic Silicon Low-g Accelerometer. *J. Microelectromech. Syst.* **2000**, *9*, 551–556. [CrossRef]
47. Greywall, D.S. MEMS-Based Inertial Switch. U.S. Patent 7218193, 15 May 2007.
48. Lin, L.; Zhao, Q.; Yang, Z.; Zhang, D.; Yan, G. Design and simulation of a 2-axis low g acceleration switch with multi-folded beams. In Proceedings of the 2014 12th IEEE International Conference on Solid-State and Integrated Circuit Technology (ICSICT), Guilin, China, 28–31 October 2014; pp. 1–3.
49. Niyazi, A.; Xu, Q.; Khan, F.; Younis, M.I. Design, Modeling, and Testing of a Bidirectional Multi-Threshold MEMS Inertial Switch. *Sens. Actuators A Phys.* **2021**, *334*, 113219. [CrossRef]
50. Xu, Q.; Wang, L.; Niyazi, A.; Younis, M.I. Multi-Threshold MEMS Shock Sensor for Quantitative Acceleration Measerements. In Proceedings of the 2021 21st International Conference on Solid-State Sensors, Actuators and Microsystems (Transducers), Orlando, FL, USA, 20–24 June 2021; pp. 120–123.
51. Currano, L.J.; Becker, C.R.; Smith, G.; Isaacson, B.; Morris, C.J. 3-Axis acceleration switch for traumatic brain injury early warning. In Proceedings of the 2012 IEEE 25th International Conference on Micro Electro Mechanical Systems (MEMS), Paris, France, 29 January–2 February 2012; pp. 484–487.
52. Liu, S.; Hao, Y.; Wang, S.; Li, D. MEMS-based Low-g Inertial Switch. *Sens. Transducers* **2014**, *176*, 78.

53. Yang, Z.; Zhu, B.; Chen, W.; Ding, G.; Wang, H.; Zhao, X. Fabrication and characterization of a multidirectional-sensitive contact-enhanced inertial microswitch with a electrophoretic flexible composite fixed electrode. *J. Micromech. Microeng.* **2012**, *22*, 045006. [CrossRef]
54. Du, L.; Li, Y.; Zhao, J.; Wang, W.; Zhao, W.; Zhao, W.; Zhu, H. A low-g MEMS inertial switch with a novel radial electrode for uniform omnidirectional sensitivity. *Sens. Actuators A Phys.* **2018**, *270*, 214–222. [CrossRef]
55. Du, L.; Yu, Y.; Yuan, B.; Guo, B.; Wang, C.; Du, C.; Liu, J. A low-g omnidirectional MEMS inertial switch with load direction identification. *Microelectron. Eng.* **2021**, 111679. [CrossRef]
56. Chen, W.; Wang, R.; Wang, H.; Sun, S. The Design, Simulation and Fabrication of an Omnidirectional Inertial Switch with Rectangular Suspension Spring. *Micromachines* **2021**, *12*, 440. [CrossRef]
57. Chen, W.; Wang, Y.; Zhang, Y.; Cheng, P.; Wang, Y.; Ding, G.; Zhao, X.; Yang, Z. Fabrication of a novel contact-enhanced horizontal sensitive inertial micro-switch with electroplating nickel. *Microelectron. Eng.* **2014**, *127*, 21–27. [CrossRef]
58. Xiong, Z.; Zhang, F.; Pu, Y.; Tang, B.; Yang, J.; Wang, C. Silicon-based, low-g microelectromechanical systems inertial switch for linear acceleration sensing application. *Micro Nano Lett.* **2015**, *10*, 347–350. [CrossRef]
59. Zhang, F.; Wang, C.; Yuan, M.; Tang, B.; Xiong, Z. Conception, fabrication and characterization of a silicon based MEMS inertial switch with a threshold value of 5 g. *J. Micromech. Microeng.* **2017**, *27*, 125001. [CrossRef]
60. Xiong, Z.; Wang, C.; Zhang, F.; Xie, J.; Shen, Z.; Tang, B. A Low-g MEMS Inertial Switch Based on Direct Contact Sensing Method. *IEEE Trans. Compon. Packag. Manuf. Technol.* **2019**, *9*, 1535–1541. [CrossRef]
61. Field, R.V.; Epp, D.S. Development and calibration of a stochastic dynamics model for the design of a MEMS inertial switch. *Sens. Actuators A Phys.* **2007**, *134*, 109–118. [CrossRef]
62. Hwang, J.; Ryu, D.; Park, C.; Jang, S.G.; Lee, C.I.; Kim, Y.K. Design and fabrication of a silicon-based MEMS acceleration switch working lower than 10 g. *J. Micromech. Microeng.* **2017**, *27*, 065009. [CrossRef]
63. Massad, J.E.; Sumall, H.; Epp, D.S.; Dyck, C.W. Modeling, Simulation, and Testing of the Mechanical Dynamics of an RF MEMS Switch. In Proceedings of the 2005 International Conference on MEMS, NANO and Smart Systems, Banff, AB, Canada, 24–27 July 2005; pp. 237–240.
64. Nie, W.-R.; Xi, Z.-W.; Xue, W.-Q.; Zhou, Z.-J. Study on Inertial Response Performance of a Micro Electrical Switch for Fuze. *Def. Technol.* **2013**, *9*, 187–192. [CrossRef]
65. Singh, V.; Kumar, V.; Saini, A.; Khosla, P.K.; Mishra, S. Design and Development of the MEMS-Based High-g Acceleration Threshold Switch. *J. Microelectromech. Syst.* **2021**, *30*, 24–31. [CrossRef]
66. Singh, V.; Kumar, V.; Saini, A.; Khosla, P.K.; Mishra, S. Response analysis of MEMS based high-g acceleration threshold switch under mechanical shock. *Int. J. Mech. Mater. Des.* **2020**, *17*, 137–151. [CrossRef]
67. Xu, Q.; Sun, B.; Li, Y.; Xiang, X.; Lai, L.; Li, J.; Ding, G.; Zhao, X.; Yang, Z. Design and characterization of an inertial microswitch with synchronous follow-up flexible compliant electrodes capable of extending contact duration. *Sens. Actuators A Phys.* **2018**, *270*, 34–45. [CrossRef]
68. Xi, Z.; Kong, N.; Nie, W.; Cao, Y.; Zheng, C. High g MEMS inertial switch capable of direction detection. *Sens. Actuators A Phys.* **2019**, *296*, 7–16. [CrossRef]
69. Kim, H.S.; Kim, J.M.; Kim, Y.K.; Jang, Y.H. MEMS acceleration switch capable of increasing threshold acceleration. *Electron. Lett.* **2012**, *48*, 1614–1616. [CrossRef]
70. Kumar, V.; Jafari, R.; Pourkamali, S. Ultra-Low Power Digitally Operated Tunable MEMS Accelerometer. *IEEE Sens. J.* **2016**, *16*, 8715–8721. [CrossRef]
71. Ma, C.W.; Huang, P.C.; Kuo, J.C.; Kuo, W.C.; Yang, Y.J. A novel inertial switch with an adjustable acceleration threshold using an MEMS digital-to-analog converter. *Microelectron. Eng.* **2013**, *110*, 374–380. [CrossRef]
72. Abbasalipour, A.; Nikfarjam, H.; Pourkamali, S. An 8-Bit Digitally Operated Micromachined Accelerometer. *J. Microelectromech. Syst.* **2020**, *29*, 1132–1136. [CrossRef]
73. Yang, Z.; Ding, G.; Cai, H.; Xu, X.; Wang, H.; Zhao, X. Analysis and elimination of the 'skip contact' phenomenon in an inertial micro-switch for prolonging its contact time. *J. Micromech. Microeng.* **2009**, *19*, 045017. [CrossRef]
74. Yang, Z.; Ding, G.; Chen, W.; Fu, S.; Sun, X.; Zhao, X. Design, simulation and characterization of an inertia micro-switch fabricated by non-silicon surface micromachining. *J. Micromech. Microeng.* **2007**, *17*, 1598–1604. [CrossRef]
75. Lee, J.I.; Song, Y.; Jung, H.K.; Choi, J.; Eun, Y.; Kim, J. Carbon nanotubes-integrated inertial switch for reliable detection of threshold acceleration. In Proceedings of the 2011 16th International Solid-State Sensors, Actuators and Microsystems Conference, Beijing, China, 5–9 June 2011; pp. 711–714.
76. Choi, J.; Lee, J.I.; Eun, Y.; Kim, M.O.; Kim, J. Aligned carbon nanotube arrays for degradation-resistant, intimate contact in micromechanical devices. *Adv. Mater.* **2011**, *23*, 2231–2236. [CrossRef]
77. Yang, Z.; Zhu, B.; Ding, G.; Wang, H.; Wang, Y.; Zhao, X. A multidirectional-sensitive inertial microswitch with electrophoretic polymer-metal composite fixed electrode for flexible contact. In Proceedings of the 2012 IEEE 25th International Conference on Micro Electro Mechanical Systems (MEMS), Paris, France, 29 January–2 February 2012; pp. 504–507.
78. Wang, Y.; Yang, Z.; Xu, Q.; Chen, W.; Ding, G.; Zhao, X. Design, simulation and characterization of a MEMS inertia switch with flexible CNTs/Cu composite array layer between electrodes for prolonging contact time. *J. Micromech. Microeng.* **2015**, *25*, 085012. [CrossRef]

79. Li, J.; Wang, Y.; Li, Y.; Fu, B.; Sun, Y.; Yao, J.; Ding, G.; Zhao, X.; Yang, Z. A contact-enhanced MEMS inertial switch with electrostatic force assistance and multi-step pulling action for prolonging contact time. *Microsyst. Technol.* **2018**, *24*, 3179–3191. [CrossRef]
80. Lee, Y.; Sim, S.M.; Kim, H.; Kim, Y.K.; Kim, J.M. Silicon MEMS acceleration switch with high reliability using hooked latch. *Microelectron. Eng.* **2016**, *152*, 10–19. [CrossRef]
81. Reddy, R.R.; Komeda, K.; Okamoto, Y.; Lebrasseur, E.; Higo, A.; Mita, Y. A zero-power sensing MEMS shock sensor with a latch-reset mechanism for multi-threshold events monitoring. *Sens. Actuators A Phys.* **2019**, *295*, 1–10. [CrossRef]
82. Ramanathan, M.; Murali, N.; Sen, P.; Pratap, R. A parametric analysis based design framework for MEMS g-switch accelerometers. *Sens. Actuators A Phys.* **2021**, *318*, 112423. [CrossRef]
83. Currano, L.J.; Bauman, S.; Churaman, W.; Peckerar, M.; Wienke, J.; Kim, S.; Yu, M.; Balachandran, B. Latching ultra-low power MEMS shock sensors for acceleration monitoring. *Sens. Actuators A Phys.* **2008**, *147*, 490–497. [CrossRef]
84. Zhang, X.; Xiang, X.; Wang, Y.; Ding, G.; Xu, X.; Yang, Z. A Heterogeneous Integrated MEMS Inertial Switch with Compliant Cantilevers Fixed Electrode and Electrostatic Locking to Realize Stable On-State. *J. Microelectromech. Syst.* **2019**, *28*, 977–986. [CrossRef]
85. Masters, N.D.; Howell, L.L. A Self-Retracting Fully-Compliant Bistable Micromechanism. *J. Microelectromech. Syst.* **2003**, *12*, 273–280. [CrossRef]
86. Hansen, B.J.; Carron, C.J.; Jensen, B.D.; Hawkins, A.R.; Schultz, S.M. Plastic latching accelerometer based on bistable compliant mechanisms. *Smart Mater. Struct.* **2007**, *16*, 1967–1972. [CrossRef]
87. Eldred, M.; Subia, S.; Neckels, D.; Hopkins, M.; Notz, P.; Adams, B.; Carnes, B.; Wittwer, J.; Bichon, B.; Copps, K.D. *Solution-Verified Reliability Analysis and Design of Bistable MEMS Using Error Estimation and Adaptivity*; Sandia Technical Reports; SAND: Livermore, CA, USA, 2006; pp. 2006–6286.
88. Zhao, J.; Liu, P.; Tang, Z.; Fan, K.; Ma, X.; Gao, R.; Bao, J. A Wireless MEMS Inertial Switch for Measuring Both Threshold Triggering Acceleration and Response Time. *IEEE Trans. Instrum. Meas.* **2014**, *63*, 3152–3161. [CrossRef]
89. Liu, M.; Zhu, Y.; Wang, C.; Chen, Y.; Wu, Y.; Zhang, H.; Du, Y.; Wang, W. A Novel Low-g MEMS Bistable Inertial Switch with Self-Locking and Reverse-Unlocking Functions. *J. Microelectromech. Syst.* **2020**, *29*, 1493–1503. [CrossRef]
90. Kim, J.; Shen, W.; Latorre, L.; Kim, C.J. A micromechanical switch with electrostatically driven liquid-metal droplet. *Sens. Actuators A Phys.* **2002**, *97*, 672–679. [CrossRef]
91. Yoo, K.; Park, U.; Kim, J. Development and characterization of a novel configurable MEMS inertial switch using a microscale liquid-metal droplet in a microstructured channel. *Sens. Actuators A Phys.* **2011**, *166*, 234–240. [CrossRef]
92. Kuo, J.C.; Kuo, P.H.; Lai, Y.T.; Ma, C.W.; Lu, S.S.; Yang, Y.J.J. A Passive Inertial Switch Using MWCNT–Hydrogel Composite with Wireless Interrogation Capability. *J. Microelectromech. Syst.* **2013**, *22*, 646–654. [CrossRef]
93. Liu, J.; Liu, Z.; Zhang, S.; Tan, Z. An Automatic-Recovery Inertial Switch Based on the Galinstan Marbles. In Proceedings of the 2021 IEEE 34th International Conference on Micro Electro Mechanical Systems (MEMS), Gainesville, FL, USA, 25–29 January 2021; pp. 818–821.
94. Lin, Y.; Yang, T.; Liu, T.T.; Chen, G.Y.; Wang, C. Analysis and Simulation of Micro-Fluidic Inertial Switch. *Key Eng. Mater.* **2012**, *503*, 348–353. [CrossRef]
95. Liu, T.T.; Su, W.; Wang, C.; Yang, T. Threshold Model of Micro-Fluidic Inertial Switch Based on Orthogonal Regression Design. *Key Eng. Mater.* **2015**, *645–646*, 455–461. [CrossRef]
96. Huh, M.; Won, D.J.; Kim, J.G.; Kim, J. Simple and robust resistive dual-axis accelerometer using a liquid metal droplet. *Micro Nano Syst. Lett.* **2017**, *5*, 5. [CrossRef]
97. Won, D.J.; Huh, M.; Lee, S.; Park, U.; Yoo, D.; Kim, J. Capacitive-Type Two-Axis Accelerometer with Liquid-Type Proof Mass. *Adv. Electron. Mater.* **2020**, *6*, 1901265. [CrossRef]
98. Liu, T.L.; Sen, P.; Kim, C.J.C. Characterization of liquid-metal Galinstan® for droplet applications. In Proceedings of the 2010 IEEE 23rd International Conference on Micro Electro Mechanical Systems (MEMS), Hong Kong, China, 24–28 January 2010; pp. 560–563.

micromachines

Article

Hydrogen Storage Performance of γ-Graphdiyne Doped Li Based on First Principles for Micro/Nano

Wenchao Tian *, Zhao Li, Chunmin Cheng, Wenhua Li, Zhiqiang Chen and Fei Xin

School of Electro-Mechanical Engineering, Xidian University, Xi'an 710000, China; zhaoli960628@163.com (Z.L.); cmcheng@whu.edu.cn (C.C.); whli@stu.xidian.edu.cn (W.L.); zqchen@xidian.edu.cn (Z.C.); fxin@xidian.edu.cn (F.X.)

* Correspondence: wctian@xidian.edu.cn; Tel.: +86-029-8820-3040

Abstract: The rapid development of micro/nano systems promotes the progress of micro energy storage devices. As one of the most significant representatives of micro energy storage devices, micro hydrogen fuel cells were initially studied by many laboratories and companies. However, hydrogen storage problems have restricted its further commercialization. The γ-graphdiyne (γ-GDY) has broad application prospects in the fields of energy storage and gas adsorption due to its unique structure with rigid nano-network and numerous uniform pores. However, the existence of various defects in γ-GDY caused varying degrees of influence on gas adsorption performance. In this study, Lithium (Li) was added into the intrinsic γ-GDY and vacancy defect γ-GDY (γ-VGDY) to obtain the Li-GDY and Li-VGDY, respectively. The first-principles calculation method was applied and the hydrogen storage performances of them were analysed. The results indicated that the best adsorption point of intrinsic γ-GDY is H2 point, which located at the centre of a large triangular hole of an acetylene chain. With large capacity hydrogen storage, doping Li atom could improve the hydrogen adsorption property of intrinsic γ-GDY; meanwhile, vacancy defect inspires the hydrogen storage performance further of Li-VGDY. The mass hydrogen storage density for Li_2H_{56}-GDY and Li_2H_{56}-VGDY model were 13.02% and 14.66%, respectively. Moreover, the Li_2H_{56}-GDY and Li_2H_{56}-VGDY model had same volumetric storage density, with values that could achieve 5.22×10^4 kg/m^3.

Keywords: γ-GDY; first-principles; dope; vacancy defect; hydrogen storage property

Citation: Tian, W.; Li, Z.; Cheng, C.; Li, W.; Chen, Z.; Xin, F. Hydrogen Storage Performance of γ-Graphdiyne Doped Li Based on First Principles for Micro/Nano. *Micromachines* **2022**, *13*, 547. https://doi.org/10.3390/mi13040547

Academic Editor: Aiqun Liu

Received: 20 December 2021
Accepted: 23 March 2022
Published: 30 March 2022

1. Introduction

Micro energy storage devices are the power core of micro/nano systems, which have been widely used in the field of microelectromechanical systems, micro/nano robots, smart portable/wearable systems and micro-implantable medical sensors, etc. The development of micro and nano technology drives the developing trend of micro/nano systems towards miniaturization, systematic and intelligence, etc. Thus, higher requirements have been proposed for its energy storage components, such as micro volume, high power and long reliability etc. [1–4].

Micro batteries, such as Li+ [5] micro batteries, Na+ [6] micro batteries and micro fuel cells [7], are common micro energy storage devices in the micro/nano system. Among them, micro fuel cells have been regarded as one of the key technologies in the field of energy due to their excellent advantages with high energy conversion efficiency, large output power and non-pollution, etc. In addition, as an ideal secondary energy, hydrogen energy has recently been considered as a green and strategic energy by the international community [8–10]. Therefore, the research and development of hydrogen fuel cells has been widely accepted by many scholars and laboratories. Meanwhile, many companies have conducted research for the commercialization of micro fuel cells actively [11]. However, in order to meet the requirements of portability and high energy density for the hydrogen micro fuel cell, it is critical to solve the problem of hydrogen storage [12–14].

Hydrogen storage methods mainly include high-pressure gaseous hydrogen storage, liquid hydrogen storage and solid hydrogen storage. Solid hydrogen storage in particular can effectively overcome the shortage of gaseous and liquid hydrogen storage with convenient transportation, high storage density and safety coefficient, etc. Carbon-based hydrogen storage materials, such as carbon nanotubes [15], activated carbon [16] and graphene [17] etc., were considered as promising solid hydrogen storage materials due to its outstanding hydrogen adsorption and release properties. Yang et al. [18] studied the hydrogen storage property of a sandwich structure composed of a carbon nitride and two graphene sheets based on the first principles. The results indicated that hydrogen could be blocked by the graphene completely and stored in this sandwich structure with higher density. Liu et al. [19] studied the hydrogen adsorption performance of Li decorated C68-GY. The results indicated that the hydrogen storage density is 8.04 wt% with adsorption energy of -0.227. Moreover, hydrogen binds with Li/C through polarization and H–H interaction among molecules. Cui et al. [20] and Liu et al. [21] studied hydrogen storage property of Ti decorated double vacancy graphene and porous graphene, respectively. Calculation results shown that the hydrogen adsorption capacity of decreased 33% after doped with Ti, in contrast, Ti-porous graphene system possessed excellent hydrogen storage property.

Graphdiyne (GDY), as a new type of all-carbon molecule, was synthesized through an in situ chemical method for the first time on a copper surface according to the research of Li et al. [22]. It has a unique 1,3-diacetylene bond [23], which can conjugate with the benzene ring to form a two-dimensional planar network structure. Meanwhile, the large triangular rings in GDY formed by alkyne bond and benzene ring improved the pore size to 0.25 nm [24]. In addition, the GDY has many excellent properties, such as, rich carbon chemical bonds, large conjugate system and better ion shuttling etc., which can maintain the long reliability of device [25]. Due to these advantages, the GDY has huge potential for its application in the field of hydrogen storage. Zhang et al. [26] investigated the intercalation and diffusion of hydrogen in the single layer and bulk GDY. The results for the first time revealed that the GDY possessed excellent hydrogen storage performance. Panigrahi et al. [27] studied the hydrogen storage property of GDY doped with light metal (Li, Na, K, Ca, Sc and Ti). Computation results showed that the Li-GDY possessed the highest hydrogen storage capacity, which reached 6.5 wt%.

Many studies of hydrogen storage equipment have focused on carbon materials, especially in the *GDY* materials. In this study, the hydrogen absorption properties of *GDY* modified structures doped with Li or vacancy defect were investigated. The calculation results were essential to understanding and analysing the adsorption mechanism and broadening the practical applications in the field of hydrogen storage.

2. Simulation Methods and Computation Models

2.1. Simulation Methods

In this study, the first-principles calculation method based on density functional theory was adopted, and CASTEP program package in Materials Studio software was used. The electron exchange correlation potential selected the Perdew–Burke–Ernzerhof (PBE) functional of generalized gradient approximation (GGA) [28,29]. The X and Y directions were superposed and the Z direction was erected to the graphene plane, respectively, to obtain calculation results. The vacuum layer was 20 Å. In order to acquire stable total system energy, considering the factors of calculation accuracy and efficiency, the plane wave truncation energy with 600 eV and the Brillouin zone K point of Monkhorst-Pack with $6 \times 6 \times 1$ were selected, respectively. The above simulation parameters can ensure that the total energy error of the system convergence was not more than 2×10^{-5} eV/atom.

2.2. Computation Models

Figure 1a,b show the computation models of hydrogen molecule and Li atom, respectively. The optimized structures of hydrogen molecule and Li atom were obtained through the CASTEP of Materials studio. The steady-state energy of hydrogen molecule (E_{H_2}) was

−31.67 eV, and the bond length of hydrogen-hydrogen was 0.746 Å. The steady-state energy of Li atom (E_{Li}) was −188.20 eV.

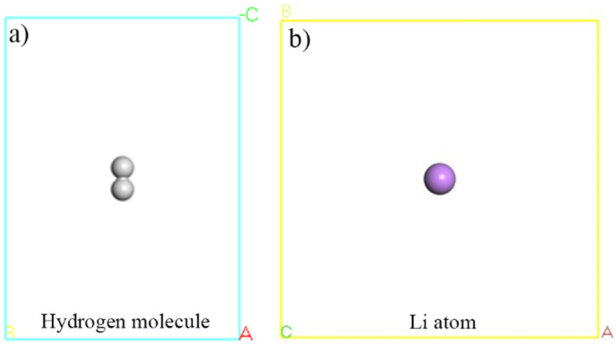

Figure 1. Computation models of hydrogen molecule and Li atom.

Figure 2 shows the initial simulation model of intrinsic γ-GDY, which is a 2 × 2 supercell, and the steady-state energy is −11,111.919 eV. In this figure, there are four different carbon–carbon (C-C) bonds, and the bond length of aromatic bond (C_1-C_2), C–C single bond (C_1-C_3), C–C triple bond (C_3-C_4), and C–C single bond (C_4-C_5) are 1.430 Å, 1.392 Å, 1.232 Å and 1.334 Å, respectively. Several related research reported the C–C bond length of γ-GDY and their results are listed in Table 1, which proved that the intrinsic γ-GDY in this study is reasonable and could be used to simulate the hydrogen adsorption process.

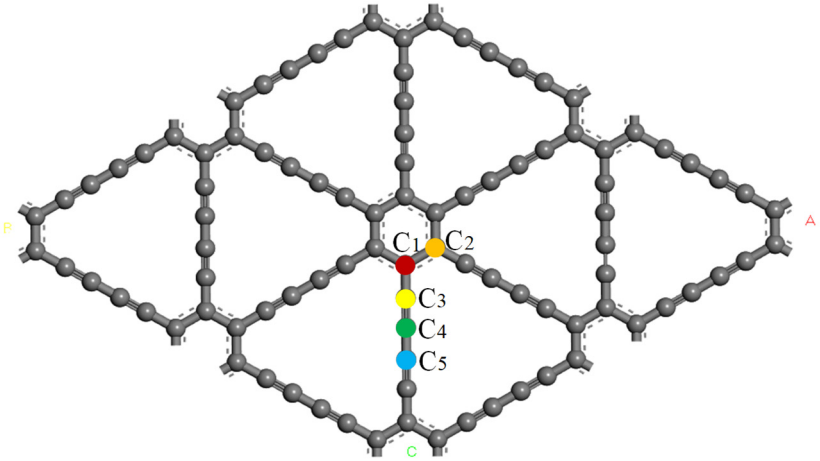

Figure 2. Supercell structure of intrinsic γ-GDY models.

Table 1. Related research of the C-C bond length of intrinsic γ-GDY.

References	C-C Single Bond (Å)	C-C Triple Bond (Å)	Aromatic Bond (Å)
Cranford [30]	1.460~1.480	1.180~1.190	1.480~1.500
Bai [31]	1.341~1.400	1.239	1.440
Mirnezhad [32]	1.404	1.219	1.423
Peng [33]	1.407	1.223	1.426
Pei [34]	1.340~1.400	1.230	1.430

Due to the particularity of the acetylene bond in the intrinsic γ-GDY structure and the similarities and differences of the C–C bond length, nine highly symmetric adsorption points were selected during the hydrogen adsorption process. Figure 3 shows the schematic diagram of nine highly symmetric adsorption points of the γ-GDY models. According to the difference location of points, three groups are divided as presented in Figure 3. Two points located at the centre of the pore were defined as hole (H). Bridge (B) referred four points in the middle of the C–C bond. Additionally, top (T) showed three points at the

directly above of the carbon (C) atom. The supercell structure of the γ-GDY was the critical factor for all points selection. H1 and H2 points were located in the centre of the benzene ring and the large triangular hole composed of the acetylene chain, respectively, and the selection of them based on all pores structure of the supercell structure. The types of all C–C bonds in the supercell structure were the crucial selection factors of B points. The C-C bond of the benzene ring referred to B1 points, the C–C single bond and triple bonds of the ethyne chain were defined as B2 and B3 points, respectively, and B4 points showed the C–C single bond which connected two C–C triple bonds. According to the hybridization mode of different C atoms in the supercell structure, the C atom on the benzene ring was selected as T1 point, and the two C atoms on the ethyne bond were selected as T2 and T3 points, respectively.

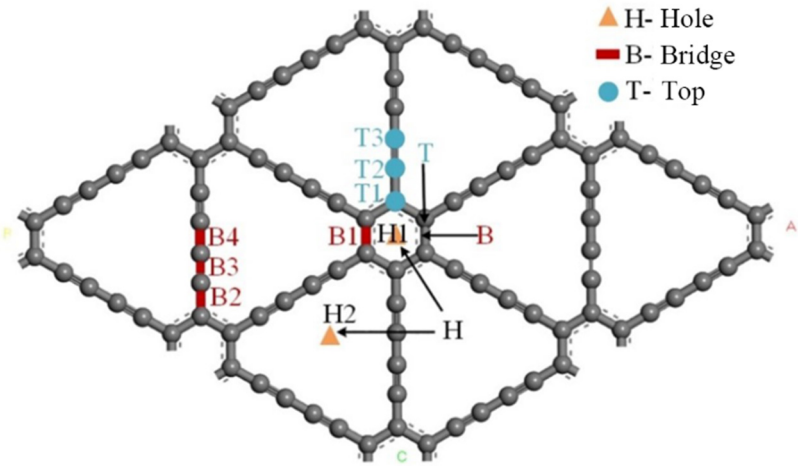

Figure 3. Schematic diagram of the nine highly symmetric adsorption points of intrinsic γ-GDY models.

Vacancy defect occurs in carbon materials inevitably. As shown in Figures 2 and 3, the intrinsic γ–GDY is divided into two symmetrical parts by the ethyne chain. The missing ethyne chain forms a new structure, known as vacancy defect γ-GDY (γ-VGDY), composed of four identical ethyne chains and a benzene ring. In order to analyse the effect of vacancy defect on the hydrogen storage performance, the γ-VGDY model is also established by the Materials studio software, as shown in Figure 4.

Figure 4. Schematic diagram of the γ-VGDY models.

3. Results and Discussion

3.1. Hydrogen Adsorption Property of Intrinsic γ-GDY

In order to investigate the hydrogen adsorption property of intrinsic γ-GDY, the hydrogen adsorption models of nine highly symmetric adsorption points are shown in Figure 5. The concentration of hydrogen molecule and initial adsorption height were set as 1 and 3 Å severally to obtain optimal hydrogen storage property. The hydrogen adsorption

energy of intrinsic γ-GDY at nine highly symmetric adsorption points was also calculated, which can be expressed in Equation (1):

$$E_{ads} = E_{GDY+H_2} - E_{GDY} - E_{H_2} \quad (1)$$

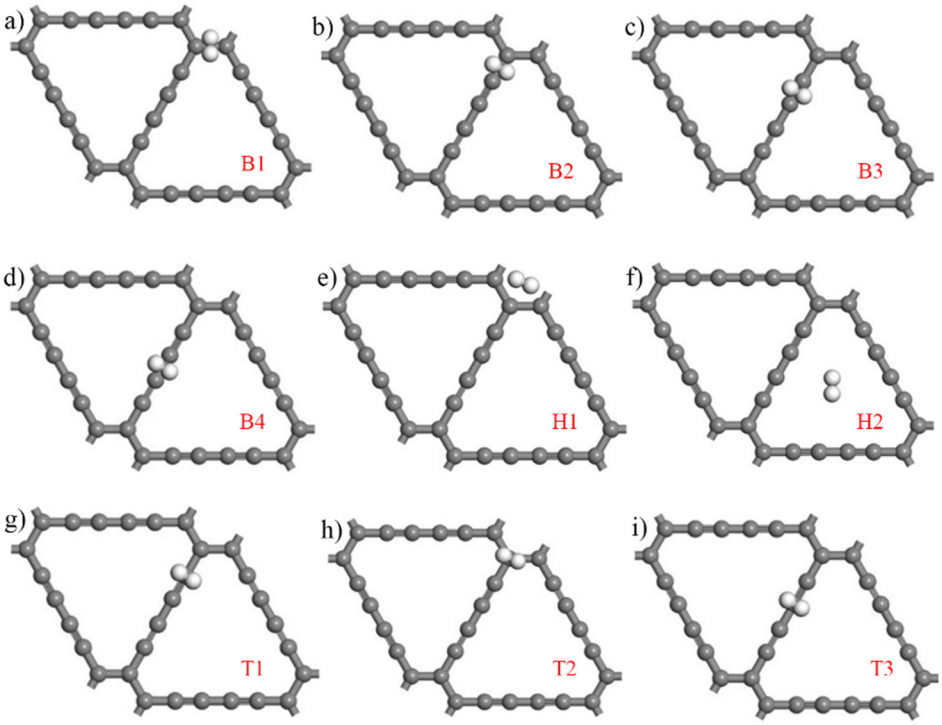

Figure 5. Hydrogen adsorption models of intrinsic γ-GDY at nine highly symmetric adsorption points. (Hydrogen molecules are expressed by white balls, (**a**–**i**) represent the hydrogen molecule adsorption points B1, B2, B3, B4, H1, H2, T1, T2 and T3, respectively).

Here, E_{GDY+H_2} is the total energy of intrinsic γ-GDY after adsorbing one hydrogen molecule, the E_{GDY} and E_{H_2} are the energy of intrinsic γ-GDY and single hydrogen molecule, respectively. If the adsorption energy is negative, it means that the system releases heat during the adsorption process, and the total energy of the system is reduced and the adsorption process more easily occurs. Thus, the higher the absolute value is, the easier the adsorption becomes. In contrast, when the adsorption energy is positive, this process needs to absorb heat, the higher absolute value shows that the adsorption of hydrogen is difficult. Table 2 shows the adsorption height and energy of nine points. As shown in this table, the H2 point possesses the largest absolute value of adsorption energy and lowest adsorption height for hydrogen, thus the H2 point is seen as the best adsorption point for intrinsic γ-GDY.

Table 2. Hydrogen adsorption height and adsorption energy of nine points.

Points	B1	B2	B3	B4	H1	H2	T1	T2	T3
Adsorption height (Å)	3.0018	3.0019	3.1911	3.1528	2.9425	2.8159	3.1024	3.1760	3.1748
Adsorption energy (eV)	−0.0215	−0.0216	−0.0315	−0.0277	−0.0326	−0.0786	−0.0289	−0.0340	−0.0281

3.2. Li Adsorption Property of Intrinsic γ-GDY and γ-VGDY

The H2 point shows the best performance of hydrogen adsorption in nine adsorption points, however, the lower adsorption energy indicates that the hydrogen storage property of intrinsic γ-GDY is not ideal. Thus, it is necessary to study the hydrogen storage property

of intrinsic γ-GDY doping with Li (Li-GDY). Figure 6 shows the initial Li atom adsorption models of intrinsic γ-GDY, which are named as the initial Li-GDY models. According to Table 2, the difference of adsorption energy values for B and T points are limited, thus the T and H points are selected to establish the adsorption models. Moreover, the Angle point (A) was introduced to enrich the diversity of simulation models. The adsorption energy of intrinsic γ-GDY to Li atom can be expressed in Equation (2):

$$E_{ads} = E_{GDY+Li} - E_{GDY} - E_{Li} \quad (2)$$

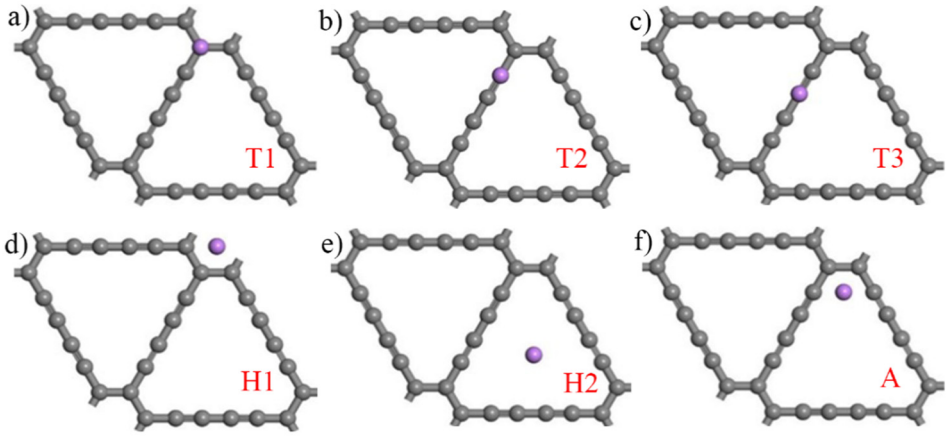

Figure 6. Six initial Li-GDY models (Purple ball is Li atom, (**a**–**f**) represent the Li atom adsorption points T1, T2, T3, H1, H2 and A, respectively).

Here, E_{GDY+Li} is the total energy of intrinsic γ-GDY after adsorbing one Li atom, the E_{GDY} and E_{Li} are the energy of intrinsic γ-GDY and single Li atom, respectively. The adsorption height and energy of intrinsic γ-GDY after doping Li atom is shown in Table 3. In this table, the adsorption energy of T1, T2, T3 and H1 points to Li atom are −1.991 eV, −1.983 eV, −2.021 eV and −1.979 eV, respectively. Meanwhile, the adsorption energy of H2 and A points to Li atom are −2.657 eV and −2.641 eV, respectively. The results indicate that the H2 and A points of intrinsic γ-GDY are the best dope points when doping a single Li atom. In the following simulation, the H2 point of intrinsic γ-GDY is selected as the dope point for the Li atom and the adsorption height is 0.084 Å.

Table 3. Adsorption height and adsorption energy of six points for Li-GDY.

Points	T1	T2	T3	H1	H2	A
Adsorption height (Å)	1.930	1.931	1.906	1.878	0.084	0.232
Adsorption energy (eV)	−1.991	−1.983	−2.021	−1.979	−2.657	−2.641

The analogous rhombic ring composed of four ethyne chains in γ-VGDY was the optimal dope area. Thus, the doping concentration of Li atoms was considered as the significant factor. Figure 7 shows the initial γ-VGDY models when doping different concentration Li atoms (Li-VGDY), which are named as the initial Li-VGDY models. The average adsorption energy of γ-VGDY to Li atoms can be expressed in Equation (3):

$$\overline{E_{ads}} = \left(E_{(x)Li+VGDY} - E_{VGDY} - xE_{Li}\right)/x \quad (3)$$

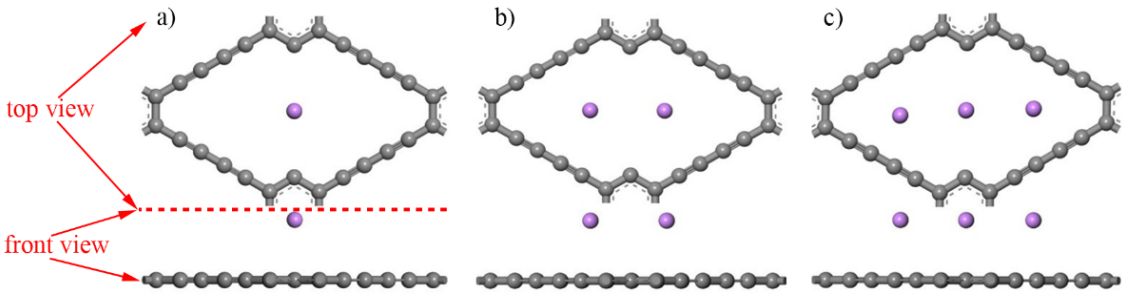

Figure 7. Three initial Li-VGDY models. (Purple ball is Li atom, (**a**–**c**) represent the Li atoms concentration 1, 2 and 3, respectively).

Here, $E_{(x)Li+VGDY}$ is the total energy of γ-VGDY after doping x Li atoms, the E_{VGDY} and E_{Li} are the energy of γ-VGDY and a single Li atom, respectively, x is the number of Li atoms. Table 4 shows the adsorption height and average adsorption energy of γ-VGDY after doping Li atoms. In this table, the average adsorption energy of γ-VGDY after doping 1, 2 and 3 Li atoms are −4.437 eV, −3.720 eV and −3.130 eV, respectively. Li-VGDY model possesses the maximal average adsorption energy, thus it is selected in the following simulation and the adsorption height of Li atom is 0.396 Å. In addition, compared with γ-GDY, the γ-VGDY expresses better doping ability of Li atoms.

Table 4. Adsorption height and adsorption energy of $Li_{(x)}$-VGDY.

Concentration	1	2	3
Adsorption height (Å)	0.396	0.402	1.253
Average adsorption energy (eV)	−4.437	−3.720	−3.310

3.3. Hydrogen Adsorption Property of Li-GDY and Li-VGDY

Because of the unacceptable hydrogen storage performance of intrinsic γ-GDY, the structure and energy of Li-GDY computation models were optimized. The adsorption characteristic parameters of LiH_{2N}-GDY system under the different density of hydrogen molecules were studied. Figure 8a–g show the hydrogen adsorption models of Li-GDY under different hydrogen concentrations (LiH_{2N}-GDY), which are named as the LiH_{2N}-GDY models. Graphene materials are permeable to hydrogen, even though it is defect free [35]. However, if hydrogen could be adsorbed on the γ-GDY by chemical bonding, it will be difficult to achieve the function of hydrogen permeation. Moreover, in order to determine the stability of hydrogen molecule adsorption on the Li-GDY surface, the adsorption energy of hydrogen (E_{ads}) was also calculated, which can be expressed in Equation (4) [19,36]:

$$E_{ads} = E_{GDY+(x)Li+(N)H_2} - E_{GDY+(x)Li+(N-1)H_2} - E_{H_2} \quad (4)$$

The average adsorption energy of hydrogen ($\overline{E_{ads}}$) can be described in Equation (5):

$$\overline{E_{ads}} = \left(E_{GDY+(x)Li+(N)H_2} - E_{GDY+(x)Li} - E_{(N)H_2}\right)/N \quad (5)$$

Here, $E_{GDY+(x)Li+(N)H_2}$ and $E_{GDY+(x)Li+(N-1)H_2}$ are the total energy of intrinsic γ-GDY doped x Li after adsorbing N and $N-1$ hydrogen molecules, respectively. $E_{GDY+(x)Li}$ is the total supercell energy of intrinsic γ-GDY doped x Li. E_{H_2} and $E_{(N)H_2}$ are the energy of single and N hydrogen molecules, respectively, and N is the number of hydrogen molecules.

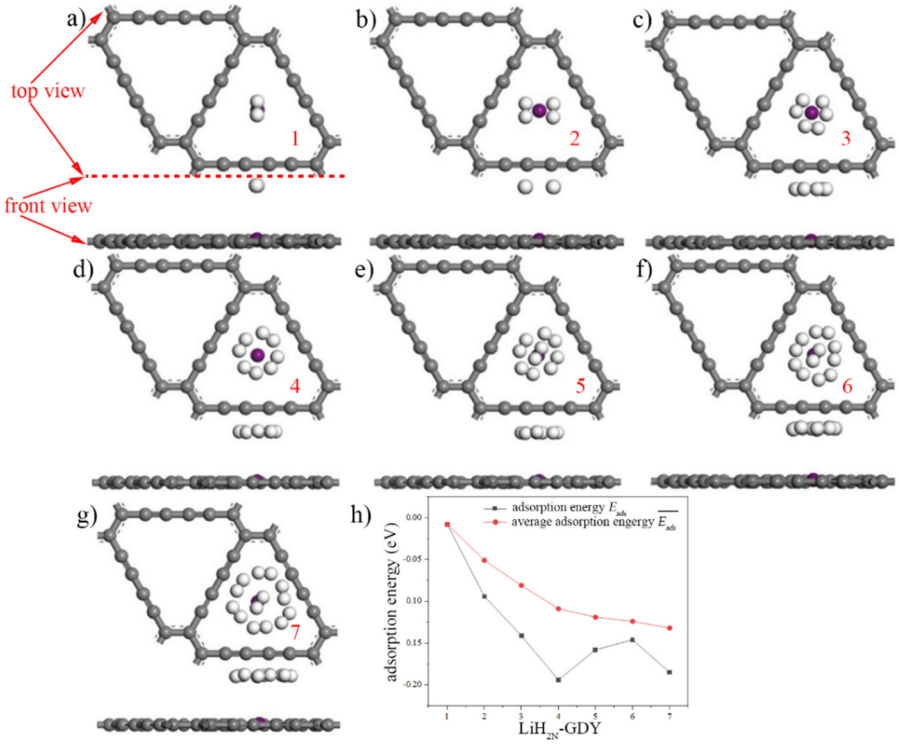

Figure 8. Seven LiH_{2N}-GDY models and adsorption energy. (Purple ball is Li atom, white balls are hydrogen molecules, (**a**–**h**) represent the LiH_{2N}-GDY models of hydrogen concentrations with 1, 2, 3, 4, 5, 6 and 7, respectively, (**h**) shows the hydrogen adsorption energy and average adsorption energy of Li-GDY).

Table 5 shows the hydrogen adsorption energy and average adsorption energy of Li-GDY. As shown in this table, when the concentration of hydrogen molecules exceeds three, the absolute value of average adsorption energy of Li-GDY surpasses the absolute value of adsorption energy of intrinsic γ-GDY in H2 point. This phenomenon indicates that Li-GDY shows better hydrogen storage property compared to the intrinsic γ-GDY when in large capacity hydrogen storage. Thus, the hydrogen storage property of intrinsic γ-GDY could be improved by the doping Li atom. When the hydrogen molecular concentration is four, the adsorption energy reaches the peak, and the value is −0.194 eV. Moreover, the hydrogen average adsorption energy of Li-GDY increases obviously with the rise in molecular concentration. When the number of hydrogen molecules are seven, the best average adsorption energy occurs, which can achieve −0.132 eV.

Table 5. Hydrogen adsorption energy and average adsorption energy of Li-GDY.

N (H_2)	1	2	3	4	5	6	7
E_{ads} (eV)	−0.008	−0.094	−0.141	−0.194	−0.158	−0.146	−0.185
$\overline{E_{ads}}$ (eV/H_2)	−0.008	−0.051	−0.081	−0.109	−0.119	−0.124	−0.132

In order to analyse the hydrogen storage property of Li-VGDY, the seven hydrogen adsorption models of Li-VGDY under different hydrogen concentrations (LiH_{2N}-VGDY) are shown in Figure 9a–g. Meanwhile, the adsorption energy of hydrogen (E_{ads}) and average adsorption energy were calculated to determine the stability of hydrogen molecule adsorption on the Li-VGDY surface, which can be expressed by Equations (6) and (7):

$$E_{ads} = E_{VGDY+(x)Li+(N)H_2} - E_{VGDY+(x)Li+(N-1)H_2} - E_{H_2} \quad (6)$$

$$\overline{E_{ads}} = \left(E_{VGDY+(x)Li+(N)H_2} - E_{VGDY+(x)Li} - E_{(N)H_2}\right)/N \quad (7)$$

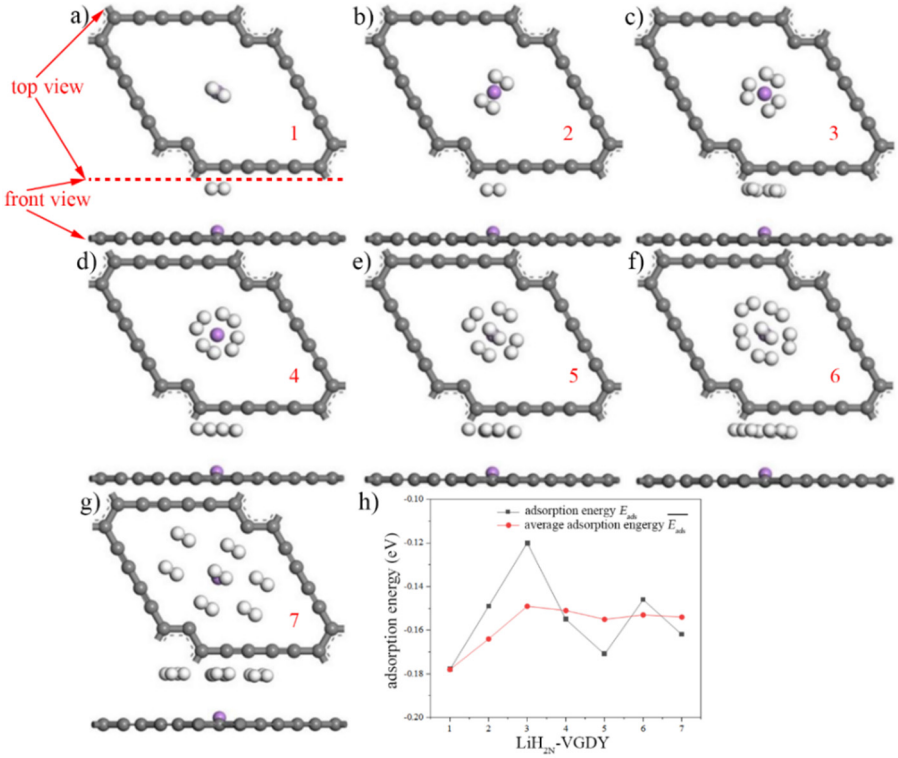

Figure 9. Seven LiH_{2N}-VGDY models and adsorption energy. (Purple ball is Li atom, white ball is hydrogen molecule, (**a**–**h**) represent the LiH_{2N}-VGDY models of hydrogen concentrations with 1, 2, 3, 4, 5, 6 and 7, respectively, (**h**) shows the hydrogen adsorption energy and average adsorption energy of Li-VGDY).

Here, $E_{VGDY+(x)Li+(N)H_2}$ and $E_{VGDY+(x)Li+(N-1)H_2}$ are the total energy of γ-VGDY doped x Li after adsorbing N and $N-1$ hydrogen molecules, respectively. $E_{VGDY+(x)Li}$ is the total supercell energy of γ-VGDY doped x Li. E_{H_2} and $E_{(N)H_2}$ are the energy of single and N hydrogen molecules, respectively, and N is the number of hydrogen molecules.

The hydrogen adsorption energy and average adsorption energy of Li-VGDY are shown in Table 6. In this table, different from the Li-GDY, the hydrogen adsorption energy of the Li-VGDY system shows fluctuation between −0.149 and 0.029 eV. In addition, the absolute value of average adsorption energy of Li-VGDY decreases with the increase in hydrogen molecular concentration. Nonetheless, the Li-VGDY possesses better average adsorption energy than Li-GDY. Meanwhile, the average adsorption energy of Li-VGDY reaches a steady state when the number of hydrogen molecules are four, which is −0.15 eV. The results indicate that the Li-VGDY has excellent stability in large capacity hydrogen storage.

Table 6. Hydrogen adsorption energy and average adsorption energy of Li-VGDY.

N (H_2)	1	2	3	4	5	6	7
E_{ads} (eV)	−0.178	−0.149	−0.120	−0.155	−0.171	−0.146	−0.162
$\overline{E_{ads}}$ (eV/H_2)	−0.178	−0.164	−0.149	−0.151	−0.155	−0.153	−0.154

3.4. The Capacity of Hydrogen Storage

High-efficiency hydrogen storage materials need to satisfy two significant conditions of larger storage capacity and higher bonding strength in the practical applications. The

mass and volumetric hydrogen storage density were proposed by the US Department of Energy to measure the performance of hydrogen storage materials.

The mass hydrogen storage density ($(\eta(wt\%))$) can be expressed in Equation (8):

$$\eta(wt\%) = \frac{2Ar_{(H)}n(H_2)}{Ar_{(n)}\cdot n(c) + Ar_{(Li)}\cdot n(Li) + 2Ar_{(H)}\cdot n(H_2)}\cdot 100\% \quad (8)$$

The volumetric hydrogen storage density ($\rho(V)$) can be described in Equation (9):

$$\rho(V) = \frac{2Ar_{(H)}n(H_2)/N_A}{a\cdot b\cdot c}\cdot 100\% \quad (9)$$

Here, the $Ar(Li)$, $Ar(H)$ and $Ar(C)$ are the relative atomic mass of Li, hydrogen and C atoms, respectively. $Ar(Li) = 7$, $Ar(H) = 1$ and $Ar(C) = 12$. The $n(Li)$, $n(H_2)$ and $n(C)$ are the number of Li atoms, hydrogen molecules and C atoms, respectively. N_A is the Avogadro constant, and the value is 6.022×10^{23}. The a, b and c represented the overall length, width and height of the model, respectively.

According to the analysis of Table 5, when the concentration of hydrogen molecules is N = 7, the LiH_{2N}-GDY system achieves the best performance of hydrogen storage. Figure 10 a shows the maximum hydrogen storage capacity model of intrinsic γ-GDY (Li_2H_{56}-GDY model). In this figure, two Li atoms are doped to the intrinsic γ-GDY, the top and bottom surface of Li-GDY adsorb seven hydrogen molecules, respectively, and the hydrogen molecules on top and bottom surface are represented by white and green balls, the purple balls represent Li atoms. The structure and energy of the model were optimized, and the adsorption energy of this system was −0.226 eV in steady state, which could meet the requirement of hydrogen storage adsorption energy. The mass and volumetric hydrogen storage densities of Li_2H_{56}-GDY system were 13.02% and 5.22×10^4 kg/m^3, and these values of intrinsic γ-GDY were 7.69% and 2.24×10^4 kg/m^3, respectively.

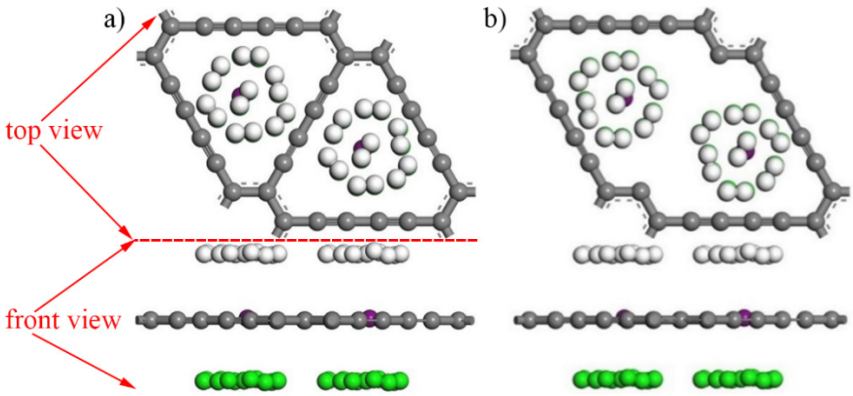

Figure 10. Maximum hydrogen storage capacity model of intrinsic γ-GDY and γ-VGDY. (**a**) Li_2H_{56}-GDY model, (**b**) Li_2H_{56}-VGDY model. (Hydrogen molecules on top and bottom surface are represented by white and green balls, the purple balls represent Li atoms).

As shown in Table 6, when the number of hydrogen molecules is one, the performance of hydrogen storage of LiH_{2N}-VGDY reaches its peak. In order to ensure the consistency of the simulation, here, the number of hydrogen molecules also selected seven. Figure 10b shows the maximum hydrogen storage capacity model of γ-VGDY (Li_2H_{56}-VGDY model). Computational results indicated that the adsorption energy of this system was −0.209 eV when in a steady state, which also could satisfy the requirement of hydrogen storage adsorption energy. Meanwhile, the mass hydrogen storage density of Li_2H_{56}-VGDY system was 14.66%, and the volumetric storage density was 5.22×10^4 kg/m^3, a value the same as the Li_2H_{56}-GDY system.

4. Conclusions

(1) The H2 point of intrinsic γ-GDY shows the best hydrogen adsorption property in nine highly symmetric adsorption points. However, the hydrogen adsorption performance of intrinsic γ-GDY is not ideal.
(2) Li atoms could be adsorbed by intrinsic γ-GDY and γ-VGDY stably.
(3) Doping Li atoms could enhance the hydrogen storage property of intrinsic γ-GDY when in large capacity hydrogen storage.
(4) Vacancy defect has a positive influence on hydrogen storage performance; Li-VGDY possesses better hydrogen storage performance than Li-GDY.

Author Contributions: W.T. guided other authors complete this paper. Z.L. wrote this paper. C.C. designed and completed related computations. W.L. offered the help of modify grammar. Z.C. and F.X. provided financial support. All authors have read and agreed to the published version of the manuscript.

Funding: This research was funded by the National Natural Science Foundation of China (No. 62104181 and No. 52106108) and Open Research Fund of State Key Laboratory (No. 6142805090204).

Conflicts of Interest: The authors declare no conflict of interest, financial or otherwise.

References

1. Liu, H.Z.; Zhang, G.H.; Zhang, X.; Chen, F.J.; Duan, H.G. Emerging miniaturized energy storage devices for microsystem applications: From design to integration. *Int. J. Extrem. Manuf.* **2020**, *2*, 042001. [CrossRef]
2. Zheng, S.H.; Shi, X.Y.; Das, P.; Wu, Z.S.; Bao, X.H. The road towards planar microbatteries and microsupercapacitors: From 2D to 3D device geometries. *Adv. Mater.* **2019**, *10*, 1900583. [CrossRef] [PubMed]
3. Li, H.L.; Lv, T.; Sun, H.H.; Qian, G.J.; Li, N.; Yao, Y.; Chen, T. Ultrastretchable and superior healable supercapacitors based on a double cross-linked hydrogel electrolyte. *Nat. Commun.* **2019**, *10*, 536. [CrossRef] [PubMed]
4. Zheng, S.H.; Ma, J.X.; Fang, K.X.; Li, S.W.; Qin, J.Q.; Li, Y.G.; Wang, J.M.; Zhang, L.Z.; Zhou, F.; Liu, F.Y.; et al. High-voltage potassium ion micro-supercapacitors with extraordinary volumetric energy density for wearable pressure sensor system. *Adv. Energy Mater.* **2021**, *11*, 2003835. [CrossRef]
5. Hafeez, H.; Shi, C.Q.; Lee, C.M.; Periyanayagam, J.J.; Kim, D.H.; Song, M.; Kim, C.S.; Zou, Z.; Xiao, J.L.; Ryu, S.Y. Improved design of highly efficient microsized lithium-ion batteries for stretchable electronics. *J. Micromech. Microeng.* **2019**, *29*, 075008. [CrossRef]
6. Zheng, S.H.; Huang, H.J.; Dong, Y.F.; Wang, S.; Zhou, F.; Qin, J.Q.; Sun, C.L.; Yu, Y.; Wu, Z.S.; Bao, X.H. Ionogel-based sodium ion micro-batteries with a 3D No-ion diffusion mechanism enable ultrahigh rate capability. *Energy Environ. Sci.* **2020**, *13*, 821–829. [CrossRef]
7. Morse, J.D. Micro-fuel cell power sources. *Int. J. Energy Res.* **2007**, *31*, 576–602. [CrossRef]
8. Dincer, I. Renewable energy and sustainable development: A crucial review. *Renew. Sustain. Energy Rev.* **2000**, *4*, 157–175. [CrossRef]
9. Bird, M.A.; Goodwin, S.E.; Walsh, D.A. Best practice for evaluating electrocatalysts for hydrogen economy. *ACS Appl. Mater. Interfaces* **2020**, *12*, 20500–50506. [CrossRef]
10. Maroufmashat, A.; Fowler, M.; Khavas, S.S.; Elkamel, A.; Roshandel, R.; Hajimiragha, A. Mixed integer linear programing based approach for optimal planning and operation of a smart urban energy network to support the hydrogen economy. *Int. J. Hydrog. Energy* **2015**, *41*, 7700–7716. [CrossRef]
11. Kundu, A.; Jang, J.H.; Gil, J.H.; Jung, G.R.; Lee, H.R.; Kim, S.H.; Ku, B.; Oh, Y.S. Micro-fuel cells—Current development and application. *J. Power Sources* **2007**, *170*, 67–78. [CrossRef]
12. Wan, C.; Zhou, L.; Xu, S.M.; Jin, B.Y.; Ge, X.; Qian, L.X.; Chen, F.Q.; Zhan, X.L.; Yang, Y.R.; Cheng, D.G. Defect engineered mesoporous graphitic carbon nitride modified with AgPb nanoparticles for enhanced photocatalytivc hydrogen evolution from formic acid. *Chem. Eng. J.* **2022**, *429*, 132388. [CrossRef]
13. Lang, C.G.; Jia, Y.; Yao, X.D. Recent advances in liquid-phase chemical hydrogen storage. *Energy Storage Mater.* **2020**, *26*, 290–312. [CrossRef]
14. Kim, T. Hydrogen generation from sodium borohydride using microreactor for micro fuel cells. *Int. J. Hydrog. Energy* **2011**, *36*, 1404–1410. [CrossRef]
15. Dillon, A.C.; Jones, K.M.; Bekkedahl, T.A.; Kiang, C.H.; Bethune, D.S.; Heben, M.J. Storage of hydrogen in single-walled carbon nanotubes. *Nature* **1997**, *386*, 377–379. [CrossRef]
16. Wang, H.L.; Gao, Q.M.; Hu, J. High hydrogen storage capacity of porous carbons prepared by using activated carbon. *J. Am. Che. Soc.* **2009**, *132*, 7016–7022. [CrossRef]
17. Zhou, M.; Lu, Y.; Zhang, C.; Feng, Y.P. Strain effects on hydrogen storage capability of metal-decorated graphene: A first-principles study. *Appl. Phys. Lett.* **2010**, *97*, 103109. [CrossRef]

18. Yang, L.; Li, X.Y.; Zhang, G.Z.; Cui, P.; Wang, X.J.; Jiang, X.; Zhao, J.; Luo, Y.; Jiang, J. Combining photocatalytic hydrogen generation and capsule storage in graphene based sandwich structures. *Nat. Commun.* **2017**, *8*, 16049. [CrossRef]
19. Liu, Y.; Gao, S.; Lu, F.; Yu, A.; Song, S.; Shi, H.; Mai, Y.; Liao, B. Hydrogen adsorption on Li decorated graphyne-like carbon nanosheet: A density function theory study. *Int. J. Hydrog. Energy* **2020**, *45*, 24938–24946. [CrossRef]
20. Cui, H.; Zhang, Y.; Tian, W.; Wang, Y.; Tong, L.; Chen, Y.; Shan, P.; Yuan, H. A study on hydrogen storge performance of Ti decorated vacancies structure on the first principle. *RSC Adv.* **2021**, *11*, 13912–13918. [CrossRef]
21. Yuan, L.; Kang, L.; Chen, Y.; Wang, D.; Gong, J.; Wang, C.; Zhang, M.; Wu, X. Hydrogen storage capacity of Ti-decorated porous graphene: First-principles investigation. *Appl. Surf. Sci.* **2017**, *434*, 843–849. [CrossRef]
22. Li, G.X.; Li, Y.L.; Liu, H.B.; Guo, Y.B.; Li, Y.J.; Zhu, D.B. Architecture of graphdiyne nanoscale films. *Chem. Commun.* **2010**, *46*, 3256–3258. [CrossRef] [PubMed]
23. Li, Y.J.; Xu, L.; Liu, H.B.; Li, Y.L. Graphdiyne and graphyne: From theoretical predictions to practical construction. *Chem. Soc. Rev.* **2014**, *43*, 2572–2586. [CrossRef] [PubMed]
24. Jia, Z.Y.; Li, Y.J.; Zuo, Z.C.; Liu, H.B.; Huang, C.S.; Li, Y.L. Synthesis and properties of 2D carbon-graphdiyne. *Acc. Chem. Res.* **2017**, *50*, 2470–2478. [CrossRef]
25. Li, Y.J.; Li, Y.L. Two Dimensional polymers-progress of full carbon graphyne. *Acta Polym. Sin.* **2015**, *2*, 147–165.
26. Zhang, H.Y.; Zhao, X.Y.; Zhang, M.; Luo, Y.H.; Li, G.H.; Zhao, M.W. Three-dimensional diffusion of molecular hydrogen in grapydiyne: A first-principles study. *J. Phys. D. Appl. Phys.* **2013**, *46*, 495307. [CrossRef]
27. Panigrahi, P.; Dhinakaran, A.K.; Naqvi, S.R.; Gollu, S.R.; Ahujia, R.; Hussain, T. Light metal decorated graphdiyne(GDY) nanosheets for reversible hydrogen storage. *Nanotechnology* **2018**, *29*, 355401. [CrossRef]
28. Avramov, P.; Kudin, K.N.; Scuseria, G.E. Single wall carbon nanotubes density of states: Comparison of experiment and theory. *Chem. Phys. Lett.* **2003**, *370*, 597–601. [CrossRef]
29. Jeloaica, L.; Sidis, V. DFT investigation of the adsorption of atomic hydrogen on a cluster-model graphite surface. *Chem. Phys. Lett.* **1999**, *300*, 157–162. [CrossRef]
30. Cranford, W.; Buehler, J. Mechanical properties of graphyne. *Carbon* **2011**, *49*, 4111–4121. [CrossRef]
31. Bai, H.C.; Zhu, Y.; Qiao, W.Y.; Huang, Y.H. Structures, stabilities and electronic properties of graphdiyne nanoribbons. *RSC Adv.* **2011**, *1*, 768–775. [CrossRef]
32. Mimezhad, M.; Ansari, R.; Rouhi, H.; Seifi, M.; Faghihnasiri, M. Mechanical properties of two-dimensional graphyne sheet under hydrogen adsorption. *Solid State Commun.* **2012**, *152*, 1885–1889. [CrossRef]
33. Peng, Q.; Ji, W.; De, S. Mechanical properties of graphyne monolayers: A first-principles study. *Phys. Chem. Chem. Phys.* **2012**, *14*, 13385–13391. [CrossRef]
34. Pei, Y. Mechanical properties of graphdiyne sheet. *Phys. B* **2012**, *407*, 4436–4439. [CrossRef]
35. Sun, P.Z.; Yang, Q.; Kuang, W.J.; Stebunov, Y.V.; Xiong, W.Q.; Yu, J.; Nair, R.R.; Katsnelson, M.I.; Yuan, S.J.; Grigorieva, I.V.; et al. Limits on gas impermeability of graphene. *Nature* **2020**, *579*, 229–232. [CrossRef] [PubMed]
36. Yuan, L.; Chen, Y.; Kang, L.; Zhang, G.; Wang, D.; Wang, C.; Zhang, M.; Wu, X. First-principles investigation of hydrogen storage capacity of Y-decorated porous graphene. *Appl. Surf. Sci.* **2017**, *399*, 463–468. [CrossRef]

micromachines

MDPI

Review

Recent Progress in the Preparation Technologies for Micro Metal Coils

Jianyong Lou *, Haixia Ren, Xia Chao, Kesong Chen, Haodong Bai and Zhengyue Wang

State Key Laboratory of Electrical Insulation and Power Equipment, School of Electrical Engineering, Xi'an Jiaotong University, Xi'an 710049, China; hxren@stu.xjtu.edu.cn (H.R.); chaoxia@stu.xjtu.edu.cn (X.C.); 3121104019@stu.xjtu.edu.cn (K.C.); baihaodong@stu.xjtu.edu.cn (H.B.); 3120304033@stu.xjtu.edu.cn (Z.W.)
* Correspondence: jylou@mail.xjtu.edu.cn

Abstract: The recent development of micro-fabrication technologies has provided new methods for researchers to design and fabricate micro metal coils, which will allow the coils to be smaller, lighter, and have higher performance than traditional coils. As functional components of electromagnetic equipment, micro metal coils are widely used in micro-transformers, solenoid valves, relays, electromagnetic energy collection systems, and flexible wearable devices. Due to the high integration of components and the requirements of miniaturization, the preparation of micro metal coils has received increasing levels of attention. This paper discusses the typical structural types of micro metal coils, which are mainly divided into planar coils and three-dimensional coils, and the characteristics of the different structures of coils. The specific preparation materials are also summarized, which provides a reference for the preparation process of micro metal coils, including the macro-fabrication method, MEMS (Micro-Electro-Mechanical System) processing technology, the printing process, and other manufacturing technologies. Finally, perspectives on the remaining challenges and open opportunities are provided to help with future research, the development of the Internet of Things (IoTs), and engineering applications.

Keywords: micro metal coil; MEMS processing technology; flexible electronic process; magnetic film; printing process

Citation: Lou, J.; Ren, H.; Chao, X.; Chen, K.; Bai, H.; Wang, Z. Recent Progress in the Preparation Technologies for Micro Metal Coils. *Micromachines* **2022**, *13*, 872. https://doi.org/10.3390/mi13060872

Academic Editors: Weidong Wang and Ruiguo Yang

Received: 17 April 2022
Accepted: 27 May 2022
Published: 31 May 2022

1. Introduction

Over the last few decades, the field of micro metal coils has evolved rapidly due to the widespread application of micro metal coils in fields such as consumer electronics, the automobile industry, aerospace, machinery, the chemical industry, medicine, among others [1–15]. Among the various types of micro metal coils, the coils based on MEMS technology and flexible electronic technology have greater research value [1–8].

The coil turns of micro metal coils are greatly increased in a limited volume, resulting in a more uniform, high-density magnetic field when working [9]. They have the advantages of miniaturization, integration, intelligence, low cost, high performance, and mass production, which are prerequisites for realizing a high level of integration and complexity in modern electronic equipment [12–16]. The micro-transformer produced by micro coil technology has low resistance, high inductance, a high coupling coefficient and quality factor, and plays an important role in switching the power supply, power conversion or signal isolation [15,16]. In particular, the DC–DC converter that is composed of a micro-transformer effectively reduces the volume of the power system and is widely used in various portable electronic products. The application of micro coils in relays makes the size of the aeroengine shrink, which promotes the development of micro-aviation [17–19].

Compared with the traditional metal coil, the flexibility and ductility of the flexible coil are significantly improved, and it is easy to bend and fold, as well as being lightweight [5,6]. As the most efficient energy supply mode in micro-energy acquisition technology, an electromagnetic energy harvester also uses flexible coils to solve the problem of ensuring

high output voltage under the premise of controlling the volume [20–22]. Micro coils can be nested on wearable system devices. Flexible sensors convert external deformation signals into electrical signals. MEMS sensors can achieve almost all sensory functions of the human body, including vision, hearing, taste, smell (such as the Honeywell electronic nose) and touch, which play an important role in health monitoring, motion monitoring, swallowing speech monitoring and intelligent rehabilitation [23–29]. With the development of micro coils, people can directly obtain certain body information in a convenient, fast, and friendly way. The wearable device based on micro coil technology is advantageous due to its small size and portability. It deeply contacts the measurement target, reduces the cost, and completes the integration of multiple functions with a certain level of accuracy [26–33]; therefore, the application of micro metal coils has greatly expanded the use of electronic devices and laid the foundation for the rapid development of consumer electronics, the automobile industry, and even the aerospace, machinery, chemical, and medical monitoring industries.

The development of micro metal coils also benefits from the significant progress of advanced microfabrication technologies, such as microelectronic technology, integrated circuit technology, and its processing technology, MEMS preparation technology, and film and flexible electronic processing technology [34–36]. The substrate materials mainly include silicon, glass, ceramic materials and flexible materials [37–42]. The hard substrate has a high degree of hardness and good dielectric properties, but for some non-planar surfaces and curved surfaces, it is necessary to use a flexible substrate to prepare sensors. At present, the organic polymer materials for flexible substrates studied by scholars in China and abroad not only have better mechanical properties, dielectric properties, and physical and chemical stability, but also have good mapping ability and flatness, and are widely used in the manufacturing of MEMS sensors [39].

Micro metal coils are mainly divided into two structural types: three-dimensional coils and planar coils. Three-dimensional coils are mainly solenoid-type micro coils, and planar coils can be subdivided into single-layer coils and multi-layer coils [40–42]. The single-layer planar coil has no magnetic core-binding circuit, and the magnetic leakage is significant. Then, the single-layer thin film magnetic core or the two-layer thin film structure and sandwich structure are introduced to remarkably improve the inductance and quality factor of the planar spiral inductor [2–5,43–46]. The solenoid based on the MEMS process has good integration performance on standard silicon substrate, and the hollow solenoid coil can reduce the influence of substrate [47–50]. Three-dimensional solenoid inductors and suspended planar inductors were fabricated on silicon and glass substrates using thick gel lithography and copper plating. Moreover, a high-performance, folded, stacked multilayer 3D magneto-inductor coil was fabricated using MEMS technology. The new folding and welding methods successfully solved the complexity of the key manufacturing process of multilayer inductors, enabling the simple, rapid and low-cost assembly of multilayer coils [47,51–55].

In this paper, the structure, preparation methods and preparation materials of micro coils are summarized. Section 2 discusses the characteristics and applicable scope of coils with different structures. The study of micro metal coils based on different processing methods and materials is emphasized in Section 3. Finally, we provide typical devices and applications of coils based on different processing methods. The challenges and open opportunities of the micro metal coil preparation process for future development are given.

2. Type and Theory of Micro Metal Coil Construction

2.1. Theory of Coil Performance

When conducting theoretical analyses of a coil, the inductance, quality factor Q and distributed capacitance of the coil are generally of highest concern. The degree of inductance of the coil depends mainly on the number of turns in the coil, the winding method, the presence or absence of a magnetic core, and the material of the core. In general, the more coils there are and the denser the wound coils, the greater the inductance. Coils with

a center of gravity have a larger inductance than coils without a center: the larger the permeability of the core, the greater the inductance. The higher the quality factor Q of a coil, the smaller the loss and the higher the efficiency. The Q value of a coil is related to the DC resistance of the wire, the dielectric loss of the skeleton, losses caused by the shield or iron core and the influence of high-frequency skin effects. There are certain capacitances between the turns, between the layers of any inductance coil, between the coil and the reference ground, and between the coil and the magnetic shield. These capacitances are called the distributed capacitances of inductance coil. If these distributed capacitances are integrated, they will become an equivalent capacitance, C, in parallel with the inductor coil. The existence of distributed capacitance decreases the Q value of a coil, and the stability thus deteriorates; therefore, the smaller the distributed capacitance of the coil, the better.

Due to the complex configuration and diversity of coils in practical applications, it is difficult to carry out complete theoretical calculations; as a result, the simplified model and equivalent circuit are hard to explain. Below, a PCB board coil is presented as an example [56]; qualitative analysis was used to determine the performance of the coil transformer. The transformer circuit model is shown in Figure 1.

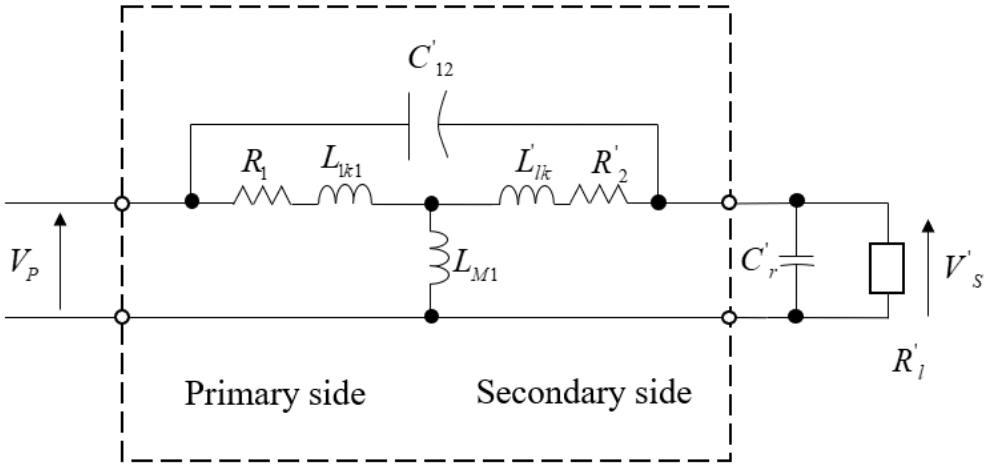

Figure 1. Circuit model of transformer.

The inductance was measured using an HP4194A impedance/gain phase analyzer. The stray inductance of primary winding could be compensated by the impedance analyzer; however, lead stray inductance between the secondary winding and the external capacitor could not be compensated as it must be included in the transformer model as part of the secondary leakage inductance. The capacitance inside a winding is far smaller than the external capacitance; therefore, their influence was ignored to simplify the analysis.

The voltage gain ratio and no-load resonant frequency of the transformer could be determined by connecting an external capacitor to the secondary winding and the measured coil inductance. This frequency characteristic is an important factor in the design of power converters for a specific switching frequency range.

2.2. The Solenoid

The solenoid coil is a three-dimensional coil in space, directly wound by metal wires. Its interior is either hollow or a metal core, and it is used to concentrate the magnetic field. When passing a current in a closed loop, the magnetic field can be generated. As a common electromagnetic component, the solenoid is widely used in various fields, as shown in Figure 2; it is used for electromagnets [57], inductors [58], converters [59], solenoid valves [60], relays [61], and so on, as a part of inductors and transformers.

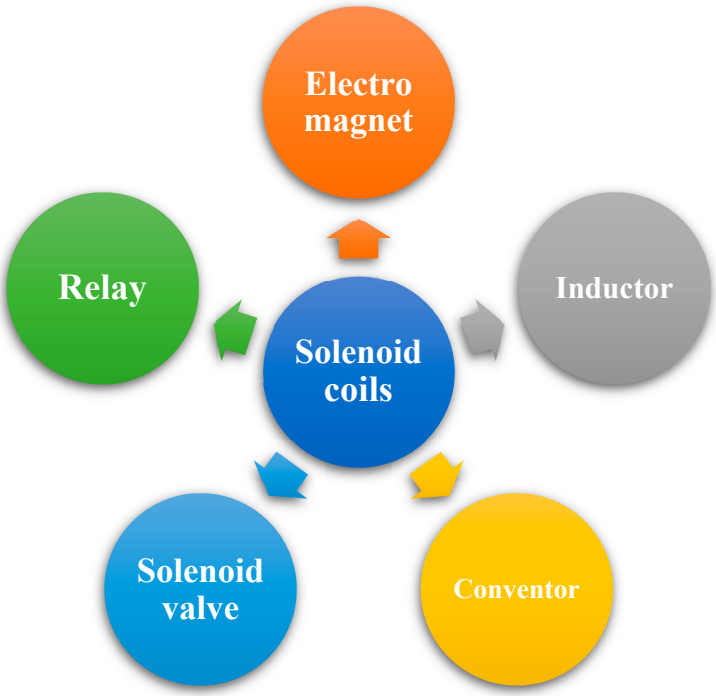

Figure 2. Main applications of solenoid coils as common electromagnetic components.

Moazenzadeh et al. [11] formed a vertical magnetic core column using a laminating process. The magnetic core material is a cobalt-based amorphous magnetic alloy, and the column is arranged on a 4-inch borosilicate silicon sheet with adhesive. The column is divided into a T column and a U column. On the T column, the solenoid is directly wound on the magnetic core by the lead-bonding machine, and then combined with the U-shaped magnetic core to form a closed magnetic circuit. The wiring bonding process is fast, and up to 40 coils can be made in 10 s. The manufactured device generates an inductance of 2.95 $\mu H/mm^3$ and 133 nJ/mm^3 in energy per unit volume at a frequency of 1 MHz. Coupling coefficients of up to 98% and power efficiencies of 64–76% for different turn ratios have been measured.

Hao et al. designed transformers with magnetic thin films for on-chip power conversion and isolation [13]. The transformer is composed of three metal layers separated by insulators, including the bottom copper layer, the top copper layer, and the middle core layer. A cobalt alloy thin film material with high permeability is used as the magnetic core, the coil is wound on the magnetic core, and the coil axis and core are parallel to the silicon substrate. It is manufactured by using standard CMOS (Complementary Metal Oxide Semiconductor) manufacturing equipment and processes. By using a high-permeability, magnetic material as the solenoid core, the inductance of the device is greatly improved, with an inductance density of up to 108 nH/mm^2. The transformer's construction has a total thickness of less than 30 µm and a volume inductance density of 3.6 $\mu H/mm^3$. By using the lamination core, the loss is controlled, and the peak quality factor (Q) at 40 MHz is 16.

The significant advantage of the solenoidal is that the spatial structure is regular, the magnetic field formed is evenly distributed in space, and the electromagnetic conversion loss is low when the same materials are used. Moreover, magnetic conductive materials can be placed in the micro-channel, which is surrounded by metal wires, to further reduce losses and constrain the magnetic field, as well as to improve the capacity and the signal's sensitivity. The closed flux chain is formed by the closed magnetic core; thus, the magnetic leakage can be well prevented. The solenoid coil can also achieve a higher inductance per unit area, and it is more convenient to increase the inductance value by increasing the coil's cross-sectional area.

2.3. Planar Micro Metal Coil

The biggest advantage of planar micro coils over solenoid-type micro coils is that mass production is cheaper and more efficient when the required size is smaller. The plane-type micro coil is different from the solenoid-type micro coil in structure and has a planar two-dimensional structure. Planar micro coils were first used in MRI (Magnetic Resonance Imaging) as surface coils [62]. The structure of the planar micro coil usually includes the upper and lower magnetic films, a metal wire coil layer in the middle, and an insulating layer used to isolate the magnetic core material and the wire.

The main structural parameters include the outer diameter of the micro coil, winding number, line width, coil spacing, and thickness. When multiple layers of coils are stacked, the number of layers also needs to be considered. Wu et al. embedded two interlaced thick copper coils in the bottom layer of silicon substrate, and prepared transformer coils with a power IC process combined with MEMS electroplating, photolithography, and deposition. Through-holes and coil grooves are etched on the surface of silicon wafers by photolithography, and low-temperature oxide deposition is followed by electroplating copper filling [16]. Additionally, a new kind of silicon-embedded coreless transformer (SECT) for isolated DC–DC converter applications is presented and demonstrated. By embedding two staggered, thick copper coils in the bottom layer of the Si substrate, the designed 2 mm^2 SECT can achieve a maximum transformer efficiency of 85% at 50 MHz. Compared to previously reported silicon-based coreless power transformers, the lower operating frequency of SECT allows for about a 50% reduction in power losses in the power MOSFETs and Schottky diodes, resulting in a 38% reduction in converter losses.

Wang et al. designed a silicon-integrated micro-transformer for an isolated bias power supply [63] and carried out fabrication and characteristic verification. The racetrack-shaped micro-transformers are designed and manufactured using an advanced double-layer metal (DLM) micromachining process. The inductance density of the DLM device exceeds 80 nH/mm^2 and the efficiency is about 78.2% at 20 MHz with a 0.5 W output. The inductance drop is less than 20%, the bias current is 0.35 A, and the DC breakdown voltage can reach 6 kV. The racetrack-type micro-transformer is designed and manufactured by a double-layer metal (DLM) micromachining process. The bottom magnetic core is electroplated on a natural oxide insulating silicon wafer to form a pattern, and two layers of copper windings are deposited on the BCB and the SU–8, with the SU–8 as the middle insulating layer. From bottom to top, there are the bottom core, the first insulating layer, the first copper coil, the second insulating layer, the second copper coil, the third insulating layer, and the top core.

Silicon-based substrates have the advantage of forming metals directly, compared with flexible substrates. By using the planar coil, we can integrate the conductor on the plane, which improves the utilization rate of axial space and increases the cross-sectional area of the magnetic core. The manufacturing process is simpler, and it is more widely used when the demand for miniaturization is higher [64]. Moreover, a higher power density can be achieved [65].

When the number of turns of the metal coil needs to be increased, and when the required number of turns exceeds a certain level, the plane area occupied by the planar coil will increase rapidly, which is not conducive to the reduction in the system's size and application in a narrow space.

2.4. Integrated Micro Coil with Flexible Substrates

Micro coils based on flexible substrates have the characteristics of bendability, biocompatibility, being lightweight, and having a low base cost. Due to the poor flexibility and ductility of the rigid base, the electronic components used in the conditions that need to be deformed cannot be on the rigid base, and they must be put on flexible substrates. Flexible electronics have broad application prospects in many fields such as healthcare, environmental monitoring, display and human–computer interaction, energy conversion, management and storage, communication, and wireless network technologies [25].

Yang et al. [66,67] adopted different MEMS processing techniques for different core materials in their research, including an electroplated nickel–iron alloy iron core and a pasted cobalt-based amorphous strip iron core. The preparation of copper coils is achieved via processes such as oxidation, photolithography, sputtering, electroplating, and etching. After the processing on the hard material is completed, the processing of the flexible substrate coil device is completed by peeling, planarizing, and pasting on the flexible substrate. The flexible base fluxgate adopts a parallel excitation method, and the primary and secondary coils are alternately wound with each other. The coil line width is 180 μm, the gap is 120 μm, the total number of turns of the coil is 100, the turn ratio of the excitation coil and the induction coil is 1:1, and the thickness of the copper wire is 4μm. The coil's spirally wound iron core is a long strip iron core with a length of 30 mm and a width of 3 mm. The thickness of the electroplated nickel–iron alloy iron core is 4 μm, the thickness of the pasted drill-based amorphous strip iron core is about 5 μm, and the pad size is 1350 μm × 1350 μm.

The flexible substrate miniature metal coil makes the device better for miniaturization and integration, and due to the large degree of deformation, the application range is wider than that of the rigid substrate. Moreover, the coil stacking is more convenient, which is convenient for improving the power density of the device. Since some parts of the metal coil need to be processed in a high-temperature environment, processing directly on the flexible film will cause damage to it. It needs to be prepared on a rigid substrate and then transferred to the flexible film, which increases the complexity of the processing technology. Moreover, since only soft magnetic material can be used as the iron core on the flexible substrate, the electromagnetic properties are weaker than traditional materials, and further research on the required soft magnetic material is required.

3. Main Processing Method

3.1. Macro Production Mode

3.1.1. Processing on PCB

The planar micro coil based on the printed circuit board (PCB) process is advantageous in terms of having a low manufacturing cost, short cycle time, and the ability for mass production.

Wei P.W. et al. [68] designed a PCB-based planar micro coil for portable NMR (Nuclear Magnetic Resonance) detection. The PCB plane micro coil is made on the double-sided PCB using a photolithography and etching process, the micro coil is obtained after the copper wire is deposited by exposure, development, and electroplating, and the two sides of the PCB are electrically connected through the PCB through-holes. The top board includes the left and right pads, the spiral micro coil and the leads. The leads are used for the connection between the left pad and the spiral micro coil. There are two through-holes in the middle of the PCB board, and the innermost end of the spiral coil and the pad on the right side of the top board are connected to the bottom board with wires through the two through-holes. Wei P.W. et al. connected the two through holes with leads on the bottom plate, so as to realize the connection between the spiral coil and the pad. In order to avoid the problems of the thin glass' intermediate layer being easily broken and the flat micro coil being easily oxidized, it is necessary to improve the structural design and adjust the subsequent process' production plan.

Although the current PCB planar micro coils are relatively inexpensive to manufacture, they have shortcomings, such as numerous steps in the process, low manufacturing resolution, and uneven RF (Radio Frequency) fields. It was found that the parasitic capacitance caused too much influence, due to multiple through-holes, to make a PCB three-dimensional coil in the study. In order to obtain a high signal-to-noise ratio (SNR), PCB planar micro coils need to be properly designed. The width of the wires and the distance between wires should be as small as possible. Due to the limited minimum resolution of PCB technology, the wire's width and spacing are both 152.4 μm, the coil's thickness is 35 μm, and the number of turns is six. Tang et al. [56] designed an isolated switching power converter coil

for a coreless PCB transformer. The transformer coils are micro two-spiral windings, which are printed directly on both sides of a double-sided PCB. The PCB laminate is made of FR4 material with a high breakdown voltage.

Previous micro-transformers typically used ferrite cores or materials to provide a closed magnetic circuit; however, the rated current and operating frequency are limited by the ferrite material due to magnetic saturation and eddy current losses. By printing the windings of the planar transformer on both sides of a double-sided printed circuit board (PCB), manual winding costs are eliminated, and the manufacturing process is facilitated. As the transformer windings are etched on the PCB surface, encapsulation processes and materials such as epoxy can be excluded. In addition to the device package, the magnetic core is eliminated, so the height of the device can be greatly reduced.

Coreless PCB transformers eliminate the application challenges of core-related transformers in low-power scenarios. The diameter of the coreless PCB transformer is about 0.46 cm, the power output of the converter is about 0.5 W, and the typical transformer efficiency is 63%. Its excellent high-frequency capability, high reliability, and low-profile construction make coreless PCB transformers a suitable choice for switching converters and microcircuits in the megahertz range.

3.1.2. Wire-Wound Coils

(1) Hand winding

Based on the capillary's characteristic of not only being able to store samples but also being able to serve as a coil bobbin, Peck et al. [69] made 28 solenoid micro coils with diameters of 50 μm to 1.8 mm by manually winding wires on the capillary. The experiment for detecting the electrical parameters of coils and the NMR experiment both show that the fabrication method is feasible, and the experiment also verifies that reducing the diameter of the solenoid micro coil results in an improvement in the detection sensitivity. In the same research group, Olson et al. improved the method of fixing the solenoid micro coil and replaced the epoxy resin with cyanoacrylate adhesive. In the experiment, the cyanoacrylate adhesive was able to penetrate into the gap between the capillary and the wire more easily. At the same time, the FC–43 solution was used to immerse the coil to reduce the magnetic susceptibility mismatch between the coil and the sample. The experimental results showed that the detection sensitivity was improved by one to two orders of magnitude. The advantage of the manual winding method is that the method is simple and suitable for manual operation; the disadvantage is that it is not easy to manufacture in batches.

(2) Wire Bonding

Based on the MEMS process, Kratt et al. [70,71] used wire bonding technology to wrap the solenoid coil wire on SU–8. First, on a silicon or glass substrate, they sprayed a layer of chrome/gold (50/500 nm) and an AZ 1518 photoresist with a UV (Ultraviolet) pattern, and wet etched the chrome/gold layer to reveal the metal that will facilitate the connection of the wire-tail's pad. Next, SU–8 pillars were fabricated on a 4-inch wafer by photolithography. Different from the traditional experience of spin-coating photoresist, the research team of the author's research group first calculated the SU–8 based on the thickness of the photolithography target. A spin-coating volume of 8 was required for the photoresist. Finally, the wire (gold wire) of the solenoid micro coil was wound in four steps: the first step was wire bonding; then, the metal pad and the gold wire ball end were treated with plasma; next, the ball end was ultrasonically welded; and then, the wire was helically wound. Finally, the end of the wire was ultrasonically re-soldered. The wire-bonding winding method is characterized by being a novel method and having the potential for mass production. This method's disadvantages include the fact that the coil fabrication is subject to a lithography process, as well as the mechanical strength of the pillars. Table 1 shows a summary of the examples of macro production mode.

Table 1. A summary of some examples of typical processing methods.

Coil Type	Ref.	Size	Coil Materials	Applications
Processing on PCB	Wei et al. [68]	5 mm	copper	NMR probe
	Tang et al. [56]	4.6 mm	copper	Isolated Switching Power Converters
Hand winding	Peck et al. [69]	50 μm–1.8 mm	copper	NMR detection in the laboratory
Wire bonding	Kratt et al. [70]	300 μm	insulated bondable gold wire	Experiment

3.2. MEMS Processing Technology

It is difficult to fabricate miniaturized and high-performance multilayer micro coils on planar substrates with conventional microelectronic technology. In recent years, the rapid development of micro-electro-mechanical systems (MEMS) technology makes it the most advanced technology in the development of miniaturized multilayer structure micro-inductors and RF MEMS devices in the world [72]. This technology is characterized by its miniaturization, diversity, and compatibility with microelectronic technology, and its processing size is generally between 1–100 μm. Products based on MEMS technology have the advantages of small size, easy integration, high sensitivity, low power consumption, high reliability, and being lightweight. The micro coil can simply be divided into a single-layer planar coil, solenoid coil, and multi-layer planar coil from the structure. The MEMS processing technology of these three types of coils is briefly introduced below.

3.2.1. Three Types of Micro Metal Coils Based on MEMS Technology

(1) Single-layer planar coil

With the rapid development of thin-film technology and microelectronics technology, magnetic thin film inductance devices are also developing toward miniaturization and integration. The most representative magnetic thin film inductance devices were proposed by Soohoo [73] in 1979 and developed in 1984 by Kawabe et al. [74]. They studied various planar micro-inductors, including single-turn, winding-type, spiral-type, zigzag-type, micro-inductors, and so on. Afterwards, the research on magnetic thin film micro-inductors began to advance very rapidly. Compared with other types of inductors, planar spiral inductors are simple to manufacture, they have good compatibility with the IC process, and they also have a low production cost. Planar spiral inductors also have the advantages of a wide frequency range and high performance at a high frequency; however, they also have small inductance at a low frequency, which is usually several NH, and they also experience resistance loss, eddy current loss, parasitic capacitor loss, and other defects. As there is no magnetic core-binding magnetic circuit, serious magnetic leakage can occur, which will interfere with the vertically integrated device [45].

To solve the magnetic flux leakage problem of planar spiral inductors, monolayer film is introduced in the hollow planar spiral inductors and magnetic core, and is distributed in the planar coil of the upper or lower section. Alternatively, two layers of magnetic core are used, and the spiral coil is placed between the two magnetic films and separated by insulating material between the coil and the magnetic thin films. The use of soft magnetic materials with high permeability at high frequencies will significantly improve the inductance and quality factor of planar spiral inductors. For example, Yamaguchi et al. [46] from Japan reported in 2000 that RF-integrated magnetic thin film micro-inductors were sputtered on the spiral coils. A layer of resistive oxide magnetic film is added at the bottom of each layer to form a sandwich structure (Figure 3). Its DC resistance is 6.8 Ω. Compared with the single-layer magnetic film structure, it is more conducive to anti-magnetic leakage, and the inductance performance is improved at 2 GHz (L = 7.9 nH, Q = 12.7). Compared with the same type of inductance with an air core, the performance is improved by 19% and 23%, respectively. The inductance is 7.7 nH at 1 GHz and the quality factor is 7, which is a key step towards the application of RF–MEMS for magnetic thin film micro-inductors. Peng S [75] also used a similar sandwich structure to build

a micro-inductor on a silicon substrate. The micro-inductor has a single layer of copper winding sandwiched between two layers of electroplated NiFe core (Figure 4). It has a footprint area of 2.9 mm^2, an inductance of 204 nH at 21.7 MHz, a DC resistance of 470 mΩ, and a peak quality factor of 9.23 at 9.2 MHz.

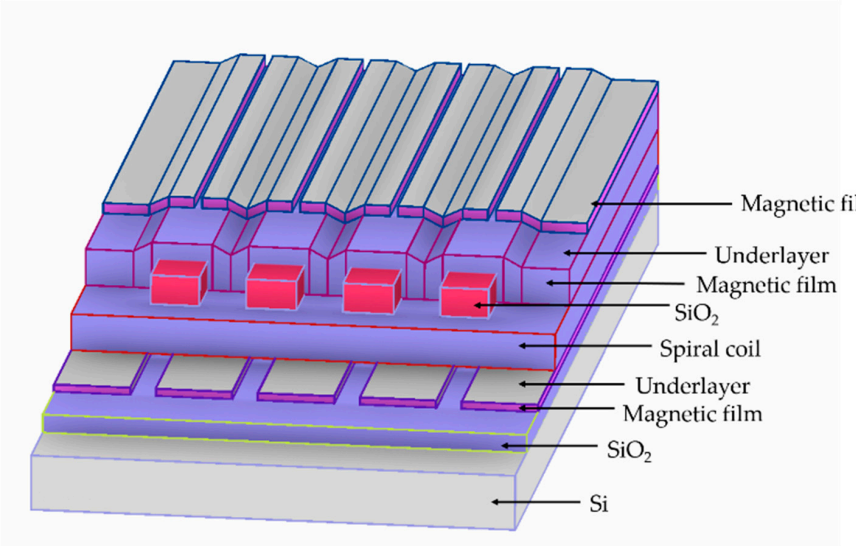

Figure 3. Schematic diagram of a sandwich inductor with a magnetic thin film.

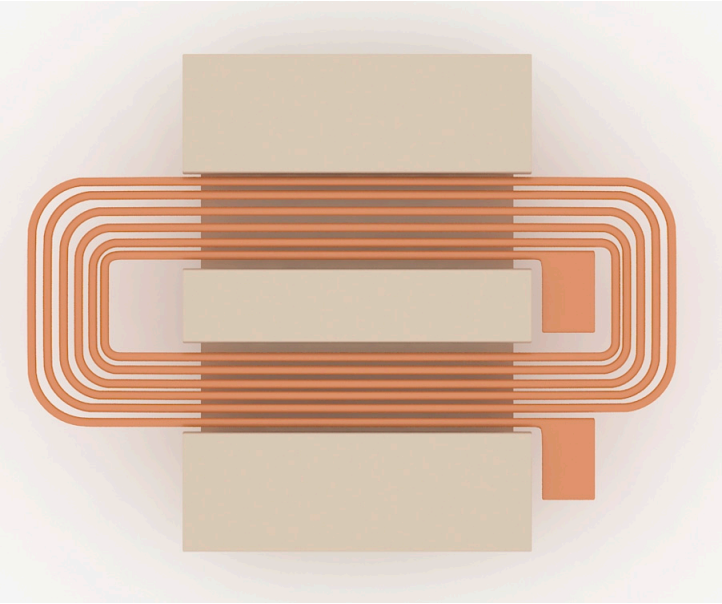

Figure 4. Sandwich structure with electroplated NiFe as the magnetic core.

In the late 1980s, portable electronic products including mobile communication products such as mobile phones, notebook computers, and computer microprocessors created higher requirements for miniaturized DC–DC converters composed of magnetic thin film micro-inductors and transformers. There were also higher requirements for frequency and power conversion efficiency for switching the power supply; therefore, increasing the switching frequency and reducing loss have become inevitable trends. The operating frequency of the magnetic thin-film micro inductor is increased from 1 KHz–1 MHz to 1–10 MHz, the inductance is greater than 1 μH, the quality factor is greater than 1, and the conversion efficiency is greater than 95%.

To improve the quality factor and self-resonant frequency of the inductor, researchers have conducted a lot of research. In 1999, K. Kamogawa et al. developed a MEMS planar helical inductor [76]. The inductance structure was developed on a 10-μm polyimide thick film insulation layer, a 0.7-μm-thick grounding aluminum layer was buried between the polyimide layer and the substrate 45.77, and the self-resonant frequency was 29.3 GHz. The maximum Q value was 45.77. In Switzerland in 2014, Jacopo Olivo et al. [77] created an inductor coil that can be used in implantable biosensors (Figure 5). The inductor is 14.88 mm × 2 mm in size and is backed by 525 μm of silicon with a 1-um silicon dioxide layer. The inductance coil is made of copper material with a thickness of about 60 μm. As the thickness of the inductance coil is increased, the quality factor of inductance will be improved. The self-resonant frequency is located at 31.3 MHz. At 5 MHz, the inductance value is 0.46 μH, and the Q factor is 13.65.

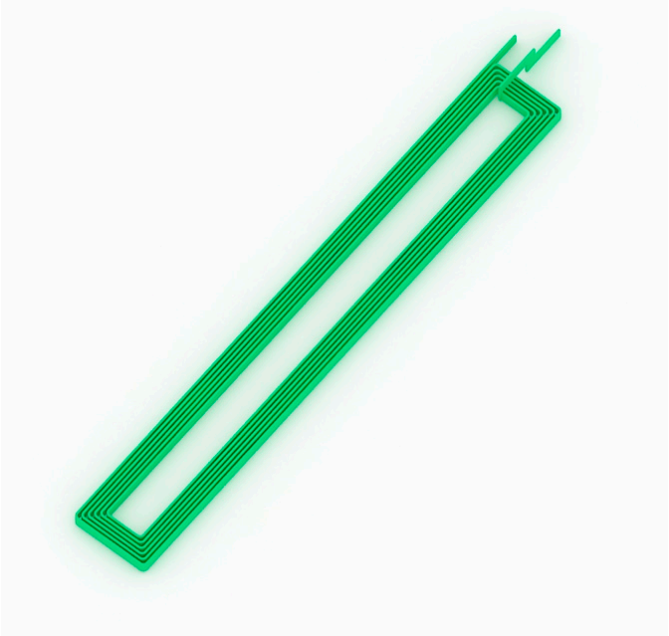

Figure 5. The inductors, with a size of 14.88 × 2 mm^2, are simulated onto a substrate of 525 μm of silicon +1 μm of silicon dioxide.

(2) Multi-layer planar coil

With the progress of technology and the reduction in the device's feature size, the area consumption caused by planar inductors has become increasingly obvious. A great deal of research has been carried out on the fabrication of miniaturized on-chip inductors with a high-quality factor and a high resonant frequency. Lakdawala et al. [78] studied the suspension inductance realized by the reactive ion etching (RIE) process; however, this method does not reduce the occupied area of the inductor. Yoon et al. [49] fabricated a three-dimensional solenoid inductor and a suspended plane inductor using the multiple exposure single development (MESD) method on silicon and glass substrates using thick gel lithography and copper electroplating. Chen et al. [79] also achieved a similar structure with SU_8 glue. This method can effectively improve the Q value of inductance and can reduce the inductance area. Three-dimensional coils, especially stacked multilayer inductors, are another option that can utilize vertical space to save on area and improve performance [80–82]. For example, in [81], the inductor can achieve an L of 60 nH and a Q of 17.5 at 70 MHz by using a 3D torus design. According to [82], for a multi-layer stacked structure, increasing the number of layers can significantly improve Q and L. Figure 6 shows the preparation process of a double-layer coil.

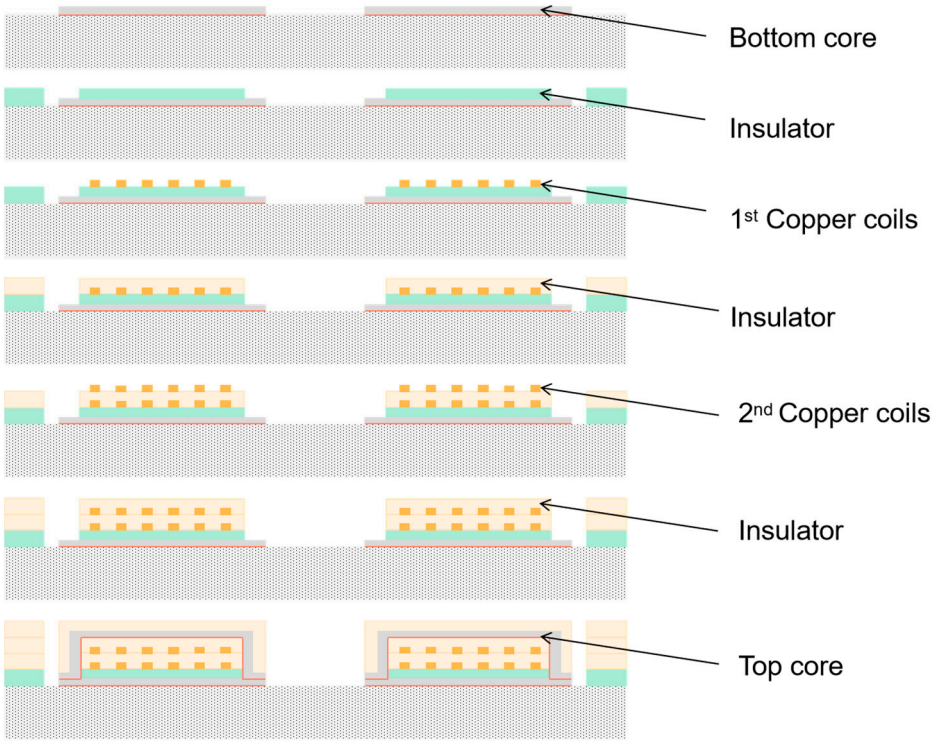

Figure 6. Double coil preparation process.

In 2014, Sun et al. produced a high-performance folded multilayer stacked 3D magneto-inductance coil using the MEMS process [51]. The coil has six layers of Cu material, a soft $Ni_{80}Fe_{20}$ magnetic core as the coil center, and soft parylene insulating material as the substrate, and can be used for wireless power transmission. This coil uses a novel folding and welding method, which successfully solves the complexity of the key manufacturing process of multilayer inductors and enables multilayer coils to assemble and fold the area of a six-layer inductor coil simply, quickly and at a low cost. When the inductance density is 100 nil/RAM2 at a 4.1 MHz operating frequency, the inductance value increases from 0.4279 μH to 12.79 μH with the increase in the layers from L to 6, with an increase of 30 times, and the Q value increases from 7.48 to 10.68, with an increase of 43%.

(3) Solenoid Coil

The majority of the first MEMS research was on the study and applications of inductors with the planar coil type because this process is relatively simple; however, even with the constant improvement in terms of technological progress and requests for the planar coil type, there are still many deficiencies. In many cases, it cannot even be used, and the MEMS-type solenoid inductors with small chip areas experience small eddy current loss, and magnetic flux can occur. It is attracting more attention because it increases efficiency by focusing on areas where the driving force is needed.

Dragan et al. [48] fabricated micro-inductors using soft magnetic CZT (Co–Zr–Ta) material as the core material. Its DC resistance is 320 mΩ, and its inductance values are 100 nH at 15 MHz and 97 nH at 30 MHz. The peak Q factor of about 15 occurs at a frequency of 30 MHz. Y.J. Kim et al. [49] proposed an inductor with a hollow ring-type geometry that introduces the air gap between the substrate and the conductor (Figure 7), which reduces stray capacitance, achieving a high Q value as a result. In addition, they studied the various effects of geometric factors. Various inductors with the inductance varying from 1 to 20 nH, and a maximum Q factor from 7 to 60, have been fabricated and measured. Lei Gu et al. [83] etched the silicon substrate into a sunken cavity, embedded the solenoid inductance in the cavity, and suspended it in the cavity, as shown in Figure 8. The loss of substrate is effectively reduced, the mechanical strength is very high, and the influence of

environmental vibration is very small. Its DC resistance is 1.27 Ω, and at 5.35 GHz, the maximum value of inductance is up to 45 nH. Similar structures have been reported in the literature [50]. Table 2 summarizes the different structures of metal coils based on MEMS machining technology.

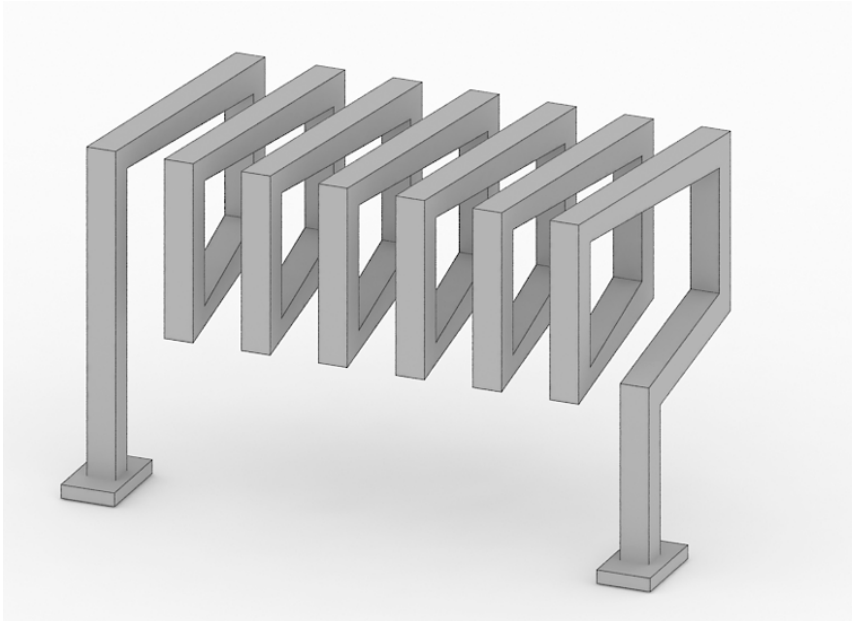

Figure 7. A schematic of an integrated solenoid-type inductor with an air gap.

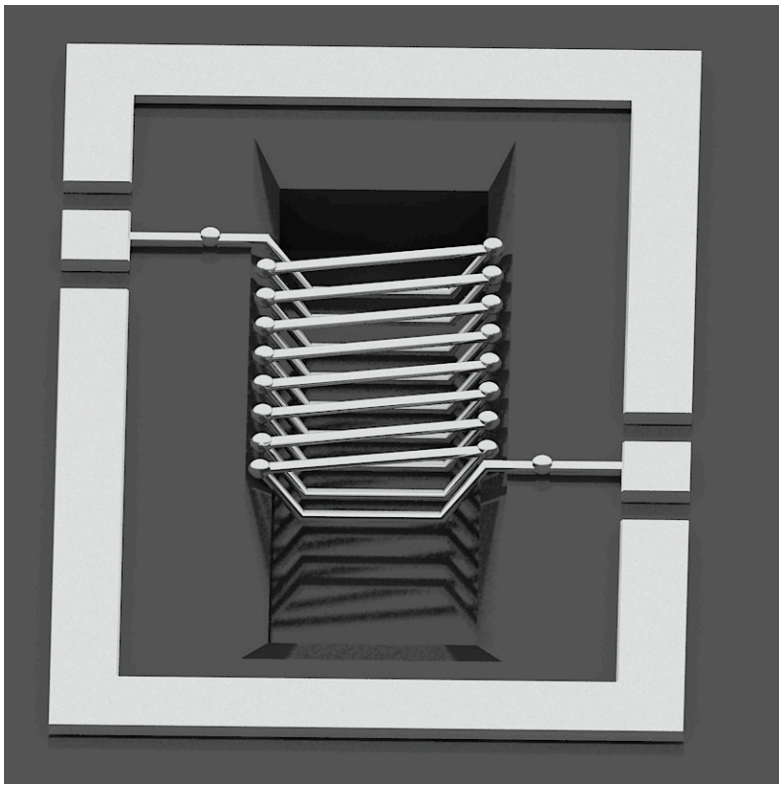

Figure 8. Structure of concave-suspended solenoid inductors.

Table 2. Metal coils with different structures based on MEMS processing technology.

Coil Type	Ref.	Special Design Structure	Size	Resistance (mΩ)	Frequency (MHz)	Inductance Value (nH)	Q
Single-layer planar coil	Yamaguchi M, et al. [46]	Sandwich construction	–	6800	1000	7.7	7
					2000	7.9×10^6	12.7
	Peng S, et al. [75]	Sandwich structure with electroplated NiFe as the magnetic core	1.7×1.7 mm^2	470	21.7	204	–
					9.2	–	9.23
	Olivo J, et al. [77]	High thickness spiral inductor, coil thickness is 60 um	14.88×2 mm^2	1058	5	460	13.65
Multilayer planar coil	Xuming Sun, et al. [51]	Parylene-based 3D high-performance folded multilayer inductors	2.1×2.1 mm^2	–	4.1	427.9 (A layer of the coil)	7.48
						12,790 (Six layers of the coil)	10.68
Solenoid coil	Dragan Dinulovic, et al. [48]	Soft magnetic CZT (Co–Zr–Ta) material as the core material	$2.6 \times 2.4 \times 0.4$ mm^3 (L × W × T)	320	15	100	–
					30	97	15
	Lei Gu, et al. [83]	The solenoid inductor is embedded in the silicon cavity	–	1270	5350	45	–

3.2.2. Materials and Processing Technology

From the point of view of MEMS processing technology, the substrate material will be different according to the use of the micro coil, and due to some special application scenarios, such as the requirements of the aerospace environment, insulation performance is also impacted. The following three parts will introduce the base material, insulation material, and coil deposition process.

(1) Substrate material

MEMS process coils can be fabricated on rigid substrates depending on the application. For example, the material properties of silicon are very suitable for the substrate material, which will be crucial for the rapid development of silicon micromachining technology in the future. Glass materials have high light transmission, high hardness, corrosion resistance, excellent biocompatibility, and other material properties, and are often processed into micro-reactors, micro-pumps, micro-accelerators and other devices in MEMS [37]. Ceramic materials, especially engineering ceramic materials, have high strength, corrosion resistance, high temperature stability, and excellent mechanical properties, and are often used to process microturbines, micro tools, and micro substrate materials [38]. The application of insulating hard and brittle materials, such as glass and ceramics, has shown a good momentum of development, and new sensors made of hard and brittle insulating materials, such as MEMS and CMOS, are increasing in demand in the Internet of Things, smartphones, and other industries. For example, sapphire glass is selected as the raw material for the fingerprint identification sensor, camera, and even display panel of Apple mobile phones. This material has extremely high hardness and good dielectric properties, showing strong performance [39].

Although these rigid substrates have a variety of applications, the study of flexible substrates is particularly important for some non-planar and flexible surface measurements, such as the measurement of tubular magnetic field distribution, wearable sensors for the measurement of human or biological surface magnetic fields, and magnetic field sensors for stress measurement. At present, the organic polymer materials used for flexible substrates are PI(polyimide), PDMS(Polydimethylsiloxane), parylene, polyethylene terephthalate (PET), silicone resin, and so on. Compared with traditional Si-based hard substrate materials, organic flexible substrate materials, in addition to being flexible and bending, also have good mechanical properties, dielectric properties, good physical and chemical stability, and so on. At the same time, these materials also have a good drawing ability and flatness, making them widely used in the manufacture of MEMS sensors. Table 3 summarizes the applications of different substrate materials.

Table 3. Summary of coil applications with different substrate materials.

Type of Substrate	References	Substrate Materials	Coil Materials	Advantages	Applications
rigid	Jiang Q, et al. [27]	Glass	Cu	High light transmittance, high hardness, corrosion resistance	ME sensor
	Wang N, et al. [63]	Si	Cu	Excellent piezoresistive properties, easily oxidized to form a layer of silica on the surface (insulating layer)	Micro-transformers
flexible	Xuming Sun, et al. [51]	Parylene substrate	Cu	Biocompatibility, flexibility, chemical inertness and optical transparency	Wireless power transmission applications
	Woytasik M, et al. [84]	Kapton and Peek	Cu	Physicochemical stability, flexibility	Non-destructive testing (NDT) techniques

(2) Insulation materials

When multi-layer coils are involved in the preparation of coils, an insulating layer is needed to separate the two coils. Common insulating materials are SiO_2, polyimide, AL_2O_3, BN, MgO, and so on. Polyimide can be used as a dielectric layer insulation material between the conductor of the inductance coil and between the conductor and magnetic core. Under the condition that the dielectric constant is similar to SiO_2, it can realize a thicker insulation layer than the PECVD (Plasma-Enhanced Chemical Vapor Deposition) SiO_2 layer (thickness is generally less than 1 μm), which can reduce various capacitance values in the device to improve the purpose of the inductance's Q value. Al_2O_3 has a high dielectric constant (about 8.1), very low metal ion permeability, strong radiation resistance, good chemical stability, high thermal conductivity, and other characteristics. Moreover, its insulation is very good, and its resistivity is $3 \times 1015\ \Omega$·m. The resistance of most insulating materials decreases exponentially with an increasing temperature at high temperatures. In this case, it is not advisable to increase the resistance simply by increasing the thickness of the insulation layer, not only because the deposition rate of the insulation layer is slow, but also because the increase in the thickness of the insulation layer also indicates an increase in the residual stress, which will lead to the insulation layer falling off.

Researchers have also performed a lot of research on the temperature resistance of the insulating layer. Hiroshi Nakai et al. [85] showed that the insulation layer prepared under the conditions of an ion beam sputtering angle of 40–45, ion beam energy of 10 keV, and substrate temperature of 800 °C has the best insulation performance at the high temperature of 800 °C. The insulation resistance of the 6.5 μm alumina layer at 820 °C is greater than 10 MΩ. The Department of Chemical Process Metrology in the United States [86] focused on the influence of transition layer materials and gas composition in the process of thermal oxidation on the microstructure, composition, and insulation of the thermal oxide layer. The insulation resistance of the thermal oxidation layer and the sputtering alumina composite insulation layer on the NiCoCrAlY transition layer is greater than 1 MΩ at 1300 K, and that of the thermal oxidation layer and the sputtering alumina composite insulation layer on the FeCrAlY transition layer is about 100 KΩ at 1300 K. Thus, it can be seen that selecting NiCoCrAlY as a transition layer is more conducive to high-temperature insulation.

Wrbanek et al. [87] from the Glenn Research Center of NASA began to study composite insulation layers in 2002. Compared with the traditional single-layer insulation layer, the application of the composite insulation layer is more conducive to eliminating pinholes running through the insulation layer in the vertical direction. In this study, aluminum oxide and stainless steel were used as test substrates, and different insulation layer combinations and deposition processes were used. It was found that the composite insulation layer of 1 μm CrC and 4 μm Al_2O_3 deposited by the electron beam on the stainless-steel substrate cleaned with H_2SO_4/H_2O_2 can obtain good high-temperature insulation: the resistance is 84 MΩ at 690 °C and 20 MΩ at 750 °C. The composite insulating layer of 1 μm ZrO_2/Y_2O_3 and 4 μmAl_2O_3 deposited by the electron beam on the alumina matrix, polished and cleaned with silica, can also obtain good high-temperature insulation: 50 MΩ at 690 °C, 17 MΩ at 750 °C, and 1.8 MΩ at 900 °C. Table 4 summarizes the high temperature characteristics of different insulating materials.

(3) Coil deposition process

There are generally two methods for coil deposition: PVD (physical vapor deposition) and chemical vapor deposition (CVD). The PVD technologies include evaporation deposition and sputtering deposition. The principle of sputtering coating is that electrons collide with argon atoms in the process of accelerating to the substrate under the action of the electric field, ionizing a large number of argon ions and electrons, and the electrons fly to the substrate. Vacuum evaporation is the vacuum chamber with a substrate pumped into a vacuum, and then the evaporation of the plating material is heated, so that its atoms or molecules from the surface of the gasification escape, the vapor flow forms, there is incident on the substrate's surface, and the condensation forms a solid film technology.

The vacuum evaporation method is advantageous because its equipment is simple, it can save on raw metal materials, has uniform surface adhesion, has a short production cycle, is environmentally friendly, and has the potential for large-scale production, among other advantages; however, given its disadvantages, such as having a higher reaction temperature, its precision control is unfavorable for the thin film deposition process. Compared with the magnetron sputtering process, the electroplating process has the advantages of a fast deposition rate, strong covering ability, strong leveling ability, and equipment economy, but it also has disadvantages such as the difficulty of controlling the composition of the coating and poor process stability. Compared with the magnetron sputtering process, the electroplating process has the advantages of a fast deposition rate, strong covering ability, strong leveling ability, and equipment economy, but it also has disadvantages such as the difficulty of controlling the composition of the coating and poor process stability. Vereecken et al. have successively studied the interaction mechanism between accelerators and chloride ions [52–55], and Pierre and Gabrielli of Marie Curie University studied the mechanism of copper plating [88]. Chemical vapor deposition (CVD) is a thin film deposition technique in which reactants (usually gases) are formed into solid products in a reaction chamber and deposited on the surface of a wafer by chemical reaction. As the reactant molecules in CVD can adsorb or diffuse on the surface of the substrate many times before decomposition and chemical reaction to form a film, which allows the reactant molecules to reach anywhere on the surface of the substrate, CVD can provide better step coverage than the physical CVD. The following two tables show the comparison of different coil deposition processes and copper films prepared by different deposition processes. Tables 5 and 6 compares different coil deposition methods.

Table 4. High-temperature characteristics of different insulating materials for metal coils.

Reference	Insulating Layer	Temperature (°C)	Insulation Resistance (MΩ)
Nakai H, et al. [85]	6.5 μm alumina	820	>10
J.Y. Park, et al. [86]	Thermal oxide layer + sputtering alumina on the NiCoCrAlY transition layer	1027	>1
	Thermal oxide layer + the sputtering alumina composite insulation layer on the FeCrAlY transition layer	1027	>0.1
John D, et al. [87]	Composited with 1 μm CrC and 4 μm Al_2O_3	690	84
		750	20
	Composited with 1 μm ZrO_2/Y_2O_3 and 4 μm Al_2O_3	690	50
		750	17
		900	1.8

Table 5. Features of different processes for metal deposition.

Process	Deposition Rate	Sedimentary Area	Cost of Equipment	Equipment Complexity	Difficulty Level
Electroplate	Quick	Large	Low	Low	Simple
Sputtering deposition	Medium	Large	High	High	Medium
Vacuum evaporation	Slow	larger	High	Medium	Medium

Table 6. Comparison of copper film growth in various methods.

Methods	CVD	PVD	Electroplating	
			Electroless	Electrolytic
Impurities	C, O	Ar	Seed layer	–
Deposition rate (nm/min)	~100	≥100	<100	~200
Process temperature (°C)	~250	RT	50~60	RT
Step coverage	Good	Fair	Good	Good
Via fill capability	Good	Poor	Fair–poor	Fair–poor
Environmental(waste)	Good	Good	Poor	Poor

3.3. Printing Process

The printing of electrons is carried out to transform specific functional materials into liquid ink (ink, paste). According to the design requirements for electronic devices and the products' performance, the film, which is large in scale and flexible, has the same volume as the electronic components (in whole or in part due to the printing or coating technology), and the system is characterized by a by-product production process. In terms of the manufacturing process, the electron-printing process is a part of additive manufacturing technology. Compared with the traditional integrated circuit process, it does not need complex processes, can reduce the loss of raw materials, and is conducive to environmental protection. The prepared products have the following characteristics: being large in area, lightweight, flexible, and bendy.

3.3.1. Micro-Contact Printing Process

Soft etching technology is based on elastic seals with a micro/nanostructure to prepare high-resolution patterns, combining the advantages of nanomaterial technology, fine processing technology, contact printing technology, interface science, and many other technologies, and has attracted wide attention in the field of materials science. This technology was proposed by the American scientist, Whitesides [89], in the late 1990s, and mainly combines top-down lithography technology and bottom-up self-assembly technology. Microcontact printing is the most widely used soft etching patterning technology, and has attracted much attention due to its fine size (micro/nano) and simple patterning process. The elastic seal material used is polydimethylsiloxane, which can be printed on rough surfaces or other surfaces, and the highest resolution is below 100 nm.

Micro-contact printing is a type of contact printing, and mainly includes elastic seal preparation, contact printing, pattern formation, and other processes. The details are as follows: polydimethylsiloxane (PDMS) is first cast on the silicon template with a microstructure, and then cured and exfoliated to obtain the replica PDMS elastomeric stamp. The "ink" (usually mercaptan alkanethiols) is then dipped and transferred to an Au-coated substrate by contact to obtain a self-assembled monolayer, which can be used as a template or the layer that cannot be easily etched to further prepare high-precision nanostructure patterns. A flowchart is shown in Figure 9 [90].

Printed substrate materials are not limited to gold; other metals are also successfully used as substrates to achieve pattern replication, such as Ag [91], Cu [92], and Pd [93]. The low cost and simplicity of the technology have inspired interest in creating smaller patterns with higher edge resolution and a broader versatility of the technology.

The seal deformation during the removal of the seal from the template, and the contact with the substrate, limits the resolution of the pattern. The PDMS crosslinking process usually leaves some fragments, which have a low molecular weight, uncured, which may pollute the substrate during contact, and thereby reduce the printing quality. When ink molecules contain polarity, the transfer of these impurities enhances the expansion of impressions in almost all organic solvents, thereby changing the size and shape of the protrusions. In order to improve the stability of the seal and the applicability of the printing pro-

cess, some new seals were invented. Schmid et al. [94] developed a hard PDMS (h–PDMS) that is more suitable for submicron graphics transmission. There are other new seal materials to achieve better mechanical properties. For example, poly(styrene–b–butadiene–styrene) and poly(styrene–b–(ethylene–co–butadiene)–b–styrene) [95] have a high modulus and toughness compared with traditional PDMS. Compared with PDMS stamps, poly(ether ester) [96] was used as a stamp material to accurately map proteins on the surface with a lower ink concentration and time. Lee et al. [97] developed a UV-curable impression material based on a functional prepolymer, which has acrylate groups for crosslinking and different monomer modifiers, and was successfully used to print sub-100 nm hexathiol patterns on gold. The mechanical properties of poly (polyurethane acrylate) impression can be adjusted by changing the modulator.

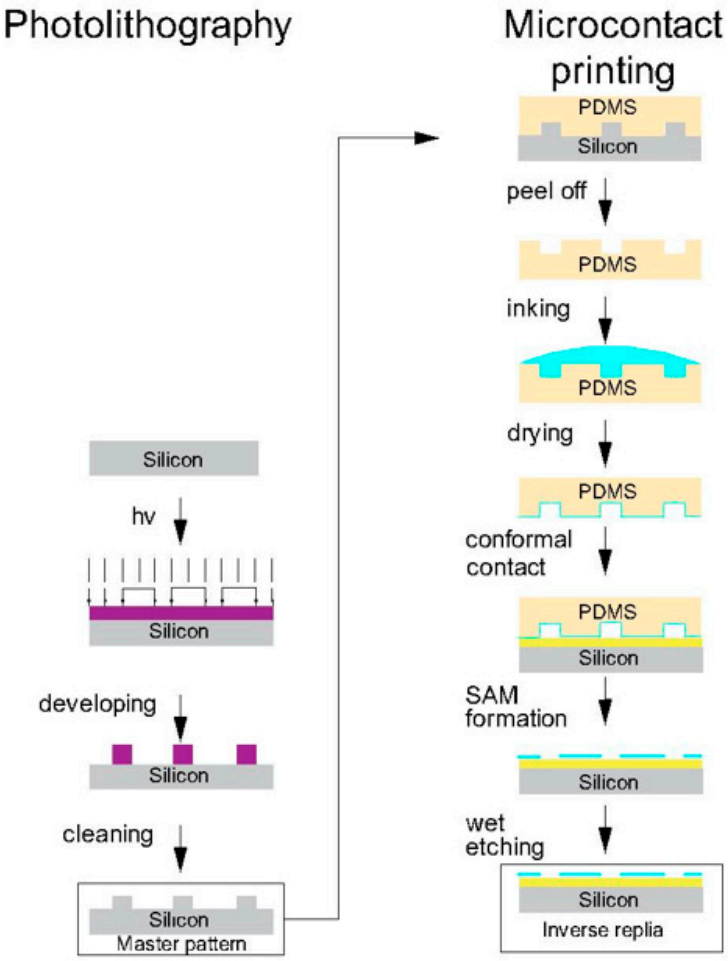

Figure 9. Flow chart of micro-contact printing.

Microcontact printing can be patterned at micron and sub-micron scales of various materials, and can achieve small molecules, polymers, and the transfer printing of other materials. It is widely used in biology, materials, and microelectronics. In the field of microelectronics, Xu [98] et al. achieved a flexible transparent conductive electrode with a large aspect ratio and a high-resolution metal mesh transparent electrode with high efficiency and low cost using micro-contact nano-imprint printing. That is, the researchers used an electric field-driven direct writing technology for molten deposition and a liquid bridge micro-transfer printing composite process. It has obvious advantages in terms of its low cost and potential for mass manufacturing, and provides a new solution with prospects for industrial applications in transparent electrode manufacturing. Figure 10 depicts the flow chart of the process.

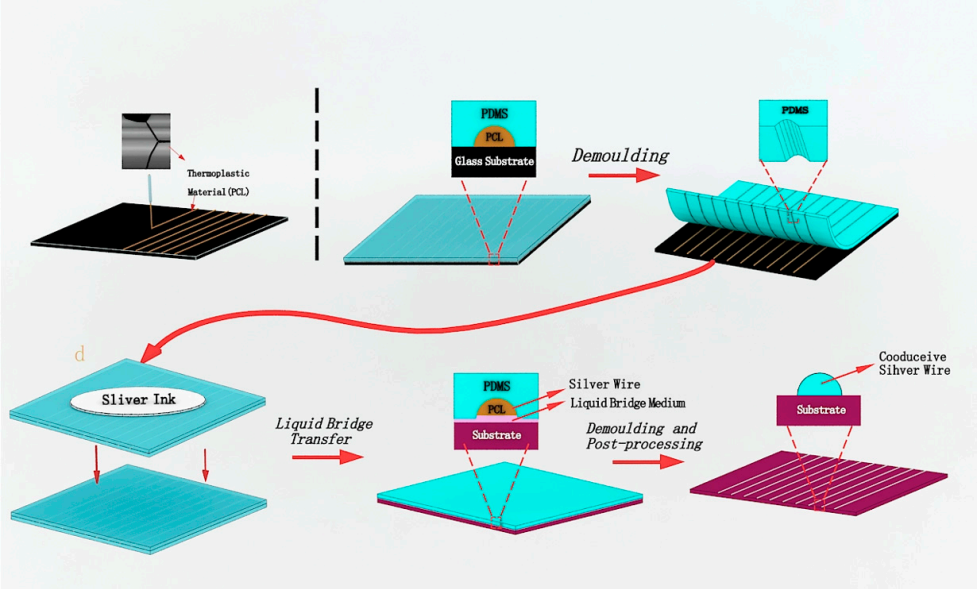

Figure 10. The schematic diagram for the fabrication of the TCE.

Figure 10 shows the first process of fabricating the PCL (Polycaprolactone) master mold using the electric-field-driven fusion direct printing technique. Secondly, vacuum casting, or scraping the liquid PDMS on the surface of the PCL master mold and curing it, occurred. Thirdly, peeling off the cured PDMS working soft mold from the PCL master mold occurred. Next, filling and preliminarily curing the nano-silver ink into the grooves of the microstructure of the PDMS soft mold occurred, followed by transferring the silver wire to the target substrate using the liquid bridge transfer process. Finally, peeling off the PDMS soft mold and sintering the transferred silver wire to form the TCE occurred (Transparent Conducting Electrodes).

3.3.2. Transfer Printing Process

The term 'flexible electronics' refers to the micro/nano electronic devices made on a flexible substrate. Flexible electronics are flexible, malleable, and biocompatible, and have been widely used in medical diagnosis, information detection, energy collection, and other fields. They have become the frontier of international research. In photolithography, soft etching, nano printing, and other processes, there are high-temperature, physical or chemical corrosion processes, but in this environment, the performance of flexible polymer substrates will be significantly reduced. In order to solve the above problems, transfer printing technology is used in the production of extensible, flexible electronics. Transfer printing technology is compatible with the semiconductor and nano manufacturing process and can highly adapt to various planar and non-planar structures. The basic principle of transfer printing is to use the difference between the two substrates and functional devices so that functional devices transfer from one substrate to another substrate, which can solve the problem of inorganic conductive materials not being able to directly grow and process on a flexible substrate. The existing transfer printing methods mainly include the rate-based transfer printing method [99,100], the micro-structure-based transfer printing method [101], the tape-based transfer printing method [102,103], and the sacrificial layer transfer printing method [104,105], according to their published time arrangement. Table 7 is the commonly used transfer printing method.

Table 7. Commonly used transfer printing methods.

Methods	Transfer of Material	Stamp	Acceptor Substrate	Sizes (μm)
Rate-based transfer printing method	Si	PDMS	GaAs, InP	0.3
	Cu	PDMS	PDMS	100
	PZT	PDMS	PDMS	300
	Ag/MgF2	PDMS	PDMS	0.225
	GaAg	PDMS	PI	–
Micro-structure-based transfer printing method	Si	PDMS	Quartz	100
	InGaAs	PDMS	PI, PET, Si	50
	Au, Ag, Cu	Hydrogels	PET, PVC	20
	Si	PDMS	Glass	15
Tape-based transfer printing method	$LiCoO_2/Li_4Ti_5O_{12}$	Tape	Ecoflex	1580
	Si	Tape	PI	250
	AuNPs	Tape	Al	10
	Au/PI	Tape	PDMS	–
Sacrificial layer transfer printing method	MOS device	PDMS	PDMS	–
	$\alpha - Si$	PDMS	PET	–
	SWNT	PU	PI	–

Zhigang Wu's research group [106] proposed the "one-step transfer printing method" for the manufacture of flexible stretchable electronics by using the rate-based transfer printing method. Graphics of different widths were made on the donor substrate, then the copper structure was transferred using pre-stretched PDMS, resulting in a structure that could still be used when it is stretched by 300%. Kim's research group [101] designed a PDMS seal into a micro pin-like structure. By applying different pressures on donor and recipient substrates to control the transfer printing process, the silicon structure was transferred to the quartz surface, and the researchers studied the mechanism via which this structure regulates transfer printing with different pressures. The transistor is fabricated and tested by this transfer printing method. Ko's group [107], from the Ulsan National Science and Technology Institute, studied the process of the absorption and release of octopus tentacles, and found that changes in humidity can regulate the change in viscosity. From this, the researchers were inspired, and developed the PDMS surface using the stamp of the micro-hole array.

The tape transfer printing method [103] uses tape as a seal for transfer printing. Many tapes have special properties, such as water-soluble tape that can dissolve in water and heat-release tape which loses viscosity after heating. Lin Yuan's research group [108] from the University of Electronic Science and Technology of China used the heat-release tape as the seal. When the temperature of the tape was lower than the release temperature, the functional structure with gold and PI could be transferred to the stamp. Then, the tape with a functional structure was placed on the PDMS recipient substrate for heating, and the tape lost viscosity and fell off. Xu's team at the University of Illinois [100] used water-soluble tape to transfer the active material of a lithium-ion battery, printed it on a recipient substrate with electrodes, and finally, dissolved the tape with water to produce a flexible and stretchable lithium-ion battery array. Figure 9 shows the tape transfer method.

With the development of micro/nano processing technology, the scope of application is becoming increasingly extensive, and the size of transfer printing graphics is developing towards miniaturization and high integration.

In terms of miniaturization, as can be seen from Table 7, the resolution of the functional structure transferred by most transfer printing methods is still only at micron or submicron scales. Although some methods conduct transfer printing at the nanoscale, the materials used for transfer printing are only suitable for metals. Based on this problem, Pang [109] and others, for the first time, put forward a new kind of auxiliary nanoscale transfer printing method with a sacrificial layer. This paper expounds on the sacrificial layer transfer process to improve the resolution and reduce the cause of the dependent variable. This method is applied to the manufacture of flexible electronics, flexible LED circuits, and flexible capacitors and tests, which demonstrates the good performance and high versatility of this method.

In terms of integration, Nishana [110] et al. discussed a dense array seal of active elastic composite material, which adopts an expandable 4 × 4 geometric design and a multi-way interconnection scheme to ensure a small footprint. It consists of 16 individual seals, each with a lead zirconate titanate (PZT) actuator and a strain gauge sensor. The drive and sensing characteristics and closed-loop feedback control were established, and the performance of the dense array seal was verified using selective pick-and-place micro-transfer printing experiments, which greatly improved efficiency and productivity.

Through the continuous integration of micro and nano processing technology in transfer printing technology, the transfer printing method is more and more extensive; however, transfer printing technology is in urgent need of a new method that can enable the resolution of the functional structure of transfer printing to reach the nanometer level, but it also needs to be highly integrated to improve the efficiency of transfer printing. Moreover, the method is as simple as possible, and is not affected by the nature of the donor substrate, the stamp, and the recipient substrate. To achieve such a breakthrough, transfer printing technology will progress greatly.

3.3.3. Ink-Jet Printing Process

Ink-jet printing technology is a complex and diverse new technology. It applies control system outputs, can print a single or diverse power supply circuit, and can support a variety of design schemes and data types, with a strong compatibility mode. Based on the control of the computer and printer, the nozzle is sprayed with a certain amount and a certain frequency of ink on the surface of the matrix, and high-precision and high-quality pattern information is drawn on the matrix, and the circuit design and electrode fabrication are completed. As the nozzle aperture is generally less than or equal to 5 μm, the extrusion of micro ink droplets spread on the substrate-formed ink dot area is small, so the printing line has good line accuracy. Ink-jet printing technology can replace the traditional printing process by using organic materials and metal composite materials based on the aqueous solution method. Ink-jet printing can be divided into continuous printing and on-demand printing according to its working principle.

Traditional ink-jet printing is the most common method of coating nano-silver ink; however, it is often necessary to adjust the preparation of high-quality nano-silver ink to match, although this also increases the development and manufacturing costs of nano-silver ink. The airflow jet printer and electrohydrodynamic ink-jet printer are introduced below.

Jet printing is a coating method that requires the lowest properties of nano-silver ink. Figure 11 shows the working principle of the jet printer [111]. In Figure 12a, the nano-silver ink is atomized first, and the ink is dispersed into liquid particles and mixed with working gas to form aerosols. In the process of air-jet printing (Figure 12b), the size of the atomized ink is about 1–5 μm, and these droplets are sent to the nozzle by high-speed air. The nozzle part will produce a ring around the airflow, aerodynamically focusing on the droplets ejected, so that the aerosol ink ejects into a stable fine line to ensure that the aerosol ink point is controlled within less than one-tenth of the diameter of the nozzle. The thinnest nozzle can print a line with a width of 5 μm. At the same time, because the ink beam at 2–5 mm of the height of the width is the same, some of the substrates can maintain the same thickness of the print line.

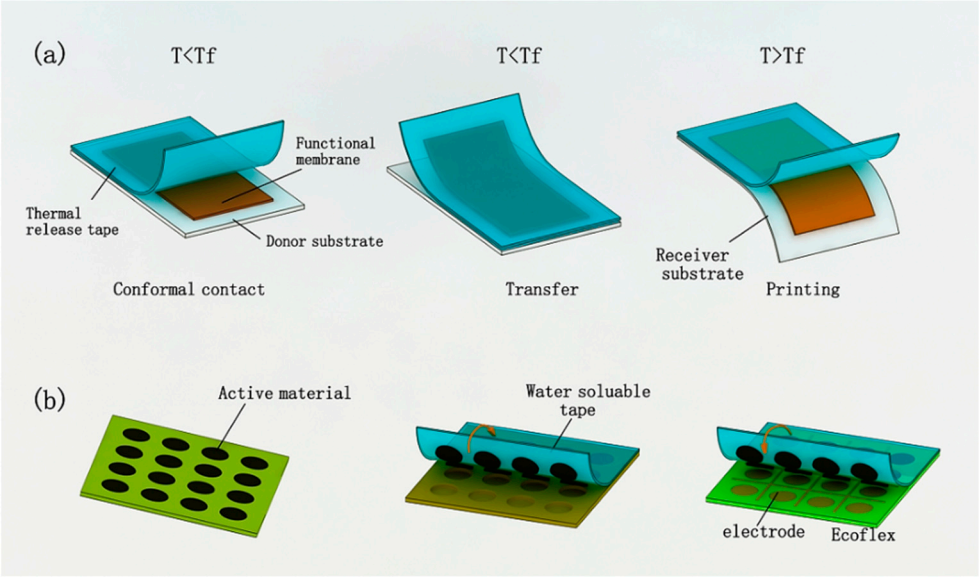

Figure 11. Tape-assisted transfer: (**a**) heat-release tape transfer, (**b**) water-soluble tape transfer.

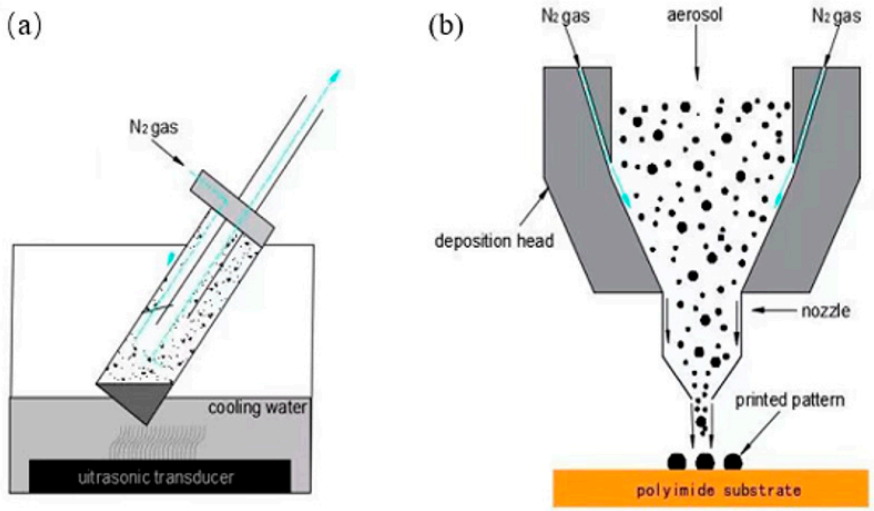

Figure 12. Schematic diagram of the working principle of the jet printer: (**a**) atomization of ink, (**b**) inkjet process.

Mahajan A et al. [112] prepared a complete nano-silver coating on a fluted substrate using this method, with a line width and spacing of about 50 μm. Electrohydrodynamic ink-jet printing uses high-voltage, electric field-stretching ink to pull the jet from the top of the meniscus and deposit it on the substrate to form a coating, as shown in Figure 11 [113]. The nano-silver ink was rheologically induced to form a Taylor cone under the action of a high-pressure electric field, and then the micro–nano jet with a diameter much smaller than the inner diameter of the jet hole was formed. The micro–nano coating was deposited on the substrate. Compared with the traditional ink-jet printing method, the resolution of the electro-fluid printing method is very high, at less than 1 μm; an applicable ink viscosity range of 1–10,000 CP is also possible. Electrohydrodynamic ink-jet printing has attracted increasing attention due to its wide range of applicable ink properties and high printing accuracy. Electrohydrodynamic ink-jet printing is used to print nano-silver ink, and the coating with a line width of 50 nm and spacing of about 500 nm can be printed at the finest level. Figure 13 shows the principle of electro-hydraulic power in inkjet printing.

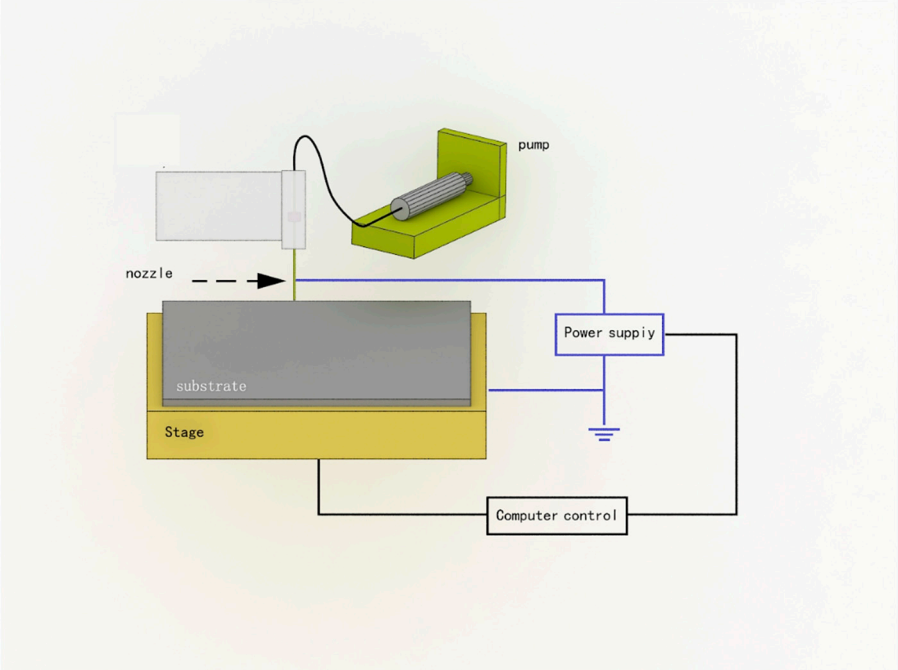

Figure 13. Ink-jet printing schematic diagram of the electric fluid power.

3.3.4. Introduction to Conductive Ink Printing

As the core material of printed electronic technology, conductive ink is one of the keys to the development of printed electronic technology. At present, the main components of conductive materials in conductive ink include carbon materials, conductive polymer materials, nano metal materials, and many kinds of mixed conductive materials. Nano metal materials have become a popular conductive component because of their excellent electrical properties and are made into conductive ink. Nano metal materials, which are commonly used as conductive components in conductive ink, include nano-gold, nano-silver, and nano-copper. Among the various conductive inks, silver- and carbon-based inks are preferred, whereas copper-based inks are the most profitable. Copper, however, has problems with oxidation, making it less suitable for printing. Nanoparticle- and particle-free alternatives are also springing up, but they cost more. Nanometer silver materials have great research significance and application prospects because of their excellent electrical conductivity, stable oxidation resistance, and relatively low manufacturing cost. This article introduces several conductive ink products already sold in the market. Table 8 is an introduction to some products.

Table 8. Conductive ink products.

Product	Manufacturer	Conductive Material	Solid Content	Viscosity	Applicable Process
EI–1104	Eletroinks	Ag	14 wt%	10 cps	Ink-jet printing
EI–906	Eletroinks	Ag/AgCl	30 wt%	16,000 cps	Silk screen printing
Ink10	FUDY	Ag (10 nm)	35 wt%	5–30 cps	Ink-jet printing
CON–INK550	Dahua Brocade	Ag (30 nm)	25–30 wt%	5–6 cps	Ink-jet printing

For all the products listed above, CON–INK550 is a new electronic material for digital print-deposited conductive circuit technology. It is compatible with Epson series nozzles (DX5, DX7), Fuji Star series and Spectra series Konica nozzles (KM512i, KM1024i), and Ricoh nozzles (Gen5, Gen5s, Gen6). Its advantages include its excellent electrical conductivity, extremely smooth printing, high nano-silver content, and good hardness and adhesion. EI–1104 and EI–906 are two products from Electroinks, a leader in particle-free conductive metal inks and advanced materials. EI–1104 inks are formulated for ink-jet deposition and

applications requiring high electrical conductivity. This unique ink provides stable injection performance at room temperature and has a long shelf life. The low curing temperature makes the EI–1100 series suitable for PI, glass, and silicon nitride. The conductive material of EI–906 is composed of silver and silver chloride, and its viscosity is very high, up to 16,000 cps, so it is suitable for screen printing.

In recent years, research on nano–metal–conductive ink for ink-jet printing has mainly been focused on improving the solvent formula properties of conductive ink to optimize the molding process and coating quality of spray printing coating or to optimize the electrical and mechanical properties of the coating under different molding conditions. Liu et al. [114] from the Harbin Institute of Technology proposed a method to prepare nano-silver ink by compounding the nano-silver particles of different sizes. The principle that large, slow-moving silver particles hinder small silver particles from moving toward the edge of the droplet during the drying process of ink droplets was adopted to avoid the coffee ring phenomenon of printing coating. The microstructure density, electrical conductivity, and bending reliability of the silver coating were improved. Teng et al. [115] dissolved silver neodecanoate in xylene to form silver conductive ink. The ink was transferred to the surface of solar cells by a direct ink-jet method, and the silver conductive mesh was obtained by a heat treatment at 350 °C. Valeton et al. [116] used the ink-jet printing method to deposit organic silver-based ink. After UV curing and hydroquinone solution treatment, a silver conductive layer was formed. Cai et al. [117] dissolved silver oxide in the methanol solution of ammonium carbamate to obtain particle-free conductive ink. Using laser direct writing technology, the organic silver compound printed on polyimide film was decomposed into silver particles, and finally the silver film with good conductivity was obtained.

With the increasing popularity of various flexible substrates in the microelectronics industry, conductive ink for printing electrons is developing in the direction of low cost, high conductivity and a low-heat treatment temperature. Particle-free conductive ink has become the focus of future development.

3.4. Other Processing Methods

3.4.1. Liquid Metals

The key advantage of using liquid metal technology is that it allows flexible, complex 3D electrical conductors to be fabricated within microchannels with very few fabrication steps, compared with using conventional machining methods to fabricate 3D micro coils [118]. The liquid metal structure has the ability to deform mechanically and can be applied to many devices that require high precision, high complexity, and high mechanical strength, such as tunable fluid antennas and pressure sensors [119]. The method of fabricating a multi-layer integrated micro coil using liquid metal is shown in Figure 14. First, the structural layer is processed by laser layering. The micro coil's structural layer is composed of three layers: a spiral channel, an interconnection, and a lead-out channel. All layers are assembled together via a stacking process. An adhesive glues the location of the wire inlet and outlet of the coil to the top of the PCB metal pad. Firm and stable contact between the micro coil structure's layer and the liquid metal is achieved through contact with the PCB. Through-holes with a diameter of 1 mm are mechanically drilled in the contact plate of the PCB. Next, liquid metal is injected from the back of the PCB, allowing the liquid metal to flow through the first copper pad on the PCB and into the spiral channel. The liquid metal flows through the interconnected layer, then through the lead-out channel back to another PCB contact pad, and finally out through the outlet drilled in the PCB. The large contact area between the liquid metal and the PCB contact pad ensures a good electrical connection with the external equipment, and the liquid metal is cooled to form a three-dimensional coil [120], which completes the preparation process of the liquid metal micro coil.

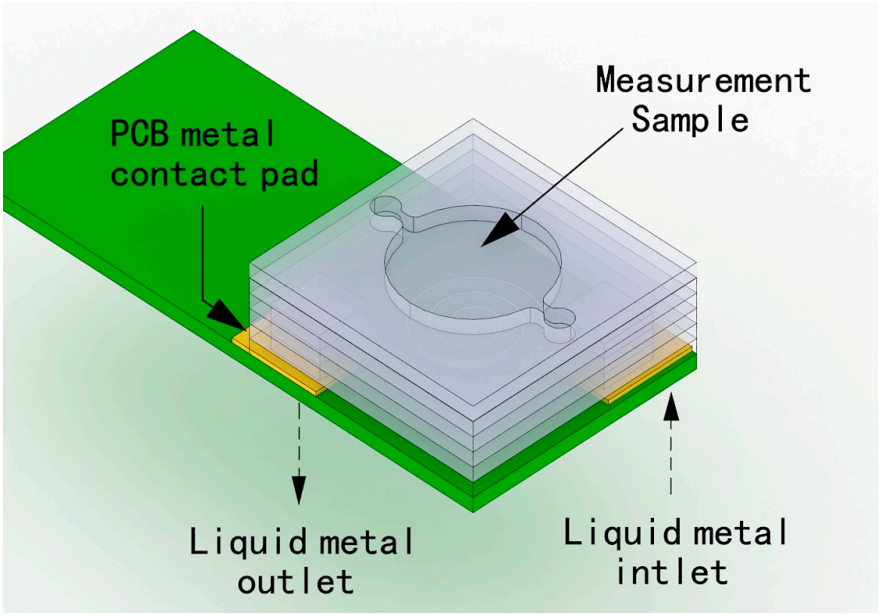

Figure 14. Liquid metal preparation of miniature coils.

3.4.2. Femtosecond Laser

With the continuous improvement of the integration and complexity of microsystems, the requirements for the preparation of three-dimensional spiral micro coils continue to increase, and the performance of micro coils as the basic components and important functional parts of microsystem chips directly affects the overall performance of microsystems. Moreover, the preparation of high-performance micro coils has a very important practical significance [121–123]. The use of femtosecond laser micromachining technology can be prepared more uniformly inside the transparent medium, has good performance, and is able to meet the actual application requirements of microsensor devices. Moreover, the preparation of three-dimensional spiral micro coils is currently a relatively advanced technology, and is based on three-dimensional micromachining femtosecond laser technology to prepare three-dimensional high-performance coils, which is mainly combined with the idea of metal "micro-curing", as proposed by Siegel et al. in 2007 [124]. The process of preparation using femtosecond laser micromachining technology is mainly divided into three steps. First of all, the femtosecond laser modification process is used to scan the spiral microchannel structure inside the material. More specifically, a femtosecond laser is used to focus on the substrate through the microscope, and laser scanning modification is carried out through a 3D processing platform and well–written program. Then, the sample undergoes wet etching, that is, the modified sample is placed in the corrosion liquid, with ultrasonic oscillation at room temperature. The purpose is to make the modified part of the sample fully react with the corrosive liquid to obtain the internal channel of the material. After the preparation of the above two steps, the internal hollowed-out microchannel is prepared. Finally, the metal is micro-cured, the sample is tightly bonded to the PDMS film, the needles of the two syringes are inserted into the PDMS, and a micro-injection pump is connected to each of the other two ends of the two entry syringes of the micro coil to heat and melt the gallium metal and inject it into a syringe. Pushing the gallium metal syringe inward while the other syringe inhales outward, the gallium metal fills the entire micro coil channel. The ultrasound should then be cooled to room temperature to peel off the PDMS film to obtain the prepared micro coils.

This method of preparing a three-dimensional spiral micro coil using femtosecond laser modification, wet etching, and metal curing can prepare a micro coil with any morphology, and during the preparation process, the parameters of the micro coil can be precisely controlled, and the accurate processing of the three-dimensional channel can be

realized. By writing a program to control the 3D platform to move along the designed trajectory, it is easy to achieve the processing of any shape of 3D microchannels. Compared with the use of the planar process after multi-layer mask preparation and layer-by-layer mask accumulation to prepare three-dimensional structural coils, this preparation method is complex and expensive. Moreover, by winding metal wires on the surface of the cylinder or plating spiral conductive wires on the surface of the cylinder, the femtosecond laser wet etching technology can prepare a micro coil that can be integrated inside the material, and there is no such complex process of layer accumulation, while more accurately making any shape of micro coil, which ensures the consistency and superiority of the performance of the micro coil. In particular, it can reduce dispersion and anti-interference, and can also flexibly increase or decrease the number of turns as needed, with a high degree of integration, which is convenient for integration with other micro coils and even microsystems. Both these micro coils and femtosecond laser wet etching techniques will play an important role in microcircuit systems.

4. Challenges and Prospects

Among the various micro metal coils summarized in this paper, the manufacturing cost of macromachining is low, but there are many processing steps. Additionally, the manufacturing resolution is low, and the RF field is not uniform. MEMS processing can make the coil size as small as possible, can increase the performance of the device, and can achieve mass production to reduce the cost. Additionally, it can be integrated with machinery, materials, manufacturing, information and automatic control, physics, chemistry, biology, and other disciplines. It has a wide range of applications in, and lays a good foundation for, the Internet of Things era, which is characterized by the "perception of everything, full of wisdom" principle; however, MEMS processing technology still faces many new problems, such as how to protect the microstructure during silicon wafer cutting to prevent silicon dust from damaging the chip. Other issues include how to prevent adhesion between moving parts and substrates in the process of releasing the microstructure, as well as stress release in device packaging and the standardization of packaging and interfaces. In addition, the reliability and reliability evaluation of packaging performance are also discussed.

As a kind of electronic manufacturing technology, the electron printing process has advantages that a silicon-based integrated circuit does not have, including its large area, flexibility and low cost, and it plays a pivotal role in MEMS and the manufacturing of other micro coils. Micro contact printing can realize the transfer printing of small molecules, polymers and other materials, and is widely used in biology, materials, and microelectronics; however, the resolution and transfer efficiency of the transfer function structure are low. Liquid metal processing makes the metal coil have a good mechanical deformation ability, which is suitable for devices requiring high precision, high complexity and high mechanical strength processing. Femtosecond laser micromachining technology is more practical in preparing 3D spiral micro coils with better performance. Table 9 shows the performance and practical applications of coils prepared based on different processes.

In engineering practice, higher requirements are put forward for the development of micro metal coils, and there are some technical difficulties in the preparation process. In order to promote the further development of the Internet of Things' (IoTs) industry, there are still some challenges in preparing high-performance, low-cost, mass-produced miniature metal coils, and the following future trends are worth paying attention to:

(1) The area of single-layer planar metal coils inevitably increases with the increase in coil turns, but the preparation process of multi-layer coils is more complicated than that of single-layer coils. In addition, due to the superposition of insulating layers, it is difficult to achieve surface planarization, which will greatly affect the photolithography effect. The effect is not improved significantly due to the limited number of accumulated layers; therefore, it is necessary to study a new type of multilayer coil with a simple and reliable preparation process and high-quality factor.

(2) Rigid substrates cannot be applied to the measurement of some non-planar surfaces and flexible surfaces. In flexible substrate processing, some links need a high-temperature environment, which will cause damage to the flexible film, in order to improve the magnetic properties. Thus, there is a need to develop more suitable methods for the combination of the materials and the substrate.
(3) The coil size is small, the degree of integration is high, and the working temperature is increased accordingly. For the vast majority of insulating materials, their resistance will decrease exponentially with the increase in the temperature at high temperatures, and the insulation performance will decrease greatly; therefore, it is necessary to study the preparation of the insulating layer of composite insulating materials with higher temperature resistance and stability.
(4) For the electronic printing process, the resolution of the functional structure transferred by most transfer printing methods is still only at a micron or sub-micron scale, so it is necessary to study a new transfer printing technology, which can improve the resolution of the functional structure of transfer printing and transfer efficiency.

Table 9. The performance and practical applications of coils prepared based on different processes.

Processing Technology	Device	Advantage	Application
Macro processing method	Detection probe	Low cost, not easily oxidized	Detection equipment such as NMR machines
	Manual winding coil on capillary	The method is simple and suitable for manual operation	Detection of coil preparation parameters under laboratory conditions
	Experimental detection coil	Novel methods with the potential for mass production	Integrated micro-inductor
MEMS Machining Method	WPT system	Wireless transmission, high Q value and high inductance increase the transmission distance and energy	Power supply for devices such as cochlear implants in biomedical fields
	Isolation miniature transformer	Small footprint, high coupling, high-voltage gain and low DCR, suitable for signal conversion in the frequency range of tens of MHz	Automotive electronics, industrial electronics, etc.
	Three-axis magnetic sensor	Surface sensor detection	Wearable equipment, nondestructive testing (NDT)
	Energy harvesting	Large functional density and small size of the devices	Health and Use Monitoring System for Defense Military Helicopters (HUMS)
Printing technology	Array electromagnetic Sensor	High density, microwire width detection coil	Nondestructive electromagnetic testing field
	Transparent conductive grid	Large aspect ratio, high resolution, large area fabrication	Touch screen, organic solar cell, transparent display
Liquid metals	Multilayer integrated NMR microcoil	Good mechanical deformation ability	Tuned fluid antenna, pressure sensor, energy harvester and other devices need high precision, high complexity, high mechanical strength processing
Femtosecond laser	3D spiral microcoil	More uniform, good performance, able to meet the practical application requirements	Micromechanical systems, microelectronic devices, micro sensors and other fields of micro-system integration

Author Contributions: J.L., project administration, writing—review and editing; H.R., writing and editing; X.C., data curation; K.C., resources; H.B., formal analysis; Z.W., supervision. All authors have read and agreed to the published version of the manuscript.

Funding: This work is supported by the National Natural Science Foundation of China (No. 50807042).

Conflicts of Interest: The authors declare no conflict of interest.

Abbreviations

MEMS	Micro-Electro-Mechanical System
RF	Radio Frequency
PI	Polyimide
PDMS	Polydimethylsiloxane
PVD	Physical Vapor Deposition
CVD	Chemical Vapor Deposition
CMOS	Complementary Metal Oxide Semiconductor
SECT	Silicon-Embedded Coreless Transformer
DLM	Double-Layer Metal
PCB	Printed Circuit Board
NMR	Nuclear Magnetic Resonance
UV	Ultraviolet
PCL	Polycaprolactone

References

1. Shinde, P.B.; Shiurkar, U.D. MEMS for detection of environmental pollutants: A review pertains to sensors over a couple of decades in 21st century. *Mater. Today Proc.* **2021**, *44*, 615–624. [CrossRef]
2. Hayat, H.; Griffiths, T.; Brennan, D.; Lewis, R.P.; Barclay, M.; Weirman, C.; Philip, B.; Searle, J.R. The State–of–the–Art of Sensors and Environmental Monitoring Technologies in Buildings. *Sensors* **2019**, *19*, 3648. [CrossRef] [PubMed]
3. Sun, J.; Tao, Z.; Li, H.; Zhu, K.; Wang, D.; Wu, H.; Xu, T. A MEMS Voice Coil Motor with a 3D Solenoid Coil. In Proceedings of the 2021 16th IEEE International Conference on Nano/Micro Engineered and Molecular Systems (NEMS), Xiamen, China, 25–29 April 2021; pp. 1745–1748.
4. Baxan, N.; Rengle, A.; Briguet, A.; Fakri–Bouchet, L.; Morin, P. High–Resolution 1H NMR Micro spectroscopy using an Implantable Micro–coil. In Proceedings of the IEEE International Conference on Electronics, Nice, France, 10–13 December 2006; pp. 359–362.
5. Li, Y.; Li, X.; Peng, F.; Zhang, H.; Guo, W.; Zhu, W.; Yang, T. Wireless energy transfer system based on high Q flexible planar–Litz MEMS coils. In Proceedings of the 8th IEEE International Conference on Nano/Micro Engineered and Molecular Systems, Suzhou, China, 7–10 April 2013; pp. 837–840.
6. Saleh, R.; Barth, M.; Eberhardt, W.; Zimmermann, A. Bending Setups for Reliability Investigation of Flexible Electronics. *Micromachines* **2021**, *12*, 78. [CrossRef] [PubMed]
7. Jin, L. Applications and Prospects of Mems Sensors in Automotive. In Proceedings of the 2021 International Conference on Intelligent Manufacturing and Industrial Automation (CIMIA 2021), Guilin, China, 26–28 March 2021; p. 012010.
8. Angadi, S.V.; Jackson, R.L. A critical review on the solenoid valve reliability, performance and remaining useful life including its industrial applications. *Eng. Fail. Anal.* **2022**, *136*, 106231. [CrossRef]
9. Meyer, C.D.; Bedair, S.S.; Morgan, B.C.; Arnold, D.P. High–Inductance–Density, Air–Core, Power Inductors, and Transformers Designed for Operation at 100–500 MHz. *IEEE Trans. Magn.* **2010**, *46*, 2236–2239. [CrossRef]
10. Li, Z.; Han, M.; Zhang, H. A novel MEMS electromagnetic energy harvester with series coils. In Proceedings of the 17th International Conference on Solid–State Sensors, Actuators and Microsystems (TRANSDUCERS & EUROSENSORS XXVII), Barcelona, Spain, 16–20 June 2013; pp. 2245–2248.
11. Moazenzadeh, A.; Suárez Sandoval, F.; Spengler, N.; Badilita, V.; Wallrabe, U. 3–D Microtransformers for DC–DC On–Chip Power Conversion. *IEEE Trans. Power Electron.* **2015**, *30*, 5088–5102. [CrossRef]
12. Sullivan, C.R.; Harburg, D.V.; Qiu, J.; Levey, C.G.; Yao, D. Integrating Magnetics for On–Chip Power: A Perspective. *IEEE Trans. Power Electron.* **2013**, *28*, 4342–4353. [CrossRef]
13. Wu, H.; Lekas, M.; Davies, R.; Shepard, K.L.; Sturcken, N. Integrated Transformers With Magnetic Thin Films. *IEEE Trans. Magn.* **2016**, *52*, 1–4. [CrossRef]
14. Kahlouche, F.; Youssouf, K.; Bechir, M.H.; Capraro, S.; Siblini, A.; Chatelon, J.P.; Buttay, C.; Rousseau, J.J. Fabrication and characterization of a planar interleaved micro–transformer with magnetic core. *Microelectron. J.* **2014**, *45*, 893–897. [CrossRef]
15. Dinulovic, D.; Shousha, M.; Haug, M.; Beringer, S.; Wurz, M.C. Comparative Study of Microfabricated Inductors/Transformers for High–Frequency Power Applications. *IEEE Trans. Magn.* **2017**, *53*, 1–7. [CrossRef]

16. Wu, R.; Sin, J.K.O.; Hui, S.Y. A novel silicon–embedded coreless transformer for isolated DC–DC converter application. In Proceedings of the 2011 IEEE 23rd International Symposium on Power Semiconductor Devices and ICs, San Diego, CA, USA, 23–26 May 2011; pp. 352–355.
17. Miao, X.; Dai, X.; Huang, Y.; Ding, G.; Zhao, X. Segmented magnetic circuit simulation of the large displacement planar micro–coil actuator with enclosed magnetic yokes. *Microelectron. Eng.* **2014**, *129*, 38–45. [CrossRef]
18. Liu, B.; Li, D. Design and Fabrication of a Micro Electromagnetic Relay. In Proceedings of the 2006 International Conference on Mechatronics and Automation, Luoyang, China, 25–28 June 2006; pp. 480–484.
19. Ren, W.; Liang, H.; Zhai, G. Thermal analysis of hermetically sealed electromagnetic relay in high and low temperature condition. In Proceedings of the 52nd IEEE Holm Conference on Electrical Contacts, Montreal, QC, Canada, 25–27 September 2006; pp. 110–116.
20. Pasharavesh, A.; Ahmadian, M.T.; Zohoor, H. On the energy extraction from large amplitude vibrations of MEMS–based piezoelectric harvesters. *Acta Mech.* **2017**, *228*, 3445–3468. [CrossRef]
21. Shi, C.; Li, F.; Zhao, J. An advanced folded piezoelectric vibration energy harvester with low resonant frequency and high power density. *AIP Adv.* **2020**, *10*, 805. [CrossRef]
22. Wang, Y.; Zhang, Q.; Zhao, L.; Tang, Y.; Shkel, A.; Kim, E.S. Vibration energy harvester with low resonant frequency based on flexible coil and liquid spring. *Appl. Phys. Lett.* **2016**, *109*, 203901. [CrossRef]
23. Jeong, S.; Song, J.; Lee, S.; Hong, S.; Sim, B.; Kim, H.; Kim, S.; Kim, J. Design, Simulation and Measurement of Flexible PCB Coils for Wearable Device Wireless Power Transfer. In Proceedings of the 2018 IEEE Wireless Power Transfer Conference (WPTC), Montreal, QC, Canada, 3–7 June 2018; pp. 1–4.
24. Teixeira, J.S.; Costa, R.S.; Pires, A.L.; Pereira, A.M.; Pereira, C. Hybrid dual–function thermal energy harvesting and storage technologies: Towards self–chargeable flexible/wearable devices. *Dalton Trans.* **2021**, *50*, 9983–10013. [CrossRef] [PubMed]
25. Chen, W.; Yan, X. Progress in achieving high–performance piezoresistive and capacitive flexible pressure sensors: A review. *J. Mater. Sci. Technol.* **2020**, *43*, 175–188. [CrossRef]
26. Spengler, N.; Moazenzadeh, A.; Meier, R.C.; Badilita, V.; Korvink, J.G.; Wallrabe, U. Micro–fabricated Helmholtz coil featuring disposable microfluidic sample inserts for applications in nuclear magnetic resonance. *J. Micromech. Microeng.* **2014**, *24*, 034004. [CrossRef]
27. Jiang, Q.; Chen, P.; Li, S.; Zhao, H.; Liu, Y.; Horikawa, S.; Chin, B.A. A highly integratable microfluidic biosensing chip based on magnetoelastic–sensor and planar coil. In Proceedings of the 2016 IEEE SENSORS, Orlando, FL, USA, 30 October–3 November 2016; pp. 1–3.
28. Shi, J.; Li, H.; Sun, B.; Zhao, X.; Ding, G.; Yang, Z. A Flexible Pressure Sensor Based on Low–Cost Electroplated–Ni Film Induced Cracking for Wearable Devices Application. In Proceedings of the 2018 IEEE 13th International Conference on Nano/Micro Engineered and Molecular Systems (NEMS), Singapore, 22–26 April 2018; pp. 432–435.
29. Su, W.; Wu, Z.; Fang, Y.; Bahr, R.; Raj, P.M.; Tummala, R.; Tentzeris, M.M. 3D printed wearable flexible SIW and microfluidics sensors for Internet of Things and smart health applications. In Proceedings of the 2017 IEEE MTT–S International Microwave Symposium (IMS), Honololu, HI, USA, 4–9 June 2017; pp. 544–547.
30. Liu, M.; Tuovinen, P.H.; Kawasaki, Y.; Yedeas, M.A.; Sekino, M. Electromagnetic and mechanical characterization of a flexible coil for transcranial magnetic stimulation. *AIP Adv.* **2019**, *9*, 035335. [CrossRef]
31. Cozzini, C.; Bobb, C.; Engström, M.; Kaushik, S.; Molthen, R.; Rettman, D.; Goruganti, V.; Chiang, W.; Wiesinger, F. PO–1038 MR–only Radiation Therapy: A silent patientfriendly workflow using a light–weight, flexible coil. *Radiother. Oncol.* **2019**, *133*, 576–577. [CrossRef]
32. Xu, W.; Cheng, T.; Wu, C.; Lu, N.; Yang, Z.; Lian, Y.; Wang, G. Ultrathin Flexible Coils for Wireless Power and Data Link in Biomedical Sensors. In Proceedings of the 2017 IEEE 12th International Conference on ASIC, Guiyang, China, 25–28 October 2017; pp. 676–679.
33. Ouyang, G.; Ezhilarasu, G.; Sun, H.; Ren, H.; Yang, Y.; Iyer, S.S. A Flexible Power Module for Wearable Medical Devices with Wireless Recharging using Corrugated Flexible Coils. In Proceedings of the 2021 IEEE 71st Electronic Components and Technology Conference (ECTC), San Diego, CA, USA, 1–4 July 2021; pp. 2266–2271.
34. Pan, T.; Baldi, A.; Davies-Venn, E.; Drayton, R.F.; Ziaie, B. Fabrication and modeling of silicon–embedded high–Q inductors. *J. Micromech. Microeng.* **2004**, *15*, 849–854. [CrossRef]
35. Wu, W.; Yi, H.; Chen, D.; Lu, R.; Yuan, T.; Chen, J.; Ni, Z. The design and fabrication of a low–field NMR probe based on a multilayer planar micro–coil. *Microsyst. Technol.* **2014**, *20*, 419–425. [CrossRef]
36. Pawinanto, R.E.; Yunas, J.; Said, M.M.; Noor, M.M.; Majlis, B.Y. Design and fabrication of PCB based planar micro–coil for magnetic MEMS actuator. In Proceedings of the 2014 IEEE International Conference on Semiconductor Electronics (ICSE2014), Kuala Lumpur, Malaysia, 27–29 August 2014; pp. 487–490.
37. Ziaie, B.; Baldi, A.; Ming, L.; Gu, Y.; Siegel, R.A. Hard and soft micromachining for biomems: Review of techniques and examples of applications in microfluidics and drug delivery. *Adv. Drug Deliv. Rev.* **2004**, *56*, 145–172. [CrossRef] [PubMed]
38. Rajurkar, K.P.; Levy, G.; Malshe, A.; Sundaram, M.M.; McGeough, J.; Hu, X.; Resnick, R.; DeSilva, A. Micro and nano machining by electro–physical and chemical processes. *CIRP Ann.* **2006**, *55*, 643–666. [CrossRef]
39. Haluzan, D.T.; Klymyshyn, D.M.; Börner, M.; Achenbach, S.; Wells, G.; Mappes, T.; Mohr, J. Stiction issues and actuation of rf liga–mems variable capacitors. *Microsyst. Technol.* **2008**, *14*, 1709–1714. [CrossRef]

40. Eduardo, F.; Kurlyandskaya, G.V.; Alfredo, G.A.; Svalov, A.V. Nanostructured giant magneto–impedance multilayers deposited onto flexible substrates for low pressure sensing. *Nanoscale Res. Lett.* **2012**, *7*, 230–235.
41. Lakamraju, N.V.; Phillips, S.M.; Venugopal, S.M.; Allee, D.R. MEMS shock sensor fabricated on flexible substrate. In Proceedings of the 2009 Flexible Electronics & Displays Conference and Exhibition, Phoenix, AZ, USA, 2–5 February 2009; pp. 1–4.
42. Hegde, R.; Ramji, K.; Swapna, P. Simulation of carbon nanotubes polymer based piezoresistive flexible pressure sensor for ultra sensitive electronic skin. In Proceedings of the 2018 2nd International Conference on Electronics, Materials Engineering & Nano–Technology (IEMENTech), Kolkata, India, 4–5 May 2018; pp. 1–5.
43. Khan, F.; Zhu, Y.; Lu, J.; Pal, J. Design and Implementation of Single–Layer Symmetric Micro–Transformers. *IEEE Trans. Magn.* **2016**, *52*, 1–5. [CrossRef]
44. Andreica, S.; Munteanu, C.; Gliga, M.; Pacurar, C.; Giurgiuman, A.; Constantinescu, C. Design of Multilayer Spiral Coils with Different Geometries to Determine the Inductance. In Proceedings of the 2020 International Conference and Exposition on Electrical And Power Engineering (EPE), Iasi, Romania, 22–23 October 2020; pp. 425–428.
45. Nakazawa, H.; Edo, M.; Katayama, Y.; Gekinozu, M.; Sugahara, S.; Hayashi, Z.; Kuroki, K.; Yonezawa, E.; Matsuzaki, K. Micro–DC/DC Converter that Integrates Planar Inductor on Power IC. *IEEE Trans. Magn.* **2000**, *36*, 3518–3520. [CrossRef]
46. Yamaguchi, M.; Baba, R.; Arai, K. Sandwich–type ferromagnetic RF integrated inductor. In Proceedings of the 2001 IEEE MTT–S International Microwave Sympsoium, Phoenix, AZ, USA, 20–24 May 2001; pp. 185–188.
47. Yoon, J.B.; Kim, B.K.; Han, C.H.; Yoon, E.; Kim, C.K. Surface micromachined solenoid on–si and on–glass inductors for rf applications. *IEEE Electron. Device Lett.* **1999**, *20*, 487–489. [CrossRef]
48. Dinulovic, D.; Shousha, M.; Haug, M. Tiny Wafer Level Chip Scale Packaged Inductive Components for High Frequency Isolated/Non–Isolated DC–DC Converters. In Proceedings of the 2021 IEEE Applied Power Electronics Conference and Exposition (APEC), Phoenix, AZ, USA, 14–17 June 2021; pp. 1743–1746.
49. Kim, Y.J.; Allen, M.G. Surface micromachined solenoid inductors for high frequency applications. *Compon. Packag. Manuf. Technol. Part C IEEE Trans.* **1998**, *21*, 26–33.
50. Zine–El–Abidine, I.; Okoniewski, M.; Mcrory, J.G. An Embedded Suspended Micromachined Solenoid Inductor. In Proceedings of the IEEE MTT–S International Microwave Symposium, San Francisco, CA, USA, 11–16 June 2006; pp. 1137–1140.
51. Sun, X.; Zheng, Y.; Peng, X.; Li, X.; Zhang, H. Parylene–based 3D high performance folded multilayer inductors for wireless power transmission in implanted applications. *Sens. Actuators A Phys.* **2014**, *208*, 141–151. [CrossRef]
52. Vereecken, P.M.; Binstead, R.A.; Deligianni, H.; Andricacos, P.C. The chemistry of additives in damascene copper plating. *IBM J. Res. Dev.* **2005**, *49*, 3–18. [CrossRef]
53. Bae, S.E.; Gewirth, A.A. In situ EC–STM studies of MPS, SPS, and chloride on Cu100: Structural studies of accelerators for dual damascene electrodeposition. *Langmuir ACS J. Surf. Colloids* **2006**, *22*, 10315–10321. [CrossRef] [PubMed]
54. Moffat, T.P.; Ou Yang, L.Y. Accelerator Surface Phase Associated with Superconformal Cu Electrodeposition. *J. Electrochem. Soc.* **2010**, *157*, 228–241. [CrossRef]
55. Hai, N.; Huynh, T.; Fluegel, A.; Arnold, M.; Mayer, D.; Reckien, W.; Bredow, T.; Broekmann, P. Competitive anion/anion interactions on copper surfaces relevant for damascene electroplating. *Electrochim. Acta* **2012**, *70*, 286–295. [CrossRef]
56. Tang, S.C.; Hui, S.Y.; Chung, S.H. A low–profile low–power converter with coreless PCB isolation transformer. *Power Electron. IEEE Trans.* **2001**, *16*, 311–315. [CrossRef]
57. Sogabe, Y.; Nii, M.; Tsukamoto, T.; Nakamura, M.; Amemiya, M. Electromagnetic Field Analyses of REBCO Roebel Cables Wound into Coil Configurations. *IEEE Trans. Appl. Supercond.* **2014**, *24*, 1–5. [CrossRef]
58. Mekaru, H.; Kusumi, S.; Sato, N.; Shimizu, M.; Yamashita, M.; Shimada, O.; Hattori, T. Development of three–dimensional LIGA process to fabricate spiral micro–coil. *Jpn. J. Appl. Phys. Part 1–Regul. Pap. Brief Commun. Rev. Pap.* **2005**, *44*, 5749–5754. [CrossRef]
59. Malla, A.; Dapino, M.J.; Lograsso, T.A.; Schlagel, D.L. Large magnetically induced strains in Ni50Mn28.7Ga21.3 driven with collinear field and stress. *J. Appl. Phys.* **2006**, *99*, 1–9. [CrossRef]
60. Taghizadeh, A.; Ghaffari, A.; Najafi, F. Modeling and identification of a solenoid valve for PWM control applications. *Comptes Rendus* Mec. **2009**, *337*, 131–140. [CrossRef]
61. Williams, J.D.; Wang, W. Microfabrication of an electromagnetic power relay using SU–8 based UV–LIGA technology. *Microsyst. Technol.* **2004**, *10*, 699–705. [CrossRef]
62. Axel, L. Surface coil magnetic resonance imaging. *J. Comput. Assist. Tomogr.* **1984**, *8*, 381–384. [CrossRef] [PubMed]
63. Wang, N.N. High Efficiency on Si–Integrated Microtransformers for Isolated Power Conversion Applications. *IEEE Trans. Power Electron.* **2015**, *30*, 5746–5754. [CrossRef]
64. Richard, J.R.; Hiatt, C.F.; DeCramer, J.; Campbell, S.A. Fabrication and Characterization of a Solenoid–Type Microtransformer. *IEEE Trans. Magn.* **2003**, *39*, 553–558.
65. Sullivan, C.R.; Sanders, S.R. Design of Microfabricated Transformers and Inductors for High–Frequency Power Conversion. *IEEE Trans. Power Electron.* **1996**, *11*, 228–238. [CrossRef]
66. Yang, S.; Liu, S.; Feng, W.; Guo, B.; Hou, X.; Li, J. SPICE circuit model of voltage excitation fluxgate sensor. *IET Sci. Meas. Technol.* **2013**, *7*, 145–150. [CrossRef]
67. Yang, S.; Liu, S.; Feng, W.; Guo, B.; Hou, X.; Li, J. Comparison of soft magnetic properties of Ni81Fe19 film with different substrates used for microfluxgate. *Micro Nano Lett.* **2013**, *8*, 602–605.

68. Wei, P.W.; Rong, S.L.; Xin, L.Z.; Zhong, H.N. The nuclear magnetic resonance probe based on a printed circuit board planar micro–coil. In Proceedings of the 2013 IEEE International Conference on Applied Superconductivity and Electromagnetic Devices, Beijing, China, 25–27 October 2013; pp. 169–172.
69. Olson, D.L.; Peck, T.L.; Webb, A.G.; Magin, R.L.; Sweedler, J.V. High Resolution Micro–coil 1H–NMR for Mass Limited Nanoliter–Volume Samples. *Science* **1995**, *270*, 1967–1970. [CrossRef]
70. Kratt, K.; Badilita, V.; Burger, T.; Korvink, J.K. A fully MEMS–compatible process for 3D high aspect ratio micro coils obtained with an automatic wire bonder. *J. Micromech. Microeng.* **2010**, *20*, 015–021. [CrossRef]
71. Kratt, K.; Badilita, V.; Emmenegger, M.; Wallrabe, U.; Korvink, J.G. Solenoidal micro coils manufactured with a wire bonder. In Proceedings of the IEEE International Conference on Micro Electro Mechanical Systems (MEMS), Tucson, AZ, USA, 13–17 January 2008; pp. 996–999.
72. Dellmann, L.; Akiyama, T.; Briand, D.; Gautsch, S.; Rooij, N. Microsystems for diverse applications using recently developed microfabrication techniques. *Proc. SPIE–Int. Soc. Opt. Eng.* **2000**, *4175*, 16–27.
73. Soohoo, R. Magnetic thin film inductors for integrated circuit applications. *IEEE Trans. Magn.* **1979**, *15*, 1803–1805. [CrossRef]
74. Kawabe, K.; Koyama, H.; Shirae, K. Planar inductor. *IEEE Trans. Magn.* **1984**, *20*, 1804–1806. [CrossRef]
75. Peng, S.; Yu, J.; Feeney, C.; Ye, T.; Wang, N. A micro–inductor with thin film magnetic core for a 20 mhz buck converter. *J. Magn. Magn. Mater.* **2020**, *524*, 167661. [CrossRef]
76. Nishikawa, K.; Sugitani, S.; Kamogawa, K.; Tokumitsu, T.; Toyoda, I.; Tanaka, M. A compact V–band 3–D MMIC single–chip down–converter using photosensitive BCB dielectric film. *IEEE Trans. Microw. Theory Tech.* **2002**, *47*, 2512–2518. [CrossRef]
77. Olivo, J.; Carrara, S.; De Micheli, G. Micro–fabrication of high–thickness spiral inductors for the remote powering of implantable biosensors. *Microelectron. Eng.* **2014**, *113*, 130–135. [CrossRef]
78. Lakdawala, H.; Zhu, X.; Luo, H.; Santhanam, S.; Fedder, G.K. Micromachined high–Q inductors in 0.18 μm Cu interconnect low–K CMOS. In Proceedings of the IEEE 2001 Custom Integrated Circuits Conference, San Diego, CA, USA, 9 May 2001; pp. 579–582.
79. Chen, Y.C.; Yong, K.Y.; Laskar, J.; Allen, M. A 2.4 GHz integrated CMOS power amplifier with micromachined inductors. In Proceedings of the 2001 IEEE MTT–S International Microwave Sympsoium, Phoenix, AZ, USA, 20–24 May 2001; pp. 523–526.
80. Yu, X.; Kim, M.; Herrault, F.; Ji, G.; Kim, J.; Allen, M.G. Silicon–embedded 3D toroidal air–core inductor with through–wafer interconnect for on–chip integration. In Proceedings of the 2012 IEEE 25th International Conference on Micro Electro Mechanical Systems (MEMS), Paris, France, 29 January–2 February 2012; pp. 325–328.
81. Jeong, J.; Lee, S.W.; Min, K.S.; Kim, S.J. A novel multilayered planar coil based on biocompatible liquid crystal polymer for chronic implantation. *Sens. Actuators A Phys.* **2013**, *197*, 38–46. [CrossRef]
82. Sun, X.; Yang, Z.; Li, Z.; Li, X.; Zhang, H. Stacked flexible parylene–based 3D inductors with Ni80Fe20 core for wireless power transmission system. In Proceedings of the 2013 IEEE 26th International Conference on Micro Electro Mechanical Systems (MEMS), Taipei, China, 20–24 January 2013; pp. 849–852.
83. Lei, G.; Li, X. Concave–suspended high–Q solenoid inductors with an RFIC–compatible bulk–micromachining technology. *IEEE Trans. Electron. Devices* **2007**, *54*, 882–885.
84. Woytasik, M.; Grandchamp, J.P.; Dufour–Gergam, E.; Gilles, J.P.; Megherbi, S.; Martincic, E.; Mathias, H.; Crozat, P. Two– and three–dimensional micro–coil fabrication process for three–axis magnetic sensors on flexible substrates. *Sens. Actuators A Phys.* **2006**, *132*, 2–7. [CrossRef]
85. Nakai, H.; Harasaki, O.; Shinohara, J. Preparation of electrical insulating films for high temperature devices by ion beam assisted plasma CVD. *Mater. Chem. Phys.* **1998**, *54*, 131–134. [CrossRef]
86. Kreider, K.G.; Semancik, S. Thermal and sputtered aluminum oxide coatings for high temperature electrical insulation. *J. Vac. Sci. Technol. A* **1985**, *3*, 2582–2587. [CrossRef]
87. Wrbanek, J.D.; Fralick, G.C.; Blaha, C.A.; Busfield, A.R.; Thomas, V.D. A Multilayered Thin Film Insulator for Harsh Environments. In Proceedings of the 38th AIAA/ASME/SAE/ASEE Joint Propulsion Conference & Exhibit, Indianapolis, Indiana, 7–10 July 2002.
88. Gabrielli, C.; Mootéguy, P.; Perrot, H.; Wiart, R. Mechanism of copper deposition in a sulphate bath containing chlorides. *J. Electroanal. Chem.* **2004**, *572*, 367–375. [CrossRef]
89. Ruiz, S.A.; Chen, C. Microcontact printing: A tool to pattern. *Soft Matter* **2007**, *3*, 168–177. [CrossRef] [PubMed]
90. Perl, A.; Reinhoudt, D.N.; Huskens, J. Microcontact Printing: Limitations and Achievements. *Adv. Mater.* **2009**, *21*, 2257–2268. [CrossRef]
91. Xia, Y.N.; Venkateswaran, N.; Qin, D.; Tien, J.; Whitesides, G.M. Use of Electroless Silver as the Substrate in Microcontact Printing of Alkanethiols and Its Application in Microfabrication. *Langmuir* **1998**, *14*, 363–371. [CrossRef]
92. Xia, Y.; Kim, E.; Mrksich, M.; Whitesides, G.M. Microcontact Printing of Alkanethiols on Copper and Its Application in Microfabrication. *Chem. Mater.* **1996**, *8*, 601–603. [CrossRef]
93. Carvalho, A.; Geissler, M.; Schmid, H.; Michel, B.; Delamarche, E. Self–assembled monolayers of eicosanethiol on palladium and their use in microcontact printing. *Langmuir* **2002**, *18*, 2406–2412. [CrossRef]
94. Schmid, H.; Michel, B. Siloxane Polymers for High–Resolution, High–Accuracy Soft Lithography. *Macromolecules* **2000**, *33*, 3042–3049. [CrossRef]
95. Trimbach, D.; Feldman, K.; Spencer, N.D.; Broer, D.J.; Bastiaansen, C.W.M. Block Copolymer Thermoplastic Elastomers for Microcontact Printing. *Langmuir* **2003**, *19*, 10957–10961. [CrossRef]
96. Trimbach, D.C.; Stapert, H.; Van Orselen, J.; Jandt, K.D.; Bastioansen, C.W.M.; Broer, D.J. Improved Microcontact Printing of Proteins using Hydrophilic Thermoplastic Elastomers as Stamp Materials. *Adv. Eng. Mater.* **2010**, *9*, 1123–1128. [CrossRef]

97. Choi, S.J.; Yoo, P.J.; Baek, S.J.; Kim, T.W.; Lee, H.H. An ultraviolet–curable moldfor sub–100–nm lithography. *J. Am. Chem. Soc.* **2004**, *126*, 7744–7745. [CrossRef]
98. Zhu, X.Y.; Xu, Q.; Li, H.K.; Yang, K.; Hu, Y.J.; Li, Z.G.; Wang, F.; Peng, Z.L.; Lan, H.B. Fabricating transparent electrodes by combined electric–field–driven fusion direct printing and the liquid bridge transfer method. *J. Phys. D Appl. Phys.* **2019**, *52*, 245103. [CrossRef]
99. Feng, X.; Meitl, M.A.; Bowen, A.M.; Huang, Y.G.; Nuzzo, R.G.; Rogers, J.A. Competing fracture in kinetically controlled transfer printing. *Langmuir* **2007**, *23*, 12555–12560. [CrossRef] [PubMed]
100. Meitl, M.A.; Zhu, Z.T.; Kumar, V.; Lee, K.J.; Feng, X.; Huang, Y.Y.; Adesida, I.; Nuzzo, R.G.; Rogers, J.A. Transfer printing by kinetic control of adhesion to an elastomeric stamp. *Nat. Mater.* **2006**, *5*, 33–38. [CrossRef]
101. Kim, S.; Wu, J.; Carlson, A.; Jin, S.H.; Kovalsky, A.; Glass, P.; Liu, Z.J.; Ahmed, N.; Elgan, S.L.; Chen, W.Q.; et al. Microstructured elastomeric surfaces with reversible adhesion and examples of their use in deterministic assembly by transfer printing. *Proc. Natl. Acad. Sci. USA* **2010**, *107*, 17095–17100. [CrossRef] [PubMed]
102. Xu, S.; Zhang, Y.; Cho, J.; Lee, J.; Huang, X.; Jia, L.; Fan, J.; Su, Y.; Su, J.; Zhang, H.; et al. Stretchable batteries with self–similar serpentine interconnects and integrated wireless recharging systems. *Nat. Commun.* **2013**, *4*, 1543. [CrossRef]
103. Sim, K.; Chen, S.; Li, Y.; Kammoun, M.; Peng, Y.; Xu, M.; Gao, Y.; Song, J.; Zhang, Y.; Ardebili, H.; et al. High Fidelity Tape Transfer Printing Based On Chemically Induced Adhesive Strength Modulation. *Sci. Rep.* **2015**, *5*, 16133. [CrossRef]
104. Kim, B.; Lee, J.; Won, S.M.; Xie, Z.Q.; Chang, J.; Yu, Y.; Cho, Y.; Jang, H.; Jeong, J.; Lee, Y.; et al. Three–dimensional silicon electronic systems fabricated by compressive buckling process. *ACS Nano* **2018**, *12*, 4164–4171. [CrossRef]
105. Kim, D.H.; Ahn, J.H.; Choi, W.M.; Kim, H.S.; Kim, T.H.; Song, J.Z.; Huang, Y.Y.; Liu, Z.G.; Lu, C.; Rogers, J.A. Stretchable and foldable silicon integrated circuits. *Science* **2008**, *320*, 507–511. [CrossRef]
106. Peng, P.; Wu, K.; Lv, L.; Guo, C.F.; Wu, Z. One-Step Selective Adhesive Transfer Printing for Scalable Fabrication of Stretchable Electronics. *Adv. Mater. Technol.* **2018**, *3*, 1700264. [CrossRef]
107. Lee, H.; Um, D.S.; Lee, Y.; Lim, S.; Kim, H.J.; Ko, H. Octopus-Inspired Smart Adhesive Pads for Transfer Printing of Semiconducting Nanomembranes. *Adv. Mater.* **2016**, *28*, 7457–7465. [CrossRef]
108. Yan, Z.; Pan, T.; Xue, M.; Chen, C.; Cui, Y.; Yao, G.; Huang, L.; Liao, F.; Jing, W.; Zhang, H.; et al. Thermal Release Transfer Printing for Stretchable Conformal Bioelectronics. *Adv. Sci.* **2017**, *4*, 1700251. [CrossRef]
109. Liu, J.; Pang, B.; Xue, R.; Li, R.; Song, J.; Zhao, X.; Wang, D.; Hu, X.; Lu, Y.; Wang, L. Sacrificial layer–assisted nanoscale transfer printing. *Microsyst. Nanoeng.* **2020**, *6*, 80. [CrossRef] [PubMed]
110. Ismail, N.; Ferreira, P.M. Active Elastomeric Composite Dense Array Stamp For Micro–transfer Printing. *Procedia Manuf.* **2020**, *48*, 64–70. [CrossRef]
111. Zhao, D.; Liu, T.; Park, J.G.; Zhang, M.; Chen, J.M.; Wang, B. Conductivity enhancement of aerosol–jet printed electronics by using silver nanoparticles ink with carbon nanotubes. *Microelectron. Eng.* **2012**, *96*, 71–75. [CrossRef]
112. Ankit, M.; Frisbie, C.; Francis, L. Optimization of aerosol jet printing for high–resolution, high–aspect ratio silver lines. *ACS Appl. Mater. Interfaces* **2013**, *5*, 4856–4864.
113. Onses, M.; Sutanto, E.; Ferreira, P.M.; Alleyne, A.G.; Rogers, J.A. Mechanisms, Capabilities, and Applications of High–Resolution Electrohydrodynamic Jet Printing. *Small* **2015**, *11*, 4237–4266. [CrossRef] [PubMed]
114. Liu, Z.; Ji, H.; Wang, S.; Zhao, W.; Huang, Y.; Feng, H.; Wei, J.; Li, M. Enhanced Electrical and Mechanical Properties of a Printed Bimodal Silver Nanoparticle Ink for Flexible Electronics. *Phys. Status Solidi* **2018**, *215*, 1800007. [CrossRef]
115. Teng, K.F.; Vest, R.W. Metallization of Solar Cells with Ink Jet Printing and Silver Metallo–Organic Inks. *IEEE Trans. Compon. Hybrids Manuf. Technol.* **1988**, *11*, 291–297. [CrossRef]
116. Valeton, J.; Hermans, K.; Bastiaansen, C.; Broer, D.; Perelaer, J.; Schubert, U.; Crawford, G.; Smith, P.; Mater, J. Room temperature preparation of conductive silver features using spin–coating and inkjet printing. *J. Mater. Chem.* **2010**, *20*, 543–546. [CrossRef]
117. Cai, Z.; Zeng, X.; Liu, J. Laser Direct Writing of Conductive Silver Film on Polyimide Surface from Decomposition of Organometallic Ink. *J. Electron. Mater.* **2010**, *40*, 301–305. [CrossRef]
118. Kong, T.F.; Peng, W.K.; Luong, T.D.; Nguyen, N.; Han, J. Adhesive–based liquid metal radio–frequency micro–coil for magnetic resonance relaxometry measurement. *Lab Chip* **2012**, *12*, 287–294. [CrossRef]
119. Do, T.N.; Phan, H.; Nguyen, T.Q.; Visell, Y. Miniature Soft Electromagnetic Actuators for Robotic Applications. *Adv. Funct. Mater.* **2018**, *28*, 180–244. [CrossRef]
120. Muttakin, I.; Soleimani, M. Interior Void Classification in Liquid Metal Using Multi–Frequency Magnetic Induction Tomography With a Machine Learning Approach. *IEEE Sens. J.* **2021**, *21*, 23289–23296. [CrossRef]
121. Kuwana, K.; Dohi, T.; Matsumoto, K.; Shimoyama, I. A Standing Micro Coil for a High Resolution MRI. In Proceedings of the IEEE International Conference on Micro Electro Mechanical Systems, Lyon, France, 10–14 June 2007; pp. 1–3.
122. Koo, C.; Godley, R.F.; Park, J.; McDougall, M.P.; Wright, S.M.; Han, A. A magnetic resonance (MR) microscopy system using a microfluidically cryo–cooled planar coil. *Lab Chip* **2011**, *11*, 2197–2203. [CrossRef] [PubMed]
123. Moffat, B.G.; Desmulliez, M.P.Y.; Brown, K.; Desai, C.; Flynn, D.; Sutherland, A. A micro–fabricated current sensor for arc fault detection of aircraft wiring. In Proceedings of the 2008 2nd Electronics System–Integration Technology Conference, Greenwich, UK, 1–4 September 2008; pp. 299–304.
124. Siegel, A.C.; Bruzewicz, D.A.; Weibel, D.B.; Whitesides, G.M. Microsolidics: Fabrication of Three–Dimensional Metallic Microstructures in Poly (dimethylsiloxane). *Adv. Mater.* **2007**, *19*, 727–733. [CrossRef]

micromachines

MDPI

Article

Manufacturing Process of Polymeric Microneedle Sensors for Mass Production

Jae Yun Baek †, Kyung Mook Kang †, Hyeong Jun Kim, Ju Hyeon Kim, Ju Hwan Lee, Gilyong Shin, Jei Gyeong Jeon, Junho Lee, Yusu Han, Byeong Jun So and Tae June Kang *

Advanced Materials Lab, Department of Mechanical Engineering, Inha University, Incheon 22212, Korea; jaeyun.baek@inha.edu (J.Y.B.); athrun93@naver.com (K.M.K.); hyeongjun2531@gmail.com (H.J.K.); juhyun4280@gmail.com (J.H.K.); Juhwanlee3260@gmail.com (J.H.L.); mysky24sky@gmail.com (G.S.); newjg91@nate.com (J.G.J.); lmy2415@gmail.com (J.L.); yousoo0519@naver.com (Y.H.); bangjun0314@gmail.com (B.J.S.)

* Correspondence: tjkang@inha.ac.kr

† These authors contributed equally to this work.

Abstract: In this work, we present a fabrication process for microneedle sensors made of polylactic acid (PLA), which can be utilized for the electrochemical detection of various biomarkers in interstitial fluid. Microneedles were fabricated by the thermal compression molding of PLA into a laser machined polytetrafluoroethylene (PTFE) mold. Sensor fabrication was completed by forming working, counter, and reference electrodes on each sensor surface by Au sputtering through a stencil mask, followed by laser dicing to separate individual sensors from the substrate. The devised series of processes was designed to be suitable for mass production, where multiple microneedle sensors can be produced at once on a 4-inch wafer. The operational stability of the fabricated sensors was confirmed by linear sweep voltammetry and cyclic voltammetry at the range of working potentials of various biochemical molecules in interstitial fluid.

Keywords: microneedle; laser machining; polylactic acid; electrochemical detection; biomolecules

Citation: Baek, J.Y.; Kang, K.M.; Kim, H.J.; Kim, J.H.; Lee, J.H.; Shin, G.; Jeon, J.G.; Lee, J.; Han, Y.; So, B.J.; et al. Manufacturing Process of Polymeric Microneedle Sensors for Mass Production. *Micromachines* **2021**, *12*, 1364. https://doi.org/10.3390/mi12111364

Academic Editor: Weidong Wang

Received: 19 October 2021
Accepted: 2 November 2021
Published: 5 November 2021

1. Introduction

The desire to lead a healthy life and increased life expectancy are gradually changing the medical service paradigm from 'diagnosis and treatment' to prevention and management [1–3]. To take advantage of this trend, user-customized healthcare technologies that aid lifestyle management, such as the management of food intakes, weight, and body shape, have received much attention [4,5]. To realize such healthcare technologies, sensors are required that are capable of accurately monitoring user biometric variables, conveniently yet inexpensively. Several multifunctional sensors have been shown to extract different types of biometric information from trace amounts of blood components [6–8] and to detect vital sign signals generated by organs, such as electromyographic and electrocardiographic signals [9,10]. Of the various sensors developed, microneedle-based sensors have been used in wearable healthcare devices owing to their advantages of minimal invasiveness and user-friendliness.

Microneedle technology was initially introduced as a new drug delivery method for drugs, vaccines, and cosmetics to overcome the physical and chemical limitations posed by the stratum corneum [11–13]. By mounting a three-electrode system consisting of working, counter, and reference electrodes, microneedles have evolved into a sensor technology to monitor the levels of biometrically valuable biochemicals in biofluids using electrochemical detection methods [14,15], such as cyclic voltammetry and chronoamperometry. Unlike subcutaneous vein detection using hypodermic needles, the microneedle sensor penetrates the skin minimally and controllably to a depth of several hundred micrometers, which provides a patient-compliant and painless way of obtaining biometric data from interstitial

fluid. The ability of the sensor to continuously acquire biometric information in real time is also considered important for its practical implementation. The detection of various analytes, such as glucose [16], L-dopa [3], alcohol [2], and uric acid [17,18], in interstitial fluid under human skin using microneedle sensors has actually been previously demonstrated.

To reduce skin inflammation, as well as to eliminate electrical background noise in electrochemical sensing, a polymeric material, having biocompatibility and biodegradability, is used as a material for microneedles. Representative materials include PLA [19,20], polyurethane (PU) [21], poly(ethylene glycol) (PEG) [22], polystyrene (PS) [23], and poly(methyl methacrylate) (PMMA) [24,25]. For the manufacturing of microneedles, they could be produced directly from the polymeric materials using methods of melt-drawing [26], droplet air blowing [27], and 3D printing [28]. Meanwhile, polymer casting processes, such as high-temperature embossing [29,30], injection molding [31], and solution casting [32,33], have been widely used to fabricate large numbers of microneedles uniformly and productively. As for a mold material of polymer castings, a silicone-based elastic polymer, such as polydimethylsiloxane, was typically used [29,32,34,35], which facilitates the molding and detachment of high-aspect-ratio polymer microneedles from the mold owing to its low surface energy. However, the elastic mold has a disadvantage in that it is easily deformed by the temperature and pressure applied to the polymer casting, which causes difficulties in reproducing the shape of the microneedle. In particular, in manufacturing a microneedle sensor that has to go through several subsequent processes, such as metal deposition and coating of a sensing material, the mold deformation is a significant cause of lowering production yield.

In this work, we present a fabrication procedure suitable for the mass production of microneedle sensors, which can be utilized for the electrochemical detection of various biomarkers in biofluids. Microneedle sensors were fabricated by thermal compression molding of PLA into a laser-machined PTFE mold. Working, counter, and reference electrodes were formed on sensor surfaces by Au sputtering through a stencil mask. The operational stabilities of the fabricated sensor were confirmed by linear sweep voltammetry (LSV) and cyclic voltammetry (CV) using a range of working potentials targeting various biochemical molecules in interstitial fluid.

2. Materials and Methods

2.1. Materials

A roll of 1.75 mm diameter PLA filament was purchased from Sondori, South Korea, and cut into lengths of $\leq$1 cm with scissors for thermocompression molding. A sheet of PTFE (3 mm thick) was purchased from Mirae International Trading, Gunpo, South Korea. The release agent (Easy-Lease™) was used to enable PLA microneedles to be detached from PTFE molds after thermocompression molding and was purchased from Easy Composites Ltd., Longton, UK. Adhesive film (Tegaderm™ transparent film dressing), which was used to attach the microneedle sensor to skin, was purchased from 3M, South Korea, and phosphate buffered saline (PBS 1X) was from Lonza, Switzerland.

2.2. Measurements and Instrumental

A computer-aided engraving machine equipped with a CO_2 laser (KL-900L, Woosung E&I Co., Pyeongtaek, South Korea) was used to fabricate PTFE molds. This machine can process an area of 1200 $\times$ 900 mm^2 with a scan resolution of 2500 dots per inch (DPI) and a positional accuracy of 10 μm, and has a laser power of up to 100 W. To process PTFE, the engraving depth was controlled by adjusting laser movement during irradiation at a fixed duty cycle of 50%. The working distance between the laser beam source and the PTFE was fixed at 1 cm. Scanning electron microscopy (CX-200TM, COXEM, Daejeon, South Korea) was used at an acceleration voltage of 10–15 KeV to observe the morphologies of the microneedles produced. Electrodes were formed by sputtering Au on sensors through a stainless steel (SUS) stencil mask using a metal sputtering unit (Q300T D Plus, Quorum, Laughton, UK) at a current of 100 mA for 420 s. Linear sweep voltammetry (LSV) and cyclic voltammetry (CV) measurements were performed using

a computer-controlled voltage meter (CS310, Corrtest Instruments, Wuhan, China) with a potential resolution of 10 µV. Operation stabilities of sensors were assessed using LSV and CV measurements, which were performed in a PBS solution at a scan rate of 5 mV/s over the potential sweep range of −1.0 to +1.0 V and +0.1 to +0.6 V, respectively, versus an Ag/AgCl reference electrode.

3. Results and Discussion

Laser Machining of the PTFE Mold

A conceptual diagram of the electrochemical detection of biomolecules in interstitial fluid using the microneedle sensor is provided in Figure 1, which shows microneedles penetrating the epidermis and accessing interstitial fluid. This fluid is representative of the fluid between cells and blood vessels and accounts for 70% of dermis by volume [36]. The composition of interstitial fluid is similar to that of blood plasma [37,38], except for high molecular weight proteins, because equilibrium between plasma and interstitial fluid is achieved by capillary walls, which allow biomolecules with molecular weights of ≤10,000 Da to pass freely.

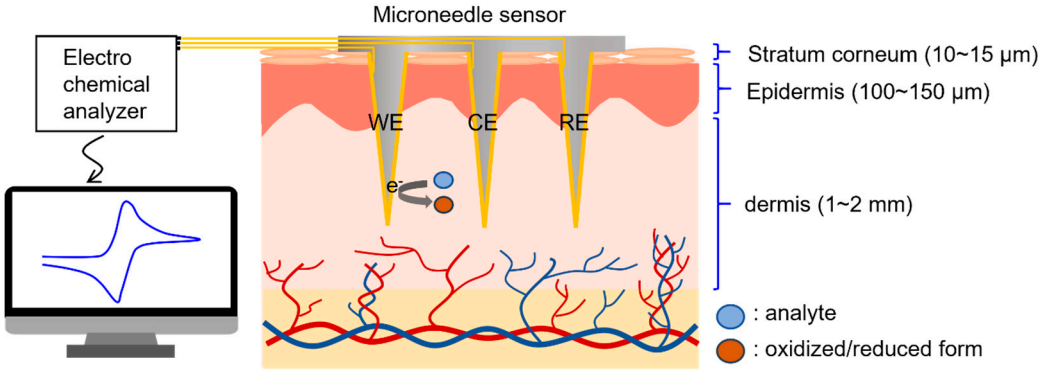

Figure 1. Illustration of the electrochemical detection of biomarkers in dermal interstitial fluid.

The microneedle sensors were designed to diagnose and monitor health by accessing interstitial fluid under the epidermis in a minimally invasive manner. To meet this design objective, a method of manufacturing biocompatible microneedles several hundred micrometers or more long with a high aspect ratio and mechanically robust enough to withstand forces during skin insertion was required.

To ensure the manufacturing process allowed straightforward control of microneedle length, we produced sensors by the thermal compression molding of PLA into laser-engraved PTFE molds. We selected PLA for this purpose having considered other candidate biocompatible materials used to produce microneedles, such as polyurethane, polyethylene, polystyrene, and poly(methyl methacrylate), because PLA is an FDA-approved generally recognized as safe (GRAS) polymer with excellent mechanical properties and electrochemical stability. The PTFE mold engraving depth, which determined the needle length after PLA molding, was adjusted by modulating the laser scan speed; other laser process parameters, such as power, duty cycle, and working distance, were fixed. A detailed description of the conditions used for laser engraving is provided in the Measurements and Instrumental section above.

A schematic of the laser engraving of PTFE molds is provided in Figure 2a. A PTFE film was engraved with a negative of microneedle shapes using a CO_2 laser. The small amount of debris generated during laser processing was removed by washing molds with acetone in an ultrasonic bath and drying at room temperature. To evaluate engraving depths, we measured the lengths of microneedles produced using molds that had been engraved using different laser scan speeds.

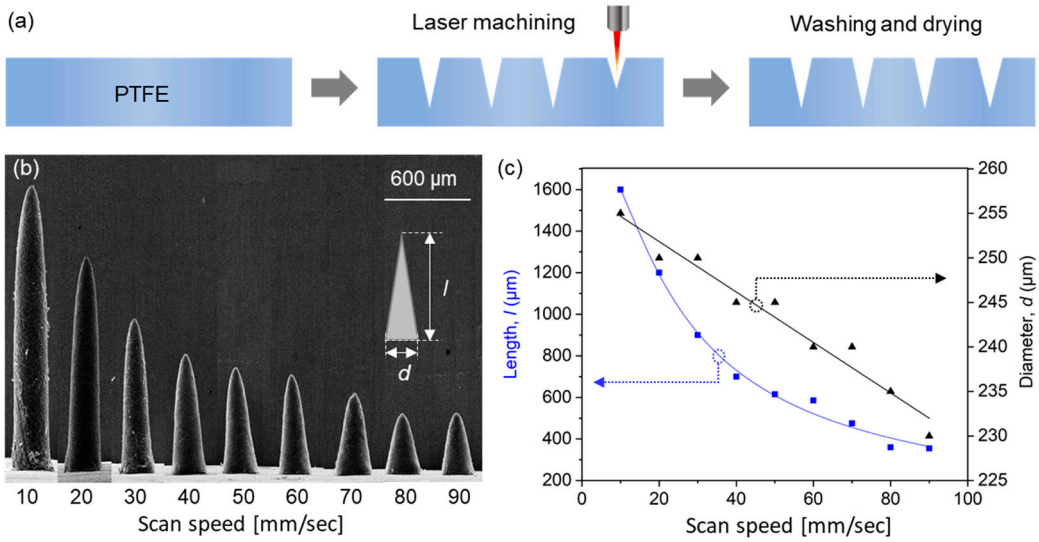

Figure 2. (**a**) Fabrication process used to produce PTFE molds by laser engraving. (**b**) SEM images of the PLA microneedles produced using molds laser machined at different scan speeds. (**c**) Lengths and diameters of fabricated microneedles.

Scanning electron microscopy (SEM) images of PLA microneedles fabricated at different laser scan speeds are shown in Figure 2b. The engraving depth increased as scan speed decreased, which was attributed to the time the laser beam impacted the PTFE surface. Microneedle lengths and diameters (defined as diameters at microneedle bases, as shown in the inset of Figure 2b) were determined by SEM. Figure 2c shows the results of measuring the average length and diameter of 10 or more microneedle specimens. As shown in the figure, microneedle lengths were adjustable from 390 to 1600 μm using scan speeds of 90 and 10 mm/s, respectively, at which needle diameters increased slightly from 232 to 255 μm, respectively, that is, they were smaller than the outer diameter of a 31-gauge syringe needle (261 μm). Given a depth from the stratum corneum to dermis of <200 μm (Figure 1) and the insertion depth to minimize the pain caused by needle insertion [39], we chose to use a needle length of 600 μm, which corresponded to a scan speed of 40 mm/s.

The microneedle sensor manufacturing procedure, which is schematically provided in Figure 3, was designed to be suitable for the mass production of multiple microneedle sensors on a 4-inch wafer. Initially, the laser-processed PTFE mold was coated with a mold release agent to facilitate the detachment of PLA microneedles (Figure 3a) and then dried under ambient conditions. PLA filaments were cut into $\leq$1 cm lengths and placed on the PTFE mold (Figure 3b), and then heat-treated in a vacuum oven for 30 min at 200 °C, which is slightly higher than the melting point of PLA (~180 °C). Thus, the heat treatment melts the PLA, which then fills the mold under vacuum conditions (Figure 3c). Thermal compression molding was then performed using a press at 220 °C and 1.0 MPa for 5 min to control the thickness of the microneedle sensor substrate and ensure the accuracy of the molding procedure (Figure 3d). To ensure a uniform temperature distribution during thermal compression, the specimen was sandwiched between two stainless steel (SUS) plates. A copper tape spacer was attached around the edges of the bottom SUS plate to produce sensors with a substrate thickness of ~200 μm. After thermal compression, the substrate with PLA microneedles was detached from the PTFE mold (Figure 3e). Subsequently, the microneedle electrodes on each sensor were separated into working, counter, and reference electrode regions by sputtering the PLA microneedle substrate with a 200 nm thick Au film through a SUS stencil mask (Figure 3f). The multiple microneedle sensors fabricated on a 4-inch diameter wafer were then separated into individual sensors by laser dicing (Figure 3g). An adhesive film was then attached to the back of each sensor to allow application to skin, and finally, a flexible flat cable (FFC) was connected to complete the sensor fabrication (Figure 3h,i).

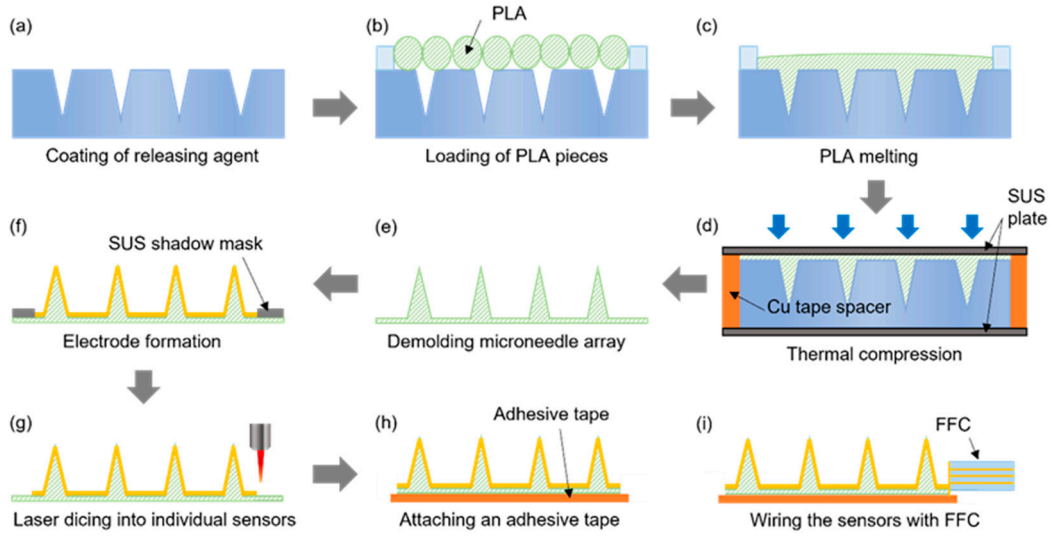

Figure 3. The procedure used to fabricate microneedle sensors. (**a**) Coating of releasing agent. (**b**) Loading of PLA pieces. (**c**) PLA melting. (**d**) Thermal compression. (**e**) Demolding microneedle array. (**f**) Electrode formation. (**g**) Laser dicing into individual sensors. (**h**) Attaching an adhesive tape. (**i**) Wiring the sensors with FFC.

Figure 4a shows an optical image of the fabricated microneedle sensors on a 4-inch wafer after the deposition of Au electrodes using the SUS stencil mask (Figure 4b). An optical image of a microneedle sensor separated from the substrate by laser dicing is shown in Figure 4c. The figure also shows the electrode area divided into working, counter, and reference electrodes. SEM confirmed that an array of microneedles on the sensor was successfully fabricated (Figure 4d). Figure 4e,f show top and side view images of a microneedle sensor equipped with an adhesive film for skin attachment and an FCC connection, respectively.

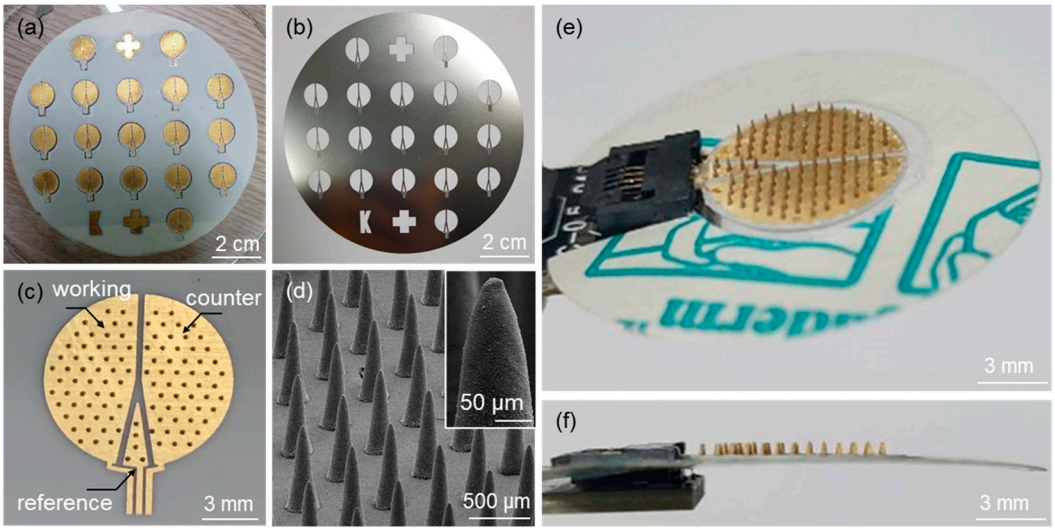

Figure 4. Optical images of (**a**) microneedle sensors fabricated on a 4-inch wafer size after the formation of Au electrodes, (**b**) the SUS stencil mask used for the Au sputtering process, and (**c**) the microneedle sensor separated from the substrate by laser dicing. (**d**) SEM image of an array of microneedles on the sensor. Optical images of (**e**) top and (**f**) side views of the microneedle sensor equipped with an adhesive film and the FCC connection.

To successfully achieve electrochemical detection of biomarkers in biofluids, the PLA microneedle sensor preferentially requires stable operation in a buffer solution for supporting biochemical molecules. To validate the operational stability of the microneedle sensor, we checked for the presence of any redox peaks possibly caused by salts in the buffer

solution by linear sweep voltammetry (LSV) and cyclic voltammetry (CV), as shown in the experimental setup in Figure 5a. A solution of phosphate buffered saline (PBS 1X, pH 7.4), which is an isotonic solution commonly used in biological research studies, was used for the tests. The scan rate was fixed at 5 mV/s and a commercial Ag/AgCl reference electrode was used. Considering the range of working potentials of various biochemical molecules (Figure 5b) [2,3,16,40,41], measurements were performed over the potential range of −1.0 to +1.0 V and +0.1 to +0.6 V, respectively, versus the Ag/AgCl reference electrode.

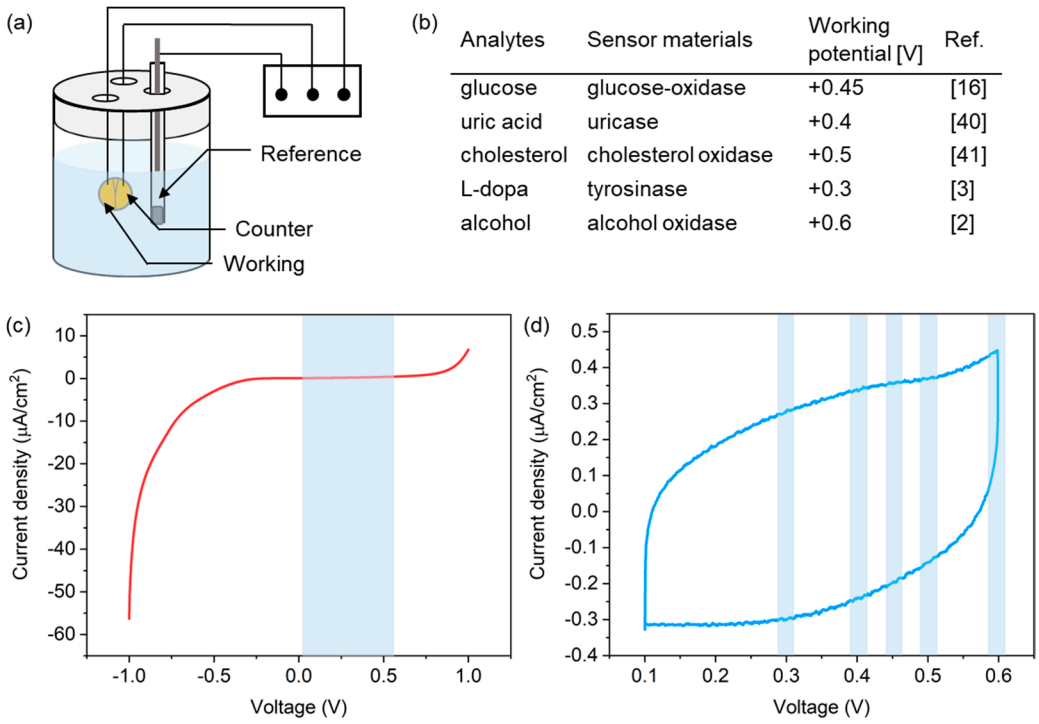

Figure 5. (**a**) Experimental setup used for LSV and CV measurements. (**b**) Working potentials of the redox reactions of several analytes. Current responses from the microneedle sensor in PBS solution during (**c**) LSV and (**d**) CV measurements in PBS.

Figure 5c shows LSV current responses observed, which indicated the absence of redox reactions in the potential range between 0.1 V and 0.6 V (indicated by the blue region in the figure), which covered all working potentials of the analytes shown in Figure 5b. A CV curve is shown in Figure 5d, and no current peak was detected at the working potentials of the redox reactions of analytes. These results indicate that the PLA microneedle sensor presented here operated stably for the detection of biochemicals.

4. Conclusions

We fabricated PLA microneedle sensors by thermocompression molding of PLA into a PTFE mold engraved by CO_2 laser machining. Microneedle geometry was controlled by modulating the laser scan speed. Microneedle lengths of 390 to 1600 μm were achieved by reducing scan speeds from 90 to 10 mm/s, respectively, while microneedle diameters increased slightly from 232 to 255 μm. Sensor fabrication was completed by forming working, counter, and reference electrodes on the sensor, which was accomplished by Au sputtering through an SUS stencil mask. The presented fabrication process was found to be highly effective at producing microneedles with high aspect ratios and various lengths reproducibly. Furthermore, the entire process was designed to be suitable for the mass production of multiple microneedle sensors on 4-inch wafers. Finally, the operation stability of the fabricated microneedle sensors was confirmed using LSV and CV measurements performed at the working potentials of various biochemical molecules in interstitial fluid.

We believed that the PLA microneedle sensors presented here are capable of providing an effective sensing platform for the detection of biochemicals of interest.

Author Contributions: Conceptualization, T.J.K., J.Y.B. and K.M.K.; Methodology, Y.H., J.L. and B.J.S.; Validation, J.H.K. and H.J.K.; Formal analysis, J.H.L., H.J.K. and J.Y.B.; Investigation, H.J.K., K.M.K. and J.Y.B.; Data curation, G.S., J.Y.B. and J.H.L.; Writing—original draft preparation, K.M.K.; Writing—review and editing, J.G.J. and J.Y.B.; Visualization, J.Y.B. and J.H.L.; Project administration, T.J.K. All authors have read and agreed to the published version of the manuscript.

Funding: This work was supported by an INHA UNIVERSITY Research Grant.

Institutional Review Board Statement: Not applicable.

Informed Consent Statement: Not applicable.

Data Availability Statement: Data are contained within the article.

Conflicts of Interest: The authors declare no conflict of interest.

References

1. Ley, S.; Hamdy, O.; Mohan, V.; Hu, F.B. Prevention and management of type 2 diabetes: Dietary components and nutritional strategies. *Lancet* **2014**, *383*, 1999–2007. [CrossRef]
2. Mohan, A.V.; Windmiller, J.R.; Mishra, R.K.; Wang, J. Continuous minimally-invasive alcohol monitoring using microneedle sensor arrays. *Biosens. Bioelectron.* **2017**, *91*, 574–579. [CrossRef] [PubMed]
3. Goud, K.Y.; Moonla, C.; Mishra, R.K.; Yu, C.; Narayan, R.; Litvan, I.; Wang, J. Wearable Electrochemical Microneedle Sensor for Continuous Monitoring of Levodopa: Toward Parkinson Management. *ACS Sens.* **2019**, *4*, 2196–2204. [CrossRef]
4. Chen, M.; Yang, J.; Zhou, J.; Hao, Y.; Zhang, J.; Youn, C.-H. 5G-Smart Diabetes: Toward Personalized Diabetes Diagnosis with Healthcare Big Data Clouds. *IEEE Commun. Mag.* **2018**, *56*, 16–23. [CrossRef]
5. Lenz, R.; Reichert, M. IT support for healthcare processes—Premises, challenges, perspectives. *Data Knowl. Eng.* **2007**, *61*, 39–58. [CrossRef]
6. Olsson, B.; Lautner, R.; Andreasson, U.; Öhrfelt, A.; Portelius, E.; Bjerke, M.; Hölttä, M.; Rosén, C.; Olsson, C.; Strobel, G.; et al. CSF and blood biomarkers for the diagnosis of Alzheimer's disease: A systematic review and meta-analysis. *Lancet Neurol.* **2016**, *15*, 673–684. [CrossRef]
7. Jickling, G.C.; Sharp, F.R. Blood Biomarkers of Ischemic Stroke. *Neurotherapeutics* **2011**, *8*, 349–360. [CrossRef] [PubMed]
8. Bryan, T.; Luo, X.; Bueno, P.R.; Davis, J.J. An optimised electrochemical biosensor for the label-free detection of C-reactive protein in blood. *Biosens. Bioelectron.* **2013**, *39*, 94–98. [CrossRef]
9. Kim, N.; Lim, T.; Song, K.; Yang, S.; Lee, J. Stretchable Multichannel Electromyography Sensor Array Covering Large Area for Controlling Home Electronics with Distinguishable Signals from Multiple Muscles. *ACS Appl. Mater. Interfaces* **2016**, *8*, 21070–21076. [CrossRef]
10. Yamamoto, D.; Nakata, S.; Kanao, K.; Arie, T.; Akita, S.; Takei, K. A Planar, Multisensing Wearable Health Monitoring Device Integrated with Acceleration, Temperature, and Electrocardiogram Sensors. *Adv. Mater. Technol.* **2017**, *2*, 2. [CrossRef]
11. Henry, S.; McAllister, D.V.; Allen, M.G.; Prausnitz, M.R. Microfabricated Microneedles: A Novel Approach to Transdermal Drug Delivery. *J. Pharm. Sci.* **1998**, *87*, 922–925. [CrossRef] [PubMed]
12. Edens, W.; Collins, M.L.; Ayers, J.; Rota, P.A.; Prausnitz, M.R. Measles vaccination using a microneedle patch. *Vaccine* **2013**, *31*, 3403–3409. [CrossRef] [PubMed]
13. Park, Y.; Park, J.; Chu, G.S.; Kim, K.S.; Sung, J.H.; Kim, B. Transdermal delivery of cosmetic ingredients using dissolving polymer microneedle arrays. *Biotechnol. Bioprocess Eng.* **2015**, *20*, 543–549. [CrossRef]
14. Mishra, R.K.; Mohan, A.M.V.; Soto, F.; Chrostowski, R.; Wang, J. A microneedle biosensor for minimally-invasive transdermal detection of nerve agents. *Analyst* **2017**, *142*, 918–924. [CrossRef]
15. Lee, W.-C.; Gurudatt, N.; Park, D.-S.; Kim, K.B.; Choi, C.S.; Shim, Y.-B. Microneedle array sensor for monitoring glucose in single cell using glucose oxidase-bonded polyterthiophene coated on AuZn oxide layer. *Sens. Actuators B Chem.* **2020**, *320*, 128416. [CrossRef]
16. Kim, K.B.; Lee, W.-C.; Cho, C.-H.; Park, D.-S.; Cho, S.J.; Shim, Y.-B. Continuous glucose monitoring using a microneedle array sensor coupled with a wireless signal transmitter. *Sens. Actuators B Chem.* **2019**, *281*, 14–21. [CrossRef]
17. Gao, J.; Huang, W.; Chen, Z.; Yi, C.; Jiang, L. Simultaneous detection of glucose, uric acid and cholesterol using flexible microneedle electrode array-based biosensor and multi-channel portable electrochemical analyzer. *Sens. Actuators B Chem.* **2019**, *287*, 102–110. [CrossRef]
18. Windmiller, J.R.; Zhou, N.; Chuang, M.-C.; Valdés-Ramírez, G.; Santhosh, P.; Miller, P.R.; Narayan, R.; Wang, J. Microneedle array-based carbon paste amperometric sensors and biosensors. *Analyst* **2011**, *136*, 1846–1851. [CrossRef]
19. Park, J.-H.; Allen, M.G.; Prausnitz, M.R. Biodegradable polymer microneedles: Fabrication, mechanics and transdermal drug delivery. *J. Control. Release* **2005**, *104*, 51–66. [CrossRef]

20. Wang, Q.L.; Zhu, D.D.; Chen, Y.; Guo, X.D. A fabrication method of microneedle molds with controlled microstructures. *Mater. Sci. Eng. C* **2016**, *65*, 135–142. [CrossRef]
21. Jang, S.-J.; Doshi, T.; Nerayo, J.; Caprio, A.; Alaie, S.; Auge, J.; Min, J.K.; Mosadegh, B.; Dunham, S. Microneedle Patterning of 3D Nonplanar Surfaces on Implantable Medical Devices Using Soft Lithography. *Micromachines* **2019**, *10*, 705. [CrossRef] [PubMed]
22. Dardano, P.; Caliò, A.; Di Palma, V.; Bevilacqua, M.F.; Di Matteo, A.; De Stefano, L. A Photolithographic Approach to Polymeric Microneedles Array Fabrication. *Materials* **2015**, *8*, 8661–8673. [CrossRef] [PubMed]
23. Luangveera, W.; Jiruedee, S.; Mama, W.; Chiaranairungroj, M.; Pimpin, A.; Palaga, T.; Srituravanich, W. Fabrication and characterization of novel microneedles made of a polystyrene solution. *J. Mech. Behav. Biomed. Mater.* **2015**, *50*, 77–81. [CrossRef]
24. Choi, S.-O.; Kim, Y.C.; Park, J.-H.; Hutcheson, J.; Gill, H.S.; Yoon, Y.-K.; Prausnitz, M.R.; Allen, M.G. An electrically active microneedle array for electroporation. *Biomed. Microdevices* **2009**, *12*, 263–273. [CrossRef]
25. Janphuang, P.; Laebua, M.; Sriphung, C.; Taweewat, P.; Sirichalarmkul, A.; Sukjantha, K.; Promsawat, N.; Leuasoongnoen, P.; Suphachiaraphan, S.; Phimol, K.; et al. Polymer based microneedle patch fabricated using microinjection moulding. *MATEC Web Conf.* **2018**, *192*, 01039. [CrossRef]
26. Lee, K.; Kim, J.D.; Lee, C.Y.; Her, S.; Jung, H. A high-capacity, hybrid electro-microneedle for in-situ cutaneous gene transfer. *Biomaterials* **2011**, *32*, 7705–7710. [CrossRef] [PubMed]
27. Kim, J.D.; Kim, M.; Yang, H.; Lee, K.; Jung, H. Droplet-born air blowing: Novel dissolving microneedle fabrication. *J. Control. Release* **2013**, *170*, 430–436. [CrossRef] [PubMed]
28. Luzuriaga, M.A.; Berry, D.R.; Reagan, J.C.; Smaldone, R.A.; Gassensmith, J.J. Biodegradable 3D printed polymer microneedles for transdermal drug delivery. *Lab Chip* **2018**, *18*, 1223–1230. [CrossRef]
29. Li, J.; Zhou, Y.; Yang, J.; Ye, R.; Gao, J.; Ren, L.; Liu, B.; Liang, L.; Jiang, L. Fabrication of gradient porous microneedle array by modified hot embossing for transdermal drug delivery. *Mater. Sci. Eng. C* **2019**, *96*, 576–582. [CrossRef]
30. Andersen, T.E.; Andersen, A.J.; Petersen, R.S.; Nielsen, L.H.; Keller, S.S. Drug loaded biodegradable polymer microneedles fabricated by hot embossing. *Microelectron. Eng.* **2018**, *195*, 57–61. [CrossRef]
31. Yung, K.L.; Xu, Y.; Kang, C.; Liu, H.; Tam, K.F.; Ko, S.M.; Kwan, F.Y.; Lee, T.M.H. Sharp tipped plastic hollow microneedle array by microinjection moulding. *J. Micromech. Microeng.* **2011**, *22*, 22. [CrossRef]
32. Park, Y.-H.; Ha, S.K.; Choi, I.; Kim, K.S.; Park, J.; Choi, N.; Kim, B.; Sung, J.H. Fabrication of degradable carboxymethyl cellulose (CMC) microneedle with laser writing and replica molding process for enhancement of transdermal drug delivery. *Biotechnol. Bioprocess Eng.* **2016**, *21*, 110–118. [CrossRef]
33. Yuan, W.; Yang, S.; Feng, Y.; Zhang, L.; Chen, N.; Jin, T. A scalable fabrication process of polymer microneedles. *Int. J. Nanomed.* **2012**, *7*, 1415–1422. [CrossRef] [PubMed]
34. Chen, M.-C.; Ling, M.-H.; Lai, K.-Y.; Pramudityo, E. Chitosan Microneedle Patches for Sustained Transdermal Delivery of Macromolecules. *Biomacromolecules* **2012**, *13*, 4022–4031. [CrossRef]
35. Nejad, H.R.; Sadeqi, A.; Kiaee, G.; Sonkusale, S. Low-cost and cleanroom-free fabrication of microneedles. *Microsyst. Nanoeng.* **2018**, *4*, 17073. [CrossRef]
36. Aukland, K.; Nicolaysen, G. Interstitial fluid volume: Local regulatory mechanisms. *Physiol. Rev.* **1981**, *61*, 556–643. [CrossRef]
37. Tran, B.Q.; Miller, P.R.; Taylor, R.M.; Boyd, G.; Mach, P.M.; Rosenzweig, C.N.; Baca, J.T.; Polsky, R.; Glaros, T. Proteomic Characterization of Dermal Interstitial Fluid Extracted Using a Novel Microneedle-Assisted Technique. *J. Proteome Res.* **2018**, *17*, 479–485. [CrossRef]
38. Samant, P.P.; Niedzwiecki, M.M.; Raviele, N.; Tran, V.; Mena-Lapaix, J.; Walker, D.I.; Felner, E.I.; Jones, D.P.; Miller, G.W.; Prausnitz, M.R. Sampling interstitial fluid from human skin using a microneedle patch. *Sci. Transl. Med.* **2020**, *12*, 571. [CrossRef]
39. Gill, H.S.; Denson, D.D.; Burris, B.A.; Prausnitz, M.R. Effect of Microneedle Design on Pain in Human Volunteers. *Clin. J. Pain* **2008**, *24*, 585–594. [CrossRef]
40. Arslan, F. An Amperometric Biosensor for Uric Acid Determination Prepared From Uricase Immobilized in Polyaniline-Polypyrrole Film. *Sensors* **2008**, *8*, 5492–5500. [CrossRef]
41. Singh, S.; Chaubey, A.; Malhotra, B. Amperometric cholesterol biosensor based on immobilized cholesterol esterase and cholesterol oxidase on conducting polypyrrole films. *Anal. Chim. Acta* **2004**, *502*, 229–234. [CrossRef]

micromachines

MDPI

Article

Transfer of Tactile Sensors Using Stiction Effect Temporary Handling

Peng Zhong [1,2], Ke Sun [1,2], Chaoyue Zheng [1,2], Heng Yang [1,2,*] and Xinxin Li [1,2]

[1] State Key Laboratory of Transducer Technology, Shanghai Institute of Microsystem and Information Technology, Chinese Academy of Sciences, Shanghai 200050, China; pengzhong@mail.sim.ac.cn (P.Z.); sunke@mail.sim.ac.cn (K.S.); osananajimi@mail.sim.ac.cn (C.Z.); xxli@mail.sim.ac.cn (X.L.)

[2] School of Microelectronics, University of Chinese Academy of Sciences, Beijing 100049, China

* Correspondence: h.yang@mail.sim.ac.cn; Tel.: +86-133-9115-1119

Abstract: A novel method for transfer of tactile sensors using stiction effect temporary handling (SETH) is presented to simplify the microelectromechanical-system (MEMS)/CMOS integration process, improve the process reliability and electrical performance, and reduce material constriction. The structure of the tactile sensor and the reroute substrate were first manufactured separately. Following the release process, the stiction-contact structures, which are designed to protect the low-stress silicon nitride diaphragm of the tactile sensor and prevent the low-stress silicon nitride diaphragm from moving during the subsequent bonding process, are temporarily bonded to the substrate owing to the stiction effect. After the released tactile sensor is bonded to the reroute substrate by Au–Si eutectic flip-chip bonding, a pulling force perpendicular to the bonded die is applied to break away the temporary supported beam of the tactile sensor, and the tactile sensor is then successfully transferred to the reroute substrate. The size of the transferred tactile sensor is as small as 180 μm × 180 μm × 1.2 μm, and the force area of the tactile sensor is only 120 μm × 120 μm × 1.2 μm. The maximum misalignment of the flip-chip bonding process is approximately 1.5 μm. The tactile sensors are tested from 0 to 17.1 kPa when the power supply is 5 V, resulting in a sensitivity of 0.22 mV/V/kPa, 0.26 mV/V/kPa, 0.27 mV/V/kPa and 0.27 mV/V/kPa, separately. The stress caused by the Au–Si eutectic flip-chip bonding ranges from −5.83 to +5.54 kPa. The temporary bonding strength caused by stiction is calculated to be larger than 7.06 kPa and less than 22.31 kPa. The shear strength of the bonded test structure is approximately 30.74 MPa and the yield of the transferred tactile sensors is as high as 90%.

Keywords: stiction effect; temporary handling; SETH; CMOS; MEMS; tactile sensor; stiction-contact; Au–Si eutectic; flip-chip

Citation: Zhong, P.; Sun, K.; Zheng, C.; Yang, H.; Li, X. Transfer of Tactile Sensors Using Stiction Effect Temporary Handling. *Micromachines* **2021**, *12*, 1330. https://doi.org/10.3390/mi12111330

Academic Editors: Weidong Wang and Ruiguo Yang

Received: 8 September 2021
Accepted: 27 October 2021
Published: 29 October 2021

1. Introduction

Numerous efforts have been made to integrate microelectromechanical systems (MEMS) and complementary metal-oxide-semiconductor (CMOS) devices [1–9]. There are two approaches for integrating MEMS sensors and actuators with CMOS devices. The first is monolithic integration, where the MEMS and CMOS devices are fabricated on the same silicon substrate using a dedicated fabrication process [10]. The second approach is hybrid integration, in which the MEMS and CMOS devices are assembled using chip-interconnection methods (i.e., tape automated bond (TAB), wire bond, and flip-chip bond) [11–16].

Monolithic integration has been widely studied owing to its advantages of lower electronic parasitics, reduced chip pinout, and smaller size. There are three methods for monolithic integration: pre-CMOS, intra-CMOS, and post-CMOS [17–20]. The classification of the three approaches is based on the sequence of fabrication of the MEMS and CMOS devices. In the pre-CMOS and intra-CMOS approaches, contamination issues should be

considered after the wafer has undergone some proprietary MEMS processes [6]. Thus, dedicated fabrication is required for the pre-CMOS and intra-CMOS. Moreover, the thermal budget should be considered in the intra-CMOS approach because of the high-temperature front-end-of-line processes [10]. In the post-CMOS approach, materials and processes used for the fabrication of MEMS devices must be carefully considered to avoid damage to the completed CMOS device during MEMS fabrication processes [21].

Hybrid integration, which enables the MEMS and CMOS devices to be fabricated independently, is currently the most common approach for MEMS and CMOS integration because of its shorter development time, lower cost, flexible material selection, and simpler fabrication process [22]. In hybrid integration technologies, flip-chip bond provides the highest packaging density, better reliability, and better electrical and thermal performance. However, with the development of advanced packaging technologies (i.e., three-dimensional packaging technology) and advanced microsystems (i.e., radio frequency devices), the average wire length of the flip-chip bond becomes significant, which can cause higher electrical parasitics between the MEMS and CMOS devices [23].

A modified flip-chip method for the transfer of released microstructures has been proposed by Singh et al. [13]. In this modified method, two types of MEMS structure are fabricated and released, followed by the fabrication of a target die, which is patterned with metal bumps. Then, the released MEMS structures and the target die are bonded by cold welding the indium solder to the copper. Finally, the bonded structure is carefully separated to break the tethers of the MEMS structures, thereby transferring the MEMS structures onto the target die. This modified method enables the MEMS and CMOS devices to be fabricated separately, simplifying the fabrication process and providing flexibility in the selection of the MEMS/CMOS process and substrate. Moreover, the signal path can be shortened, which improves the electronic performance of the integrated device. However, the released MEMS microstructures, only supported by polysilicon tethers, are at risk of being damaged by shear forces during the bonding and transferring processes. Moreover, the displacement of MEMS structures caused by shear force decreases the alignment precision of the flip-chip bonding.

In this study, a novel method for transfer of tactile sensors using stiction effect [24] temporary handling (SETH) is presented to simplify the MEMS/CMOS integration process, improve the process reliability and electrical performance, and reduce material constriction. The tactile sensor and reroute substrate are first manufactured separately. Then, the tactile sensor is released and placed into deionized (DI) water for 24 h to bond the stiction-contact structures temporarily to the substrate through the stiction effect, thereby avoiding the damage and movement of the diaphragm of the tactile sensor during subsequent flip-chip bonding. Next, the released tactile sensor is bonded to the reroute substrate by Au–Si eutectic flip-chip bonding. Finally, a pulling force perpendicular to the bonded die is applied to break away the temporary supported beam of the tactile sensor, and the tactile sensor is then transferred to the reroute substrate. The size of the transferred tactile sensor is as small as 180 μm × 180 μm × 1.2 μm, and the force area of the tactile sensor is only 120 μm × 120 μm × 1.2 μm. The maximum misalignment of the flip-chip bonding process is approximately 1.5 μm. The stress caused by the Au–Si eutectic flip-chip bonding is from −5.83 to +5.54 kPa. The tactile sensors are tested from 0 to 17.1 kPa when the power supply is 5 V, resulting in a sensitivity of 0.22 mV/V/kPa, 0.26 mV/V/kPa, 0.27 mV/V/kPa and 0.27 mV/V/kPa, separately. The shear strength of the bonded test structure is approximately 30.74 MPa and the yield of the transferred tactile sensors is as high as 90%.

2. Design Principle

The principle of CMOS-compatible batch transfer of tactile sensors using SETH is shown in Figure 1. First, the tactile sensor is manufactured, and the stiction-contact structures, which are designed to protect the low-stress silicon nitride (LS-Si_xN_y) diaphragm of the tactile sensor, are temporarily bonded to the thermal oxide layer owing to the stiction

effect, as shown in Figure 1a. Next, the CMOS device and metal electrode used for bonding are fabricated, as shown in Figure 1b. Thereafter, the MEMS tactile sensor is bonded to the CMOS device, as shown in Figure 1c. Finally, the MEMS tactile sensor is transferred to the CMOS device by applying a pulling force perpendicular to the bonded device, as shown in Figure 1d.

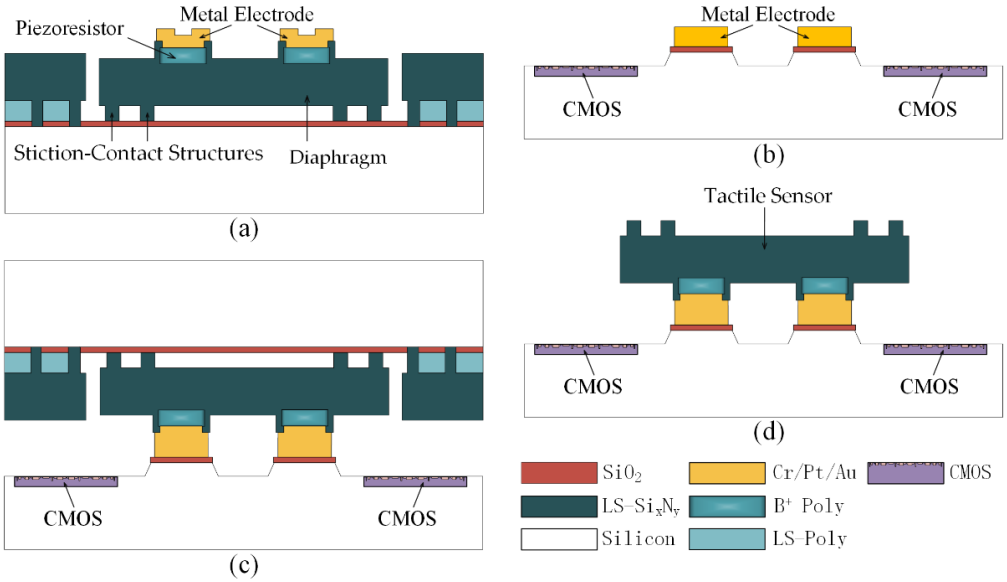

Figure 1. Design process flow of complementary metal-oxide-semiconductor (CMOS)-compatible batch transfer of tactile sensor using stiction effect temporary handling (SETH). (**a**) Tactile sensor is manufactured, and the stiction-contact structures are temporary bonded to the substrate; (**b**) CMOS device and the metal electrode used for bonding are fabricated; (**c**) MEMS tactile sensor is bonded to the CMOS device; (**d**) microelectromechanical system (MEMS) tactile sensor is transferred to the CMOS device by applying a pulling force perpendicular to the bonded device.

2.1. Design of Tactile Sensor

To verify the principle of CMOS-compatible batch transfer of tactile sensors using SETH, a tactile sensor with a low-stress silicon nitride diaphragm was designed for transfer to the reroute substrate. The process flow is similar to that shown in Figure 1. Figure 2a shows a schematic of the designed tactile sensor, and Figure 2b shows a cross-sectional cut of the tactile sensor along line A–A′. Figure 2c shows a schematic of the reroute substrate, and Figure 2d shows a schematic of the transferred tactile sensor. As shown in Figure 2a, the dimensions of the low-stress silicon nitride diaphragm are 120 μm × 120 μm × 1.2 μm, and four p-type resistors are formed on the edge of the silicon nitride diaphragm surface, where the component of the stress tensor in silicon nitride diaphragm is found to be largest through simulation using COMSOL, as shown in Figure 3. The size of the designed transferred tactile sensor is 180 μm × 180 μm × 1.2 μm and the center diaphragm of the tactile sensor is 120 μm × 120 μm × 1.2 μm, the area outside the center diaphragm is designed for Au-Si eutectic bonding, as shown in Figure 3a,c. As the diaphragm of the tactile sensor is fabricated by LPCVD isotropic low-stress silicon nitride, the density, Young's modulus, and Poisson's ratio of the low-stress silicon nitride used for COMOSL simulation are set as 3000 kg/m^3, 360.5 GPa and 0.24 [25], separately. Figure 3b shows that the largest stress is approximately 98.59 MPa under 35 kPa pressure, which occurs at the edge of the silicon nitride diaphragm. Figure 3d shows that the maximum displacement occurs at the center of the silicon nitride diaphragm, and its value is approximately 0.25 μm. The four piezo resistors are connected using heavily doped polysilicon to form a flat surface, and a composite metal layer with a flat surface is then deposited on the heavily doped polysilicon to a form the Wheatstone bridge and the metal electrodes designed for Au-Si eutectic bonding, as shown in Figure 2a,b. The composite metal layer with a flat surface

increases the bonding area of metal electrodes, thereby improving the bonding strength of Au-Si eutectic bonding process. The sensitivity of the tactile sensor is

$$S = \frac{\Delta V}{\Delta P} = \frac{\pi_{44} a^2}{4h^2} V_{cc} \quad (1)$$

where ΔV and ΔP are the changes in the output voltage of the Wheatstone bridge and the pressure of the silicon nitride diaphragm, respectively, π_{44} is the piezoresistive coefficient of polysilicon, a is the half side length of the silicon nitride diaphragm, and h is the thickness of the silicon nitride diaphragm. Theoretically, the sensitivity of the tactile sensor is 2.55 mV/kPa when the power supply is 5 V.

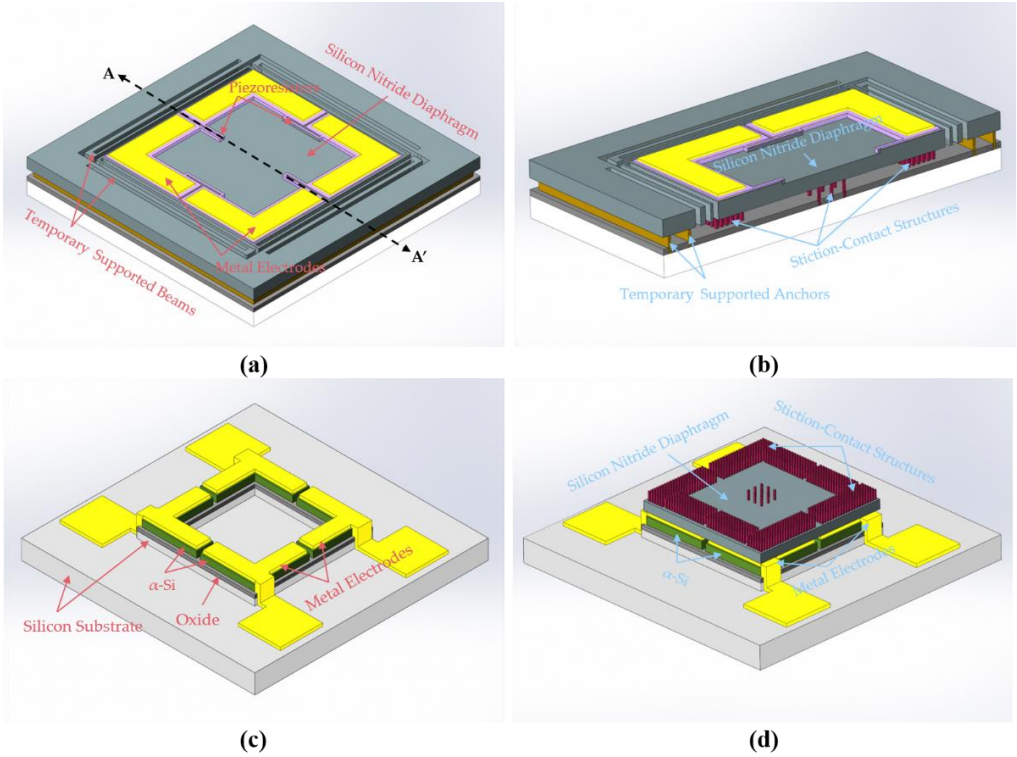

Figure 2. (**a**) Schematic of the tactile sensor; (**b**) Cross-section cut along the line A–A′ in (**a**); (**c**) Schematic of the reroute substrate; (**d**) Schematic of the transferred device.

2.2. Design of Stiction-Contact Structures

Previous studies have suggested that electrostatic forces, van der Waals forces, or surface tension may be responsible for sticking or stiction [26,27], which causes the permanent attachment of slender surface micromachined structures to the underlying substrate after drying [28]. To conceptualize the scale of the stiction forces, the three causes are each illustrated using an ideal system consisting of two smooth parallel surfaces with separation d and shared area S.

The electrostatic force results from electrostatic charging or differences in the work functions of the two smooth parallel surfaces, and the work function differences yield at most 1 V potentials in equilibrium [26]. Neglecting the internal space charge regions, the electrostatic force, F_{EL}, is [26]

$$F_{EL} = \frac{\varepsilon_0 U^2}{2d^2} \cdot S \quad (2)$$

where ε_0 and U are the relative permittivity of the air gap and the potential difference between the two parallel surfaces, respectively.

The van der Waals force results from the interaction between the instantaneous dipole moment of atoms. The expression for the van der Waals force, F_{VDW}, can be expressed as [29]:

$$F_{VDW} = \frac{A}{6\pi d^3} \cdot S \tag{3}$$

where A is the Hamaker constant. For the SiO_2–air–SiO_2 case, the Hamaker constant is 5.4×10^{-20} J [30].

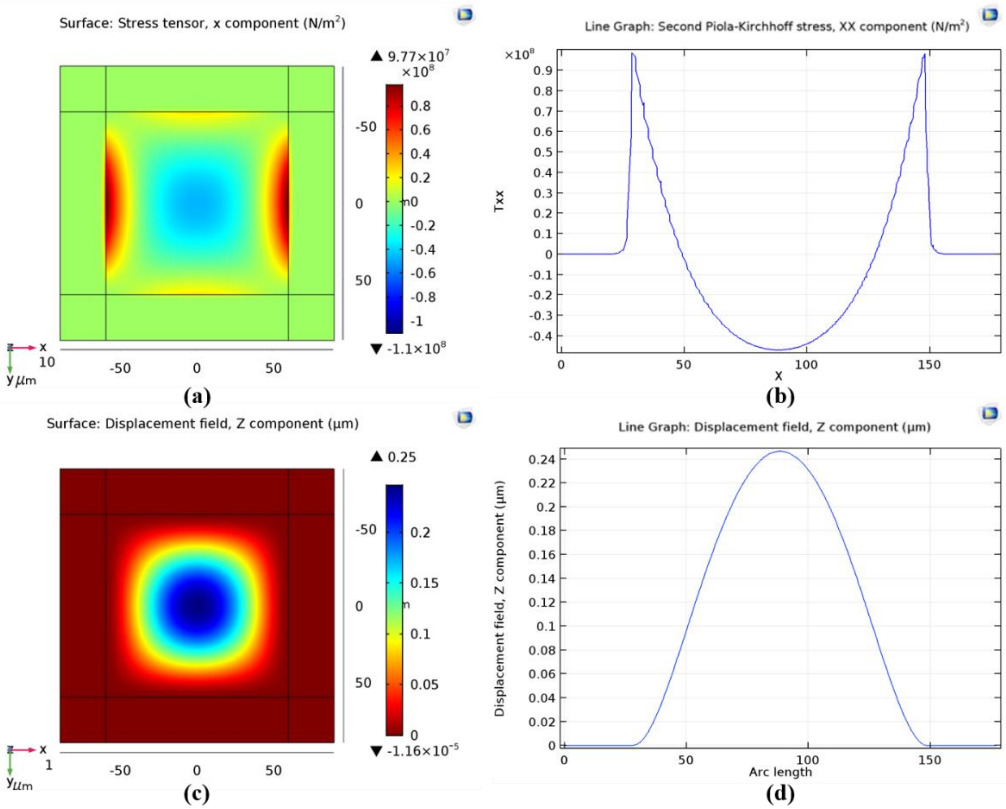

Figure 3. COMSOL simulation results of tactile sensor. (**a**) Stress simulation of the silicon nitride diaphragm; (**b**) Stress simulation result shows that the maximum stress occurs at the edge of the silicon nitride diaphragm, and its value is 98.59 MPa; (**c**) Displacement simulation of the silicon nitride diaphragm; (**d**) Displacement simulation result shows that the maximum displacement occurs at the center of the silicon nitride diaphragm, and its value is 0.25 μm.

The surface tension of the diminishing liquid induces an attractive capillary force during the drying of capillary liquids trapped in the two parallel surfaces, and the capillary force, F_{CF}, can be described as [26]

$$F_{CF} = \frac{\gamma(\cos\theta_1 + \cos\theta_2)}{d} \cdot S \tag{4}$$

where γ is the surface tension (73 mN/m for water), and θ_1 and θ_2 are the contact angles between the two parallel surfaces.

As Equations (2)–(4) show, when the distance between two smooth parallel surfaces is larger than 10 nm, the electrostatic force and van der Waals force can be negligible compared with the surface tension; thus, the total adhesion forces between two smooth parallel surfaces can be simplified as

$$F_{Total\_AF} = F_{EL} + F_{VDW} + F_{CF} \approx \frac{\gamma(\cos\theta_1 + \cos\theta_2)}{d} \Delta S \tag{5}$$

To ensure that the tactile sensor can be successfully transferred to the reroute substrate, as shown in Figure 2d, the temporary bonding strength caused by stiction should be less than the bonding strength of the flip-chip bonding. As Equation (5) shows, the total adhesion forces can be decreased by reducing the shared area between two parallel surfaces. Therefore, different areas of stiction-contact structures (from 2916 to 9000 μm^2) are designed to reduce the shared area between the silicon nitride diaphragms of the tactile sensor and substrate. A cross-sectional schematic view of the stiction-contact structures is shown in Figure 2b. In addition, the stiction-contact structures can prevent the silicon nitride diaphragm from moving in the subsequent bonding process because of its temporary bonding to the substrate, thereby improving the alignment precision of flip-chip bonding.

To ensure that the deadhesion process does not damage the bonding strength of the transferred device, the Au–Si eutectic bonding technique was employed to ensure the bonding strength of the subsequent flip-chip bonding process, in which the bonding strength is usually larger than 16 MPa in the laboratory [31]. Moreover, the metal electrode area for Au–Si eutectic bonding is designed to be 12,320 μm^2, which is much larger than the designed area of stiction-contact structures, so that the adhesion forces caused by stiction can be negligible compared with the Au–Si eutectic bonding strength.

As Equations (2)–(5) show, the total adhesion forces can be decreased by increasing the distance between two parallel surfaces. When the designed distance between the stiction-contact structures and substrate is 200 nm, the corresponding temporary bonding strength can be calculated as 0.73 MPa in theory. Assuming that the stiction occurs at the center of the silicon nitride diaphragm and the temporary bonding strength caused by stiction is 10 MPa, which is much larger than 0.73 MPa, the stress and displacement of the silicon nitride diaphragm are simulated by COMSOL (5.3, COMSOL, Inc., Burlington, Mam, USA), as shown in Figure 4. As the stiction-contact structures of tactile sensor are fabricated by LPCVD isotropic low-stress silicon nitride, the density, Young's modulus, and Poisson's ratio of the stiction-contact structures in COMSOL simulation are set as 3000 kg/m^3, 360.5 GPa and 0.24 [25], separately. The designed dimensions of the stiction-contact structures in the center of low-stress silicon nitride diaphragm are 2 μm × 2 μm × 1.2 μm, as shown in Figure 4a,c. As Figure 4b shows, the maximum stress distributed at the edge of the silicon nitride diaphragm, and its value is approximately 167.71 MPa under 10 MPa pressure. Therefore, the silicon nitride diaphragm is not damaged by stiction because the fracture strength of the low-pressure chemical vapor deposition (LPCVD) silicon nitride (6.9 GPa at 298 K) [25] is much higher than 167.71 MPa. Figure 4d shows that the maximum displacement occurs at the center of the silicon nitride diaphragm, and its value is approximately 0.25 μm.

2.3. Design of Test Structures

Metal electrodes with a width of 22 μm and a length of 81 μm were designed to estimate the Au–Si eutectic bonding strength of the transferred device, and the schematic of the test structure is similar to that shown in Figure 2c. After the test structures have been bonded by the Au–Si eutectic bonding technique, the bonding strength can be estimated by a shear force test, as shown in Figure 5a. In addition, 20 different types of cantilever beam with a width of 3 μm and a 20–400 μm length were designed to estimate the magnitude of the temporary bonding strength caused by stiction, as shown in Figure 5b. When the tips of the cantilever beams are fixed on the substrate after drying, the minimum temporary bonding strength caused by the stiction can be estimated as

$$F_{\mathrm{TBS\_S}} = \frac{2Et^3}{3L^3}d \tag{6}$$

where E is the Young's modulus of the cantilever beam material, 260.5 GPa at 298 K for LPCVD silicon nitride [24]; t and L are the thickness and length of the cantilever beam, respectively; and d is the distance between the cantilever beam and the substrate.

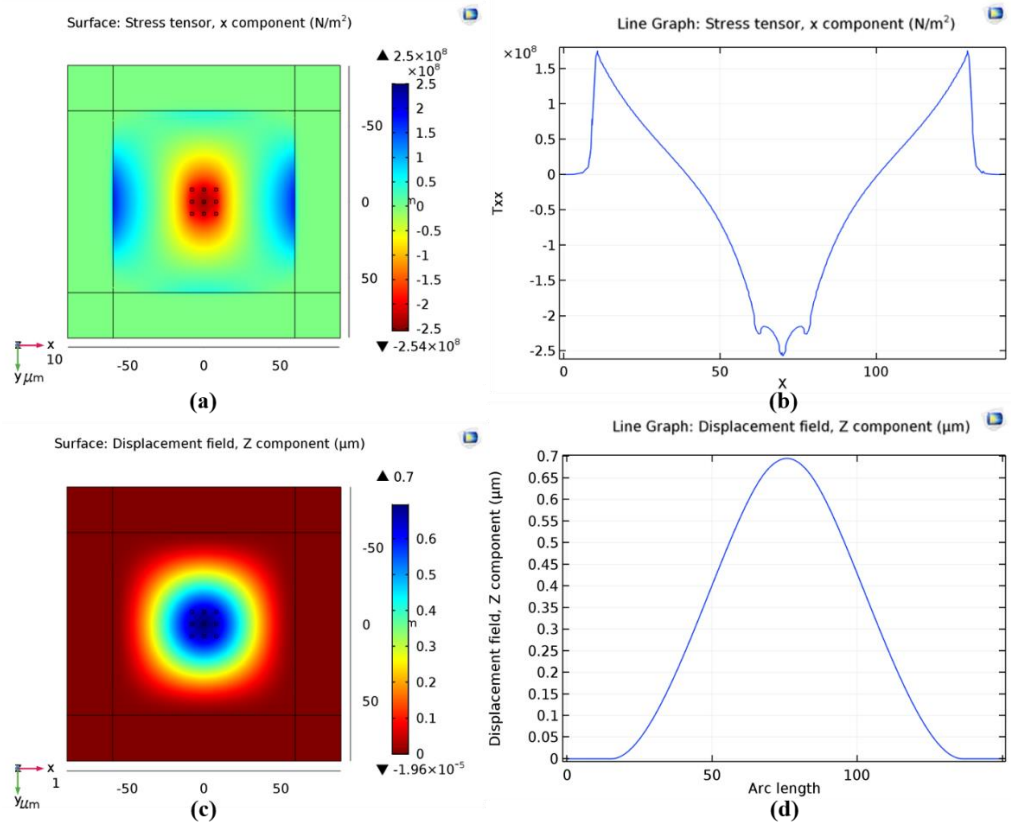

Figure 4. COMSOL simulation results of the stress and displacement of silicon nitride diaphragm caused by stiction effect. (**a**,**b**) Maximum stress occurs at the edge of the silicon nitride diaphragm, and its value is approximately 167.71 MPa; (**c**,**d**) Maximum displacement occurs at the center of the silicon nitride diaphragm, and its value is approximately 0.69 μm.

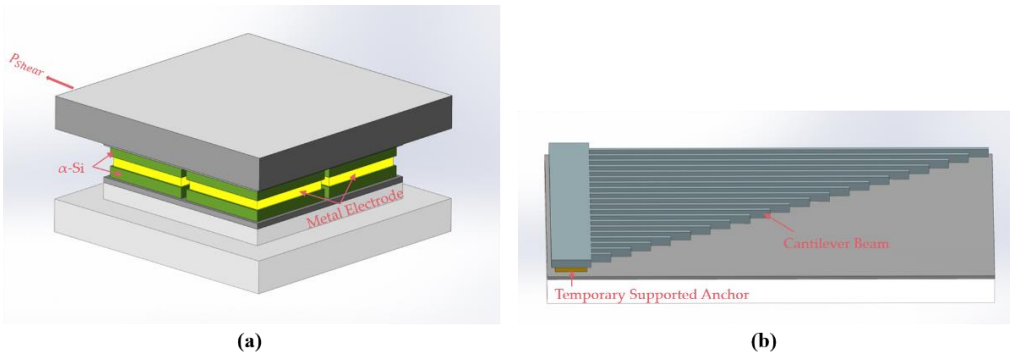

Figure 5. (**a**) Schematic of Au–Si eutectic bonding strength estimated by shear force test; (**b**) Prototype of 20 different types of cantilever beam designed to estimate the magnitude of the temporary bonding strength caused by stiction.

3. Fabrication

The process flow of the tactile sensor with a silicon nitride diaphragm is depicted in Figure 6, and the detailed fabrication process is described below.

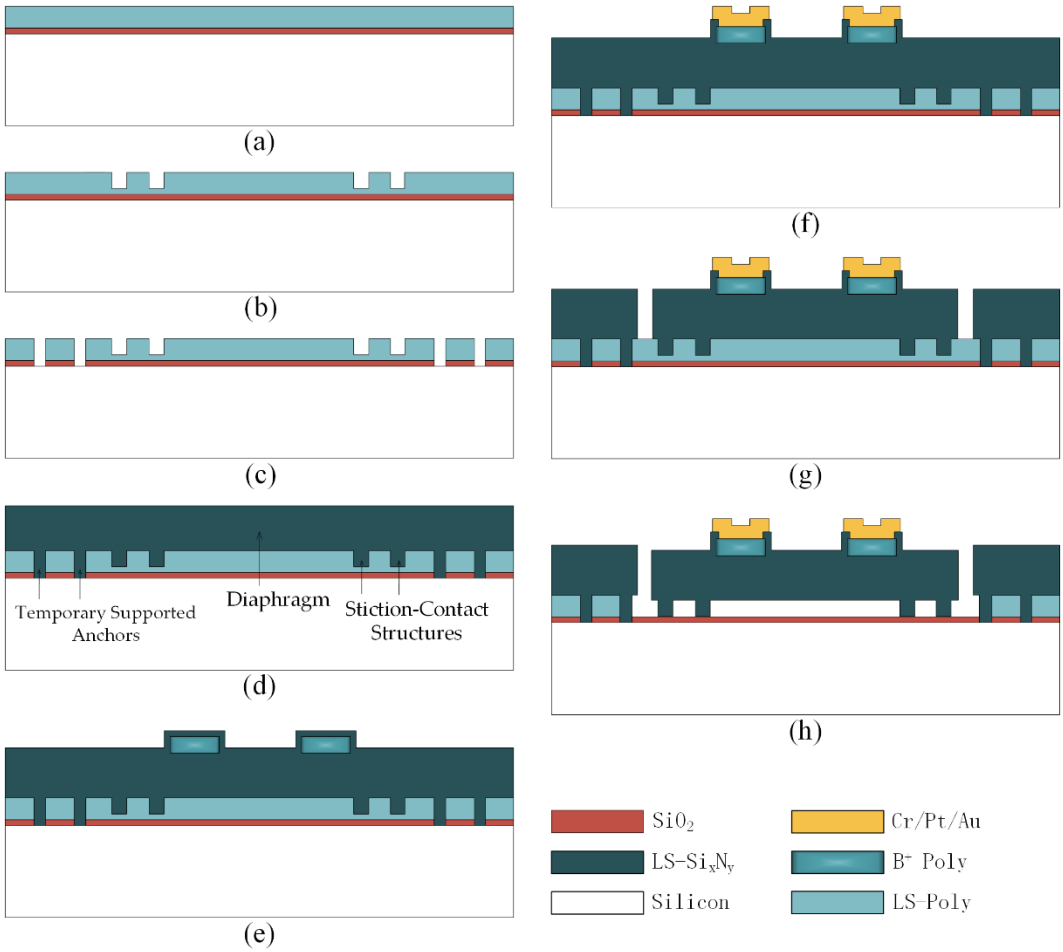

Figure 6. Process flow of the tactile sensor with a silicon nitride diaphragm. (**a**) A 450 nm-thick SiO_2 layer is thermally grown to protect the substrate, followed by the deposition of 800 nm-thick sacrificial layer; (**b**) etching and LPCVD deposition to determine the distance between the stiction-contact structures and the substrate; (**c**) etching to form the channel for temporary supported anchors; (**d**) formation of the diaphragm of the tactile sensor, stiction-contact structures, and temporary supported anchors; (**e**) the 200 nm-thick low-stress silicon nitride layer is deposited after the formation of the piezoresistors; (**f**) a composite metal layer of Cr/Pt/Au is sputtered and patterned on the piezoresisitors after the contact windows of the piezoresisitors are formed; (**g**) formation of the release channel of the polysilicon sacrificial layer; (**h**) the XeF_2 etching technique is employed to remove the polysilicon sacrificial layer, followed by the stiction-contact structures temporarily bonded to the substrate using the stiction effect.

(a) A SiO_2 layer with a thickness of 450 nm is thermally grown to protect the substrate from being damaged by the subsequent etching and release processes. Then, a layer of 800 nm-thick low-stress polysilicon is deposited as the sacrificial layer of the tactile sensor by the LPCVD technique, as shown in Figure 6a.

(b) The polysilicon is etched to the SiO_2 layer using the deep reactive ion etching (DRIE) technique. Then, a layer of 200 nm-thick low-stress polysilicon is deposited by the LPCVD technique, and its thickness determines the distance between the stiction-contact structures and the substrate, as shown in Figure 6b.

(c) The 1 µm-thick low-stress polysilicon is etched using the DRIE technique. The 450 nm-thick SiO_2 layer is subsequently etched to the silicon substrate by the reactive ion etching (RIE) technique, as shown in Figure 6c.

(d) A low-stress silicon nitride layer with a thickness of 1 µm is deposited by the LPCVD technique to form the diaphragm of the tactile sensor, stiction-contact structures, and temporary supported anchors of the silicon nitride diaphragm, as shown in Figure 6d.

(e) A 300 nm-thick LPCVD low-stress polysilicon layer is deposited and heavily doped by boron implantation, followed by the DRIE technique to form the piezoresistors of the tactile sensor. Next, a low-stress silicon nitride layer with a thickness of 200 nm is deposited by the LPCVD technique to protect the piezoresistors, as shown in Figure 6e.

(f) The 200 nm-thick low-stress silicon nitride layer is etched using the RIE technique to form the contact windows of the piezoresistors. Then, a composite metal layer of Cr/Pt/Au is sputtered and patterned on the piezoresistors, as shown in Figure 6f. The Pt layer of Cr/Pt/Au prevents the Au–Si alloy formed by the subsequent Au–Si eutectic flip-chip bonding process from penetrating the metal pads. The thicknesses of the Cr, Pt, and Au are 50 nm, 100 nm, and 300 nm, respectively.

(g) The release channel of the polysilicon sacrificial layer is formed by the DRIE technique after the 1.2 μm-thick low-stress silicon nitride layer is etched to the polysilicon sacrificial layer, as shown in Figure 6g.

(h) The XeF_2 etching technique is employed to remove the polysilicon sacrificial layer. The released device is then placed in DI water for 24 h and dried at room temperature for 24 h to bond the stiction-contact structures temporarily to the substrate using the stiction effect, as shown in Figure 6h.

The process flow of the reroute substrate is shown in Figure 7, and the detailed fabrication process is described below.

Figure 7. Process flow of the reroute substrate. (**a**) Oxidation to form the hard mask; (**b**) formation of the etching window of the KOH; (**c**) formation of the convex structure with a height of 7 μm; (**d**) deposition of the 1 μm-thick layer of amorphous silicon (α-Si) used for subsequent Au–Si eutectic bonding; (**e**) formation of the composite metal Ti/Au layer used to reroute the tactile sensor.

(a) A SiO_2 layer with a thickness of 200 nm is thermally grown as the hard mask in the following KOH wet etching process, as shown in Figure 7a.

(b) The 200 nm-thick SiO_2 layer is etched using the RIE technique to expose the etching window of the KOH, as shown in Figure 7b.

(c) A convex structure with a height of 7 μm is formed during the KOH wet etching process to provide a space for the tactile sensor after bonding, as shown in Figure 7c.

(d) A 1 μm-thick layer of amorphous silicon (α-Si) is deposited by plasma-enhanced chemical vapor deposition (PECVD) for subsequent Au–Si eutectic bonding, as shown in Figure 7d.

(e) Finally, a composite metal Ti/Au layer is sputtered on the α-Si layer to reroute the tactile sensor, in which the Ti layer is used to decompose the native oxide on the surface of the α-Si. The thicknesses of the Ti and Au are 50 nm and 400 nm, respectively, as shown in Figure 7e.

An optical microscope view of the fabricated tactile sensor and reroute substrate is shown in Figure 8. The optical microscope view of the fabricated tactile sensor is shown

in Figure 8a, and enlarged views of the temporary supported beam and the silicon nitride diaphragm of the tactile sensor are shown in Figure 8b,c, respectively. An optical microscope view of the fabricated reroute substrate is shown in Figure 8d. As Figure 8a–c show, the temporary supported beam and the silicon nitride diaphragm are colored under a microscope owing to the thin-film interference phenomenon, and the thin-film interference phenomenon is caused by the stiction, which temporarily bonds the temporary supported beam and the stiction-contact structures under the silicon nitride diaphragm to the substrate.

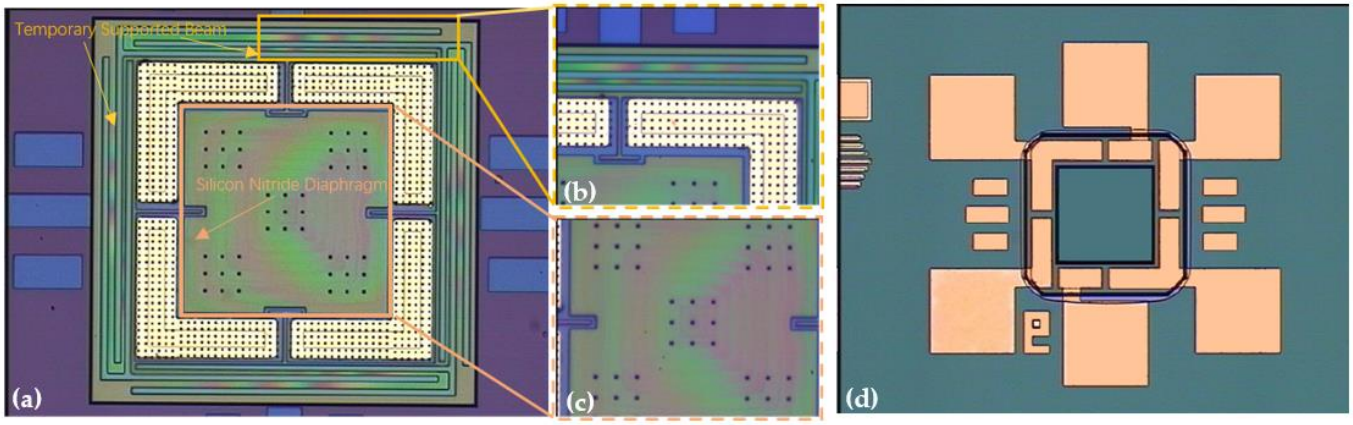

Figure 8. Optical microscope view of fabricated tactile sensor and rerouted substrate. (**a**) Optical microscope view of the fabricated tactile sensor; (**b**) enlarged optical microscope view of the temporary supported beam of the fabricated tactile sensor; (**c**) enlarged optical microscope view of the silicon nitride diaphragm of the tactile sensor; (**d**) optical microscope view of the fabricated reroute substrate.

To analyze the stiction of the fabricated tactile sensor further, scanning electron microscopy (SEM) was employed. The SEM view of the temporary supported beam of the fabricated tactile sensor is shown in Figure 9. Figure 9b shows an enlarged view of the temporary supported beam shown in Figure 9a. As the Figure shows, the temporary supported beam is temporarily bonded to the substrate owing to the stiction effect.

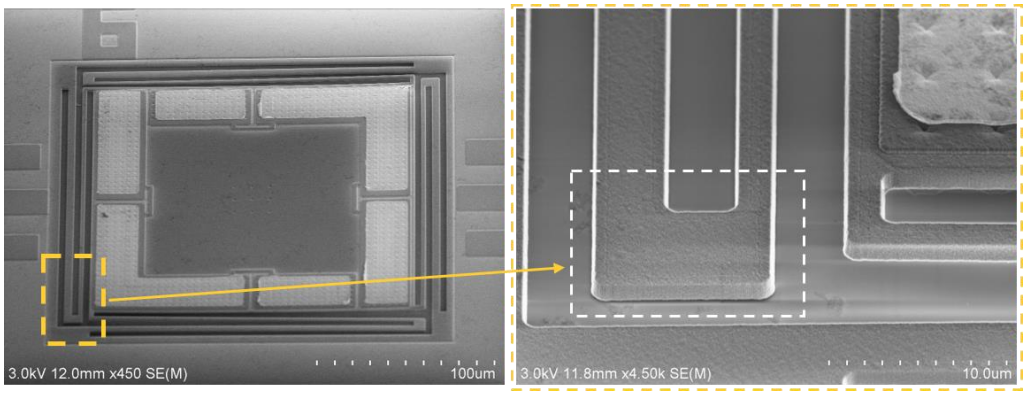

(**a**) (**b**)

Figure 9. Scanning electron microscopy (SEM) view of the temporary supported beam of the fabricated tactile sensor. (**a**) SEM view of the fabricated tactile sensor; (**b**) enlarged view of the temporary supported beam shown in (**a**).

4. Results and Discussion

The fabricated tactile sensor was first bonded to the reroute substrate by Fintech FinePlacer Lambda (Finetech GmbH & Co. KG, Berlin, Germany), and the temperature, force, and time of the flip-chip bonding process were 380 °C, 20 N, and 300 s, respectively.

Then, the tactile sensor was transferred to the reroute substrate by applying a pulling force perpendicular to the bonded device, as shown in Figure 10. The tactile sensors with the designed stiction-contact structure areas from 2916 to 9000 μm^2 were transferred to the reroute substrate, and the optical microscopic view of the transferred devices with minimum and maximum stiction-contact structure areas are shown in Figure 10a,b, respectively. The metal bonding electrode deviations between the tactile sensor and the reroute substrate were measured to estimate the precision of the transferred device after the flip-chip bonding process, as shown in Figure 11. The metal electrode deviations of the top, right, bottom, and left are shown in Figure 11b–e, respectively. As shown in Figure 11b–e, the maximum measured deviation after the flip-chip bonding process is approximately 1.5 μm, which is sufficient for the proposed SETH integration process.

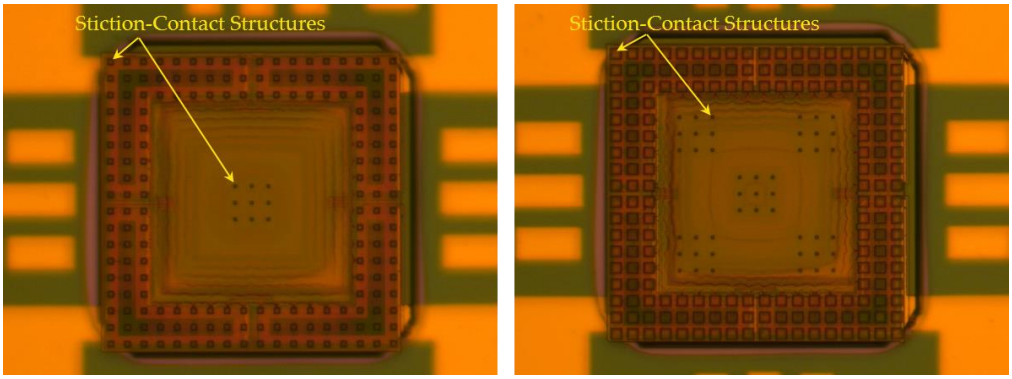

Figure 10. Optical microscopic view of the transferred devices. (**a**) Transferred device with minimum areas (2916 μm^2) of stiction-contact structures; (**b**) Transferred device with maximum areas (9000 μm^2) of stiction-contact structures.

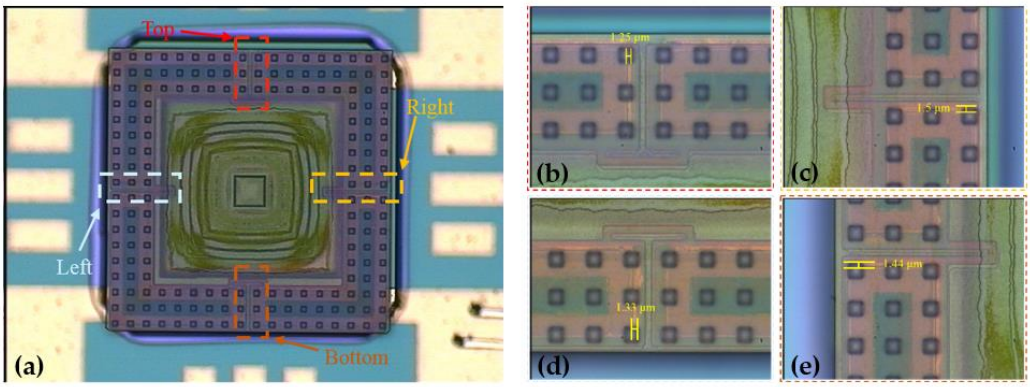

Figure 11. Microscopic view of transferred device and flip-chip bonding precision after the Au–Si eutectic flip-chip bonding process. (**a**) Microscopic view of transferred device; (**b**–**e**) Deviations of the top, right, bottom, and left metal electrode between the tactile sensor and the reroute substrate of approximately 1.25, 1.5, 1.33, and 1.44 μm, respectively.

SEM was employed to analyze further the broken area of the temporary support beams of the tactile sensor after the transfer process. The SEM view of the broken area of the temporary support structures of the tactile sensor is shown in Figure 12a, and Figure 12b–d shows an enlarged SEM view of the broken area shown in Figure 12a. As Figure 12b–e show, the broken area was at the edge of the metal bonding electrode, and the silicon nitride diaphragm of the tactile sensor was not damaged after the transfer process.

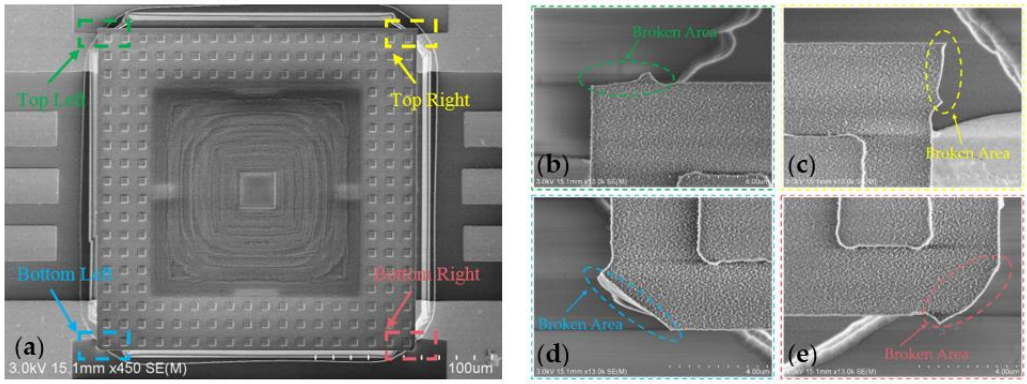

Figure 12. SEM view of the broken area of the temporary support structures of the tactile sensor. (**a**) SEM view of transferred device; (**b**–**e**) enlarged SEM views of the broken area shown in (**a**).

As Figures 11a and 12a show, the size of the transferred tactile sensor is 180 μm × 180 μm × 1.2 μm, and the force area of the tactile sensor is only 120 μm × 120 μm × 1.2 μm. Moreover, the force application accuracy is extremely high because the designed full-scale force of the designed tactile sensor is only approximately 0.5 mN, and there is no suitable instrument to measure the sensitivity of the transferred tactile sensor directly. Therefore, different masses of the beam-shaped copper wire weights with a diameter of 85 μm are made to measure the sensitivity of the transferred tactile sensor, and the measurement principle of the beam-shaped copper wire weight is shown in Figure 13. As Figure 13 shows, one end of the beam-shaped copper wire weight is placed on the sensitive membrane of the transferred tactile sensor, and the other end is placed on the test stage. The force applied to the transferred tactile sensor is half of the mass of the beam-shaped copper wire weight.

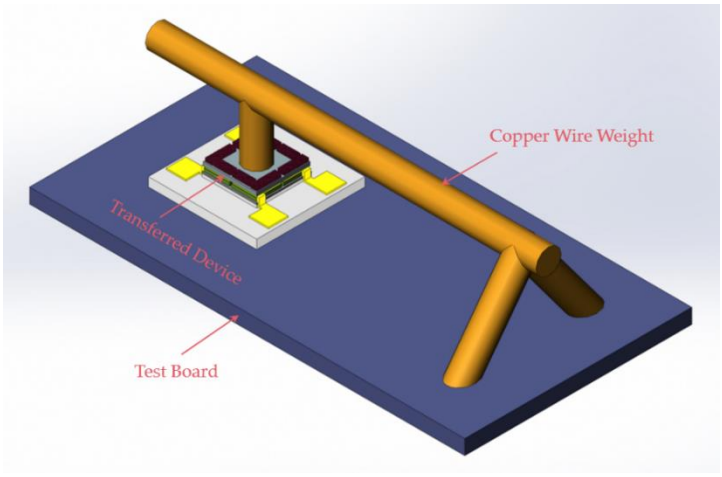

Figure 13. Schematic of the measurement principle of beam-shaped copper wire weights.

As the tip of the copper wire weight is hard and uneven, which will damage the 1.2 μm-thick silicon nitride diaphragm of the tactile sensor when the copper wire weight is placed on the silicon nitride diaphragm, the surface of the copper wire weight is wrapped with a layer of HT901 silicon adhesive sealant and cured for 24 h at room temperature to make soften the tip of the copper wire weight. A layer of CRC PLASTICOTE 70 clear protective lacquer is then coated on the surface of the cured silicon adhesive sealant and cured for 12 h at room temperature to prevent the adhesive force of the silicon adhesive sealant from damaging the 1.2 μm-thick silicon nitride diaphragm, as shown in Figure 14. The masses of the different beam-shaped copper wire weights are measured using a Mettler Toledo AL104, with a readability of 0.1 mg, and the test results are shown in Table 1. The

different masses of the manufactured beam-shaped copper wire weights are shown in Figure 15.

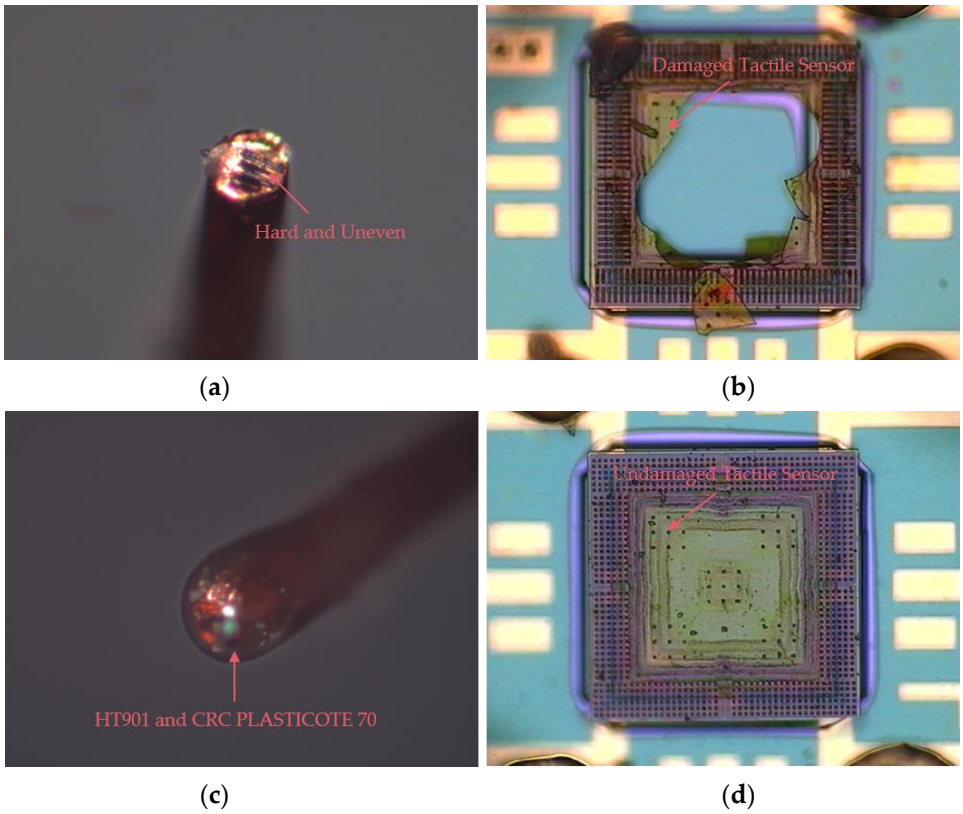

Figure 14. Tip of the copper wire weight. (**a**) The tip of the copper wire weight is hard and uneven; (**b**) The 1.2 μm-thick silicon nitride diaphragm is damaged during the test; (**c**) The layer of CRC PLASTICOTE 70 clear protective lacquer coated on the surface of the cured silicon adhesive sealant prevents the 1.2-μm-thick silicon nitride diaphragm from being damaged during the test; (**d**) The 1.2 μm-thick silicon nitride diaphragm is not damaged after the test.

Table 1. Different masses of the beam-shaped copper wire weights measured by Mettler Toledo AL104.

Number	Measured Mass (mg)	Pressure Applied on Transferred Device (kPa)
1	9.2	3.1
2	17.2	5.9
3	26.7	9.1
4	35.9	12.2
5	43.3	14.7
6	50.2	17.1

The experimental setup used for measuring the sensitivity of the tactile sensor is shown in Figure 16. As shown in Figure 16, the input voltage of the Wheatstone bridge formed by the four piezoresistors of the transferred tactile sensor was first set to 5 V by Agilent E3631A (Agilent Tec., Santa Clara, CA, USA), and the corresponding output voltage value of the Wheatstone bridge was then recorded using Agilent 34401A when different masses of the beam-shaped copper wire weights were placed on the force area of the transferred tactile sensor under the microscope. The sensitivity measurement results of the tactile sensors are shown in Figure 17. As Figure 17 shows, the power supply of the transferred tactile sensor is 5 V, the output voltage of the Wheatstone bridge changes from 0 to 23.22 mV when the pressure applied to the transferred tactile sensors changes from 0

to 17.1 kPa, and the sensitivity of the four transferred tactile sensors are 0.22 mV/V/kPa, 0.26 mV/V/kPa, 0.27 mV/V/kPa and 0.27 mV/V/kPa, separately.

Figure 15. Different masses of manufactured beam-shaped copper wire weights.

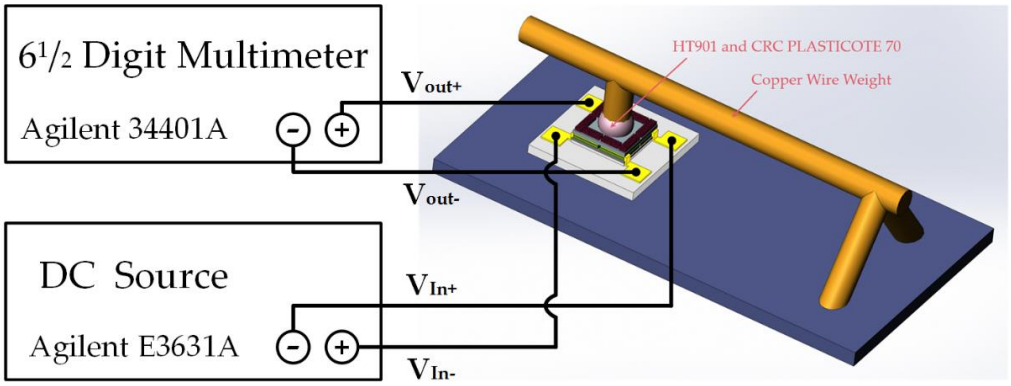

Figure 16. Schematic of the actual measurement setup.

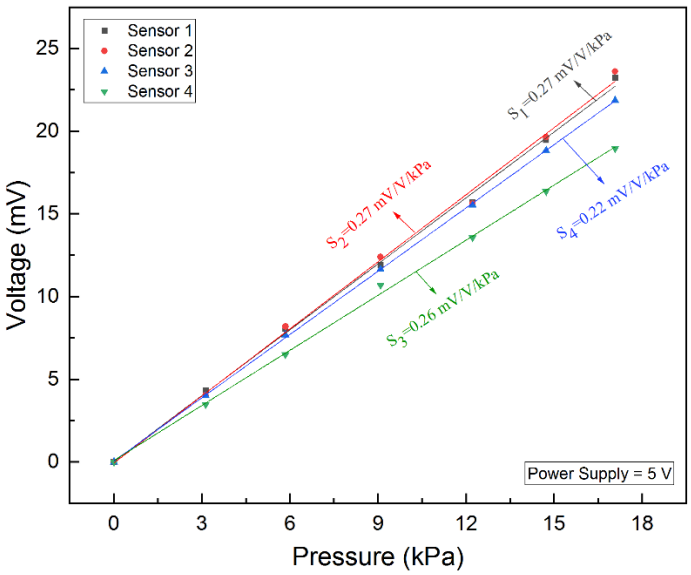

Figure 17. Sensitivity measurement result of the transferred tactile sensors.

Because the stress caused by the Au–Si eutectic flip-chip bonding process will affect the resistance of the four piezoresistors slightly, the output voltages of the Wheatstone bridge of the transferred tactile sensor were measured by an MPI TS2000-SE four-point probe before and after the flip-chip bonding process to estimate the stress caused by the Au–Si eutectic flip-chip bonding process, and the test result is shown in Figure 18. As Figure 18 shows, the output voltage difference of the Wheatstone bridge before and after the flip-chip bonding process was obtained from −7.76 to +7.25 mV, and the corresponding stress can be calculated from −5.83 kPa to +5.54 kPa, which indicated that the stress caused by the Au–Si eutectic flip-chip bonding process can be acceptable [32].

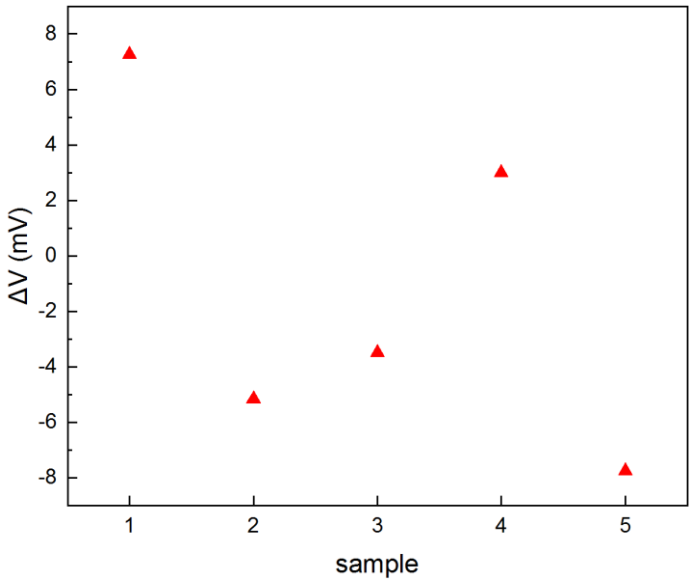

Figure 18. Output voltage difference of the Wheatstone bridge before and after the flip-chip bonding process.

The shear strength of the Au–Si eutectic bonding was tested using a Dage Series 4000 Bondtester (Nordson TEST & INSPECTION, Aylesbury, Buckinghamshire, UK), and the test structure is shown in Figure 4a. The area of the metal electrodes used for the Au–Si eutectic bond was approximately 0.34 mm^2. The shear strength of the bonded test structure was approximately 30.74 MPa. To estimate the temporary bonding strength caused by stiction, the tips of silicon nitride cantilever beams with a length larger than 80 μm were then bonded to the substrate after the designed test structures shown in Figure 4b were placed in deionized (DI) water for 24 h and dried at room temperature for 24 h. The optical microscopic and SEM views of the cantilever beams are shown in Figure 19a–d, respectively. As the designed distance between the silicon nitride cantilever beams and substrate was 1 μm, using Equation (6), the temporary bonding strength can be calculated to be larger than 7.06 kPa and less than 22.31 kPa. Due to the bonding strength of the transferred tactile sensors are much larger than the temporary bonding strength caused by stiction, the tactile sensors can be easily transferred to the reroute substrate, and the yield of the transferred tactile sensors is as high as 90%.

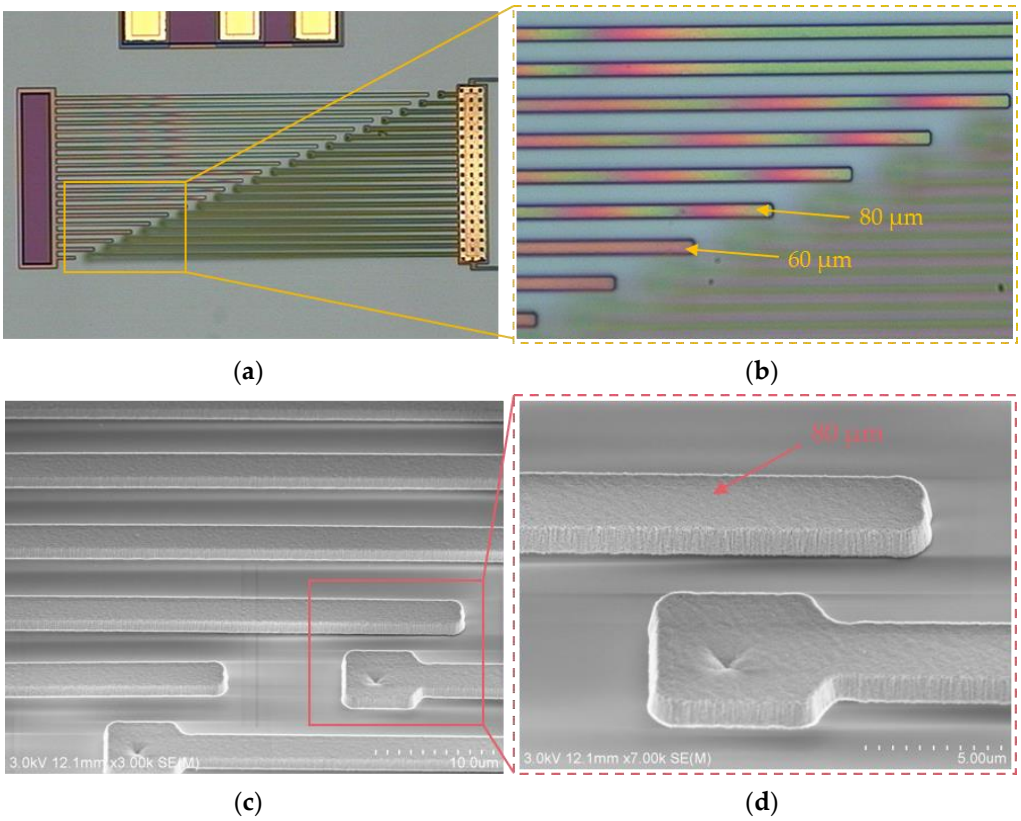

Figure 19. Optical microscopic and SEM views of the cantilever beams after drying at room temperature for 12 h. (**a**) Optical microscopic view of the silicon nitride cantilever beams; (**b**) enlarged optical microscope view of the silicon nitride cantilever beams shows that the tips of silicon nitride cantilever beams longer than 80 μm are bonded to the substrate; (**c**) SEM views of the silicon nitride cantilever beams; (**d**) enlarged SEM view of the silicon nitride cantilever beams shows that the tips of silicon nitride cantilever beams longer than 80 μm are bonded to the substrate.

5. Conclusions

This paper presented a novel method for CMOS-compatible batch transfer of tactile sensors using SETH process and Au–Si eutectic flip-chip bonding process, which allowed the tactile sensor and the CMOS devices to be manufactured separately to simplify the MEMS/CMOS integration process, improve the process reliability, and electrical performance, and reduce material constriction. The tactile sensor with a low-stress silicon nitride diaphragm was transferred to the reroute substrate successfully. The size of the transferred tactile sensor was as small as 180 μm × 180 μm × 1.2 μm, and the force area of the tactile sensor was only 120 μm × 120 μm × 1.2 μm. The tactile sensor was released and placed into deionized (DI) water for 24 h to bond the stiction-contact structures temporarily to the substrate through the stiction effect, thereby avoiding the damage and movement of the diaphragm of the tactile sensor during subsequent flip-chip bonding. The temporary bonding strength was calculated to be larger than 7.06 kPa and less than 22.31 kPa. The maximum misalignment of the flip-chip bonding process was approximately 1.5 μm. The stress caused by the Au–Si eutectic flip-chip bonding was from −5.83 to + 5.54 kPa. The tactile sensors were tested from 0 to 17.1 kPa, resulting in a sensitivity of 0.22 mV/V/kPa, 0.26 mV/V/kPa, 0.27 mV/V/kPa and 0.27 mV/V/kPa, separately. The shear strength of the bonded test structure was approximately 30.74 MPa and the yield of the transferred tactile sensors is as high as 90%.

Author Contributions: P.Z. contributed to the whole work, including design, fabrication, and testing of the device; K.S. contributed to the test idea; C.Z. helped to implement part of the fabrication;

H.Y. contributed to the research idea and provided guidance to the work; X.L. contributed research guidance to the work. All authors have read and agreed to the published version of the manuscript.

Funding: This work was funded by The National Natural Science Foundation of China (61734007).

Acknowledgments: The authors appreciate the financial support from the National Natural Science Foundation of China (61734007) and Shanghai Municipal Science and Technology Commission (project 18dz1100600). The authors also appreciate the assistance of the engineers at the State Key Laboratory of Transducer Technology.

Conflicts of Interest: The authors declare no conflict of interest.

References

1. Ishihara, T.; Suzuki, K.; Suwazono, S.; Hirata, M.; Tanigawa, H. CMOS integrated silicon pressure sensor. *IEEE J. Solid-State Circuits* **1987**, *22*, 151–155. [CrossRef]
2. Lo, C.-C.; Chen, F.; Fedder, G.K. Integrated HF CMOS-MEMS square-frame resonators with on-chip electronics and electrothermal narrow gap mechanism. In Proceedings of the IEEE International Conference on Solid-State Sensors, Seoul, Korea, 5–9 June 2005; pp. 2074–2077.
3. Tsai, M.H.; Liu, Y.C.; Liang, K.C.; Fang, W. Monolithic CMOS-MEMS pure oxide tri-axis accelerometers for temperature stabilization and performance enhancement. *J. Microelectromech. Syst.* **2015**, *24*, 1916–1927. [CrossRef]
4. Merdassi, A.; Yang, P.; Chodavarapu, V. A wafer level vacuum encapsulated capacitive accelerometer fabricated in an unmodified commercial MEMS process. *Sensors* **2015**, *15*, 7349–7359. [CrossRef] [PubMed]
5. Niklaus, F.; Andreas, C.F. Heterogeneous 3D integration of MOEMS and ICs. In Proceedings of the IEEE International Conference on Optical Mems & Nanophotonics, Singapore, 31 July–4 August 2016; pp. 1–2.
6. Yang, H.S.; Bakir, M.S. Interconnect Technologies for Heterogeneous 3D Integration: CMOS and MEMS. *Mater. Res. Soc. Symp. Proc.* **2010**, *1249*, 1249–1261. [CrossRef]
7. Qu, H. CMOS MEMS Fabrication Technologies and Devices. *Micromachines* **2016**, *7*, 14. [CrossRef] [PubMed]
8. Andreas, C.F.; Fredrik, F.; Martin, L.; Simon, J.B.; Stemme, G.; Roxhed, N.; Niklaus, F. Integrating MEMS and ICs. *Microsyst. Nanoeng.* **2015**, *1*, 15505.
9. Uranga, A.; Verd, J.; Barniol, N. CMOS-MEMS resonators: From devices to applications. *Microelectron. Eng.* **2015**, *132*, 58–73. [CrossRef]
10. Fedder, G.K.; Howe, R.T.; Liu, T.J.K.; Quevy, E.P. Technologies for cofabricating MEMS and electronics. *Proc. IEEE* **2008**, *96*, 306–322. [CrossRef]
11. Basavanhally, N.; Lopez, D.; Aksyuk, V.; Ramsey, D.; Bower, E.; Cirelli, R.; Ferry, E.; Frahm, R.; Gates, J.; Klemens, F.; et al. High-Density Solder Bump Interconnect for MEMS Hybrid Integration. *IEEE Trans. Adv. Packag.* **2007**, *30*, 622–628. [CrossRef]
12. Cohn, M.B.; Böhringer, K.F.; Noworolski, J.M.; Singh, A.; Keller, C.G.; Goldberg, K.Y.; Howe, R.T. Microassembly technologies for MEMS. *Proc. SPIE Micromach. Microfabr.* **1998**, *3513*, 2–16.
13. Singh, A.; Horsley, D.A.; Cohn, M.B.; Pisano, A.P.; Howe, R.T. Batch transfer of microstructures using flip-chip solder bonding. *IEEE J. Microelectomechanical Syst.* **1999**, *8*, 27–33. [CrossRef]
14. Fischer, A.C.; Korvink, J.G.; Roxhed, N.; Stemme, G.; Wallrabe, U.; Niklaus, F. Unconventional applications of wire bonding create opportunities for microsystem integration. *J. Micromechanics Microengineering* **2013**, *23*, 083001. [CrossRef]
15. Waber, T.; Pahl, W.; Schmidt, M.; Feiertag, G.; Stufler, S.; Dudek, R.; Leidl, A. Flip-chip packaging of piezoresistive barometric pressure sensors. *Proc. SPIE* **2013**, *8763*, 87632D1–87632D8.
16. Oouchi, A. Plastic molded package technology for MEMS sensor evolution of MEMS sensor package. In Proceedings of the 2014 International Conference on Electronics Packaging (ICEP), Toyama, Japan, 23–25 April 2014; pp. 371–375.
17. Baltes, H.; Brand, O. CMOS-based microsensors and packaging. *Sens. Actuators A Phys.* **2001**, *92*, 1–9. [CrossRef]
18. Liu, M.C.; Dai, C.L.; Chan, C.H.; Wu, C.C. Manufacture of a polyaniline nanofiber ammonia sensor integrated with a readout circuit using the CMOS-MEMS technique. *Sensors* **2009**, *9*, 869–880. [CrossRef] [PubMed]
19. Baltes, H.; Brand, O.; Hierlemann, A.; Lange, D.; Hagleitner, C. CMOS MEMS—Present and Future. In Proceedings of the Fifteenth IEEE International Conference on Micro Electro Mechanical Systems, Las Vegas, NV, USA, 24 January 2002; pp. 459–466.
20. Toshifumi, K.; Daisuke, Y.; Takaaki, M.; Motohashi, G.; Kagaya, K.; Ito, H.; Ishihara, N.; Toshiyoshi, H.; Machida, K.; Masu, K.; et al. Novel Sensor Structure and Its Evaluation for Integrated Complementary Metal Oxide Semiconductor Microelectromechanical Systems Accelerometer. *Jpn. J. Appl. Phys.* **2013**, *52*, 06GL04.
21. Baltes, H.; Brand, O.; Fedder, G.K.; Hierold, C.; Korvink, J.G.; Tabata, O. CMOS—MEMS. *Adv. Micro Nanosyst.* **2005**, *2*, 43–56.
22. Witvrouw, A. CMOS-MEMS Integration: Why, How, and What? In Proceedings of the IEEE ACM International Conference on Computer-Aided Design, San Jose, CA, USA, 5–9 November 2006; pp. 826–827.
23. Yang, H.S.; Bakir, M.S. 3D integration of CMOS and MEMS using mechanically flexible interconnects (MFI) and through silicon vias (TSV). In Proceedings of the Electronic Components and Technology Conference, Las Vegas, NV, USA, 1–4 June 2010; pp. 822–828.
24. Fearing, R.S. Survey of sticking effects for Micro parts handling. *IEEE Int. Conf. Intell. Robot. Syst.* **1995**, *2*, 212–217.

25. Chuang, W.H.; Luger, T.; Fetting, R.K.; Ghodssi, R. Mechanical Property Characterization of LPCVD Silicon Nitride Thin Films at Cryogenic Temperatures. *J. Microelectromechanical Syst.* **2004**, *13*, 870–879. [CrossRef]
26. Alley, R.L.; Cuan, G.J.; Howe, R.T.; Komvopoulos, K. The effect of release-etch processing on surface microstructure stiction. In Proceedings of the Tech Digest IEEE Solid-state Sensor & Actuator Workshop, Hilton Head, SC, USA, 22–25 June 1992; pp. 202–207.
27. Rob, L.; Tilmans, A.C.; Elders, J.; Elwenspoek, M. Stiction of surface micromachined structures after rinsing and drying: Model and investigation of adhesion mechanisms. *Sens. Actuators A Phys.* **1994**, *43*, 230–238.
28. Scheeper, P.R.; Voorthuyzen, J.A.; Olthuis, W.; Bergveld, P. Investigation of attractive forces between PECVD silicon nitride microstructures and an oxidized silicon substrate. *Sens. Actuators A Phys.* **1992**, *30*, 231–239. [CrossRef]
29. Krupp, H. Particle adhesion theory and experiment. *Adv. Coll. Interf. Sci.* **1967**, *1*, 111–239.
30. Haisma, J.; Spierings, G.A.C.M.; Biermann, U.K.P.; Pals, J.A. Silicon-on-Insulator wafer bonding-wafer thinning technological evaluations. *Jpn. J. Appl. Phys.* **1989**, *28*, 1426–1443. [CrossRef]
31. Jing, E.; Xiong, B.; Wang, Y.L. Low-temperature Au/a-Si wafer bonding. *J. Micromach. Microeng.* **2011**, *21*, 015013. [CrossRef]
32. Aron, M.; Kwok, C.Y. Evaporated Thick Polysilicon Film with Low Stress and Low Thermal Budget. *J. Microelectromechanical Syst.* **2013**, *22*, 825–827.

MDPI
Grosspeteranlage 5
4052 Basel
Switzerland
www.mdpi.com

Micromachines Editorial Office
E-mail: micromachines@mdpi.com
www.mdpi.com/journal/micromachines

Academic Open
Access Publishing

mdpi.com

ISBN 978-3-7258-1543-2